Department of Chemistry
University of Liège

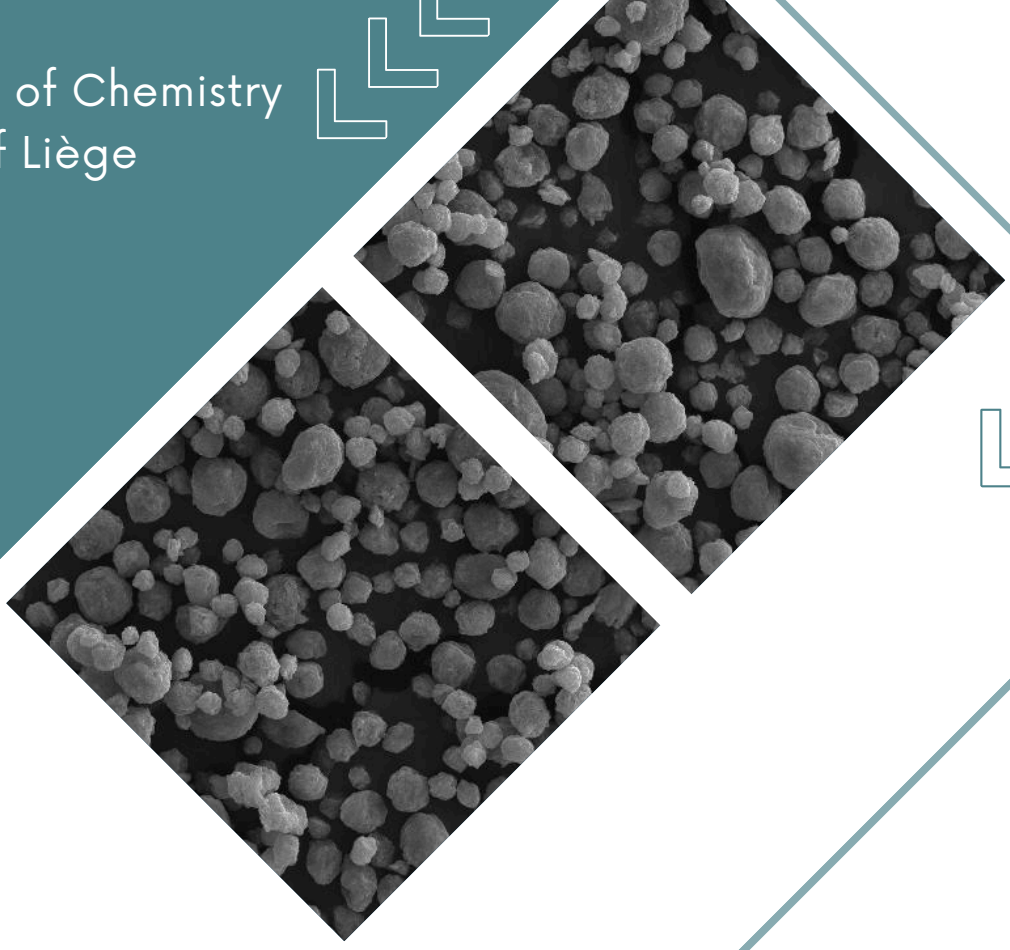

Design and Development of Advanced Electrode Materials for Li-ion and Zn-ion Batteries

Thesis submitted by Edith Roex
for the degree of Doctor in Sciences

2023-2024

LIÈGE université Sciences

Greenmat

Design and Development of Advanced Electrode Materials for Li-ion and Zn-ion batteries

Thesis presented by Edith Roex
For the grade of Doctor in Sciences
at Department of Chemistry
University of Liège

September 2024

Assessment committee

Prof. Gauthier Eppe	President	University of Liège
Prof. Frédéric Hatert	Secretary	University of Liège
Dr. Frédéric Boschini	Supervisor	University of Liège
Dr. Abdelfattah Mahmoud	Co-supervisor	University of Liège
Dr. Jolanta Swiatowska	Examiner	CNRS-Chimie ParisTech
Dr. Pierre-Emmanuel Lippens	Examiner	University of Montpellier
Dr. Nicolas Eshraghi	Examiner	Umicore

Abstract

Global energy demand is rapidly increasing and is projected to double by 2050, creating a need for reliable electricity supply and efficient energy storage systems. Renewable energies like solar and wind are promising but require effective storage solutions to manage intermittency. Lithium-ion batteries (LIBs) are popular thanks to their high energy density and long cycle life but face challenges in cost, material availability, and safety. Rechargeable aqueous zinc-ion batteries (ZIBs) are emerging as a promising alternative for grid storage applications. This thesis explores both LIBs and ZIBs to address energy storage needs for various applications.

The first part of this work focuses on developing and designing new anode materials for LIBs. Novel organopalladium complexes are investigated, with the iodo-organopalladium complex showing the highest specific capacity and excellent cycling stability. The structural and morphological properties were examined by combining several characterization techniques: NMR, XRD, SEM, and TEM. The particles morphology of the iodo-organopalladium complex is then optimized using the double emulsion-evaporation technique to enhance its electrochemical performance.

The second part of this thesis shifts to aqueous zinc-ion batteries, emphasizing the need for stable and efficient cathode active materials. Vanadium pentoxide (V_2O_5) is identified as a promising candidate but faces challenges like vanadium dissolution, low electronic conductivity, structural collapse, and volume changes caused by Zn^{2+} insertion/extraction during cycling. Therefore, in this work, we investigate several solutions to address these issues and enhance the cathode material performance. V_2O_5 microspheres are first produced via a spray-drying process. A comparative analysis of spray-dried V_2O_5, spray-dried V_2O_5/xCNTs composites, and commercial V_2O_5 highlights the benefits of morphological design and carbon nanotubes addition in enhancing the electrochemical performance of V_2O_5 as cathode material for zinc-ion batteries. Then, in order to prevent the dissolution of vanadium pentoxide, a novel V_2O_5/polydopamine/CNT electrode is developed, showing outstanding performance and long-term stability. Another strategy concerning the introduction of Na^+ ions into the structure of V_2O_5 was explored in this thesis. This part presents the synthesis of three pure sodium vanadium oxide phases through an aqueous route: $Na_2V_6O_{16}\cdot 1.5H_2O$, $Na_{0.33}V_2O_5$ and $Na_{1.16}V_3O_8$. The high-temperature XRD analysis

was coupled with TGA/DSC to investigate the formation mechanism of the non-hydrated phases. The comparison of these materials reveals that the hydrated $Na_2V_6O_{16}\cdot 1.5H_2O$ material offers the highest specific capacity and superior cycling stability due to the stabilizing effect of sodium ions and water.

As the final step of this research, we evaluate the spray-dried V_2O_5 and the three sodium vanadium oxide materials developed during this thesis in larger-scale pouch-type zinc-ion batteries. Although the capacities achieved are nearly comparable to those in Swagelok cells, the results emphasize the necessity for further optimization in pouch cell configuration and electrode preparation to improve cycle life for large-scale ZIB applications.

The different strategies investigated in this work allowed us to enhance the electrochemical performance of both LIBs and aqueous ZIBs.

Résumé

La demande énergétique mondiale augmente rapidement et devrait doubler d'ici 2050, créant un besoin crucial pour une alimentation électrique fiable et des systèmes de stockage d'énergie efficaces. Les énergies renouvelables telles que le solaire et l'éolien sont prometteuses, mais nécessitent des solutions de stockage efficaces pour gérer leur intermittence. Les batteries lithium-ion sont populaires en raison de leur haute densité énergétique et de leur longue durée de vie, mais elles rencontrent des défis en termes de coût, de disponibilité des matériaux et de sécurité. Les batteries zinc-ion aqueuses émergent comme une alternative prometteuse pour le stockage et la conversion d'énergie à l'échelle du réseau. Cette thèse explore à la fois les batteries lithium-ion et les batteries zinc-ion aqueuses pour répondre aux besoins de stockage d'énergie pour diverses applications.

La première partie de ce travail se concentre sur le développement et la conception de nouveaux matériaux d'anode pour les batteries Li-ion. Trois complexes organo-palladium novateurs sont étudiés et le complexe iodo-organo-palladium delivre la plus haute capacité spécifique et offre une excellente stabilité de cyclage. Les propriétés structurales et morphologiques ont été étudiées en combinant plusieurs techniques de caractérisation telles que la RMN, la DRX, la MEB et la MET. La morphologie des particules du complexe iodo-organopalladium est ensuite optimisée par double émulsion-évaporation pour améliorer les performances électrochimiques.

La deuxième partie de cette thèse se concentre sur les batteries aqueuses zinc-ion, en mettant l'accent sur la nécessité de développer des matériaux actifs de cathode stables et efficaces. Le pentoxyde de vanadium (V_2O_5) est identifié comme un candidat prometteur mais rencontre des problèmes tels que la dissolution du vanadium, une faible conductivité électronique, une dégradation de la structure et des variations de volume causés par l'insertion/extraction des ions zinc lors du cyclage. Par conséquent, ce travail explore plusieurs solutions pour résoudre ces problèmes et améliorer les performances du matériau de cathode. Des microsphères de V_2O_5 sont d'abord produites via un processus de séchage par atomisation. Une analyse comparative du V_2O_5 commercial, du V_2O_5 et des composites V_2O_5/xCNTs préparés par la méthode de séchage par atomisation met en évidence les avantages du contrôle de la morphologie et de l'ajout de nanotubes de carbone pour améliorer les performances électrochimiques du V_2O_5 en tant que matériau actif de cathode pour les

batteries zinc-ion. Ensuite, afin de limiter la dissolution du pentoxyde de vanadium, une nouvelle électrode V_2O_5/polydopamine/CNT est développée, montrant des performances électrochimiques exceptionnelles avec une bonne stabilité à long terme. Une autre stratégie concernant l'introduction d'ions Na^+ pour stabiliser la structure du V_2O_5 lors du cyclage a été explorée dans cette thèse. Cette partie présente la synthèse par voie aqueuse de trois phases d'oxyde de vanadium et de sodium : $Na_2V_6O_{16}\cdot 1.5H_2O$, $Na_{0.33}V_2O_5$ and $Na_{1.16}V_3O_8$. L'analyse par DRX à haute température a été couplée à l'ATG/DSC pour étudier le mécanisme de formation des phases non hydratées. La comparaison de ces trois matériaux révèle que le matériau hydraté $Na_2V_6O_{16}\cdot 1.5H_2O$ offre la plus haute capacité spécifique et une stabilité de cyclage supérieure grâce à l'effet stabilisant des ions sodium et des molécules d'eau.

Pour clôturer cette thèse, nous évaluons le V_2O_5 obtenu par atomisation et les trois matériaux d'oxyde de vanadium et de sodium développés pendant cette thèse dans des batteries zinc-ion de type « pouch-cell ». Il est important de tester les matériaux à plus grande échelle afin d'évaluer leur capacité à répondre aux exigences de performances et de durabilité des batteries commerciales. Bien que les capacités atteintes soient presque comparables à celles obtenues en cellules Swagelok (échelle laboratoire), les résultats soulignent la nécessité d'une optimisation supplémentaire de la configuration des « pouch-cells » et de la préparation des électrodes pour améliorer la durée de vie pour les applications à grande échelle.

Les différentes stratégies mises en place dans ce travail nous ont permis d'améliorer les performances électrochimiques des batteries Li-ion et des batteries Zn-ion aqueuses.

Table of contents

List of figures

List of tables

List of abbreviations

at. %	Atomic percentage
BET	Brunauer–Emmett–Teller
CB	Carbon Black
CE	Coulombic Efficiency
Complex 3	$IPd(4\text{-}AcOC_6H_4)(PPh_3)_2$
Complex 4	$BrPd(4\text{-}AcOC_6H_4)(PPh_3)_2$
Complex 5	$ClPd(4\text{-}AcOC_6H_4)(PPh_3)_2$
CNT	Carbon NanoTube
CV	Cyclic Voltammetry
EC	Ethylene Carbonate
EDX	Energy Dispersive X-ray Spectroscopy
EIS	Electrochemical Impedance Spectroscopy
DFT	Density Functional Theory
DMC	Dimethyl Carbonate
DSC	Differential Scanning Calorimetry
FTIR-ATR	Fourier Transformed Attenuated Total Reflectance Infrared
FWHM	Full Width at Half Maximum
HTXRD	High-Temperature X-Ray Diffraction
LIB	Lithium-Ion Battery
MWCNT	Multi Walled Carbon Nanotube
NIB	Sodium-Ion Battery
NMR	Nuclear Magnetic Resonance
NMP	N-Methyl-2-Pyrrolidone
NVO	Sodium Vanadium Oxide
OCV	Open Circuit Voltage
PC	Propylene Carbonate
PDA	PolyDopAmine
PVDF	PolyVinyliDene Fluoride
R_{ct}	Charge Transfer Resistance
R_{ele}	Electrolyte Resistance
SD	Spray-Dried
SEI	Solid Electrolyte Interface
SEM	Scanning Electron Microscopy
TEM	Transmission Electron Microscopy
TGA	ThermoGravimetric Analysis
TMS	TétraMéthylSilane
V_2O_5	Vanadium pentoxide

V_2O_5/PDA/CNT	Self-standing electrode of vanadium pentoxide encapsulated by polydopamine
V_2O_5-SD	Spray-dried vanadium pentoxide
V_2O_5/xCNTs	Spray-dried vanadium pentoxide with x wt% of carbon nanotubes
vs	versus
wt%	weight percentage
XPS	X-Ray Photoelectron Spectroscopy
XRD	X-Ray Diffraction
ZIB	Zinc-Ion Battery
$Zn(CF_3SO_3)_2$	Zinc trifluoromethanesulfonate
$ZnSO_4$	Zinc sulfate

Chapter I: Introduction – State of the art and objectives

1. The history and development of batteries

Today batteries have become so commonplace that they often go unnoticed. This incredible invention boasts a rich and fascinating history, and it holds a promising future.

In 1800, Alessandro Volta stacked disks of copper and zinc separated by cloth soaked in saline solution (Figure I-1) [1]. Despite the passage of time, the fundamental principle governing the operation of batteries has remained consistent. The chemical energy stored in the battery, arising from the potential difference between the active components, called electrodes, making up a battery, can be converted into electric energy. The key component in the voltaic pile is the cloth soaked in salty water, later called the electrolyte, as it serves to separate the active components and plays the role of an ion-transporting medium.

Figure I-1: Voltaic pile built in 1800 [1].

This work revolutionized everyday life and had a profound impact on the advancement of electrochemical systems research. Gaston Planté invented in 1859 the first rechargeable battery, called the secondary battery. Comprising lead as the electrode material and sulfuric acid as the electrolyte, this invention marked a pivotal moment, intensifying interest in batteries. Indeed, at this time, batteries can transport energy but also store the energy produced for later use. Secondary batteries can be reused and recharged by applying an electric current to reverse the reaction, regenerating the anode and cathode materials. This added ability to batteries created two branches in the battery history: the non-rechargeable batteries (nowadays referred to as primary batteries) and the rechargeable batteries (also known as accumulators or secondary batteries). In 1866, Leclanché presented his battery featuring a zinc rod negative electrode and a manganese carbon mixture immersed in an ammonium chloride solution. Its concept is still used in the consumer primary batteries (Figure I-2). The next discovery was the nickel-cadmium battery by Jungner in 1901. Despite this breakthrough, the field experienced limited innovation for over a century as batteries built on the early principles of Leclanché, Jungner, and Planté effectively fulfilled the technological requirements of the era [1].

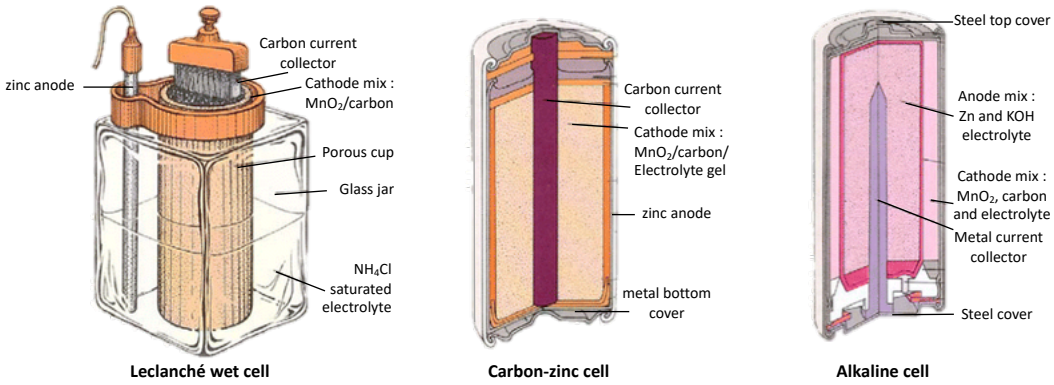

Figure I-2: The Leclanché cell and its evolution to form commercial carbon zinc and alkaline cells [1].

The landscape shifted significantly in the 1960s with the emergence of new battery applications, including portable medical devices, military devices, consumer electronic devices, etc. Therefore, a reduction in weight and size and a higher energy density were needed. The breakthrough came with the development of lithium batteries [1]. Lithium is the lightest metal with a high theoretical specific capacity of 3860 mAh g^{-1} [2]. At the end of the 1970s, the first lithium batteries arrived at the market. Initially, all the batteries developed in the early phase of the lithium battery technology were of the primary type. Nevertheless, the success of these batteries sparked interest in transitioning to secondary batteries. A significant advancement was the discovery of materials, later called "insertion" or "intercalation" materials, which could reversibly accept and release lithium ions within their open structure. Thanks to Whittingham's research on the cathode, Exxon manufactured the first secondary battery in 1977 based on TiS_2 and lithium metal as cathode and anode respectively [1]. Nevertheless, Li-metal tends to form dendrites during cycling (Figure I-3), which leads to safety issues and causes short circuits [3,4]. The replacement of lithium metal with a less aggressive anode material was necessary. The successful strategy involved the combination of two insertion electrodes. Throughout the charging and discharging cycles, lithium ions move back and forth across the separator through the electrolyte, becoming intercalated in the active materials (Figure I-5).

In 1980, John B. Goodenough developed the first lithium-ion cathode by replacing Whittingham's titanium disulfide with lithium cobalt oxide ($LiCoO_2$) [1]. In 1985, Akira Yoshino and his team pioneered the development of carbon-based anodes, specifically utilizing petroleum-coke [5]. This innovation aimed to replace lithium, ultimately enabling the production of lithium-ion batteries (LIBs) with enhanced reliability for extended cycling. In 1991, Sony commercialized a rechargeable battery composed of lithium cobalt oxide and

graphite as cathode and anode material, respectively [4]. The three scientists (Whittingham, Goodenough, and Yoshino) received the Nobel prize in Chemistry in 2019.

Lithium-ion batteries are today the power sources of choice for a series of portable devices and, more recently, electric vehicles, because of their inherent advantages such as high energy density, high working voltage and stability during cycling. In 2004, Tesla used LIBs as supplying system in their project to build an all-electric car [6]. That was the start of LIBs-based electric vehicles (EVs) as we see them more and more on our roads. All these trends are responsible for the dominant position of LIBs in the rechargeable battery market [7]. However, the increasing concerns about limited lithium resources, high cost, and safety and recyclability issues strongly limit their further development for large-scale applications, like grid-scale application [8,9].

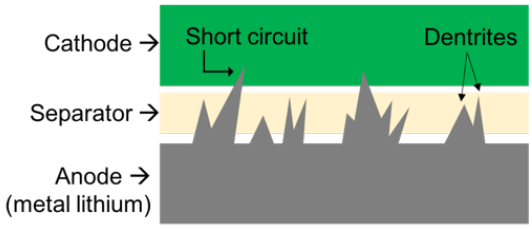

Figure I-3: Dendrites growth from lithium metal anode.

2. The energy needs and resources

Now, more than ever, global warming, energy production, and energy storage are topics at the center of discussions. The energy demand, driven by both global population growth and today's lifestyles does not stop to increase and is projected to almost double by 2050 (Figure I-4) [10]. With a general electricity grid already facing stability challenges at peak times and a policy encouraging the use of electricity instead of fossil resources, guaranteeing the electric energy supply is becoming more and more of a concern [11]. Renewable energies, particularly solar photovoltaics and wind power, emerge as effective solutions to generate electricity while mitigating CO_2 emissions. However, addressing the challenges of intermittency and instability associated with these sources remains imperative. An intriguing solution lies in the ability to store generated energy for later use, bridging the gap between production and demand [12]. Combining renewable energy sources with efficient energy storage systems could offer a promising alternative to traditional fossil fuel supplies. Consequently, there is a need to develop energy storage technologies that are eco-friendly, cost-effective, safe, sustainable, and suitable for large-scale implementations [10,13,14].

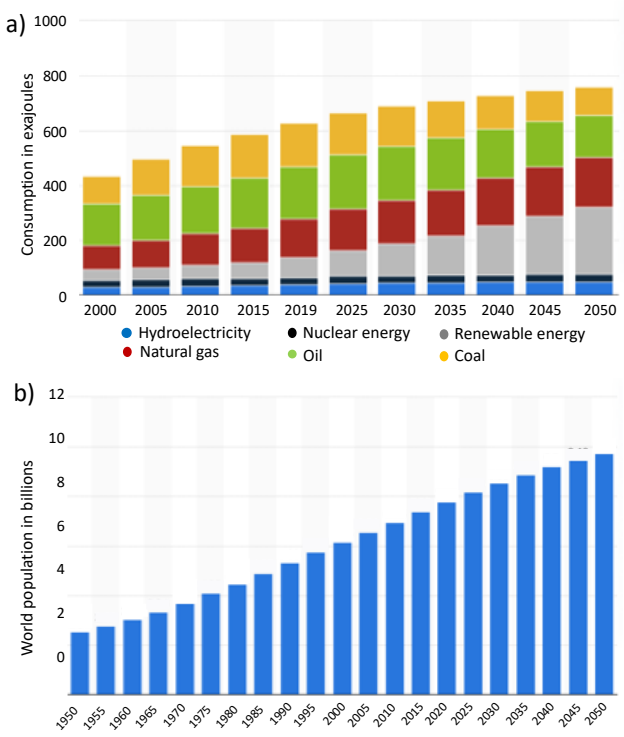

Figure I-4: Evolution of (a) the energy consumption worldwide and (b) the world's population and prediction up to 2050 [15,16].

Among the various energy storage systems, lithium-ion battery (LIB) technology stands out as one of the most popular, competitive, and attractive systems. This is attributed to its high energy density, long cycle life, and lightweight nature. Lithium-ion batteries have proven to be the dominant power source across a wide range of applications, spanning from portable devices to electric vehicles. Nevertheless, grid energy storage is probably the only domain where lithium cannot outdo its rival with its high energy density [17]. The gravimetric energy density is less important than volumetric energy density and price for the grid storage of renewable energies (e.g., near a wind park where the electric energy is produced), as weight does not matter in this locally fixed application [18]. Despite their advantages, lithium-ion batteries pose challenges such as high energy costs for manufacturing and recycling, low relative abundance of materials, and safety concerns [10]. Therefore, there is a growing concern and interest in developing alternative systems beyond lithium-ion batteries. Some technologies based on a more abundant element emerged in the last few years. Sodium and potassium batteries have attracted attention because they are also composed of an alkali ion. Moreover, given that aluminum foil can be used as current collector, they are lighter and cheaper [19]. However, the quest for suitable cathode and anode materials remains challenging due to the large ionic radii of K^+ and Na^+ and the associated low energy density [7]. Energy

storage systems based on multivalent ions like Ca^{2+}, Mg^{2+}, Al^{3+}, and Zn^{2+} are also under development. Their major advantages are improved safety, high abundance of their polyvalent cations, and high volumetric energy density [20]. Nevertheless, the best type of rechargeable battery utilizing materials that satisfy almost all criteria in terms of eco-friendliness, low cost, simplicity, safety, and recyclability, is the aqueous rechargeable zinc-ion battery (ZIB) [18].

To respond to the energy demand and global population growth, developing other batteries beyond the Li-ion market is important and necessary. In this thesis, two types of batteries are studied: LIBs and ZIBs. Each type of battery has its own point of interest: LIBs will continue to dominate the market for electronic devices and mobility applications, while ZIBs will be interesting for grid energy storage applications.

3. Lithium-ion batteries

3.1. The functioning principle of lithium-ion batteries

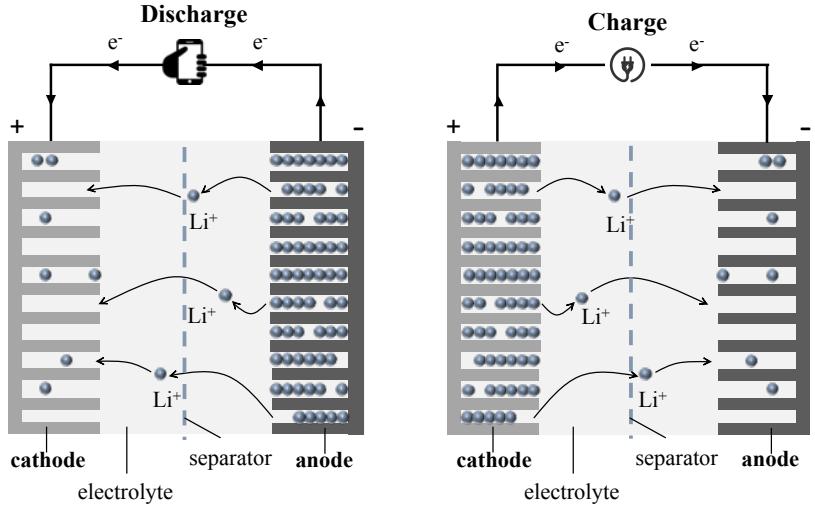

Figure I-5: The functioning principle of a lithium-ion battery.

A lithium-ion battery comprises two electrodes called cathode and anode, between which the electrolyte and separator are located. The electrolyte serves as an ion-conducting medium, while the separator is an electronically insulating porous membrane. Throughout the charging and discharging cycles, lithium ions move back and forth across the separator, becoming intercalated in the active materials. During discharge, lithium-ion migrates from the anode through the electrolyte and the separator to the cathode. Simultaneously, electrons

are released and flow through an external electrical connection. The process is reversed during the charging phase [4]. Figure I-5 depicts a schematic of a typical Li-ion battery design.

The traditional positive and negative electrode materials are lithium cobalt oxide and graphite [21]. However, lithium cobalt oxide is not safe, toxic, and also expensive as cobalt ore is scarce. The main alternative materials for cobalt oxide are metal transition oxide, polyanion compounds, or metal halides. Some commercial alternatives for graphite exist, such as soft and hard carbons or lithium titanate. Studies are also underway to investigate conversion anode materials [17]. These anode materials are discussed in more detail in the next section.

3.2. State of the art of anode materials for Li-ion batteries

Theoretically, lithium metal is the most interesting anode material due to its high capacity and low potential. However, as discussed before, lithium is highly reactive and tends to form dendrites during cycling causing safety issues and short circuits.

In practice, graphite is the anode material of choice in commercial Li-ion batteries because of its advantages: low cost, high electronic conductivity, good capacity (372 mAh g^{-1}), and low lithiation potential vs. Li/Li^+. Lithium ions are intercalated between layers of graphite. 1 Li atom can be stored per 6 C atoms, leading to a capacity of 372 mAh g^{-1} [22]. Nevertheless, like this value is rather limited, intensive research working on anode materials with higher performance are conducted. Some anode materials are under investigation: carbon materials [23,24], alloy-based materials [25], metal oxides [26], sulfides [27], nitrides [28], and more recently, organic compounds [29–32]. Figure I-6 represents the redox potential *vs.* Li/Li^+ and the corresponding specific capacity of anode materials under research. The selection of a suitable anode material greatly impacts the energy density of Li-ion batteries [17,33,34]. Organic compounds do not appear in Figure I-6 because the potential and the capacity depend highly on the molecule's structure.

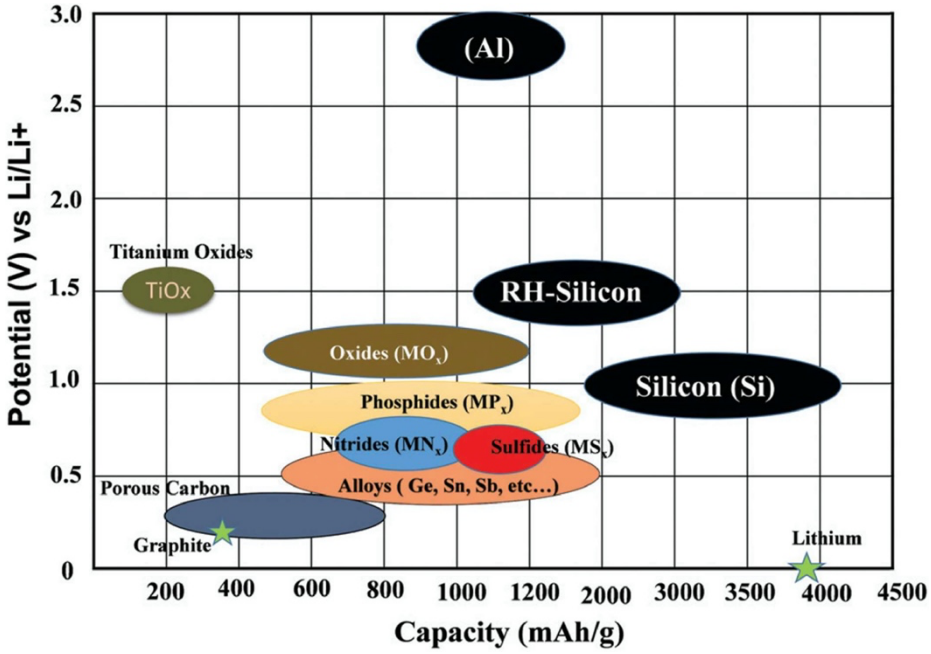

Figure I-6: Approximate range of average discharge potentials and specific capacity of the most common anode materials for lithium-ion batteries [35].

Based on their lithiation/delithiation mechanisms, these materials can be classified into three main groups: intercalation (carbon materials, lithium titanates, titanium oxide), alloys (Si, Ge, Sn, etc), and conversion materials (transition metal oxides, metal oxides, sulfides) [35]. The reaction mechanisms occurring in organic compounds are governed by conversion or intercalation charge-storage mechanisms, depending on the molecular structure [36]. Therefore, organic compounds are discussed separately.

As discussed below, intercalation materials are interesting for their price, safety, prolonged cycle life but offer a low capacity. On the contrary, conversion materials and alloy-based materials attract intensive research attention due to their higher capacities, even if their reaction mechanisms are still unclear. These materials also suffer from a large volume expansion (up to 300%) during the lithiation process and, consequently poor cycling and destruction of solid electrolyte interface (SEI) protective layer. Nevertheless, strategies are under study in order to overcome these issues.

The battery's capacity and performance depend not only on the intrinsic characteristics of the anode material but also on its morphology. Consequently, the suitable and appropriate structural design employed is much more important than the material selected [17].

3.2.1. Intercalation materials

a) Carbon-based materials

Carbon materials, with their diverse features and structures, have gained recognition as practical options for anode materials in lithium-ion batteries (LIBs). This acknowledgment is based on their favorable characteristics, including easy accessibility, mechanical and thermal durability, electrochemical resilience, cost-effectiveness, and the ability to efficiently undergo lithium intercalation and reversible de-intercalation [35].

Carbon materials are classified into two main categories depending on their structure: graphitizable and non-graphitizable carbon. Compared to graphitizable materials, non-graphitizable carbon generally has low density, porous surface, small crystallites, and relatively random orientation of crystallites [37,38].

Graphite is the most known graphitizable material because it is the anode material of choice in commercial batteries [35]. Graphite presents advantages such as low cost, widespread availability high electronic conductivity, low lithiation potential vs. Li/Li^+ and good capacity (372 mAh g^{-1}). However, the lithium intercalation between carbon layers leads to a volume expansion of about 10 % [39]. Moreover, graphite demonstrates insufficient electrochemical performance, especially under low temperatures. This deficiency is mainly attributed to increased resistance within the electrode's bulk, the charge-transfer process, and the formation of a passivation layer at the interface between the electrolyte and electrode [35].

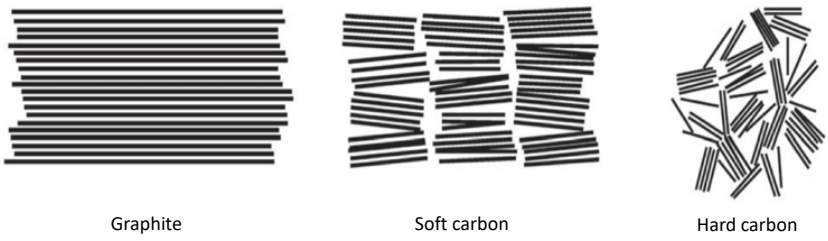

Figure I-7: Schematic representation of graphite, soft and hard carbon [40].

Alternative carbonaceous materials, such as soft carbons (SC) and hard carbons (HCs), have been explored as substitute anode materials to enhance the performance characteristics of lithium-ion batteries (LIBs). The amorphous structure and large graphite grains of soft carbon allow fast charging in LIBs, but it is constrained by a low specific capacity of 250 mAh g^{-1} [41]. On the contrary, hard carbons have small graphite grains with disordered

orientations and nanovoids between them. They are less susceptible to exfoliation. Hard carbon is a high capacity and high cycle life material but with a low coulombic efficiency due to the large SEI formation [35,41]. Moreover, the void spaces significantly reduce the particle density, further decreasing volumetric capacity.

b) Titanium-based materials

Exhibiting compelling characteristics, including low toxicity, good safety, excellent lifecycle performance, and minimal volume fluctuations (< 4 %) during the processes of lithium de-insertion and insertion, titanium oxide has been widely studied in LIBs [42].

The spinel $Li_4Ti_5O_{12}$ has been also considered as a promising anode candidate for rechargeable Li-ion batteries due to its impressive reversibility in Li-ion reactions. $Li_4Ti_5O_{12}$ can accommodate three lithium ions at 1.55 V (vs. Li/Li^+), resulting in a theoretical specific capacity of 175 mAh g^{-1}. Its high working potential contributes to safety by minimizing dendrite formation [35]. Other advantages are its influence on solid electrolyte interface, its low volume expansion during lithiation/delithiation (0.2 %), and the small voltage hysteresis in its charge-discharge profile [33]. While intercalation materials are valued for safety, high potential, and structural stability during cycling, they often exhibit lower performance levels [43].

3.2.2. Alloy-based materials

Some metals and semi-conductors such as aluminium, germanium, silicon, tin, antimony or lead form electrochemically an alloy with lithium according to this reaction:

$$M + x\ Li^+ + x\ e^- \rightarrow Li_xM$$

These elements possess a notable advantage with a high theoretical specific capacity, ranging from two to ten times higher than carbon [17]. Their capacities vary from 410 mAh g^{-1} for zinc [44] up to 4211 mAh g^{-1} for silicon [45]. Consequently, these materials could potentially satisfy the global energy demand. Nevertheless, alloying anodes generally suffer from poor electrical conductivity and short cycle life. This is attributed to significant volume expansion during the lithiation/delithiation, leading to structure issues, electrode cracks, and loss of electrical contact [17]. Additionally, the volume change can destroy the solid electrolyte interface (SEI) protective layer, resulting in continuous electrolyte decomposition, lithium loss, and increasing cell impedance. Strategies to overcome these issues are under

investigation: the downsizing from micro to nanoscale particles and the fabrication of composites are the most promising [25,34,46].

3.2.3. Conversion materials

Conversion-type electrode materials emerge as highly promising candidates to replace current intercalation-type electrode materials. This is due to their exceptionally high theoretical capacity, generally ranging from 500 to 1500 mAh g^{-1}, attributed to the involvement of a high number of electrons [47]. Transition metal compounds such as oxides, phosphides, sulfides, and nitrides are the most studied conversion materials [47–50], and the most attention is deserved to transition metal oxides.

During the first cycle, metallic nanoparticles are formed, and thanks to the large interface surface, the decomposition of the matrix Li_cX is facilitated for the next charge [47–49]. The reaction potential can easily be tuned by changing the anion and the transition metal, as they are directly interconnected [48]. Nevertheless, as a strong structural reorganization occurs, it induces a large volume expansion like for alloys leading to particle decohesion and low cyclability. These compounds also exhibit a large voltage hysteresis depending on the anionic species and a low coulombic efficiency in the first cycle. Moreover, the highly active M nanoparticles formed may contribute to electrolyte decomposition [51]. Despite their considerable advantages, these materials still face several issues that require further investigation.

3.2.4. Organic compounds

Organic materials, particularly aromatic carbonyl derivatives, exhibit outstanding electrochemical performance comparable to, or even surpassing, that of inorganic materials due to their ability to transfer multiple electrons. Moreover, the organic electrode materials are potentially low-cost, recyclable, and safe (less exothermic) when fully discharged. The wide diversity of organic redox systems and the design flexibility at the molecular level are also advantages of organic compounds [36]. The introduction of an electron-withdrawing group into the redox-active organic molecule results in an increased redox potential. This phenomenon occurs as the electron cloud surrounding the redox center of the organic material is drawn towards more electronegative groups. Conversely, the addition of an electron-donating group produces the opposite effect [36]. However, before

commercialization, there is a need to clarify charge/ion transport mechanisms and enhance electrode stability and electronic conductivity. Various organic materials have been reported including polymers [31], carbonyl-π-based materials [52,53], free radicals compounds [54], and organometallic compounds [55–59]. Organometallic complexes with organic linkers and metal ions offer the advantage of possessing bifunctional properties of organic and metal moieties [60]. Consequently, our group has been interested in the improvement of the electrochemical performance of organometallic complexes, specifically on organopalladium complexes, as new active anode materials for Li-ion batteries. This interest is driven by the versatility of palladium, which exhibits multiple oxidation states.

3.3. Impact of particle size and morphology

As discussed before, one of the main challenges in successfully developing high-capacity anode technology is overcoming issues of volume variation, voltage hysteresis, low electronic conductivity, and cyclability [61]. Various strategies such as molecular engineering, nanosizing, and combination with other materials like carbon additives can be realized to improve these drawbacks [36]. D-Y Wang. *et al.* reported that it is necessary to design new structures of organometallic complexes to improve the capacity and the stability of this type of electrode. The utilization of nanostructured hybrid electrode materials or hollow structures holds great promise for enhancing electrochemical performances. Indeed, the better the accommodation of strain, the better the cycle life, and the higher the surface-to-volume ratio, the higher the lithium diffusion rate. Various hollow structures have already been developed: single-shelled, yolk-shelled, and multi-shelled hollow nanostructures [51,62]. In this work, we will be interested in single-shelled structure, which represents the fundamental form of a hollow structure. Template-assisted methods are usually used to prepare hollow structure, however they do not offer high yield. In this thesis, we used a more innovative method in the battery domain: the double emulsion (w/o/w) evaporation technique. This method allows the production of small and spherical particles with a thin and porous shell. The thin shell minimizes the diffusion path for electrons and ions during the discharge/charge process, and the introduction of porosity enhances the specific surface area in contact with the electrolyte [63]. Moreover, particle morphology, size, porosity and agglomeration can be easily tuned by the double emulsion method [64].

4. Sustainable technology beyond lithium-ion batteries: zinc-ion batteries

As mentioned earlier, lithium-ion batteries currently stand as the most widely used battery storage option. However, the lithium-ion supply chain will soon be very constrained. This shortage will become even greater as governments around the world pass laws that accelerate the transition to electric vehicles and renewable energies. In response to this impending shortage, the development of new battery technologies becomes increasingly crucial. Lithium-ion batteries will not be replaced in electric vehicles because, in terms of light batteries and energy density, lithium will still dominate the mobility applications. However, the scenario is different for renewable energy storage. In this context, the primary requirements are a low lifetime cost and high safety.

Alternative battery technologies must use materials that fulfill a maximum of the following criteria: great earth-abundance, eco-friendly, cheap, easy to process, low toxicity, and high safety. While sodium and potassium batteries have gained attention, safety concerns persist, and finding suitable cathode and anode materials remains challenging due to the large ionic radii of K^+ and Na^+ [7,65]. Energy storage systems that fulfill some of these criteria are multivalent-ion batteries (Ca^{2+}, Mg^{2+}, Al^{3+}, Zn^{2+}) [20]. Their major advantages over LIBs are their improved safety, high abundance of their polyvalent cations, and high volumetric energy density. Among various alternatives, the aqueous rechargeable zinc-ion battery (ZIB) emerges as a promising candidate, outperforming LIBs in terms of eco-friendliness, low cost, simplicity, safety, and recyclability [18,66]. The interest in aqueous ZIBs has significantly increased over the past decade, evident from the rising number of annual publications on the subject (Figure I-8).

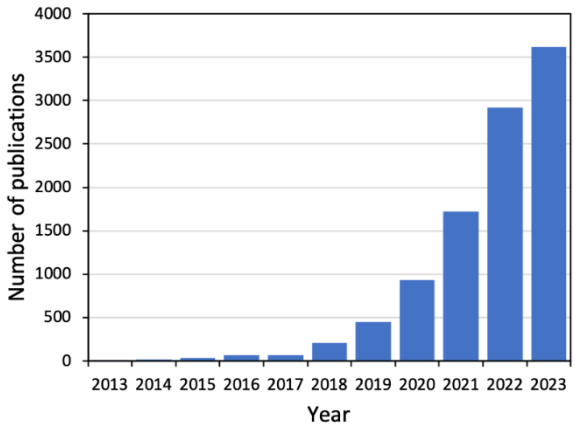

Figure I-8: Total number of scientific publications on aqueous ZIB published in the last ten years (Data collected in December 2023 from Google Scholar. Keywords used: "aqueous zinc-ion batteries" OR "aqueous zinc-ion battery" OR "aqueous Zn-ion battery").

Aqueous zinc-ion batteries seem to be a compelling candidate to beat lithium-ion batteries for energy storage applications owing to the notable advantages associated with zinc metal. Zn boasts a relatively low redox potential (-0,76V, Zn vs SHE) and a very high volumetric capacity (5855 mAh.cm^{-3}), even higher than the one of lithium (Table I-1). The cost-effectiveness derived from the natural abundance and extensive production of zinc further enhances its interest [65]. The high ionic conductivity of the aqueous solution allows to achieve high-rate performance. Indeed, Zn-ion batteries offer many important advantages compared to lithium-ion batteries such as: high safety, supply chain security, sustainability, and high theoretical volumetric energy density [20].

Table I-1: A comparison of properties of monovalent/multivalent metals [11].

Charge carriers	Electrode potential vs SHE [V]	Shannon's ionic radius [Å]	Hydrated ionic radius [Å]	Specific gravimetric capacity (mAh g^{-1})	Specific volumetric capacity (mAh cm^{-3})
Li	-3.04	0.76	3.40-3.82	3862	2066
Na	-2.71	1.02	2.76-3.60	1166	1129
K	-2.93	1.38	2.01-3.31	685	586
Mg	-2.37	0.72	3.00-4.70	2205	3832
Ca	-2.87	1	4.12-4.20	1337	2072
Zn	-0.76	0.74	4.04-4.30	820	5855
Al	-1.66	0.535	4.80	2980	8046

The safety concerns associated with lithium-ion batteries arise from their flammable organic electrolytes. Moreover, many of its production steps must take place in a highly controlled atmosphere because of lithium's violent reactivity with water. In contrast, the manufacturing process of zinc-ion batteries (ZIBs) is safer, easier, and more cost-effective, primarily due to the use of a water-based electrolyte. This characteristic positions ZIBs as a favorable option in markets where LIBs face restrictions due to safety concerns and in applications where an exceptionally high energy density is not a critical requirement.

Beyond safety, the earth-abundance of electrode materials in ZIBs also makes them well-suited for scaling up in mass production. In fact, the zinc metal used as the material of choice for commercial ZIBs is nearly five times more abundant in the earth's crust than lithium [67]. The earth-abundance advantage is valid for the cathode material as well, as ZIBs allow the

use of abundant metallic oxides. The most reported materials in the literature are manganese-based and vanadium-based oxides, especially MnO_2 and V_2O_5 [20]. Manganese and vanadium are respectively the 12th and 18th most abundant elements in the earth's crust while cobalt and lithium are 29th and 35th (Table I-2). In addition, the materials used in ZIBs can be extracted in an eco-friendly manner. Their extraction does not require millions of cubic meters of freshwater or even organic solvents. Finally, electrolytes generally used are zinc salts whose supply should not be a problem for potential commercialization either.

It has been estimated that the cost of ZIBs is five times cheaper than LIBs based on low-cost electrode materials (V_2O_5 - 12 €/kg[68], Zn – 2.3€/kg [69]) and zinc sulfate electrolyte [70]. The combination of low-cost materials and fabrication, and ease of overall battery assembly of ZIBs, helps to meet the requirements for large-scale storage production and application.

Table I-2: Table reporting the abundance in the earth's crust of the most used elements in LIBs and ZIBs.

Elements	**Mn**	**V**	**Zn**	**Co**	**Li**
Abundance in Earth's crust (%)	0.11	0.019	0.0078	0.003	0.0017

The high theoretical volumetric energy density of ZIBs is also a significant advantage over LIBs. Considering the relative high capacity density of Zn (5855 mAh cm^{-3}) and based on the V-based material, an energy density of of 450 Wh L^{-1} has been realized [11].

Due to their remarkable safety features, low cost, high volumetric energy density, and ease of processing, ZIBs hold substantial promise for grid energy storage applications. Although, an aqueous zinc-ion battery based on zinc, MnO_2, and zinc sulfate is nearly commercialized as a home battery by Salient Energy in Canada [71].

Other possible applications for ZIBs could be, for example, their use in flexible rechargeable batteries in wearable electronics. These ZIBs offer outstanding safety performances under severe conditions, as tests have shown that they can be bent, cut, hammered, punctured, or even set on fire without alarming consequences [18].

4.1. Functioning principle of zinc-ion batteries

Like lithium-ion, the zinc-ion battery functions using intercalation material. Typically, during the discharge process, the zinc metal at the anode is oxidized to form zinc-ion that are transported through the electrolyte towards the cathode where they are inserted in the

crystalline structure (Figure I-9). The separator allows the small zinc ions to pass but prevents the electrodes from touching. This process is reversed during charge.

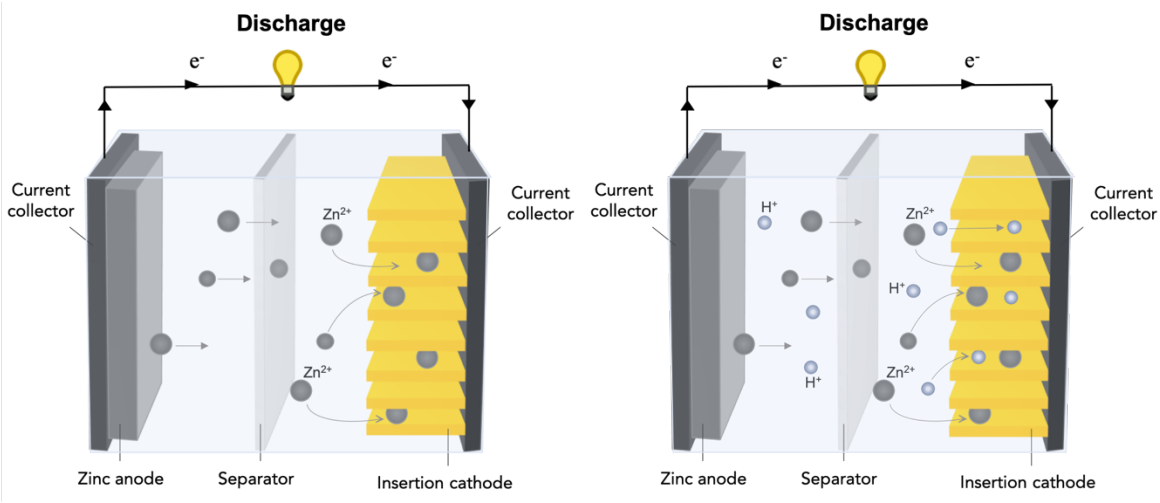

Figure I-9: A zinc-ion battery based on Zn^{2+} insertion/extraction (left) and H^+/Zn^{2+} insertion/extraction (right).

The mechanism behind these redox reactions is still under debate to this day. The above-mentioned Zn^{2+} insertion/extraction mechanism is the main mechanism but probably not the only process taking place. According to current literature, the redox reactions in aqueous ZIB systems can involve three different mechanisms depending on the cathode materials, working potential, and electrolyte [7]:

- Zn^{2+} insertion/extraction
- H^+/Zn^{2+} insertion/extraction
- chemical conversion reaction

The latter is not represented in Figure I-9 because is not often encountered and is specific to cathode materials not studied in this work.

To date, most of the works regarding aqueous ZIBs report zinc metal as anode while the choice of cathode material is not so evident between manganese or vanadium-based materials [72–75], Prussian blue analogs [76,77], and more recently organic compounds [78–81]. The common aqueous electrolytes used in ZIBs are zinc sulfate ($ZnSO_4$) and zinc triflate ($Zn(CF_3SO_3)_2$) solutions due to their excellent properties as discussed hereafter [82].

4.2. Aqueous electrolytes

The most important difference between LIBs and aqueous ZIBs comes from the electrolyte nature. Aqueous electrolytes offer advantages in terms of being more environmentally friendly, cost-effective, safer, and having higher ionic conductivity compared to organic electrolytes. However, they suffer from other issues. According to the Pourbaix diagram of water (Figure I-10a), water molecules can be decomposed to release hydrogen or oxygen in function of the applied potential and pH of the electrolyte. Therefore, when designing a new system for aqueous zinc-ion batteries (ZIBs), several crucial aspects need consideration: (1) the working potential of electrode materials should locate between the potential window of the hydrogen evolution reaction (HER) and oxygen evolution reaction (OER), (2) the pH of the electrolyte, and (3) the current collector must be stable within the working voltage range and at the pH selected [65]. Additionally, in aqueous electrolytes, Zn^{2+} is frequently presents in the form of $Zn(H_2O)_6^{2+}$. This indicates a heightened need to overcome both desolvation energy and insertion energy during the Zn^{2+} insertion process. Tackling these aspects is crucial for the advancement and enhancement of effective and stable aqueous zinc-ion battery systems.[83].

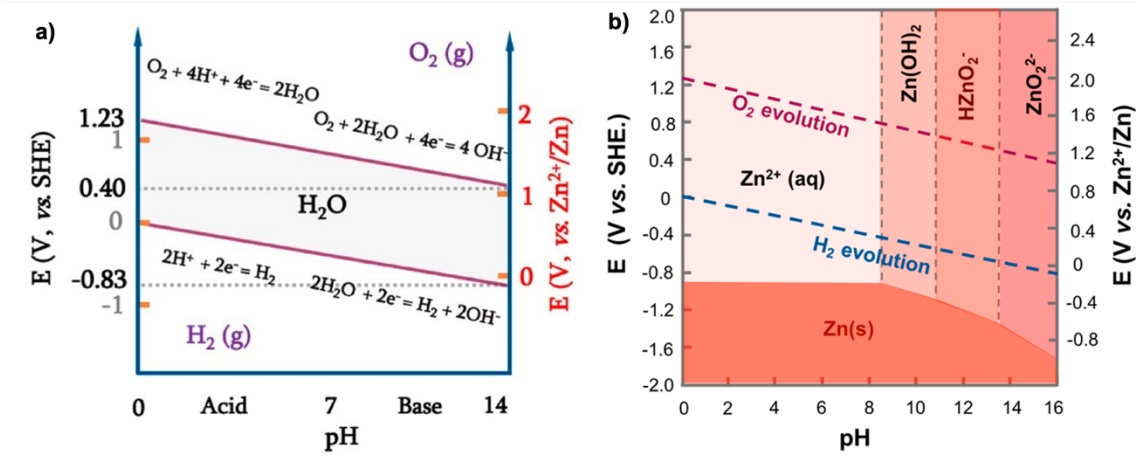

Figure I-10: Pourbaix diagrams of (a) water and (b) zinc metal [65]

The composition and concentration of the electrolyte are crucial parameters as they directly impact the pH value. The ideal aqueous electrolyte should possess a wide electrochemical window, be compatible with all the battery components, and be eco-friendly, with a low toxicity and low cost. Alkaline electrolyte has been excluded because of the high dissolution of zinc metal resulting in the formation of byproducts at the anode as shown in the Pourbaix

diagram of zinc (Figure I-10b) and explained in point I.4.3. Using alkaline electrolyte leads to fast capacity fading and low coulombic efficiency. On the other hand, a neutral or mild acidic electrolyte is considered the most promising electrolyte in the literature. This choice allows a higher working potential and limits side reactions [65,82].

Up to now, various zinc salts have been studied, each demonstrating different electrochemical properties. Owing to its low cost, $ZnSO_4$, is the most widely used salt. However, during the discharge, a byproduct, called zinc hydroxide sulfate (ZHS, $Zn_4(OH)_6SO_4 \cdot nH_2O$) is formed and influences the reaction mechanism [84,85]. Another zinc salt extensively studied due to its higher stability is $Zn(CF_3SO_3)_2$. The better electrochemical performance of this electrolyte is attributed to the bulky $CF_3SO_3^-$ anion that reduces the coordination number of H_2O molecules surrounding Zn^{2+} and decreases the solvation effect [86]. Despite its superior performance, this electrolyte is more expensive, limiting its suitability for large-scale applications. Other zinc salts such as $Zn(NO_3)_2$, $Zn(CH_3COO)_2$, $Zn(ClO_4)_2$ and $ZnCl_2$ solutions have been investigated as electrolytes but exhibit lower electrochemical performance [65,73,82].

The concentration of the electrolyte is also a determinant factor to tailor the electrolyte performances because it has an impact on the solvation chemistry. The more concentrated the aqueous electrolyte, the smaller the hydration number and radius of hydrated Zn^{2+}, easier is the intercalation/deintercalation of zinc ions into the structure [65,86,87]. In this thesis, we opted for $Zn(CF_3SO_3)_2$ 3M because it offers high electrochemical performance and is widely studied [82].

4.3. Anode materials

Zinc metal is extensively used as an anode material not only in zinc-ion batteries (ZIBs) but also in other zinc-based battery systems like Zn-air, Ni-Zn, and Zn-MnO_2 batteries owing to their excellent inherent properties. Combined with a high abundance, low cost, non-toxicity, and high electrical conductivity, zinc metal has a high theoretical capacity (5854 mAh cm^{-3} and 820 mAh g^{-1}) and suitable redox potential (-0.76V vs SHE) in aqueous solution as shown in Table I-1[65,88]. Furthermore, zinc is a metal that is very easy to handle, as it is nonreactive towards oxygen or the humidity in the air. This characteristic eliminates the need for an inert atmosphere during the assembly of electrochemical test cells, unlike sodium, potassium, and lithium [7]. The existing manufacturing infrastructure for zinc electrodes in alkaline batteries helps to meet the requirements in terms of cost and ease of scaling up [11].

As explained in the Pourbaix diagram (Figure I-10 b), in alkaline electrolytes, by-products are formed by dissolution-precipitation processes, passivating the active surface. However, this issue can be limited by using neutral or mildly acid electrolytes [65,89]. Additionally, the acidity level of the electrolyte plays a role in the severity of hydrogen evolution and corrosion. Higher acidity leads to increased hydrogen evolution and corrosion, resulting in continuous consumption of zinc metal and electrolyte, consequently leading to low plating/stripping coulombic efficiency [65,90]. In addition, dendrites are formed upon repeated cycling, especially at high current densities but they can be alleviated in mild acidic electrolyte [91]. Various strategies have been reported to address these challenges [20,88–92]. For example, the structural design of the zinc anode can be optimized, and the interface between the anode and electrolyte can be modified by forming a conductive protective layer (carbon, polymer, Au, or metal oxide) [93]. Working on the electrolyte and additives is also a good solution [92].

Other materials such as $ZnMo_6S_8$, Mo_6S_8, and $Na_{0.14}TiS_2$ can be used as Zn^{2+} intercalation/extraction anode materials with superior cycling stability compared to zinc metal [94,95]. In this case, Zn^{2+} is either present in the electrolyte or incorporated in the cathode material. However, despite their cycling stability, zinc metal remains the anode material of choice due to the lower energy density and poor conductivity offered by these alternative materials [92].

Although zinc metal anode material presents problems like dendrite formation or corrosion, it is not the limiting electrode in ZIBs. Therefore, we focused our research on the cathode material using zinc foil directly and mildly acid electrolyte to mitigate issues associated with the anode material.

4.4. Cathode materials

Above all, finding a suitable cathode material is crucial because the cathode is currently the limiting electrode in ZIBs. The cathode material requires an extremely specific structure that allows the intercalation/deintercalation of zinc ions. Although the ionic radius of Zn^{2+} is similar to Li^+, the hydrated radius of the zinc ion is much larger hampering the intercalation/deintercalation kinetic (Table I-1). Therefore, cathode materials used in LIBs may not be suitable in ZIBs. Larger structures such as a tunnel or a planar setup of the crystal should be favorable. Four categories of cathode materials have been developed in the last few years: manganese- [96–99] and vanadium-based materials [72–75], Prussian blue analogs [76,77],

and organic compounds [78–81] (Figure I-11). Other materials like cobalt oxide, carbon, and MXene have also recently been studied but do not show competitive advantages compared to Mn-based or V-based materials [13].

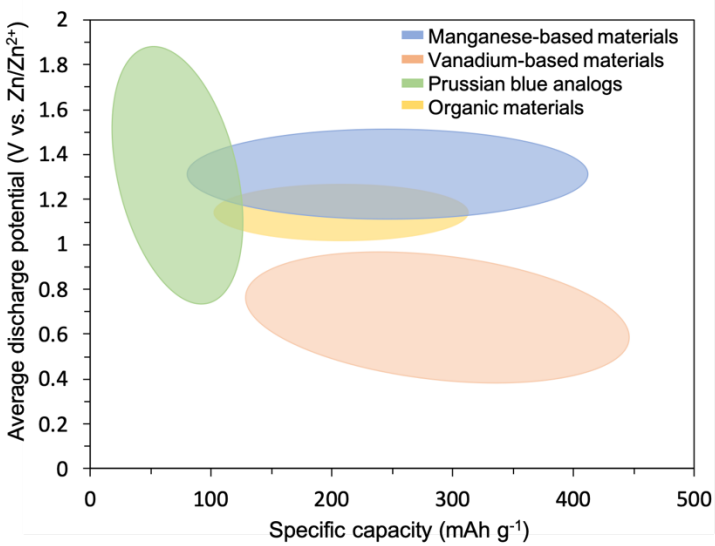

Figure I-11: Specific capacities and average discharge potentials of most studied cathode materials in ZIBs (adapted from [11,13]).

4.4.1. Manganese-based materials

The manganese-based materials have drawn much attention since the beginning of the development of ZIBs due to their several advantages. They have been widely used because manganese is the 10th most abundant element in the Earth's Crust, environmentally benign, cheap, and possesses variable oxidation states. Manganese oxides have been reported as the first cathode materials in ZIBs and show variable crystal structures suitable for the intercalation/deintercalation of Zn^{2+} [13]. Manganese dioxide has been extensively studied since the discovery of alkaline batteries and stands as the most frequently reported manganese oxide material in ZIBs [100,101]. It offers different crystallographic structures classified into 3 categories chain/tunnel/layered-type structure depending on the polymorph (Figure I-12), a good theoretical capacity (308 mAh g^{-1}), and a high operating voltage (~1.3 V vs Zn/Zn^{2+}) [102–104]. Besides MnO_2, other manganese materials like Mn_2O_3[96], Mn_3O_4[105] or $ZnMn_2O_4$[86] have been developed as cathode materials for ZIBs. Although the specific capacities of this type of cathode materials are especially high, Mn-based cathodes suffer nonetheless from manganese dissolution and low electronic conductivity resulting in rapid capacity fading and poor rate capabilities [13,18]. While these issues could be solved by some

optimizing solutions, such as adding additives, these limitations indicate that the optimal material has not yet been identified. This underscores the necessity to shift research focus towards exploring alternative materials for more effective and sustainable solutions.

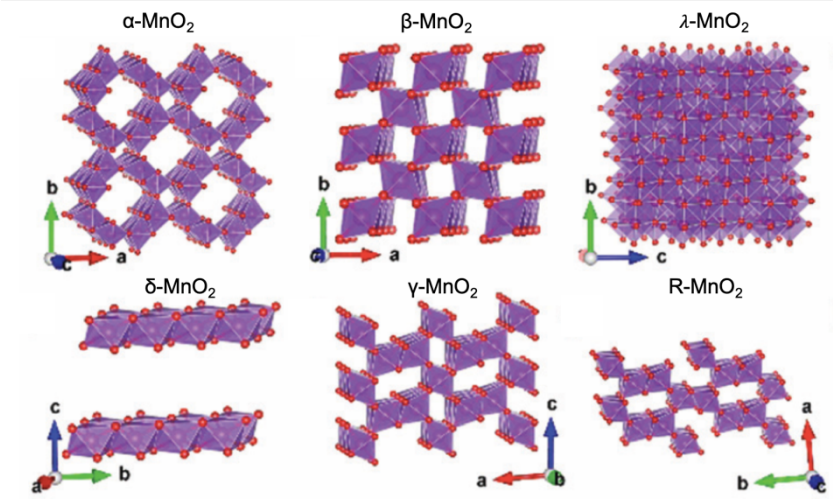

Figure I-12: Crystal structures of MnO_2 polymorphs [104].

4.4.2. Vanadium-based materials

Currently, vanadium-based materials, and especially V_2O_5 materials, are probably the second most attractive and studied materials used for ZIB cathodes. Like manganese, vanadium is abundant and shows variable valence states. In vanadium oxides, the vanadium-oxygen coordination polyhedron can be tetrahedral, square pyramidal, distorted octahedral, and even regular octahedral, depending on the oxidation state of vanadium atom (Figure I-13) [11,13,104]. The flexible VOx polyhedron unit in vanadium-based compounds can be arranged into various open structures, including 1D tunnels, 2D layers, and 3D frameworks, through different connections. This structural flexibility promotes an optimal insertion of the zinc ions into the crystalline structure accompanied by changes in the oxidation state [83]. The vanadium oxide with tunnel-structure is more stable during repeated Zn^{2+} insertion/extraction, whereas layered structure delivers higher specific capacity. These two structures will be discussed more deeply later. In addition, compared to manganese-based materials, vanadium-based cathode material offers high specific capacity and rate capability, long cycle life, and lower dissolution but low operating voltage (~ 0.8V) [13,102] .

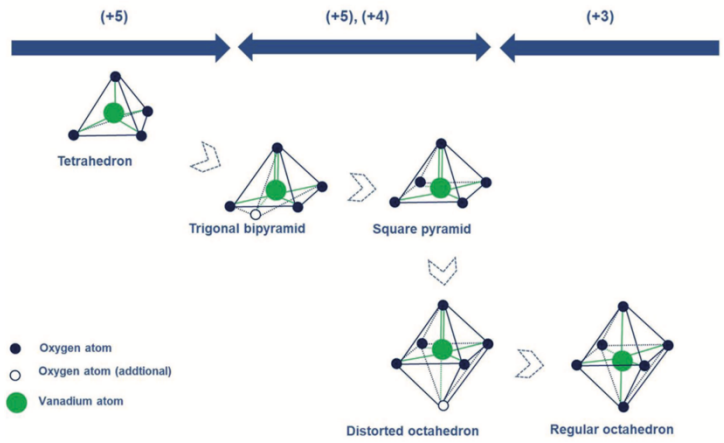

Figure I-13: Metamorphosis of the vanadium coordination polyhedral [11].

Vanadium pentoxide is of great interest owing to its incredibly high theoretical capacity, 589 mAh g^{-1} based on two-electron redox centers (V^{5+}/V^{3+} redox couple) [18,102]. It possesses a layered structure with appropriate layer spacing that facilitates zinc ion mobility. Despite its good electrochemical performance, the reaction mechanism of V_2O_5 as cathode material in aqueous zinc-ion batteries is still under debate.

The activation process occurring in the first cycles is often attributed to the insertion of water molecules into the structure leading to a gradual expansion of the interlayer distance [106,107]. During this phase, the Zn^{2+} intercalation contribution increases. Then, three different structural changes have been proposed in the literature during cycling. The insertion of Zn^{2+} leading to the formation of $Zn_xV_2O_5$ during cycling was proposed by Zhou et al[73]. Then, Zhang et al., demonstrated the co-insertion of hydrated Zn ion into the V_2O_5 structure [74]. Finally, according to Chen et al., During the first discharge, orthorhombic V_2O_5 underwent a phase transition into zinc pyrovanadate, with the newly formed zinc pyrovanadate demonstrating reversible Zn^{2+} insertion and deinsertion in the following cycles [72]. In addition, it has been reported that a mass of complex byproducts was produced/decomposed during the discharge/charge cycling of vanadium oxides [84].

V_2O_5 cathode presents several disadvantages such as high toxicity, low ion diffusion, poor electrical conductivity, slight vanadium dissolution in aqueous electrolyte, and volume changes caused by Zn^{2+} insertion/extraction during cycling. Moreover, the layered structure of V_2O_5 suffers from instability during repeated intercalation of ions [18,20,102,108]. Fortunately, several strategies have been applied to address these issues, and are discussed in point I.4.5.

Introducing guest species as metal ions (Li^+, Na^+, Ca^{2+}, Zn^{2+}, Fe^{2+}) acting as pillars into the structure of V_2O_5 is promising to stabilize the host structure upon cycling [104]. For these materials, the capacity will generally be limited but the structure stabilized.

In the following, the focus is made on V_2O_5 and $M_xV_2O_5$ (where M = alkali, alkaline or transitional metal), as they were the first vanadium oxides used in ZIBs and are currently the most studied in the literature [109,110].

4.4.3. Prussian blue analogs

Prussian blue analogs (PBA) with their non-toxic nature, low cost and simple way of synthesis have emerged as interesting cathode materials for ZIBs [103]. Their general formula is $M[Fe(CN)_6]$ (M = Fe, Co, Ni, Cu or Mn), and corresponds to a face-centered cubic structure. They show excellent cycle life due to their open-framework structure and large channels [13]. The most studied PBAs are zinc hexacyanoferrates (ZnHCF) [111] and copper hexacyanoferrates (CuHCF) [112]. They exhibit a high operating voltage (~1.7 V) but a low specific capacity (lower than 100 mAh g^{-1}) which is their main disadvantage as represented in Figure I-11 [103].

4.4.4. Organic materials

In addition to inorganic materials, organic compounds have also been recently pursued in aqueous ZIBs. They are interesting due to their lightweight, sustainability, cost-effectiveness, multiple electron reactions, and adjustable electrochemical windows. Furthermore, their excellent mechanical flexibility and stability position them for promising applications in wearable electronic devices [103,104]. Quinone-based electrodes have been extensively investigated among organic materials due to their high stability in water [11,79,103]. During the discharge, the zinc ions are reversibly coordinated to the reduced carbonyl groups. This reaction mechanism is called the "ion-coordination" mechanism and differs significantly from that of inorganic materials. However, the performance of many small organic molecules is hindered by the hydrolysis of discharge products. Polymers like polyaniline [113], polycathecol [80] and polydopamine [81] have been designed as cathode materials for ZIBs. Stabilized by their larger π-conjugated structure, they exhibit remarkable cycling performance compared to small molecules [114]. Nevertheless, the substantial molecular

weight and poor conductivity of polymer cathodes pose challenges to their practical capacity. These emerging organic compounds are still in their early stages of development, requiring further research to enhance their capacity and energy density.

4.5. Challenges and optimization of V_2O_5 as cathode material

As discussed previously, V_2O_5 is a promising candidate for rechargeable aqueous zinc ion batteries because it has the highest theoretical capacity of vanadium-based cathode material and a suitable structure for zinc ion insertion/extraction. However, its use in large-scale applications is constrained by some drawbacks that require solutions [115,116]:

(1) *Vanadium dissolution*. The active material's quantity may decrease due to the slight dissolution of V_2O_5 in acidic aqueous electrolyte. Additionally, this dissolution might prompt the generation of by-products or side reactions, causing structural degradation.

(2) *Structure instability*. The interlayer spacing of V_2O_5 layered structure enables the insertion of zinc ions. However, the high charge density of zinc ions generates electrostatic force with the cathode material and the larger radius of hydrated zinc ions can cause stress and structural collapse.

(3) *Low electronic conductivity*. V_2O_5 displays inadequate electronic conductivity, potentially leading to an extended activation period.

(4) *Limited practical capacity*. The specific capacity obtained in most studies is much lower than the theoretical, limiting the practical capacity of V_2O_5 in zinc-ion batteries.

In recent years, various strategies, as illustrated in Figure I-14, have been applied to address these challenges and to improve the electrochemical performance of V_2O_5 as cathode material in ZIBs [13,115,116]. For example, design modifications can be implemented to increase active sites and ensure good stability in order to optimize the capacity of the material [117–121]. Then, working on the nature and concentration of the electrolyte enables to limit the issues of stability and dissolution [82]. The dissolution can also be alleviated, and the conductivity increased by adding carbon sources, or by coating the material with carbon sources, conductive polymer, or other materials [122–126]. Lastly, pre-intercalating guest species (metal ions, water molecules, organic materials etc) into the structure of V_2O_5 has been much developed to enhance material stability [75,127–132].

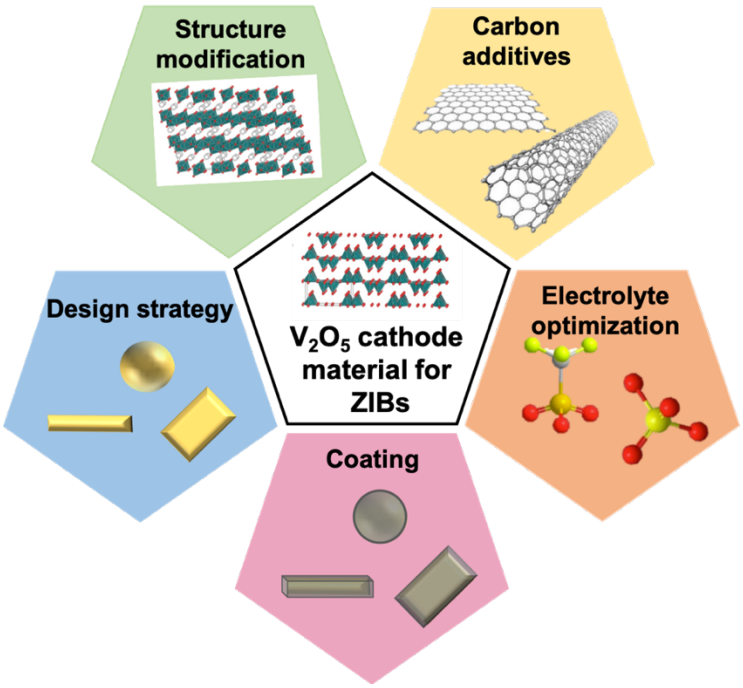

Figure I-14: Strategies of optimization for V_2O_5 materials as cathode material in ZIBs.

a) Electrolyte optimization

Many studies have been devoted to the modification of electrolytes to impede zinc dendrites and also alleviate the cathode dissolution. The pre-addition of relevant salts into the electrolyte has proven to be an effective approach to limit the manganese- and vanadium-based cathode materials dissolution. For example, the introduction of $MnSO_4$ or Na_2SO_4 as additive significantly enhance the overall performance of manganese and sodium vanadate-based materials in aqueous ZIBs [133–135]. H. Chen *et al* also showed that the cyclic stability of V_2O_5@CNTs is improved using 1M $ZnSO_4$ / 1M Na_2SO_4 mixed electrolyte [122]. The addition of Na^+ results in the reduction of zinc dendrite growth. Another promising strategy involves adjusting the electrolyte concentration, impacting solvation chemistry. The fabrication of an ultraconcentrated electrolyte, 21 M LiTFSI/1 M $Zn(CF_3SO_3)_2$, has been investigated by Hu's group [66]. The huge amount of anions salt is preferentially bonded to Zn^{2+} than water molecules. This kind of water-in-salt electrolyte displays a coulombic efficiency around 100% and suppresses the dendrite growth and water consumption [115]. However, both Zn^{2+} and Li^+ can be inserted/extracted meaning that a hybrid-ion battery is obtained in this case. Then, as Zhang *et al*. have proved, a higher salt concentration (3M $Zn(CF_3SO_3)_2$) can reduce the water activity and improve the stability of V_2O_5 electrode [86]. Therefore, in our thesis, we fixed 3 M as $Zn(CF_3SO_3)_2$ electrolyte concentration.

Finally, to minimize the cathode dissolution and anode passivation/corrosion, gel electrolytes can be used instead of liquid electrolyte [136]. Their best advantages are their high flexibility, excellent electrochemical properties, and desirable integrity [116]. However, their development is limited by their low ionic conductivity and unsatisfactory electrode/electrolyte interface compared to liquid electrolytes [13].

b) Design strategy

It is well known that the morphology of cathode material plays a critical role in the electrode activation process, capacity, and stability [106,137,138]. Tuning the morphology is an effective way to improve the electrochemical performance of V_2O_5 cathodes in ZIBs. V_2O_5 materials can be shaped via various techniques like hydrothermal, solvothermal, solid-state or spray-drying. Table I-3 resumes the state of the art of V_2O_5 materials prepared via different procedures. Nevertheless, the optimization of architecture design does not solve the issue of low electronic conductivity.

Table I-3: State of the art of electrochemical performances of V_2O_5 materials in ZIBs.

Ref	Material	Morphology	Treatment	Electrolyte	Capacity (mAh g^{-1})	Cycles	Retention (%)
[119]	V_2O_5	hollow spheres	solvothermal	$ZnSO_4$ saturated	280 (0.2 A g^{-1})	6200 (10 A g^{-1})	82.5
[139]	V_2O_5	microspheres	spray-drying	$Zn(CF_3SO_3)_2$ 2M	401 (0.1 A g^{-1})	1000 (5 A g^{-1})	73
[74]	V_2O_5	bulk	commercial	$Zn(CF_3SO_3)_2$ 3M	470 (0.2 A g^{-1})	4000 (5 A g^{-1})	91.1
[140]	V_2O_5 MOF	nanosheets	hydrothermal	$Zn(CF_3SO_3)_2$ 3M	450 (0.1 A g^{-1})	2000 (2 A g^{-1})	86.8
[141]	V_2O_5	nanosheets	hydrothermal	$Zn(CF_3SO_3)_2$ 3M	452 (0.1 A g^{-1})	5000 (10 A g^{-1})	92
[142]	$V_2O_5{\cdot}2.2H_2O$	nanosheets	in situ	$Zn(CF_3SO_3)_2$ 3M	450 (0.1 A g^{-1})	3000 (5 A g^{-1})	72
[143]	$V_2O_5{\cdot}1.6H_2O$	nanosheets	hydrothermal	$Zn(CF_3SO_3)_2$ 3M	426 (0.1 A g^{-1})	5000 (10 A g^{-1})	95

c) Addition of carbon additives

Adding carbon additives to V_2O_5 materials emerges as a promising solution to enhance Zn-ion battery performance by improving the electronic conductivity and stability of the material. The state of the art of articles exploring this strategy is summarized in Table I-4. However, this strategy does not prevent the cathode material dissolution unless a protective shell is realized as discussed in the next point.

Table I-4: State of the art of V_2O_5 materials combined with carbon additives in ZIBs.

Ref	Material	Morphology	Treatment	Electrolyte	Capacity ($mAh\ g^{-1}$)	Cycles	Retention (%)
[122]	V_2O_5@CNT	spheres	solvothermal	$ZnSO_4$ saturated (3,65M)	268 (500 A g^{-1})	6000 (5 A g^{-1})	72
[144]	V_2O_5 nanofibers /CNT	nanopapers	dispersion/ filtration	$ZnSO_4$ (2M)	375 (1000 A g^{-1})	500 (10 Ag^{-1})	80
[145]	CNT@V2O5	nanopapers	melt-infiltration	$Zn(CF_3SO_3)_2$ (3M)	315 (400 A g^{-1})	500 (0.4 Ag^{-1})	80.1
[146]	V_2O_5 nanobelts/CNT	Film	hydrothermal	$Zn(CF_3SO_3)_2$ (3M)	380 (200 A g^{-1})	1000 (5 A g^{-1})	95
[147]	V_2O_5 nanobelts/ rGO	flake-like structure	hydrothermal	$ZnSO_4$ (3M)	170 (100 A g^{-1})	200 (0.1 A g^{-1})	79
[148]	V_2O_5/graphene	nanosheets	2D template (ion adsorption)	$ZnSO_4$ (3M)	489 (100 A g^{-1})	3000 (30 A g^{-1})	86
[149]	V_2O_5/acetylene black	nanosheets	hydrothermal	$Zn(CF_3SO_3)_2$ (3M)	452 (100 A g^{-1})	5000 (10 A g^{-1})	92

d) Coating the cathode material

Surface modification/coating of the cathode material stands out as another effective strategy to prevent cathode dissolution. Coating vanadium-based cathode material with carbon, graphene, or conducting polymer not only limits the cathode dissolution but also enhances the electronic conductivity of the material and prevents structural instability [13].

A carbon coating has been studied as an efficient way to enhance other batteries performance by protecting the particle surface from side reactions and volume variations, as well as improving the electronic conductivity and stability of the material [150,151].

Polymers, when used as a protective coating, can buffer volume expansion, and diminish the solubility of V_2O_5 in the aqueous electrolyte by acting as a barrier thanks to their stable and covalently connected structure. Polyaniline, polypyrrole, and poly(3,4-ethylenedioxythiophene) have already been investigated as conductive and stable polymers for coating V_2O_5 material in zinc-ion batteries [125,126,152]. They appear to be effective in increasing the energy density, rate capability, and cycle life of ZIBs.

e) Pre-insertion of ions

The common V_2O_5 cathode material has a layered structure. The vanadium and oxygen formed VO_5 square pyramids (see Figure I-13) that share edges and corners to form V_4O_{10} layers. The layers interact through van der Waals forces [116]. The interlayer spacing equal to 4.4 Å allows the insertion of Zn^{2+} [153]. However, after a certain number of cycles, the structure of V_2O_5 collapses due to the voluminous hydrated zinc ions and H_2O molecules that are inserted into and extracted from the dense cathode material during the cycling. The introduction of molecules (water [131] or organic molecules [154–156]), and/or metal ions such as Na^+, [75,157] Ca^{2+}, [158] Zn^{2+}, [117,130] K^+,[159] or Mg^{2+},[160] into the structure is a common strategy aiming to improve reaction kinetics and structural stability. Typically, metal ions or water molecules act as pillars expanding the interlayer spacing to facilitate the insertion/extraction of Zn^{2+} and limit the activation period. Nevertheless, the theoretical capacity will always be sacrificed at the cost of stability using this strategy.

5. Thesis overview

5.1. Motivation and aims

The global energy demand is rapidly increasing, making reliable and efficient energy storage solutions crucial for a stable electricity supply and for satisfying today's lifestyle. Lithium-ion batteries have gained popularity due to their high energy density and long cycle life. However, challenges related to cost, material availability, and safety limit their widespread adoption. This situation has led to increased interest in alternative storage solutions such as rechargeable aqueous zinc-ion batteries, which offer potential benefits for grid-scale applications. This thesis is motivated by the need to develop advanced battery materials to enhance the performance of both lithium-ion and aqueous zinc-ion batteries to meet the growing energy storage demands effectively, addressing the current limitations of these technologies.

The first objective is to design and synthesize novel anode materials for LIBs, with a particular focus on organopalladium complexes, to achieve higher specific capacities, and long cycle life. This involves optimizing the particle morphology and electrode preparation. The second objective is to investigate and enhance the performance of cathode materials for ZIBs, focusing on the use of vanadium pentoxide (V_2O_5). By improving the electrochemical properties of V_2O_5 through morphological modifications, carbon nanotubes integration, coating with polydopamine and insertion of sodium ions, the research attempts to develop high-performance, stable cathode materials for ZIBs. Finally, the scaling up of some of these materials is investigated in pouch-type cell configuration, ensuring their applicability for real-world energy storage solutions.

5.2. Thesis outlines

This dissertation is presented in seven chapters.

After *chapter I* that provides an overview of the history and development of batteries, energy needs, and state of the art of Li-ion and Zn-ion batteries, this dissertation is divided into two main parts:

The first part, presented in *chapter II*, concerns the synthesis and development of three organopalladium complexes, $XPd(4\text{-}AcOC_6H_4)(PPh_3)_2$, where X = I, Br, and Cl, as new anode active materials for Li-ion batteries. Our interest in this new type of anode material is driven by the versatility of palladium, which exhibits multiple oxidation states. After proving that the complex with the iodine ligand, $[IPd(4\text{-}AcOC_6H_4)(PPh_3)_2]$, exhibits the best electrochemical performance, we optimized its architecture design. The double emulsion-evaporation technique is used to tailor the morphology and enhance the electrochemical performance of the complex in LIBs.

The second part of this thesis includes chapters III to VI and concerns the development and optimization of V_2O_5 as cathode active material in rechargeable aqueous zinc-ion batteries.

Chapter III is devoted to the spray-drying of vanadium pentoxide. A comparative study with commercial V_2O_5 is realized and shows the benefit of the architecture design of vanadium pentoxide on the electrochemical performance of ZIBs. The influence of carbon nanotubes addition before spray-drying is also investigated in this chapter.

Chapter IV describes the preparation of a self-standing electrode, V_2O_5/PDA/CNTs. V_2O_5 material is coated by polydopamine through a self-polymerization process of dopamine and characterized by SEM, TEM, TGA, FTIR-ATR, and XPS. We showed that the synergistic combination of PDA coating with carbon nanotubes incorporation emerges as a promising strategy for enhancing the electrochemical performance and stability of V_2O_5 in zinc-ion batteries.

Chapter V focuses on sodium vanadium oxides. These materials are prepared by inserting Na^+ ions into V_2O_5 to stabilize its structure for cycling. Three pure phases are synthesized by an aqueous route, characterized and investigated in ZIBs: $Na_2V_6O_{16}\cdot 1.5H_2O$, β-$Na_{0.33}V_2O_5$, and $Na_{1.16}V_3O_8$. The effect of the lyophilized precursors on the phase formation mechanism is investigated for the first time using high-temperature X-ray diffraction.

Chapter VI presents a preliminary study of spray-dried V_2O_5 and the three NVO materials previously synthesized as cathode materials for ZIBs in pouch-type cells to study the prospect of large-scale applications.

Chapter VII summarizes the major findings of this thesis and provides suggestions for future works.

6. References

1 B. Scrosati, *Journal of Solid State Electrochemistry*, 2011, **15**, 1623–1630.

2 J. M. Tarascon and M. Armand, *Materials for Sustainable Energy*, 2010, **414**, 171–179.

3 M. Yoshio* and H. Noguchi, in *Lithium-Ion Batteries*, Springer New York, New York, NY, 2009, pp. 1–40.

4 K.-C. Moeller, S. Leuthner, K. Vuorilehto, C. Wurm, Oettinger Oswin, S. Wittkaemper and R. Zauter, *Lithium-Ion Batteries: Basics And Applications*, 2018.

5 C. Dong, W. Dong, X. Lin, Y. Zhao, R. Li and F. Huang, *EnergyChem*, 2020, **2**, 100045.

6 M. N. Eisler, *IEEE Spectr*, 2016, **53**, 34–55.

7 G. Fang, J. Zhou, A. Pan and S. Liang, *ACS Energy Lett*, 2018, **3**, 2480–2501.

8 Y. Yang, E. G. Okonkwo, G. Huang, S. Xu, W. Sun and Y. He, *Energy Storage Mater*, 2021, 36, 186–212.

9 Y. Chen, Y. Kang, Y. Zhao, L. Wang, J. Liu, Y. Li, Z. Liang, X. He, X. Li, N. Tavajohi and B. Li, *Journal of Energy Chemistry*, 2021, 59, 83–99.

10 D. Larcher and J. M. Tarascon, *Nat Chem*, 2015, **7**, 19–29.

11 M. Song, H. Tan, D. Chao and H. J. Fan, *Adv Funct Mater*, 2018, **28**, 1–27.

12 M. Larry, Master thesis, University of Liege, 2021.

13 S. Mallick and C. R. Raj, *ChemSusChem*, 2021, **14**, 1987–2022.

14 T. Lehtola and A. Zahedi, *Sustainable Energy Technologies and Assessments*, 2019, **35**, 25–31.

15 Statista, Energy consumption worldwide from 2000 to 2019, with a forecast until 2050, by energy source, https://www.statista.com/statistics/222066/projected-global-energy-consumption-by-source/, (accessed 5 May 2024).

16 Statista, Development of the world population from 1950 to 2050, https://www.statista.com/statistics/262875/development-of-the-world-population/, (accessed 5 May 2024).

17 P. U. Nzereogu, A. D. Omah, F. I. Ezema, E. I. Iwuoha and A. C. Nwanya, *Applied Surface Science Advances*, 2022, **9**, 100233.

18 A. Konarov, N. Voronina, J. H. Jo, Z. Bakenov, Y. K. Sun and S. T. Myung, *ACS Energy Lett*, 2018, **3**, 2620–2640.

19 K. Kubota, M. Dahbi, T. Hosaka, S. Kumakura and S. Komaba, *The Chemical Record*, 2018, **18**, 459–479.

20 J. Ming, J. Guo, C. Xia, W. Wang and H. N. Alshareef, *Materials Science and Engineering R: Reports*, 2019, **135**, 58–84.

21 N. Nitta and G. Yushin, *Particle and Particle Systems Characterization*, 2014, **31**, 317–336.

22 J. Sun, *Open Aircraft Performance Modeling Based on an Analysis of Aircraft Surveillance Data*, 2019.

23 A. Ambrosi, C. K. Chua, A. Bonanni and M. Pumera, *Chem Rev*, 2014, **114**, 7150–7188.

24 S. W. Lee, N. Yabuuchi, B. M. Gallant, S. Chen, B. S. Kim, P. T. Hammond and Y. Shao-Horn, *Nat Nanotechnol*, 2010, **5**, 531–537.

25 C. M. Park, J. H. Kim, H. Kim and H. J. Sohn, *Chem Soc Rev*, 2010, **39**, 3115–3141.

26 P. Poizot, S. Laruelle, S. Grugeon, L. Dupont and J. Tarascon, *Nature*, 2000, **407**, 496–499.

27 L. Ji, Z. Lin, M. Alcoutlabi and X. Zhang, *Energy Environ Sci*, 2011, **4**, 2682–2689.

28 J. L. C. Rowsell, V. Pralong and L. F. Nazar, *J Am Chem Soc*, 2001, **123**, 8598–8599.

29 H. Fei, X. Liu and Z. Li, *Chemical Engineering Journal*, 2015, **281**, 453–458.

30 R. Systems, .

31 Y. Liang, Z. Tao and J. Chen, *Adv Energy Mater*, 2012, **2**, 742–769.

32 B. A. Kahsay, F. M. Wang, A. G. Hailu and C. H. Su, *Polymers (Basel)*, 2020, **12**, 1–10.

33 J. Lu, Z. Chen, F. Pan, Y. Cui and K. Amine, *Electrochemical Energy Reviews*, 2018, **1**, 35–53.

34 N. Nitta, F. Wu, J. T. Lee and G. Yushin, *Materials Today*, 2015, **18**, 252–264.

35 Md. H. Hossain, M. A. Chowdhury, N. Hossain, Md. A. Islam and M. H. Mobarak, *Chemical Engineering Journal Advances*, 2023, **16**, 100569.

36 A. A. Pavlovskii, K. Pushnitsa, A. Kosenko, P. Novikov and A. A. Popovich, *Materials*, 2022, **16**, 177.

37 Y. Nishi, *The chemical record*, 2001, **a**, 406–413.

38 G. Crabtree, E. Kócs and L. Trahey, *MRS Bull*, 2015, **40**, 1067–1076.

39 E. Moyassari, T. Roth, S. Kücher, C.-C. Chang, S.-C. Hou, F. B. Spingler and A. Jossen, *J Electrochem Soc*, 2022, **169**, 010504.

40 Y. Nishi, *Chemical record*, 2001, **1**, 406–413.

41 J. Gnanaraj, R. Lee, A. Levine, J. Wistrom, S. Wistrom, Y. Li, J. Li, K. Akato, A. Naskar and M. Paranthaman, *Sustainability*, 2018, **10**, 2840.

42 H. Shi, C. Shi, Z. Jia, L. Zhang, H. Wang and J. Chen, *RSC Adv*, 2022, **12**, 33641–33652.

43 F. M. J. Liu, X. Wei, *Lithium Titanate-Based Lithium-Ion Batteries*, 2019.

44 Y. Hwa, J. H. Sung, B. Wang, C. M. Park and H. J. Sohn, *J Mater Chem*, 2012, **22**, 12767–12773.

45 F. De Angelis, R. Proietti Zaccaria, E. Miele, S. Goriparti, C. Capiglia and E. Di Fabrizio, *J Power Sources*, 2014, **257**, 421–443.

46 Michelet Cédric, University of Nantes, 2015.

47 S. H. Yu, X. Feng, N. Zhang, J. Seok and H. D. Abruña, *Acc Chem Res*, 2018, **51**, 273–281.

48 J. Cabana, L. Monconduit, D. Larcher and M. R. Palacín, *Advanced Materials*, 2010, **22**, 170–192.

49 M. D. Bhatt and J. Y. Lee, *Int J Hydrogen Energy*, 2019, **44**, 10852–10905.

50 Bernardi Jérôme, Université de Montpellier II, 2008.

51 Y. Lu, L. Yu and X. W. (David) Lou, *Chem*, 2018, **4**, 972–996.

52 M. Armand, S. Grugeon, H. Vezin, S. Laruelle, P. Ribière, P. Poizot and J. M. Tarascon, *Nat Mater*, 2009, **8**, 120–125.

53 M. E. Bhosale, S. Chae, J. M. Kim and J. Y. Choi, *J Mater Chem A Mater*, 2018, 6, 19885–19911.

54 H. Oubaha, J. F. Gohy and S. Melinte, *Chempluschem*, 2019, **84**, 1179–1214.

55 Z. Liu, L. Feng, X. Su, C. Qin, K. Zhao, F. Hu, M. Zhou and Y. Xia, *J Power Sources*, 2018, **375**, 102–105.

56 Y. Song, L. Yu, Y. Gao, C. Shi, M. Cheng, X. Wang, H. J. Liu and Q. Liu, *Inorg Chem*, 2017, **56**, 11603–11609.

57 H. Fei, X. Liu, Z. Li and W. Feng, *Dalton Transactions*, 2015, **44**, 9909–9914.

58 X. Han, F. Yi, T. Sun and J. Sun, *Electrochem commun*, 2012, **25**, 136–139.

59 Y. Mao, Q. Kong, B. Guo, X. Fang, X. Guo, L. Shen, M. Armand, Z. Wang and L. Chen, *Energy Environ Sci*, 2011, **4**, 3442–3447.

60 Dan-Yang Wang, Ruilan Liu, Wei Guo, Gang Li and Yongzhu Fu, *Coord Chem Rev*, 2021, 429.

61 J. Jiang, Y. Li, J. Liu, X. Huang, C. Yuan and X. W. Lou, *Advanced Materials*, 2012, **24**, 5166–5180.

62 D. Demirocak, S. Srinivasan and E. Stefanakos, *Applied Sciences*, 2017, **7**, 731.

63 Y. Yan, G. Guo, T. Li, D. Han, J. Zheng, J. Hu, D. Yang and A. Dong, *Electrochim Acta*, 2017, **246**, 43–50.

64 Y. J. Oh, J. Lee, J. Y. Seo, T. Rhim, S. H. Kim, H. J. Yoon and K. Y. Lee, *Journal of Controlled Release*, 2011, **150**, 56–62.

65 X. Jia, C. Liu, Z. G. Neale, J. Yang and G. Cao, *Chem Rev*, 2020, **120**, 7795–7866.

66 P. Hu, M. Yan, T. Zhu, X. Wang, X. Wei, J. Li, L. Zhou, Z. Li, L. Chen and L. Mai, *ACS Appl Mater Interfaces*, 2017, **9**, 42717–42722.

67 Abundance in Earth's Crust of the elements, https://periodictable.com/Properties/A/CrustAbundance.v.log.html, (accessed 21 April 2023).

68 LIVE Vanadium Price, https://vanadiumprice.com/, (accessed 7 February 2024).

69 Glacier Media Group, https://www.mining.com/markets/commodity/zinc/, (accessed 7 February 2024).

70 D. Kundu, B. D. Adams, V. Duffort, S. H. Vajargah and L. F. Nazar, *Nat Energy*, 2016, **1**, 1–14.

71 Ryan Brown, *Power Mag*.

72 X. Chen, L. Wang, H. Li, F. Cheng and J. Chen, *Journal of Energy Chemistry*, 2019, **38**, 20–25.

73 J. Zhou, L. Shan, Z. Wu, X. Guo, G. Fang and S. Liang, *Chemical Communications*, 2018, **54**, 4457–4460.

74 N. Zhang, Y. Dong, M. Jia, X. Bian, Y. Wang, M. Qiu, J. Xu, Y. Liu, L. Jiao and F. Cheng, *ACS Energy Lett*, 2018, **3**, 1366–1372.

75 P. He, G. Zhang, X. Liao, M. Yan, X. Xu, Q. An, J. Liu and L. Mai, *Adv Energy Mater*, 2018, **8**, 1–6.

76 L. Zhang, L. Chen, X. Zhou and Z. Liu, *Sci Rep*, 2015, **5**, 1–11.

77 Z. Liu, P. Bertram and F. Endres, *Journal of Solid State Electrochemistry*, 2017, **21**, 2021–2027.

78 N. Patil, C. de la Cruz, D. Ciurduc, A. Mavrandonakis, J. Palma and R. Marcilla, *Adv Energy Mater*, 2021, **11**, 1–14.

79 Q. Zhao, W. Huang, Z. Luo, L. Liu, Y. Lu, Y. Li, L. Li, J. Hu, H. Ma and J. Chen, *Sci Adv*, 2018, **4**, 1761.

80 N. Patil, J. Palma and R. Marcilla, *Polymers (Basel)*, 2021, **13**, 1673.

81 X. Yue, H. Liu and P. Liu, *Chemical Communications*, 2019, **55**, 1647–1650.

82 S. Huang, J. Zhu, J. Tian and Z. Niu, *Chemistry - A European Journal*, 2019, **25**, 14480–14494.

83 Y. Ding, L. Zhang, X. Wang, L. Han, W. Zhang and C. Guo, *Chinese Chemical Letters*, 2023, **34**, 107399.

84 G. Yang, Q. Li, K. Ma, C. Hong and C. Wang, *J Mater Chem A Mater*, 2020, **8**, 8084–8095.

85 W. Liu, L. Dong, B. Jiang, Y. Huang, X. Wang, C. Xu, Z. Kang, J. Mou and F. Kang, *Electrochim Acta*, 2019, **320**, 134565.

86 N. Zhang, F. Cheng, Y. Liu, Q. Zhao, K. Lei, C. Chen, X. Liu and J. Chen, *J Am Chem Soc*, 2016, **138**, 12894–12901.

87 C. H. Lee and S. K. Jeong, *Chem Lett*, 2016, **45**, 1447–1449.

88 H. Jia, Z. Wang, B. Tawiah, Y. Wang, C. Y. Chan, B. Fei and F. Pan, *Nano Energy*, 2020, **70**, 104523.

89 X. Zhang, J. P. Hu, N. Fu, W. Bin Zhou, B. Liu, Q. Deng and X. W. Wu, *InfoMat*, 2022, **4**, 1–28.

90 S. Yang, H. Du, Y. Li, X. Wu, B. Xiao, Z. He, Q. Zhang and X. Wu, *Green Energy & Environment*, 2023, **8**, 1531–1552.

91 C. Li, X. Xie, S. Liang and J. Zhou, *Energy & Environmental Materials*, 2020, 1–14.

92 T. Wang, C. Li, X. Xie, B. Lu, Z. He, S. Liang and J. Zhou, *ACS Nano*, 2020, **14**, 16321–16347.

93 F. Tao, Y. Liu, X. Ren, J. Wang, Y. Zhou, Y. Miao, F. Ren, S. Wei and J. Ma, *Journal of Energy Chemistry*, 2022, **66**, 397–412.

94 W. Li, K. Wang, S. Cheng and K. Jiang, *Adv Energy Mater*, 2009, **21**, 4593-4607.

95 Y. Cheng, L. Luo, L. Zhong, J. Chen, B. Li, W. Wang, S. X. Mao, C. Wang, V. L. Sprenkle, G. Li and J. Liu, *ACS Appl Mater Interfaces*, 2016, **8**, 13673–13677.

96 B. Jiang, C. Xu, C. Wu, L. Dong, J. Li and F. Kang, *Electrochim Acta*, 2017, **229**, 422–428.

97 Y. Zhao, Y. Zhu and X. Zhang, *InfoMat*, 2020, **2**, 237–260.

98 M. H. Alfaruqi, S. Islam, D. Y. Putro, V. Mathew, S. Kim, J. Jo, S. Kim, Y. K. Sun, K. Kim and J. Kim, *Electrochim Acta*, 2018, **276**, 1–11.

99 S. Islam, M. H. Alfaruqi, V. Mathew, J. Song, S. Kim, S. Kim, J. Jo, J. P. Baboo, D. T. Pham, D. Y. Putro, Y. K. Sun and J. Kim, *J Mater Chem A Mater*, 2017, **5**, 23299–23309.

100 W. Xu and Y. Wang, *Nanomicro Lett*, 2019, **11**, 1–30.

101 J. Shin, J. K. Seo, R. Yaylian, A. Huang and Y. S. Meng, *International Materials Reviews*, 2020, **65**, 356–387.

102 V. Mathew, B. Sambandam, S. Kim, S. Kim, S. Park, S. Lee, M. H. Alfaruqi, V. Soundharrajan, S. Islam, D. Y. Putro, J. Y. Hwang, Y. K. Sun and J. Kim, *ACS Energy Lett*, 2020, **5**, 2376–2400.

103 D. Selvakumaran, A. Pan, S. Liang and G. Cao, *J Mater Chem A Mater*, 2019, **7**, 18209–18236.

104 B. Tang, L. Shan, S. Liang and J. Zhou, *Energy Environ Sci*, 2019, **12**, 3288–3304.

105 J. Hao, J. Mou, J. Zhang, L. Dong, W. Liu, C. Xu and F. Kang, *Electrochim Acta*, 2018, **259**, 170–178.

106 A. I. Volkov, A. S. Sharlaev, O. Ya. Berezina, E. G. Tolstopjatova, L. Fu and V. v. Kondratiev, *Mater Lett*, 2022, **308**, 0–4.

107 R. Li, H. Zhang, Q. Zheng and X. Li, *J Mater Chem A Mater*, 2020, **8**, 5186–5193.

108 Y. Zhang, A. Chen and J. Sun, *Journal of Energy Chemistry*, 2021, **54**, 655–667.

109 T. Lv, Y. Peng, G. Zhang, S. Jiang, Z. Yang, S. Yang and H. Pang, *Advanced Science*, 2023, **2206907**, 1–49.

110 G. Li, L. Sun, S. Zhang, C. Zhang, H. Jin, K. Davey, G. Liang, S. Liu, J. Mao and Z. Guo, *Adv Funct Mater*, 2024, **34**, 2301291

111 M. S. Chae and S. T. Hong, *Batteries*, 2019, **5**, 1–13.

112 Z. Jia, B. Wang and Y. Wang, *Mater Chem Phys*, 2015, **149**, 601–606.

113 C. Kim, B. Y. Ahn, T. S. Wei, Y. Jo, S. Jeong, Y. Choi, I. D. Kim and J. A. Lewis, *ACS Nano*, 2018, **12**, 11838–11846.

114 Z. Li, J. Tan, X. Zhu, S. Xie, H. Fang, M. Ye and J. Shen, *Energy Storage Mater*, 2022, **51**, 294–305.

115 W. Zhang, C. Zuo, C. Tang, W. Tang, B. Lan, X. Fu, S. Dong and P. Luo, *Energy Technology*, 2021, **9**, 1–20.

116 F. Wan and Z. Niu, *Angewandte Chemie - International Edition*, 2019, **58**, 16358–16367.

117 D. Kundu, B. D. Adams, V. Duffort, S. H. Vajargah and L. F. Nazar, *Nat Energy*, 2016, **1**, 1–28.

118 D. Kundu, S. Hosseini Vajargah, L. Wan, B. Adams, D. Prendergast and L. F. Nazar, *Energy Environ Sci*, 2018, **11**, 881–892.

119 H. Qin, L. Chen, L. Wang, X. Chen and Z. Yang, *Electrochim Acta*, 2019, **306**, 307–316.

120 C. Q. Feng, S. Y. Wang, R. Zeng, Z. P. Guo, K. Konstantinov and H. K. Liu, *J Power Sources*, 2008, **184**, 485–488.

121 E. Roex, F. Boschini, V. Delaval, A. Schrijnemakers, R. Cloots and A. Mahmoud, *Journal of Electroanalytical Chemistry*, 2023, **929**, 117133.

122 H. Chen, H. Qin, L. Chen, J. Wu and Z. Yang, *J Alloys Compd*, 2020, **842**, 155912.

123 Q. Pang, C. Sun, Y. Yu, K. Zhao, Z. Zhang, P. M. Voyles, G. Chen, Y. Wei and X. Wang, *Adv Energy Mater*, 2018, **8**, 1–9.

124 B. Yin, S. Zhang, K. Ke, T. Xiong, Y. Wang, B. K. D. Lim, W. S. V. Lee, Z. Wang and J. Xue, *Nanoscale*, 2019, **11**, 19723–19728.

125 X. Qin, X. Wang, J. Sun, Q. Lu, A. Omar and D. Mikhailova, *Front Energy Res*, 2020, **8**, 1–6.

126 Y. Du, X. Wang, J. Man and J. Sun, *Mater Lett*, 2020, **272**, 127813.

127 X. Guo, G. Fang, W. Zhang, J. Zhou, L. Shan, L. Wang, C. Wang, T. Lin, Y. Tang and S. Liang, *Adv Energy Mater*, 2018, **8**, 1–7.

128 Z. Peng, Q. Wei, S. Tan, P. He, W. Luo, Q. An and L. Mai, *Chemical Communications*, 2018, **54**, 4041–4044.

129 F. Ming, H. Liang, Y. Lei, S. Kandambeth, M. Eddaoudi and H. N. Alshareef, *ACS Energy Lett*, 2018, **3**, 2602–2609.

130 L. Wang, K. W. Huang, J. Chen and J. Zheng, *Sci Adv*, 2019, **5**, 1–11.

131 M. Yan, P. He, Y. Chen, S. Wang, Q. Wei, K. Zhao, X. Xu, Q. An, Y. Shuang, Y. Shao, K. T. Mueller, L. Mai, J. Liu and J. Yang, *Advanced Materials*, 2018, **30**, 1–6.

132 Y. Liu and Y. Gong, *Nanoscale*, 2023, **15**, 6273–6284.

133 S. H. Kim and S. M. Oh, *J Power Sources*, 1998, **72**, 150–158.

134 X. Wu, Y. Xiang, Q. Peng, X. Wu, Y. Li, F. Tang, R. Song, Z. Liu, Z. He and X. Wu, *J Mater Chem A Mater*, 2017, **5**, 17990–17997.

135 F. Wan, L. Zhang, X. Dai, X. Wang, Z. Niu and J. Chen, *Nat Commun*, 2018, **9**, 1–11.

136 H. Zhang, X. Liu, H. Li, B. Qin and S. Passerini, *ACS Appl Mater Interfaces*, 2020, **12**, 15305–15312.

137 Y. Li, P. Xu, J. Jiang, J. Yao, B. Huang and J. Yang, *Mater Today Commun*, 2021, **26**, 101849.

138 B. Sambandam, V. Soundharrajan, S. Kim, M. H. Alfaruqi, J. Jo, S. Kim, V. Mathew, Y. K. Sun and J. Kim, *J Mater Chem A Mater*, 2018, **6**, 3850–3856.

139 P. Hu, T. Zhu, J. Ma, C. Cai, G. Hu, X. Wang, Z. Liu, L. Zhou and L. Mai, *Chemical Communications*, 2019, **55**, 8486–8489.

140 W. Zhou, J. Chen, M. Chen, X. Xu, Q. Tian, J. Xu and C. P. Wong, *RSC Adv*, 2019, **9**, 30556–30564.

141 X. Wang, L. Ma and J. Sun, *ACS Appl Mater Interfaces*, 2019, **11**, 41297–41303.

142 J. Zhao, H. Ren, Q. Liang, D. Yuan, S. Xi, C. Wu, W. Manalastas, J. Ma, W. Fang, Y. Zheng, C. F. Du, M. Srinivasan and Q. Yan, *Nano Energy*, 2019, **62**, 94–102.

143 X. Wang, L. Ma, P. Zhang, H. Wang, S. Li, S. Ji, Z. Wen and J. Sun, *Appl Surf Sci*, 2020, **502**, 144207.

144 Y. Li, Z. Huang, P. K. Kalambate, Y. Zhong, Z. Huang, M. Xie, Y. Shen and Y. Huang, *Nano Energy*, 2019, **60**, 752–759.

145 X. Wang, L. Wang, B. Zhang, J. Feng, J. Zhang, X. Ou, F. Hou and J. Liang, *Journal of Energy Chemistry*, 2021, **59**, 126–133.

146 Y. Wang, X. Liu, G. Xu, Y. Liang, W. Ni, B. Wu and L. Yang, *Ionics (Kiel)*, 2022, **28**, 4709–4718.

147 S. Wang, K. Zhu, L. Yang, H. Li, S. Wang, S. Tang, M. Zhang, A. Abliz and F. Zhao, *Ionics (Kiel)*, 2020, **10**, 1-32

148 X. Wang, Y. Li, S. Wang, F. Zhou, P. Das, C. Sun, S. Zheng and Z. S. Wu, *Adv Energy Mater*, 2020, **10**, 1–9.

149 X. Wang, L. Ma and J. Sun, *ACS Appl Mater Interfaces*, 2019, **11**, 41297–41303.

150 M. Wilhelm, R. Adam, A. Bhardwaj, I. Neumann, S. H. Cho, Y. Yamada, T. Sekino, J. Tao, Z. Hong, T. Fischer and S. Mathur, *Adv Eng Mater*, 2023, **25**, 2200765.

151 Q. Li, Y. Chen, J. He, F. Fu, F. Qi, J. Lin and W. Zhang, *Energy Technology*, 2017, **5**, 665–669.

152 D. Xu, H. Wang, F. Li, Z. Guan, R. Wang, B. He, Y. Gong and X. Hu, *Adv Mater Interfaces*, 2019, **6**, 1–8.

153 D. Chen, X. Rui, Q. Zhang, H. Geng, L. Gan, W. Zhang, C. Li, S. Huang and Y. Yu, *Nano Energy*, 2019, **60**, 171–178.

154 C. Yin, C. Pan, X. Liao, Y. Pan and L. Yuan, *ACS Appl Mater Interfaces*, 2021, **13**, 39347–39354.

155 R. Li, F. Xing, T. Li, H. Zhang, J. Yan, Q. Zheng and X. Li, *Energy Storage Mater*, 2021, **38**, 590–598.

156 S. Li, X. Wei, C. Wu, B. Zhang, S. Wu and Z. Lin, *ACS Appl Energy Mater*, 2021, **4**, 4208–4216.

157 B. She, L. Shan, H. Chen, J. Zhou, X. Guo, G. Fang, X. Cao and S. Liang, *Journal of Energy Chemistry*, 2019, **37**, 172–175.

158 C. Xia, J. Guo, P. Li, X. Zhang and H. N. Alshareef, *Angewandte Chemie - International Edition*, 2018, **57**, 3943–3948.

159 Z. Xie, J. Lai, X. Zhu and Y. Wang, *ACS Appl Energy Mater*, 2018, **1**, 6401–6408.

160 F. Ming, H. Liang, Y. Lei, S. Kandambeth, M. Eddaoudi and H. N. Alshareef, *ACS Energy Lett*, 2018, **3**, 2602–2609.

Chapter II: Organopalladium complexes ($XPd(4\text{-}AcOC_6H_4)(PPh_3)_2$, with X = I, Br and Cl) as anode materials for Li-ion batteries: synthesis and optimization

In the first part of this chapter, we study the electrochemical performance of three novel organopalladium complexes ($XPd(4\text{-}AcOC_6H_4)(PPh_3)_2$, with X = I, Br and Cl) synthesized in Laboratory of Macromolecular Chemistry and Organic Catalysis, as anode materials in lithium-ion batteries. The cyclic voltammetry and galvanostatic cycling results show that the nature of the halogen ligand (X = I, Br, and Cl) highly impacts the reaction mechanism during the first discharge and cycling performance. The iodo-organopalladium complex anode material shows the highest specific capacity and a high capacity retention after 200 cycles at a current density of 50 mA g^{-1} with an average discharge capacity of about 170 mAh g^{-1}.

A deeper investigation of this last material was conducted and discussed in this chapter's second part. The double emulsion-evaporation technique was used and optimized to control the particle morphology of the $[IPd(4\text{-}AcOC_6H_4)(PPh_3)_2]$ complex obtained after synthesis to show the influence of the particle morphology on the improvement of electrochemical performance. The structural and morphological properties were investigated by combining NMR analysis, XRD, SEM, and TEM. Moreover, the effect of electrode slurry homogenization duration was explored and investigated. After double emulsion, the optimized $IPd(4\text{-}AcOC_6H_4)(PPh_3)_2$ electrode material exhibits a higher specific discharge capacity of 740 mAh g^{-1} at 50 mA g^{-1}. These results indicate that the particle morphology and duration of slurry homogenization have a great influence on the improvement of specific capacity, cyclability, and rate capability of $[IPd(4\text{-}AcOC_6H_4)(PPh_3)_2]$ as anode material for Li-ion batteries.

Keywords: Organo-palladium(II) complexes, electrochemical performance, lithium-ion batteries, conversion reaction, anode, double emulsion-evaporation

K. S. Etsè, F. Boschini, C. Karegeya, **E. Roex**, G. Zaragoza, A. Demonceau, R. Cloots, A. Mahmoud, "Exploring organo-palladium(II) complexes as novel organometallic materials for Li-ion batteries," *Electrochimica Acta*, vol 337, 2020.

E. Roex, K. S. Etsè, R. Cloots, F. Boschini, and A. Mahmoud, "Improving the electrochemical performances of organo-palladium (II) complex as promising anode material for Li-ion batteries: Effect of double emulsion preparation," *Journal of Power Sources,* vol. 496, 2021.

1. Introduction

As explained previously, the energy demand continues to grow dramatically worldwide due to population explosion, depletion of fossil fuel reserves, and technological advances. Lithium-ion batteries (LIBs) have been widely studied and used for several decades because they possess many advantages, such as good cycling, high capacity, and high energy density [1,2]. Nowadays, trade lithium batteries are composed of graphite and metal oxide as anode and cathode active materials respectively [3]. Nevertheless, studies are still in progress to develop novel advanced anode and cathode materials with higher energy density and longer cycle life to meet the requirements of the new technologies and devices. Generally, electrode materials studied are based on transition metal oxides, polyanion compounds [4,5], graphitic and hard carbon, and more recently on organic molecules and polymers [6–9]. The wide diversity of organic redox systems and the design flexibility at the molecular level are advantages of organic compounds but they suffer from low electrical conductivity [10]. Organometallic compounds composed of organic linkers and metal ions have the advantage to possess unique electrical and chemical properties [11]. However, according to our knowledge, only a few organometallic compounds have been reported in the literature as electrode materials for rechargeable batteries. Ferrocene, linked to polymers, has proven to be an effective and good candidate as cathode material for LIBs [11–15]. Moreover, another ferrocene derivative has also been reported by Z. Liu *et al.* as an anode material in LIBs [16]. Other materials such as polypyrrole-iron-oxygen [17], transition metal carbodiimides[18], Co- or Zn- based coordination polymer[7,19], metal-1,4,5,8-naphthalenetetracarboxylates[20], and metal dicarboxylates [7,21] have been investigated as anode materials for Li-ion batteries and exhibit excellent electrochemical performance. These publications prompted us to publish our preliminary results on the electrochemical properties of organopalladium complexes as new active anode materials for Li-ion batteries. Because of its many oxidation states, palladium is particularly suitable for redox processes. In K. S. Etsè *et al.*, we are reporting for the first time the synthesis and full characterization of [XPd(4-$AcOC_6H_4$)(PPh_3)$_2$] (X = I, Br and Cl) palladium complexes and their application as novel anode material for Li-ion batteries [22].

Since electrochemical performances are related to material particle formulation (size and shape) [23], improving the electrochemical performances of the most efficient organo-palladium complex, [IPd(4-$AcOC_6H_4$)(PPh_3)$_2$], is a great challenge. Indeed, conversion materials face challenges due to their intrinsically poor electronic and ionic conductivity, high volume expansion, and large cell polarization [24]. Various architectures have been

designed to overcome these problems by providing void space in the structure [23,24]. The hollow structure is the most frequently used structure to solve these issues because it is believed to withstand high volumetric expansion and stress [24]. Moreover, their high surface-to-volume ratio greatly enhances the lithium diffusion rate. Hollow spheres are usually obtained by the template-assisted method, although complicated and limited by the yield [25–28]. In this research, a double emulsion (water-in-oil-in-water) followed by solvent evaporation has been selected and optimized. This technique has already been used by Yan.Y *et al,* in 2017 to prepare carbon-coated $MnFe_2O_4$ nanoparticles and its efficiency has been proven to enhance the electrochemical performance of the material [29]. Indeed, this process allows control of the morphological properties of the material. Small and spherical particles with a thin and porous shell can be obtained using this method. A thin shell reduces the diffusion path for electrons and ions during the discharge/charge process, whereas by introducing porosity, the specific surface in contact with the electrolyte increases [29]. Moreover, particle morphology, size, and aggregation can be easily tuned by the double emulsion method [30].

In the first part of this chapter, we report the characterization and electrochemical results needed for our further scientific research on [XPd(4-$AcOC_6H_4$)(PPh_3)$_2$] (X = I, Br and Cl) palladium complexes. Then, the double emulsion-evaporation technique is used to prepare and control the morphology of the most efficient organopalladium complex with the general formula [IPd(4-$AcOC_6H_4$)(PPh_3)$_2$]. The electrochemical performance of the newly formulated material is evaluated as anode material for LIBs and compared with particles initially obtained by precipitation.

2. Experimental part

2.1. Synthesis of [XPd(4-$AcOC_6H_4$)(PPh_3)$_2$] (X = I, Br and Cl)

The trans-halogeno(4-acetoxyphenyl)bis(triphenylphosphine) palladium(II) complexes, [trans-XPd(4-$AcOC_6H_4$)(PPh_3)$_2$] with X = I (3), Br (4) and Cl (5), were easily prepared according to the method described by Flemming (Figure II-1) [31] in Laboratory of Macromolecular Chemistry and Organic Catalysis. This method is based on the ability of aryl iodides to oxidatively add to tetrakis(-triphenylphosphine)palladium(0). Thus, the reaction of 4-acetoxyiodobenzene (4-$AcOC_6H_4I$) (1) with $Pd(PPh_3)_4$ (2) in toluene at room temperature led to the desired compound (3) with an excellent yield of 95% after filtration

and purification. It should be noted that toluene is a solvent of choice for this reaction because it makes it possible to precipitate the complex while maintaining free triphenylphosphine in the solution. The latter can then be easily removed after filtration of the complex and washing. Next, halogen exchange allowed to prepare the bromo (4) and chloro (5) analogs of complex 3. In practice, the iodo compound (3) in solution in dichloromethane was reacted repeatedly with a saturated aqueous solution of KBr or KCl at room temperature. Halogen exchange was followed by ^{31}P NMR spectroscopy. Finally, the bromo (4) and chloro (5) complexes were obtained in good yields (88% and 90%, respectively), as light yellow powders.

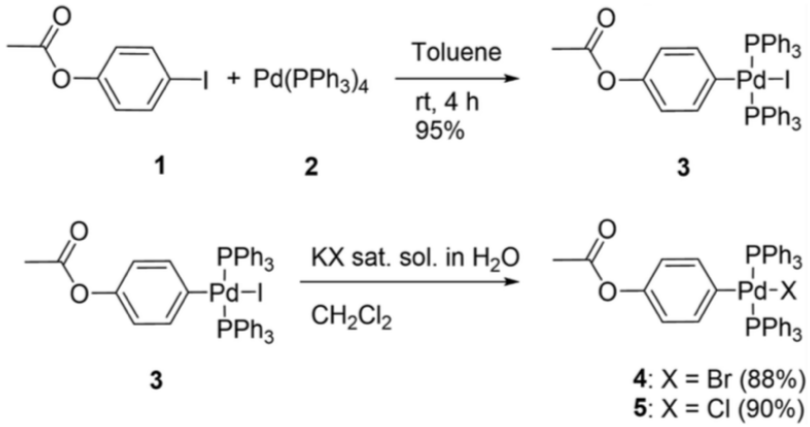

Figure II-1: Synthesis of palladium complexes with X=I, Br or Cl.

The ^{1}H, ^{13}C, and ^{31}P NMR spectra of complexes 3-5 have all been recorded to check their purity and deduce their structure. They are reported in the paper of K. S. Etsè *et al*.

2.2. Double emulsion of $IPd(4\text{-}AcOC_6H_4)(PPh_3)_2$

Spherical particles of the iodo-organopalladium complex were prepared using a water-in-oil-in-water (w/o/w) emulsion method (Figure II-2) adapting the protocol detailed in the reference of Y. J. Oh et al [30]. 500 mg of the iodocomplex (synthesis in point II.2.1.) were dissolved in 5 ml of methylene chloride. An aqueous solution of calcium chloride (1 ml / 0.25 %) was added to the methylene chloride and sonicated with a probe sonicator (power: 20 %, time: 12 seconds). The primary emulsion obtained was poured into 25 mL of PVA (4 wt%). After homogenization at a rate of 15 000 rpm (ultraturrax IKA T25) for one minute, the solution was added into 400 ml of PVA solution (0.4 wt%) in a round bottom flask. The secondary emulsion was stirred under argon for 4 h to remove the methylene chloride and

then centrifugated at 10 000 rpm for 10 minutes to collect the particles. The particles were then washed 3 times with distilled water and lyophilized for 24 h.

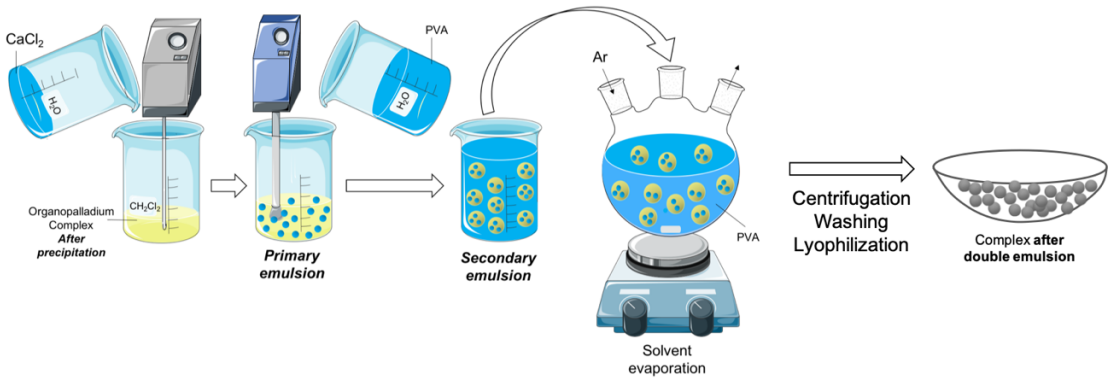

Figure II-2: Scheme of double emulsion technique – solvent evaporation.

2.3. Structural and morphological characterization technique

Nuclear Magnetic Resonance

^{1}H and ^{31}P NMR spectroscopy measurements were carried out at room temperature using a Bruker DRX NMR spectrometer operating at 400.13 and 162 MHz, respectively. Chemical shifts were quoted in parts per million downfield from TMS and were referenced from the residual solvent peaks (CH_2Cl_2: 5.32 ppm) or TMS (0 ppm).

Scanning Electron Microscopy

The particles size and morphology of the different crystals were characterized by scanning electron microscopy (SEM). The SEM morphological analysis of the materials was performed using a FEG-ESEM XL30 (FEI) with an accelerating voltage of 15 kV under high vacuum. Samples were deposited on carbon tapes. The sputtering deposition was done with the gold target under the argon atmosphere (Balzers, SCD004, Sputter coater).

Transmission Electron Microscopy

Transmission electron microscopy (TEM) was used to characterize the particles size and the interior of the particles. Samples were put in suspension in water and deposited on a copper grid. Grids were dried under vacuum. The TEM morphological analysis of the materials was performed using a PHILIPS M100 at an accelerating voltage of 100 kV. Micrographs were analyzed by using the megaview GII (Olympus) software.

X-ray diffraction

X-ray diffraction (XRD) was carried out to study the stability of the structure after different durations of homogenization. The electrode film was separated from the Cu foil and analyzed over the 2θ range from 5° to 80° with a Bruker D8 Twin-Twin powder diffractometer using Cu Kα radiation.

2.4. Electrochemical characterization technique

The composite electrodes were prepared by dispersing 60 wt% complex, 30 wt% carbon black (CB), and 10 wt% polyvinylidene fluoride (PVDF) binder in 1-methyl-2-pyrrolidinone (NMP) and stirring the mixture into a homogeneous slurry for 2 h. Afterward, the prepared slurry was deposited by the doctor-blade technique onto a copper foil current collector and dried at 110°C under vacuum overnight. The active material loading was in the range of 1-2 mg cm^{-2}. The Lithium half-cell of the prepared electrode was assembled using coin cells (2032, R-type), in an argon-filled glovebox. Celgard membrane was used as a separator and a disc of metal lithium foil served as anode and also reference electrode. 1 M $LiPF_6$ in a 1:1 (v:v) organic solvent mixture of EC and DMC with 10% fluoroethylene carbonate and 2% vinylene carbonate solution was used as electrolyte. The comparison of the rate capability of the different studied complexes was performed via the galvanostatic charge/discharge tests at different current densities between 0.01V and 3.0 V vs. Li/Li^+ using a LAND battery test system (Wuhan, China). The specific capacity is calculated based on the anode active material mass. Cyclic voltammetry was carried out on a Bio-Logic Science instrument at a scan rate of 0.1 mV s^{-1} in a voltage window of 0.01-3.0 V vs. Li/Li^+.

3. Results and discussion

3.1. Three novel organopalladium complexes, [XPd(4-$AcOC_6H_4$)(PPh_3)$_2$] (X = I, Br and Cl), as anode materials for LIBs

3.1.1. Particle morphology

The XPd(4-$AcOC_6H_4$)(PPh_3)$_2$ complexes with X = I (3), Br (4) and Cl (5), were easily prepared according to the method described in point II.2.1. . To control the particle size of the powdered complexes, two synthetic approaches were considered. First, complex 3 was synthesized under highly diluted conditions (0.005 M). One day was necessary for the

reaction to be complete. The complex was then isolated by precipitation by adding n-pentane into the reaction mixture and filtration. Examination of the resulting powder by SEM reveals the presence of relatively large particles with a particle size of about 60 µm and a poorly defined morphology (Figure II-3a). To reduce the particle size, the powder obtained above was suspended in pentane and stirred under ultrasound for 4-20 h. As shown in Figure II-3b, this treatment yields polished particles of about 20 µm. Also, note that a prolonged irradiation time did not further reduce the particle size. Unlike the synthesis under highly diluted conditions, the use of a concentrated mixture of the reagents (0.1 M) led to the precipitation of the complex after only 4 h. Analysis of the isolated powder reveals the formation of well-defined but relatively large particles. The other two complexes 4 and 5, prepared from 3, have different morphologies. Thus, the particles in samples 4 and 5 are less thick but much larger than those of complex 3 (Figure II-4).

In order to reduce the particle size, the powders were heated in a CEM Discover microwave reactor at 60 °C with a power of 250 W under air flow. After 6 h of irradiation, relatively fine powders are obtained. The morphology and the particle size of the palladium complexes 3-5 were again investigated by SEM (Figure II-5). Figure II-5a and b show SEM images collected at different magnifications of compound 3. The low-magnification image of 3 (Figure II-5a) shows that the sample is composed of uniform particles whereas the high-magnification image (Figure II-5b) shows that the particle sizes are in the range of 0.50-1.00 µm. The SEM micrographs also indicate that by replacing iodine in complex 3 with bromine in complex 4, the particles are slightly more agglomerated and larger (0.50-2.00 µm) (Figure II-5c and d) whereas by replacing iodine with chlorine to afford complex 5, the particles are less agglomerated and smaller (Figure II-5e and f).

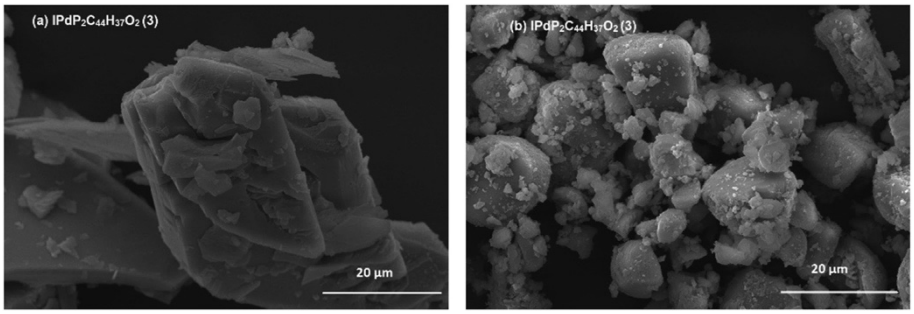

Figure II-3: SEM micrographs of complex 3 obtained (a) after synthesis under highly diluted conditions (0.005 M) and (b) after treatment with ultrasound for 20 h.

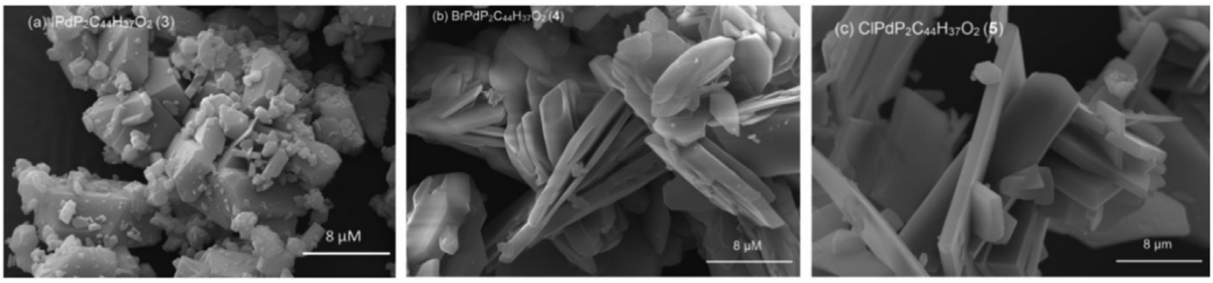

Figure II-4: SEM micrographs of complexes 3-5 obtained after synthesis under more concentrated conditions (0.1 M).

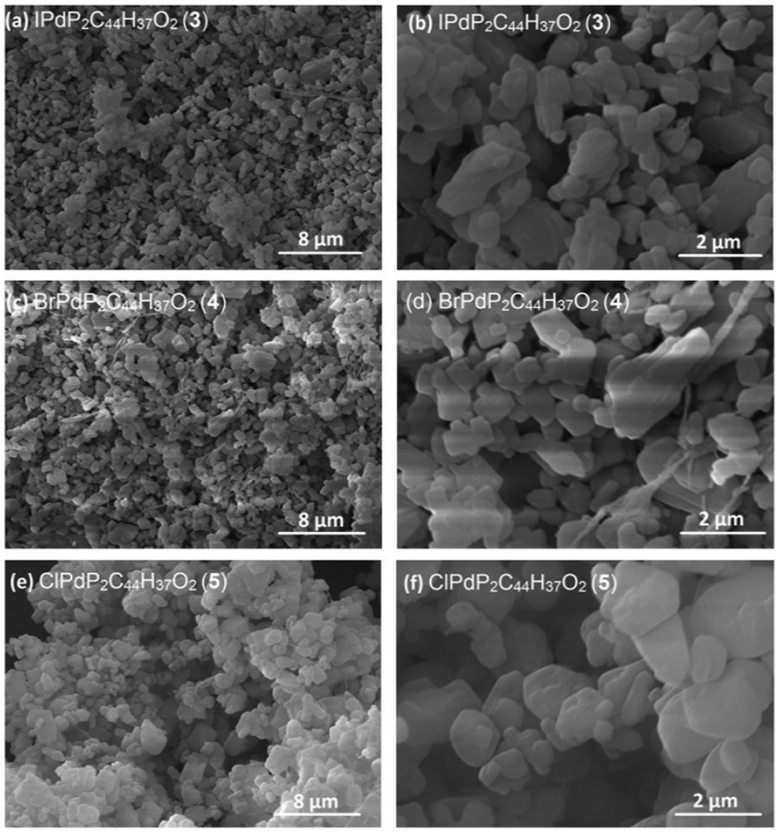

Figure II-5: SEM micrographs of complexes 3-5 under different magnifications.

3.1.2. Electrochemical characterization

With regard to investigating and comparing the electrochemical properties of the prepared palladium-based anode materials, the electrochemical behavior was determined by applying cyclic voltammetry (CV) between 0.01 and 3.0 V vs. Li/Li^+. As shown in Figure II-6, the first discharge corresponding to the first lithiation process for the three complexes under investigation, is not similar to those observed for the following cycles. Additionally, the CV profiles differ from one complex to another and completely differ from that of metallic

palladium [32]. Thus, the first discharge curve for the iodo complex (3) (Figure II-6c) shows three main peaks at 2.35 V, 1.51 V, and 0.90 V. The brominated complex (4) (Figure II-6a) has a very small peak at 1.81 V and two large overlapping peaks at 1.44 and 1.04 V, while the chlorinated analog (5) (Figure II-6b) has a very small peak at 1.76 V and an intense peak at 1.23 V. These results show the important role played by the halogen ligand of the Pd-based complexes on the reaction mechanism during the first discharge. Indeed, attaching an electron-withdrawing group ($\chi_{Cl} > \chi_{Br} > \chi_{I}$) to the redox-active organic molecule increases the redox potential because the electron is attracted toward a higher electronegative group [10]. The observed redox peaks correspond mainly to the Pd^{+II}/Pd^{0} redox couples in the complexes during the first lithiation, indicating that the reaction during the first discharge is highly irreversible and is associated with the decomposition of the complexes upon initial conversion reaction with lithium. Indeed, the cathodic peak intensity strongly decreases in the second cycle and then stabilizes. It should also be noted that the small peak at 0.67 V in the first discharge curves of the three complexes corresponds to the decomposition of the electrolyte and the formation of the solid electrolyte interface layer (SEI) [33,34]. On the other hand, whatever the studied complex, the charge curve profiles are similar during the first three cycles, and the low-intensity anodic peaks observed at 1.13 V, 1.25 V, and 1.2 V for complexes 3, 4, and 5, respectively, correspond to the delithiation of the electrode which leads to the partial or complete oxidation of Pd^{0}.

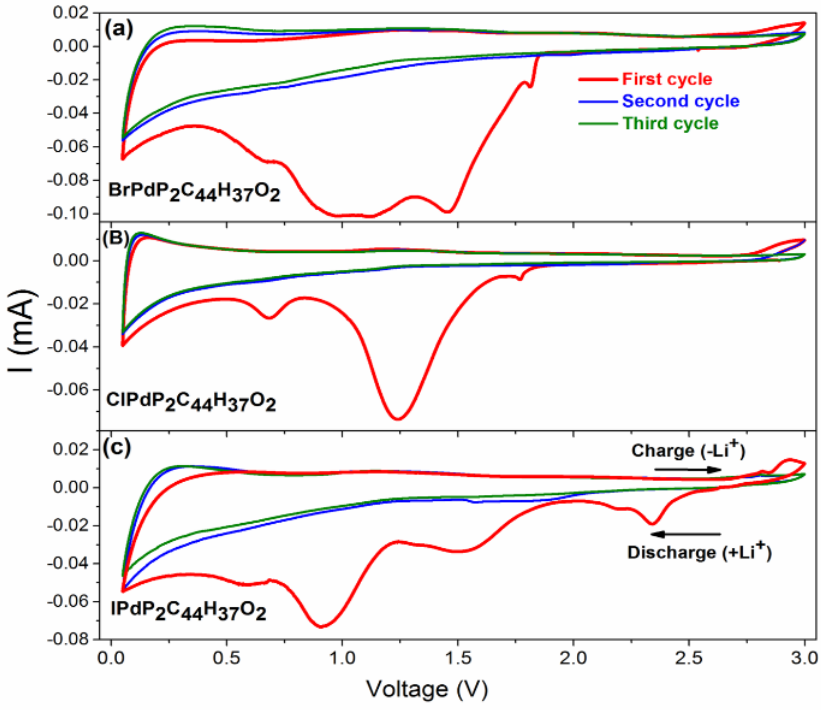

Figure II-6: Cyclic voltammograms of complexes 3-5 at a scan rate of 0.1 mV s^{-1} in the voltage window 0.01-3.0 V.

Examination of the cell voltage vs. specific capacity plots (Figure II-7) reveals that for the three complexes, the first discharge voltage curve is extremely different from the other cycles, as already observed by cyclic voltammetry (Figure II-6). During the first discharge, the three materials (3, 4, and 5) deliver initial capacities of 1089, 444, and 684 mAh g^{-1}, respectively, these obtained discharge capacities are higher than the theoretical values equal to 60, 63, and 67 mAh g^{-1} based on Pd(II) as active redox center. Although the origin of these extra capacities is not yet clear, electrolyte reduction at the surface of the active material carbon, and electrolyte decomposition that lead to the formation of the SEI layer at the electrode are plausible explanations. For the second cycle at 20 mA g^{-1}, the reversible discharge capacities drop drastically to ~224, ~121, and ~100 mAh g^{-1} for complexes 3, 4, and 5, respectively. The significant irreversible behavior in the first cycle and the marked differences between the first discharge curve and the following curves strongly suggest a conversion mechanism at the initial discharge.

Figure II-8a, illustrates the cycling performance of anode materials 3-5 in lithium half-cells under current densities of 20, 50, 100, and 500 mA g^{-1}. The three samples show good cycling stability during five cycles at different current densities, suggesting that they exhibit moderate cyclability at different C-rates, even for the fastest rate of 500 mA g^{-1}. In addition, the obtained capacity of the three samples decreases with increasing rate and, for all current densities explored, anode material 3 exhibits the highest specific capacity among the three with delivered capacities of 209, 169, 142, and 97 mAh g^{-1} at current densities of 20, 50, 100, and 500 mA g^{-1}, respectively. It indicates that the electrochemical performance clearly depends on the nature of the halogen ligand. Furthermore, electrode 3 possesses good capacity retention (Figure II-8b) compared to 4 and 5. After long-term cycling during 200 cycles at a current density of 50 mA g^{-1}, an average specific discharge capacity of about 170 mAh g^{-1} is maintained between 0.01 and 3.0 V with a capacity retention of about 99%.

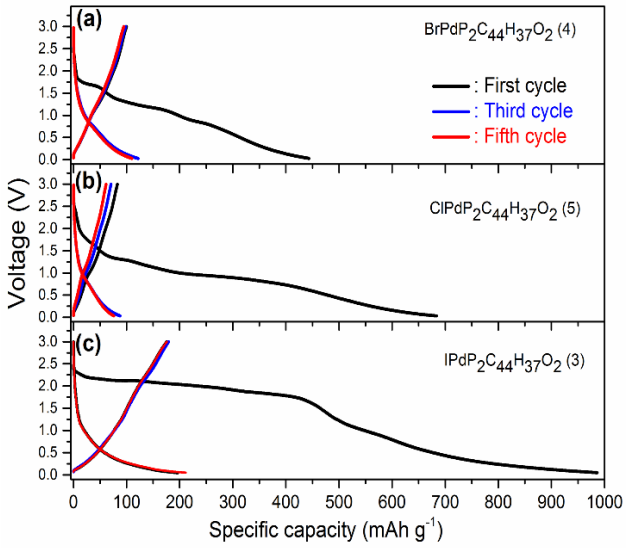

Figure II-7: Representative galvanostatic charge/discharge plots at a current density of 20 mA g^{-1} for particles of complexes 3-5 as anode materials for lithium-ion batteries.

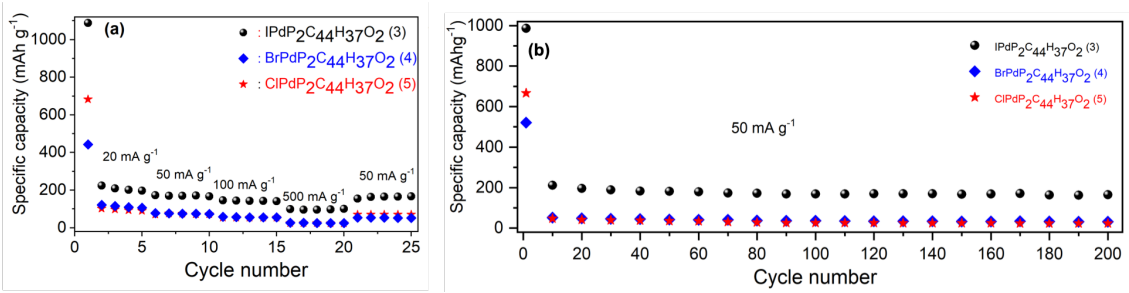

Figure II-8: (a) Evolution of the discharge capacity obtained for complexes 3-5 on cycling at increasing current density rates from 20 to 500 mA g^{-1}. The voltage window explored was 0.01-3.0 V.(b) Evolution of the discharge capacity as a function of the number of cycles at a current density of 50 mA g^{-1}.

Figure II-9a presents the Nyquist plots recorded for XPd(4-$AcOC_6H_4$)(PPh_3)$_2$ (X = I, Br, Cl) at OCV (open circuit voltage) before applying the current. All the impedance spectra are formed of similar semicircles at high-frequency domain and lines in the low-frequency domain corresponding to a diffusion phenomenon. The (RQ)Q equivalent circuit was used to analyze the impedance spectra in order to extract the resistance of the electrolyte and of the charge transfer (Figure II-9b). The resistance of the electrolyte is low and nearly similar for the three electrodes because the identical electrolyte was used to assemble the three cells. However, the charge transfer resistance is clearly different for the three electrodes. IPd(4-$AcOC_6H_4$)(PPh_3)$_2$ shows the lower charge transfer resistance of 506 Ω and the highest resistance (769 Ω) was obtained for ClPd(4-$AcOC_6H_4$)(PPh_3)$_2$ (Table *II-1*). These results are in good agreement with the electrochemical performance obtained for the three electrodes. Indeed, IPd(4-$AcOC_6H_4$)(PPh_3)$_2$ presents the best electrochemical performance which is related to the improved charge transfer reaction kinetics.

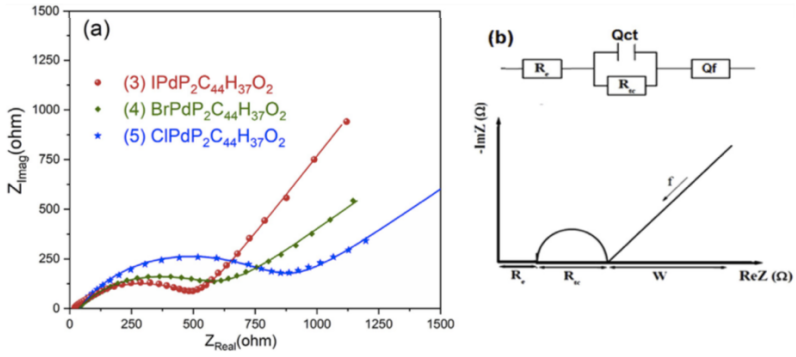

Figure II-9: (a) Nyquist diagrams of impedance measurements of XPd(4-AcOC$_6$H$_4$)(PPh$_3$)$_2$ (X = I, Br, Cl) based electrode material cells at Open circuit voltage (Voc). (b) Model used for the analysis of the impedance spectra and Nyquist plot.

Table II-1: Calculated resistances using Randles equivalent circuit: the resistances of electrolyte (R_{ele}) and charge transfer (R_{ct}) of XPd(4-AcOC$_6$H$_4$)(PPh$_3$)$_2$ based electrode material cells.

	R_{ele} (Ω)	**R_{ct} (Ω)**
IPd(4-AcOC$_6$H$_4$)(PPh$_3$)$_2$	26.6 (1)	506 (1)
BrPd(4-AcOC$_6$H$_4$)(PPh$_3$)$_2$	36.1 (1)	534 (1)
ClPd(4-AcOC$_6$H$_4$)(PPh$_3$)$_2$	39.9 (1)	769 (1)

Now remains to explain the preponderant role of the iodo ligand. To gain more insights into the nature of the PdX and Pd-C bonds in square-planar trans-[(Ph$_3$P)$_2$Pd(Ph)X] complexes, Flemming and co-workers have examined in detail the trans influence of all three halogens and the relative affinities of halide anions for the palladium center [31]. Their findings can be extended to the trans-[(Ph$_3$P)$_2$Pd(4-AcOC$_6$H$_4$)X] complexes used here as organometallic-based negative electrodes for Li-ion batteries. Thus, as mentioned in the paper, the length of Pd-X bonds and Pd-C bond trans influence, indicate that the Pd-I seems to be the weakest bond of the three complexes indicated by the XPdC(Ar) bond distances in chloro (2.0079 Å), bromo (2.0077 Å), and iodo (2.017 Å) complexes. Furthermore, in complexes 3-5, the ^{13}C NMR chemical shift of the aryl quaternary carbon IPd-C(Ar) is the highest (154.05 ppm). This trend reveals that the (Ph$_3$P)$_2$PdX group's electron donating power increases when halogens change from I, Br to Cl. It was proven that the charge capacity is directly linked to the electron-donating/withdrawing nature of the functional group [35].

3.2. Optimization of electrochemical performance of the iodo-complex [IPd(4-$AcOC_6H_4$)$(PPh_3)_2$]

As explained previously, we focused our research on the palladium complex containing iodine ligand [IPd(4-$AcOC_6H_4$)$(PPh_3)_2$] because it presents the best electrochemical performance in comparison to [BrPd(4-$AcOC_6H_4$)$(PPh_3)_2$] and [ClPd(4-$AcOC_6H_4$)$(PPh_3)_2$]. The trans-iodo(4-acetoxyphenyl)bis(triphenylphosphine)palladium was synthesized according to the oxidative addition procedure reported in section II.2.1. . Then, a double emulsion-evaporation technique illustrated in section II.2.2. , is used to control and accommodate the architecture of particles.

Characterizations using proton and phosphorous NMR were performed with a view to ensure the complex chemical structure and purity. The singlet around 2.14 ppm observed in ^1H NMR is easily attributed to the methyl of the acetyl and the two doublets at 6.0 and 6.6 ppm correspond to the hydrogens of the phenyl in 4-acetoxyphenyl ligand attached to the palladium. The set of multiplets around 7.4 ppm integrating for 30 protons attests to the presence of the two triphenylphosphine ligands (Figure II-10a). The signals of these protons are separated in a set of two peaks. Indeed, the chemical environment of the two protons at the ortho position on each phenyl ring is quite different from that of the meta and para due to the influence of the phosphorous atom. In consequence, for the six phenyl rings, the ortho twelve protons shifted downfield. On the contrary, the meta and para positioned protons chemical environment is quite similar and they appear at more close chemical shifts and were overlaid to form one set of multiplet for eighteen protons [31]. In addition, the single peak at 22.7 ppm in ^{31}P NMR confirms the trans position of the phosphines and therefore the formation of the desired product (Figure II-10b).

In view to warrant the integrity of the complex after double emulsion formulation, proton, and phosphorous NMR were realized and compared to those of the synthesized compound (Figure II-10 c, d). As shown in Figure II-10c, the proton spectrum of the formulated product is similar to that of the initial compound obtained after synthesis and precipitation. The peak at 1.5 ppm can be attributed to water coming from the residual water adsorbed on the active material or from the NMR solvent and sample preparation. In ^{31}P NMR spectrum, in addition to the intense peak at 22.7 ppm of the initial product, a less important peak is observed at 23.56 ppm (Figure II-10d). The peak at 23.56 ppm reminds that of the complex where the iodine atom is replaced by chlorine [22]. Indeed, in the double emulsion procedure, calcium chloride is used as a porogen agent. We can therefore assume that [IPd(4-$AcOC_6H_4$)$(PPh_3)_2$]

undergoes halogen metathesis reaction with chlorine atom of $CaCl_2$ leading to [ClPd(4-$AcOC_6H_4$)(PPh_3)$_2$] complex. Nevertheless, the [ClPd(4-$AcOC_6H_4$)(PPh_3)$_2$] proportion is around 3%. This low percentage value is logical since only 1 ml of calcium chloride (0.25 %) is used during the formulation. It is well established that only the use of high among saturated $CaCl_2$ or KCl solution could lead to the notable formation of the chlorinated complex. Furthermore, this percentage is very low, and the effect of such by-product could be considered marginal. According to these results, it comes out clear that the formulation procedure used herein does not modify or affect the molecular structure of the starting material. The morphology of the shaped material is therefore envisaged in the next step to ensure the formulated procedure's efficiency.

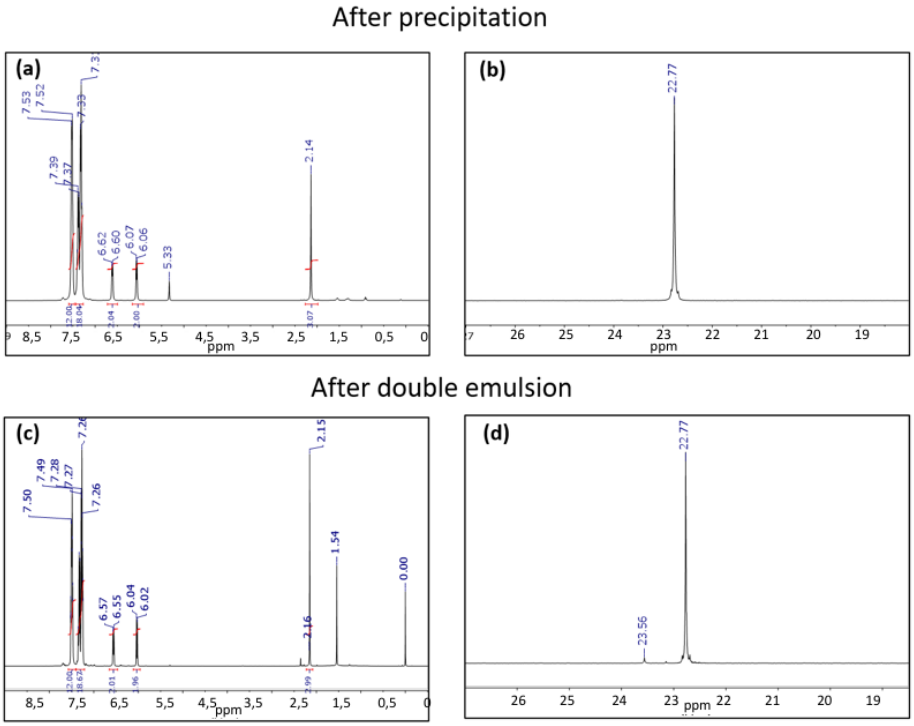

Figure II-10: (a) ^{1}H and (b) ^{31}P NMR spectra of $IPdP_2C_{44}H_{37}O_2$ after synthesis compared to (c) ^{1}H and (d) ^{31}P NMR spectra of $IPdP_2C_{44}H_{37}O_2$ after double emulsion realized in CD_2Cl_2 at 298 K.

3.2.1. Morphological characterization

The morphological aspects of the particles were investigated by combining scanning and transmission electron microscopy techniques (SEM and TEM). The SEM image presented in Figure II-11a clearly shows that particles after precipitation are irregularly shaped and dense with particle size lower than 2 µm. This observation is confirmed by TEM (Figure II-11c). As expected, after double emulsion, spherical hollow microparticles with particle

size lower than 15 µm is obtained (Figure II-11b, e) and detected by SEM analysis. Most of the particles with a size larger than 2 µm are hollow and the thickness of the shell is lower than 500 nm as shown in Figure II-11b and Figure II-11e. Moreover, the TEM image (Figure II-11d) showed that microparticles but also some nanoparticles are formed during this process. Although the material is essentially composed of microparticles, we detected a domain with nanoparticles (size below 15 nm) as presented in Figure II-11f.

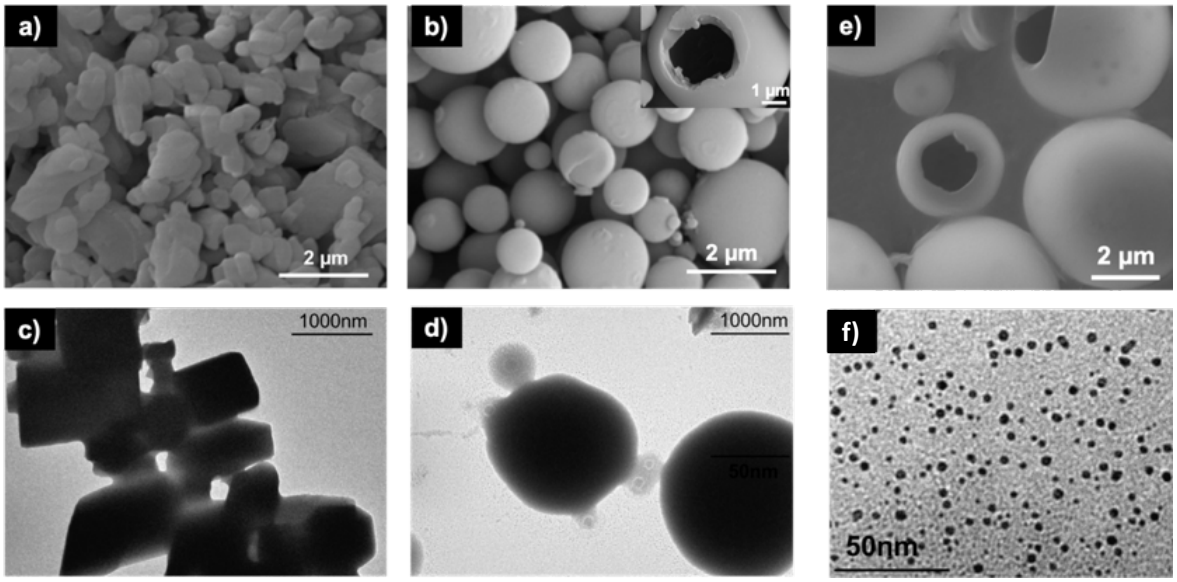

Figure II-11: SEM (a, b, e) and TEM (c, d and f) images of organopalladium complex after precipitation (a, c) and prepared by double emulsion (b, d, e and f).

3.2.2. Electrochemical characterizations

The electrochemical activity of the complex after precipitation and after double emulsion was evaluated as anode material for lithium-ion batteries in half-cells configuration at 25 °C (see protocol in point II.2.4.) using cyclic voltammetry and galvanostatic measurements. Three durations of the electrode slurry homogenization have been tested: 2 h, 24 h, and one week. As described in Figure II-12, no difference was detected from the electrochemical performance standpoint between 2 h and 24 h. Therefore, this work focuses on extreme conditions that correspond to 2 h and one week of electrode slurry homogenization.

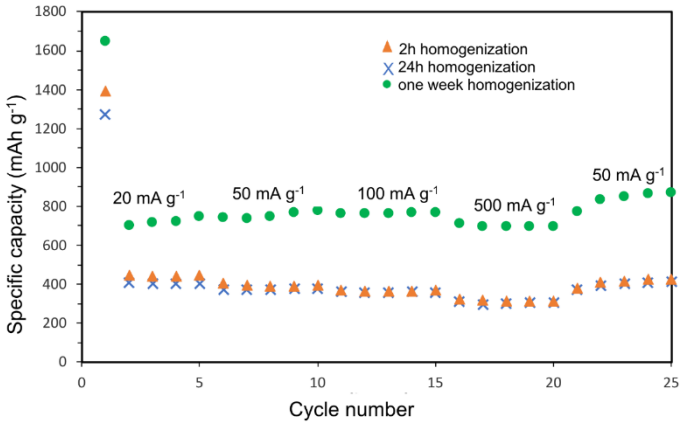

Figure II-12: Galvanostatic rate capability (discharge) of particles prepared by double emulsion and with a slurry homogenization of 2 h, 24 h or one week at increasing current density rates from 20 to 500 mA g^{-1}.

The CV curves of electrodes with different particle designs are compared in Figure II-13. Results of electrodes prepared after 2 h homogenization are first discussed. For the compound shaped by double emulsion (Figure II-13c), four cathodic peaks (0.83 V, 0.97 V, 1.5 V, 1.75 V) are detected during the first cycle while the subsequent cycles present only two cathodic peaks (0.8 V,1.8 V) with low intensity. This result suggests a conversion reaction during the first discharge as described in our previous work [22]. As compared to cyclic voltammetry profiles after precipitation, the intercalation of Li^+ in the structure after the double emulsion is extremely obvious as demonstrated by the peaks at 0.8 V and at ~1.8 V during the second and third discharge process. These peaks correspond mainly to Pd^{+II}/Pd^0 redox couple [31,36,37]. It clearly demonstrates that the double emulsion has a positive influence and leads to the superior structural stability of the electrode particles. Moreover, two broad anodic peaks around 1.2 and 2.6 V are detected in all cycles corresponding to the Pd^0/Pd^{+II} redox couple. As CV curves nearly overlap upon further scans, it implies excellent electrochemical reversibility for the next cycles. The presence of anodic and cathodic peaks at subsequent cycles suggests that particles prepared by double emulsion are more electroactive than the initial ones. Indeed, for irregular particles, three main cathodic peaks were detected (0.67 V, 0.92 V, 1.50 V) at the first cycle while no anodic and cathodic were formally detected at the subsequent cycles (Figure II-13a) suggesting less electrochemical activity. This result should be confirmed by galvanostatic charge/discharge measurements, but some hypotheses and insights reported in the literature can explain these results. Assuming that some electrochemical reactions are hard to be triggered in bulk materials, designing nanoparticles or hollow microparticles would reduce this issue and the reaction kinetics would increase [4,24,38]. Moreover, considering that the surface to volume ratio is

higher in these types of architecture, the presence of active sites for lithium storage is increased [23,24,39].

Since it was suggested that long electrode slurry homogenization can play an important role in enhancing the electrochemical performance of the electrode materials for LIBs, recent studies have shown that efficient homogenization allows obtaining the best particle size distribution and uniform dispersion of the electrode material framework [40]. Therefore, we explore the effect of homogenization duration on the electrochemical performance of the material. As seen in Figure II-13, the CV peaks of particles prepared by precipitation and with a slurry homogenization of one week (Figure II-13b) are almost similar to the one of particles prepared by double emulsion and homogenized for 2 h (Figure II-13c). This observation means that the morphology and the duration of homogenization are significant and important parameters to improve the electrochemical performances of this kind of electrode material. As seen in Figure II-13d, like for electrodes prepared by precipitation, the first discharge is different from other cycles which confirms a conversion reaction. Then, two broad anodic peaks around 1.2 and 2.6 V are also detected in subsequent cycles corresponding probably to the Pd^{0}/Pd^{+II} redox couple. Two cathodic peaks that can be related also to the Pd^{+II}/Pd^{0} redox couple are present after the first cycle. Therefore, particles prepared by double emulsion are also homogenized for one week and tested in half-cell configuration.

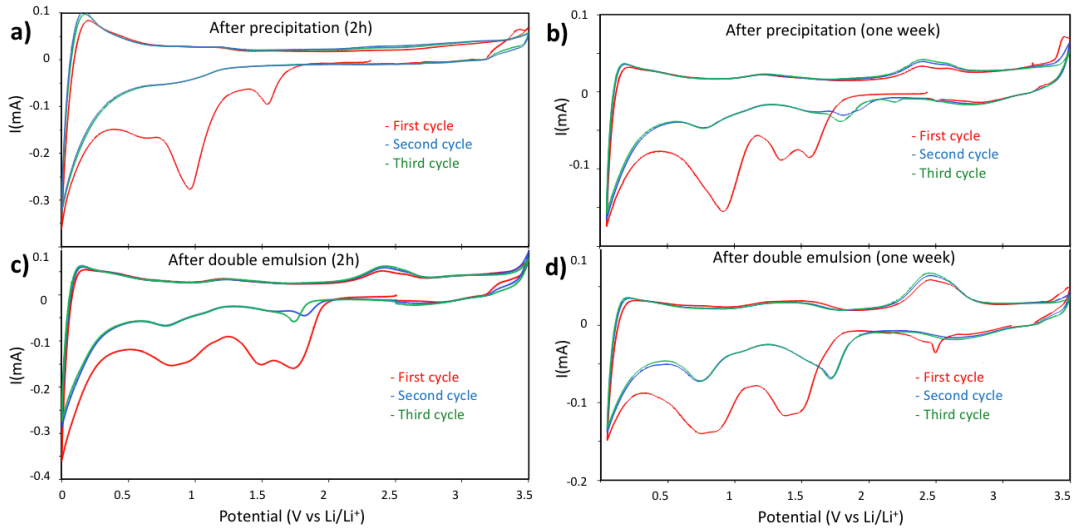

Figure II-13: Cyclic voltammetry profiles recorded at scan rate 0.1 mV s^{-1} in the voltage range of 0.05-3.5 V of the organopalladium complex obtained after precipitation and formulated by double emulsion technique (a,c: 2h and b,d: one week electrode slurry homogenization).

To confirm these results, electrochemical performances of the complex were evaluated by galvanostatic charge/discharge tests under different current densities between 0.05 and 3.0 V. This potential range has been chosen because no reaction occurs upon 3 V as seen on cyclic voltammetry profiles. Figure II-14 presents the half-cell potential vs specific capacity curves profiles of the three initial charge/discharge cycles at a current density of 20 mA g^{-1} for material prepared by precipitation and formulated by double emulsion. In both cases, the first discharge curve is different compared to other subsequent cycles as observed on cyclic voltammetry profiles, and presents a much higher specific capacity, especially after double emulsion. The origin of the additional contribution is still unclear, although one can suspect that the reduction of the electrolyte over the material–carbon interface, the electrolyte decomposition, and the formation of the solid electrolyte interface (SEI) at the electrode interface contributes to the extra capacity obtained in the initial cycle. The higher the surface area, the higher the reactivity of the particles with electrolyte, and therefore, the irreversible capacity of the first discharge increases for particles prepared by double emulsion [23,41]. Moreover, the irreversible lithium loss can also be due to an incomplete conversion reaction of the complex, which is common for most conversion anode materials for LIBs [42].

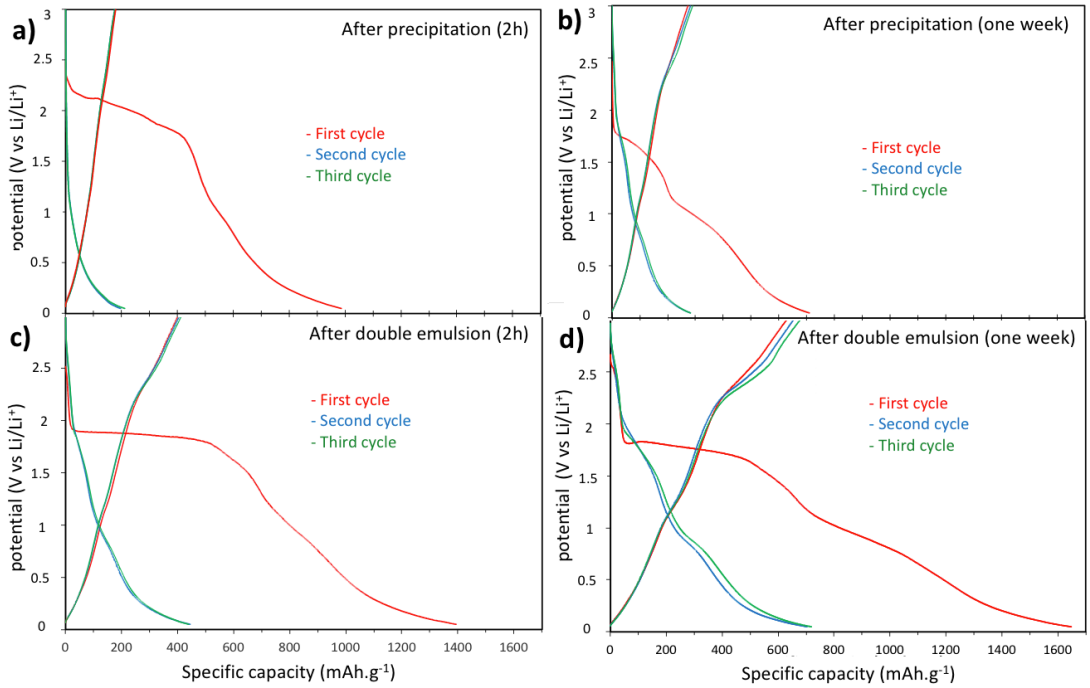

Figure II-14: Charge/discharge curves for the three first cycles at a current density of 20 mA g^{-1} of organopalladium complex after precipitation and prepared by double emulsion (a,c: 2h and b,d: one week electrode slurry homogenization).

Figure II-15 illustrates the rate capability of both types of particles after 2 h and one week of slurry homogenization in lithium half cells under current densities of 20, 50, 100, and 500 mA g^{-1}. Low capacities were obtained for the electrode homogenized only for 2 h compared to one week which is probably due to the heterogeneous distribution of the carbon black and binder and in the active electrode material (Figure II-15a). On the other hand, after one week of homogenization (Figure II-15b), both electrodes exhibit a good cycling capability for all current densities, however, the electrode prepared by double emulsion presents higher specific capacities. The improvement of electrochemical performance thanks to long time slurry homogenization can be explained by an efficient homogenization and uniform dispersion of the electrode material framework. Moreover, as revealed by the XRD patterns presented in the Figure II-16, an amorphization of the material occurs after one-week homogenization. As demonstrated by C. Kim et al, amorphous conversion materials exhibit better electrochemical performance than crystalline because they are able to better overcome problems relating to conversion materials [43]. In addition, the XRD patterns shown in Figure II-16 indicate that the electrode material contains also Pd(0). It was confirmed that the presence of Pd(0) is beneficial for the performance because it improves the electronic conductivity of the electrode material [44] and thus increases the amount of lithium inserted into the electrode during cycling [45–47]. The electrode prepared by double emulsion delivers a high specific capacity of 740 mAh g^{-1} at the current density of 50 mA g^{-1} compared to 270 mAh g^{-1} for the complex prepared by precipitation. Based on Pd^{+II}/Pd^{0} redox couple, the theoretical capacity should be only 60 mAh g^{-1}, which is much lower than the practical capacity. Recent works on organic and organometallic compounds demonstrate that organics moieties (C=C and C=O bonds) and the metal could store lithium, leading to a higher capacity [48–51]. The reaction with organic moieties could be attributed to the peaks on CV curves (Figure II-13) [50]. Indeed, according to the works of X. Han et al. and Z. Man et al. [50,51], the electrochemical lithium addition reaction to the unsaturated carbons of benzene rings occurs at potentials below 1V. Furthermore, it was shown that lithiation reactions with the C=C groups of phenyl rings could be observed as small reduction peaks at ~0.72, 0.12, and 0.06 V, as well as the formation of the SEI layer[52,53]. Since the formation of SEI is observed below 0.8 V, in the CV curves (Figure II-13), the peaks of C=C bonds reaction occurring at potential lower than 0.8 V are probably masked by the strong SEI peak. The reaction of lithium with the carbonyl groups is detected at potentials above 1.04 V [50,51] The peak observed between 1 and 1.25 V could correspond to the reaction of Li with the C=O and is probably partially overlayed by other peaks. If we consider that all C=C and C=O

bonds can react with lithium and the redox reaction with the palladium, the theoretical capacity of the organopalladium complex is about 1014 mAh g^{-1}. The discharge capacities delivered by the complex formulated by double emulsion are 718, 740, 762, and 695 mAh g^{-1} at current densities of 20, 50, 100, and 500 mA g^{-1} respectively. These results indicate that the design and size of the particles contribute significantly to the improvement of specific capacity and rate capability of the organopalladium complex [IPd(4-$AcOC_6H_4$)(PPh_3)$_2$]. This observation can be explained by the fact that hollow microparticles are able to accommodate and withstand high volumetric expansion and stress, well known for conversion anode materials [29]. Moreover, in both nanoparticles and hollow microparticles, the reduction of the diffusion path length of lithium leads to the enhancement of specific capacity [23,24].

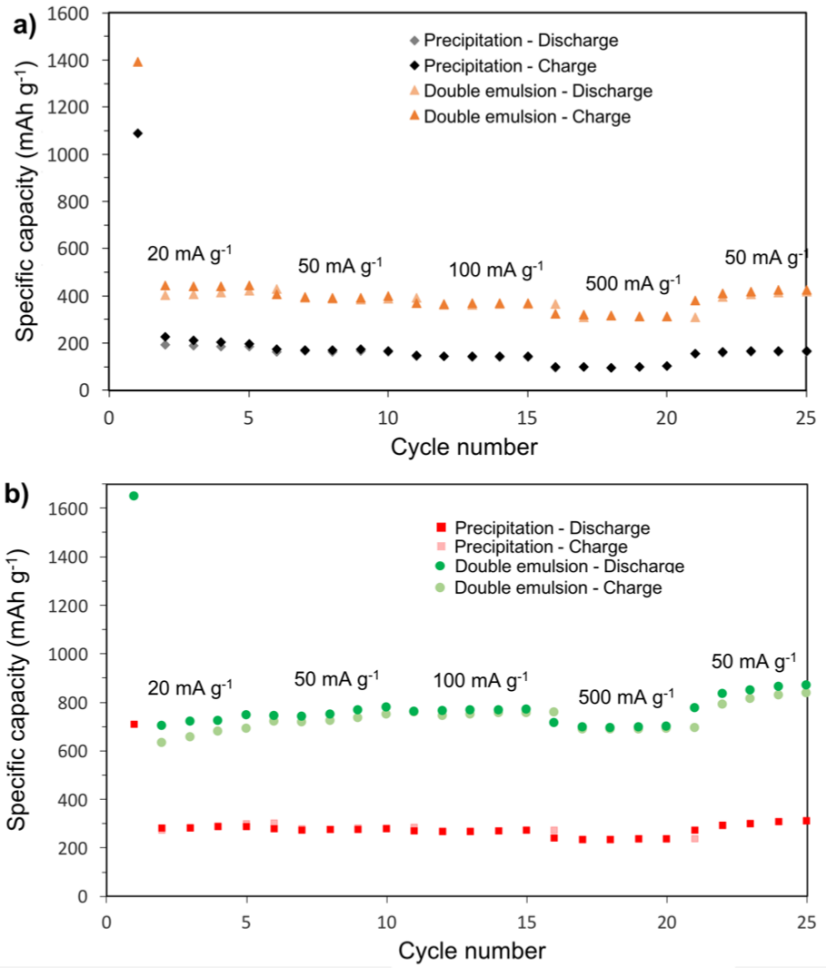

Figure II-15: Galvanostatic rate capability of electrodes prepared by precipitation and formulated by double emulsion and homogenized for (a) 2 h and (b) one week at increasing current density rates from 20 to 500 mA g^{-1} in the voltage range of 0.01-3 V.

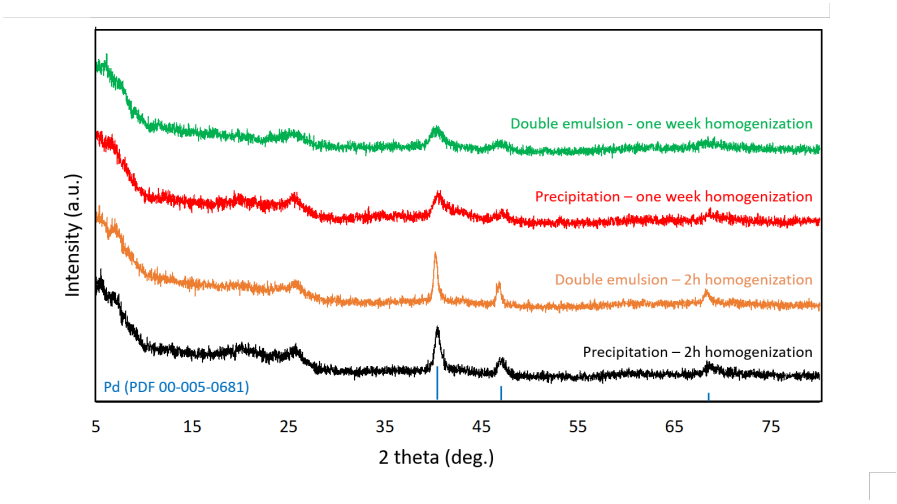

Figure II-16: XRD patterns of electrodes obtained after 2h and one week slurry homogenization.

Further electrochemical characterization was therefore carried out only for the electrode homogenized for one week to examine the evolution of the capacity and the coulombic efficiency with the cycle number at 50 mA g^{-1} during 105 cycles. Figure II-17 shows the evolution of the capacity with the cycle number of both electrodes (after precipitation and formulated by double emulsion) at the current density of 50 mA g^{-1}. The first five cycles are recorded at 20 mA g^{-1} to activate and maximize the material's capacity during cycling as Islam et al. recommended [54]. In both cases, a capacity increase with cycling is observed, the electrode prepared by precipitation delivers a relatively initial capacity of ~250 mAh g^{-1} that increases to ~390 mAh g^{-1}. However, the electrode formulated by double emulsion delivers an initial capacity of about 800 mAh g^{-1} that increases continuously during 90 cycles to reach a very high capacity of 1100 mAh g^{-1} and then stabilizes for 15 cycles. Both electrodes gain approximately 50% capacity between the first and the 100th cycle. This continuous increase can be attributed to a constant activation process linked to an evolution of the structure and therefore an improvement of the ion mobility and exchange [55]. The organic part of the complex (phenyl groups) becomes active along with cycling which leads to an increase in the delivered specific capacity [56]. The capacity can finally be stabilized when the whole molecule is electrochemically active. For both electrodes the efficiency is initially low and increases continuously during the first five cycles, then it stabilizes at around 97 %. Although the cycling mechanism has yet to be determined, the rate capability, specific capacity, and cycling stability of spherical particles obtained by double emulsion are obviously higher than non-shaped microparticles.

Although some of the observations and results presented in this work allow us to give an early response to the reactions and processes taking place in the system, it is important to mention that the exact mechanisms and electrochemical processes of lithium storage in organic and organometallic material mechanism is still complicated, unclear and remain controversial [48–51]. It would be interesting to pursue the research and to study the electrochemical mechanism of the complex in detail using the DFT method and in-situ NMR to explain the origin of the outstanding electrochemical performance of the complex prepared by double emulsion and homogenized for one week.

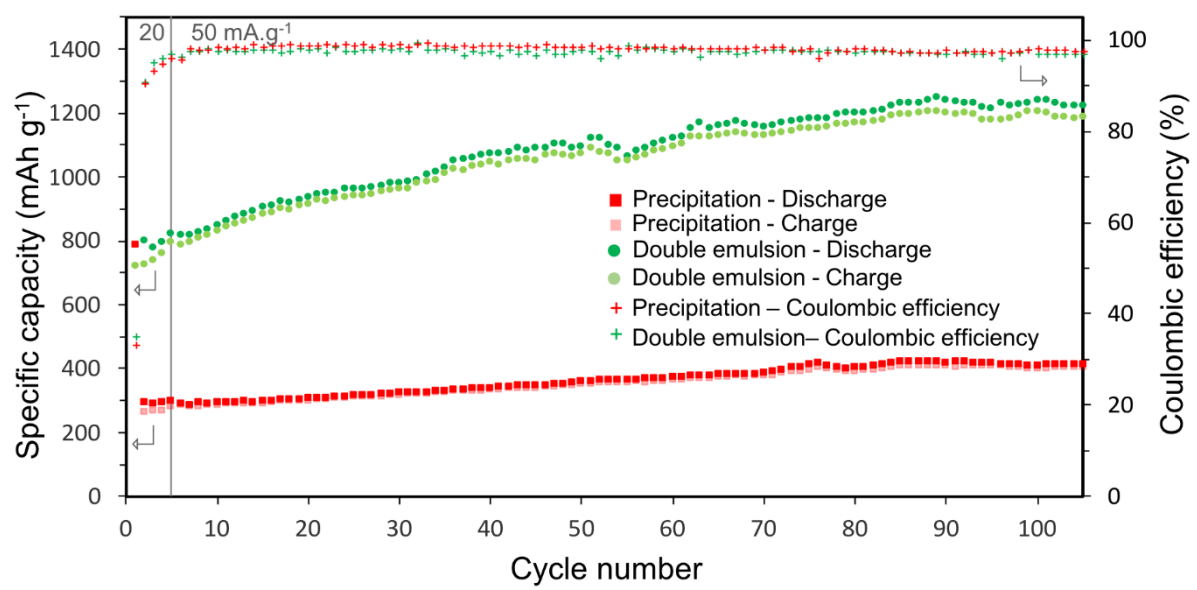

Figure II-17: Cycling performance of electrodes prepared by precipitation or formulated by double emulsion, and homogenized for one week at current density 20 mA g^{-1} for the five first cycles and at 50 mA g^{-1} for the next cycles in the voltage range of 0.05-3 V.

4. Conclusion

Three new pure palladium complexes, trans-XPd(4-AcOC$_6$H$_4$)(PPh$_3$)$_2$ with X = I, Br, and Cl, were synthesized by precipitation and fully investigated as anode materials for Li-ion batteries in the first part of this chapter. The anode active materials deliver a first irreversible discharge followed by reversible charge/discharge cycles. The cyclic voltammetry and galvanostatic cycling results show that the nature of the halogen ligand (X = I, Br, and Cl) highly impacts the reaction mechanism during the first discharge and cycling performance. The palladium complex containing iodine ligand [IPd(4-AcOC$_6$H$_4$)(PPh$_3$)$_2$] shows the best electrochemical performance by delivering an average discharge capacity of about 170 mAh g^{-1} at 50 mA g^{-1}. Nevertheless, this value is still low compared to other organometallic compounds and graphite.

The double emulsion-evaporation technique was used to control and accommodate the architecture of particles prepared initially by precipitation. Spherical hollow or dense micro- and nanoparticles are obtained by double emulsion. Moreover, it is found that the duration of electrode slurry homogenization also has an important influence on electrochemical performance. When tested as the anode material in half cells LIBs, the as-prepared iodocomplex spheres homogenized for one week delivered the highest initial capacities of ~800 mAh g^{-1} at a current density of 50 mA g^{-1} and 1100 mAh g^{-1} after 110 cycles (three times of the capacity of the graphite: commercial anode for LIBs). As demonstrated, the electrode architecture design and homogenization duration are key parameters for enhancing the electrochemical performance of the organopalladium complex as anode material for LIBs.

5. References

1 D. Demirocak, S. Srinivasan and E. Stefanakos, *Applied Sciences*, 2017, **7**, 731.

2 N. Nitta, F. Wu, J. T. Lee and G. Yushin, *Materials Today*, 2015, **18**, 252–264.

3 M. Wakihara, *Materials Science and Engineering: R: Reports*, 2001, **33**, 109–134.

4 K. Cao, T. Jin, L. Yang and L. Jiao, *Mater Chem Front*, 2017, **1**, 2213–2242.

5 A. S. Aricò, P. Bruce, B. Scrosati, J. M. Tarascon and W. van Schalkwijk, *Nat Mater*, 2005, **4**, 366–377.

6 N. Nitta and G. Yushin, *Particle and Particle Systems Characterization*, 2014, **31**, 317–336.

7 H. Fei, X. Liu and Z. Li, *Chemical Engineering Journal*, 2015, **281**, 453–458.

8 X. Han, G. Qing, J. Sun and T. Sun, *Angewandte Chemie*, 2012, **124**, 5237–5241.

9 Y. Liang, Z. Tao and J. Chen, *Adv Energy Mater*, 2012, **2**, 742–769.

10 A. A. Pavlovskii, K. Pushnitsa, A. Kosenko, P. Novikov and A. A. Popovich, *Materials*, 2022, **16**, 177.

11 K. Tamura, N. Akutagawa, M. Satoh, J. Wada and T. Masuda, *Macromol Rapid Commun*, 2008, **29**, 1944–1949.

12 C. Su, L. Wang, L. Xu and C. Zhang, *Electrochim Acta*, 2013, **104**, 302–307.

13 K. S. Park, S. B. Schougaard and J. B. Goodenough, *Advanced Materials*, 2007, **19**, 848–851.

14 W. E. Geiger, *Organometallics*, 2007, **26**, 5738–5765.

15 H. Zhong, G. Wang, Z. Song, X. Li, H. Tang, Y. Zhou and H. Zhan, *Chemical Communications*, 2014, **50**, 6768–6770.

16 Z. Liu, L. Feng, X. Su, C. Qin, K. Zhao, F. Hu, M. Zhou and Y. Xia, *J Power Sources*, 2018, **375**, 102–105.

17 Y. Mao, Q. Kong, B. Guo, X. Fang, X. Guo, L. Shen, M. Armand, Z. Wang and L. Chen, *Energy Environ Sci*, 2011, **4**, 3442–3447.

18 M. T. Sougrati, A. Darwiche, X. Liu, A. Mahmoud, R. P. Hermann, S. Jouen, L. Monconduit, R. Dronskowski and L. Stievano, *Angewandte Chemie International Edition*, 2016, **55**, 5090–5095.

19 Y. Song, L. Yu, Y. Gao, C. Shi, M. Cheng, X. Wang, H. J. Liu and Q. Liu, *Inorg Chem*, 2017, **56**, 11603–11609.

20 X. Han, F. Yi, T. Sun and J. Sun, *Electrochem commun*, 2012, **25**, 136–139.

21 H. Fei, X. Liu, Z. Li and W. Feng, *Dalton Transactions*, 2015, **44**, 9909–9914.

22 K. S. Etsè, F. Boschini, C. Karegeya, E. Roex, G. Zaragoza, A. Demonceau, R. Cloots and A. Mahmoud, *Electrochim Acta*, 2020, **337**, 135659.

23 F. De Angelis, R. Proietti Zaccaria, E. Miele, S. Goriparti, C. Capiglia and E. Di Fabrizio, *J Power Sources*, 2014, **257**, 421–443.

24 Y. Lu, L. Yu and X. W. (David) Lou, *Chem,* 2018, **4**, 972–996.

25 X. Wang, J. Feng, Y. Bai, Q. Zhang and Y. Yin, *Chem Rev*, 2016, **116**, 10983–11060.

26 L. Yu, H. Hu, H. Bin Wu and X. W. D. Lou, *Advanced Materials*, 2017, **29**, 1604563

27 Z. Wang, L. Zhou and X. W. Lou, *Advanced Materials*, 2012, **24**, 1903–1911.

28 X. W. Lou, L. A. Archer and Z. Yang, *Advanced Materials*, 2008, **20**, 3987–4019.

29 Y. Yan, G. Guo, T. Li, D. Han, J. Zheng, J. Hu, D. Yang and A. Dong, *Electrochim Acta*, 2017, **246**, 43–50.

30 Y. J. Oh, J. Lee, J. Y. Seo, T. Rhim, S. H. Kim, H. J. Yoon and K. Y. Lee*, Journal of Controlled Release*, 2011, **150**, 56–62.

31 J. P. Flemming, M. C. Pilon, O. Y. Borbulevitch, M. Y. Antipin and V. V. Grushin, *Inorganica Chim Acta,* 1998, **280**, 87–98.

32 V. C. Diculescu, A. M. Chiorcea-Paquim, O. Corduneanu and A. M. Oliveira-Brett, *Journal of Solid State Electrochemistry*, 2007, **11**, 887–898.

33 B. Philippe, A. Mahmoud, J. B. Ledeuil, M. T. Sougrati, K. Edström, R. Dedryvère, D. Gonbeau and P. E. Lippens, *Electrochim Acta*, 2014, **123**, 72–83.

34 A. Mahmoud, M. Chamas and P. E. Lippens, *Electrochim Acta*, 2015, **184**, 387–391.

35 Z. Lv, Z. Wang and J. Chen, RSC Adv, 2019, **9**, 22401–22409.

36 A. F. Henwood, M. Lesieur, A. K. Bansal, V. Lemaur, D. Beljonne, D. G. Thompson, D. Graham, A. M. Z. Slawin, I. D. W. Samuel, C. S. J. Cazin and E. Zysman-Colman, *Chem Sci*, 2015, **6**, 3248–3261.

37 C. Amatore, G. Broeker, A. Jutand and F. Khalil, *J Am Chem Soc*, 1997, **119**, 5176–5185.

38 S. H. Yu, X. Feng, N. Zhang, J. Seok and H. D. Abruña, *Acc Chem Res*, 2018, **51**, 273–281.

39 A. J. Downard, A. M. Bond, A. J. Clayton, L. R. Hanton and D. A. McMorran, *Inorg Chem*, 1996, **35**, 7684–7690.

40 C. Te Hsieh, C. Y. Lin, Y. F. Chen and J. S. Lin, *Electrochim Acta*, 2013, **111**, 359–365.

41 X. Chen, C. Yu, X. Guo, Q. Bi, M. Sajjad, Y. Ren, X. Zhou and Z. Liu, *Nano*, 2018, **13**, 1850103

42 X. M. Lin, J. L. Niu, J. Lin, L. M. Wei, L. Hu, G. Zhang and Y. P. Cai, *Inorg Chem*, 2016, **55**, 8244–8247.

43 C. Kim, H. Kim, Y. Choi, H. A. Lee, Y. S. Jung and J. Park, *ACS Omega*, 2018, **3**, 7655–7662.

44 P. Yu, B. S. Haran, J. A. Ritter, R. E. White and B. N. Popov, *J Power Sources*, 2000, **91**, 107–117.

45 C. Huang, J. Mahmood, Z. Wei, D. Wang, S. Liu, Y. Zhao, H. J. Noh, J. Ma, J. Xu and J. B. Baek, *Mater Today Energy*, 2019, **14**, 100359.

46 C. Hung, 2002, 1–8.

47 S. Sarkar, D. Mukherjee and S. Sampath, *J Power Sources*, 2017, **362**, 80–85.

48 Z. Q. Jin, Y. G. Liu, W. K. Wang, A. B. Wang, B. W. Hu, M. Shen, T. Gao, P. C. Zhao and Y. S. Yang, *Energy Storage Mater*, 2018, **14**, 272–278.

49 G. Li, H. Yang, F. Li, F. Cheng, W. Shi, J. Chen and P. Cheng, *Inorg Chem*, 2016, **55**, 4935–4940.

50 Z. Man, P. Li, D. Zhou, R. Zang, S. Wang, P. Li, S. Liu, X. Li, Y. Wu, X. Liang and G. Wang, J Mater Chem A Ma*ter*, 2019, **7**, 2368–2375.

51 X. Han, G. Qing, J. Sun and T. Sun, *Angewandte Chemie - International Edition*, 2012, **51**, 5147–5151.

52 Z. Lei, Q. Yang, Y. Xu, S. Guo, W. Sun, H. Liu, L. P. Lv, Y. Zhang and Y. Wang, *Nat Commun*, 2018, **9**, 1–13.

53 J. Wu, X. Rui, G. Long, W. Chen, Q. Yan and Q. Zhang, *Angewandte Chemie - International Edition*, 2015, **54**, 7354–7358.

54 S. Islam, M. H. Alfaruqi, V. Mathew, J. Song, S. Kim, S. Kim, J. Jo, J. P. Baboo, D. T. Pham, D. Y. Putro, Y. K. Sun and J. Kim, *J Mater Chem A Mater*, 2017, **5**, 23299–23309.

55 Z. L. Wang, D. Xu, H. G. Wang, Z. Wu and X. B. Zhang, *ACS Nano*, 2013, **7**, 2422–2430.

56 L. Wang, M. Zhao, J. Qiu, P. Gao, J. Xue and J. Li, *Energy Technology*, 2017, **5**, 637–642.

Chapter III: Spray-dried V_2O_5 as cathode material for high-performance aqueous zinc ion batteries and influence of carbon nanotubes addition before spray-drying

Rechargeable aqueous zinc-ion batteries (ZIBs) have recently received increasing attention thanks to their high safety, low cost, and material abundance. Nevertheless, finding a suitable cathode material with a high capacity and good stability remains a challenge. To solve this problem, we prepared vanadium pentoxide microspheres with high-performance through a one-step spray-drying process. The structural and morphological properties of the prepared material were investigated by combining XRD, SEM, TEM, laser granulometry and BET measurement. Microsphere particles with a particle size in the range of 1 – 10 µm are obtained and result from the agglomeration of nanoparticles. A comparative study with commercial V_2O_5 is realized and shows the benefit of the architecture design of vanadium pentoxide on the electrochemical performance of ZIBs. Spray-dried V_2O_5 demonstrates excellent rate capability, and good stability with remarkably high capacities of 495 mAh g^{-1} and 240 mAh g^{-1} at low (0.1 A g^{-1}) and high current densities (5 A g^{-1}) respectively. Excellent capacity retention of 93% is observed after 1000 cycles at high current density. The influence of carbon nanotubes addition during spray-drying proess is also studied in this chapter. By enhancing the electronic conductivity, protecting the V_2O_5 surface and increasing the specific surface area, CNTs addition is favorable to the electrochemical properties of V_2O_5/xCNTs. The performance and the stability of vanadium pentoxide as cathode material for ZIBs are highly improved by combining these two methods: optimization of architecture design and carbon nanotubes addition. The experimental results suggest a promising potential for V_2O_5 microspheres as cathode material in aqueous zinc-ion batteries.

Keywords: vanadium pentoxide, microspheres, morphology design, carbon nanotubes addition, spray-drying, aqueous zinc-ion batteries.

E. Roex, F. Boschini, V. Delaval, A. Schrijnemakers, R. Cloots, and A. Mahmoud, "Spray-dried V_2O_5 as cathode material for high-performance aqueous zinc-ion batteries," *Journal of Electroanalytical Chemistry*, vol. 929, January, 2023.

1. Introduction

The global electricity energy demand is expected to almost double by 2050 [1]. With a general electricity grid that is already experiencing stability problems at peak times and a policy that is encouraging the use of electricity instead of fossil resources, guaranteeing the electric energy supply is becoming more and more of a concern [2]. Renewable energies such as wind and solar energy are good alternatives to provide electricity without increasing carbon dioxide emissions. Nevertheless, the intermittent nature of these energy sources requires the development of eco-friendly, safe, sustainable, and large-scale energy storage technologies [3,4]. Although lithium-ion batteries technology offers high energy density and long cycle life, the high price of lithium resources and safety issues make LIBs far from satisfactory for large-scale applications [5]. The best type of rechargeable battery that uses materials meeting nearly all the criteria required to outperform the LIB in terms of eco-friendliness, low cost, simplicity, safety, and recyclability, is the aqueous rechargeable zinc-ion battery [6,7]. ZIBs are considered one of the most promising secondary batteries for the future, as Zn has a relatively low redox potential (-0.76V, Zn vs SHE) and a very high volumetric capacity (5855 mAh cm^{-3}), even higher than the one of lithium. The high ionic conductivity of the aqueous solution is advantageous to achieve high-rate performance. Moreover, the assembling of ZIBs in ambient air makes them safe, economical, and simple [2,8].

The electrochemical performance of ZIBs highly depends on their cathode material properties. The kinetics is limited by the strong electrostatic interaction among Zn^{2+} ions and cathode material structure because of the high charge of Zn^{2+} [9–11]. Due to the larger solvated ion radius and divalent charge of Zn^{2+}, the cathode material needs a very specific structure that allows insertion/extraction of Zn^{2+} and that can stabilize the discharged/charged mode of the battery over a long period. For instance, a few cathode materials have been investigated as suitable hosts for divalent ion Zn^{2+} such as manganese-based, vanadium-based, Prussian blue analogs, and more recently organic materials [6,12–15]. Compared with MnO_2 and Prussian blue analogs, vanadium-based materials offer a higher reversible capacity, better rate capability, and longer cycle life.

V_2O_5 can deliver a high theoretical capacity of 589 mAh g^{-1} based on the two-electron redox centers [1]. Moreover, the variable valence state and earth abundance of vanadium make these compounds a promising choice for ZIBs [16]. However, the V_2O_5 compounds present issues such as low average operating voltage and unsatisfying cycling and rate performance due to their unstable structure during the discharge/charge process [10,17]. Vanadium-based materials

are affected by poor electronic conductivity, structural collapse, and volume changes caused by Zn^{2+} insertion/extraction during cycling. Several strategies can be used to solve these issues [17,18]: insertion of metal ions in cathode material [19–23], adjustment of structural water [5], optimization of electrolyte [1,24–26], selection of conductive additives [27,28], and optimization of architecture design [29–32]. More details about these strategies are given in section 4.5 in Chapter I.

It is well known that the morphology of cathode material plays a critical role in the electrode activation process, capacity, and stability [33–35]. Tuning the morphology is an effective way to improve the electrochemical performance of V_2O_5 cathodes in ZIBs. V_2O_5 materials can be shaped through various techniques such as hydrothermal [9], solvothermal [31] or spray-drying [16] techniques. Table I-3 summarizes the state of the art of V_2O_5 materials prepared via different procedures. Nevertheless, the optimization of architecture design of the electrode particles does not solve the issue of low electronic conductivity.

Therefore, the introduction of highly conductive materials such as carbon additives to V_2O_5 materials appears to be a viable solution to improve the electronic conductivity of the material [36,37]. The choice of carbon source, the thickness, the porosity, and the electrode homogeneity have a great influence on the electrochemical performance of the electrode material. Various studies investigating this strategy on V_2O_5 in zinc-ion batteries have been undertaken and are reported in Table I-4. Carbon nanotubes have excellent mechanical strength, and their electronic conductivity can be as high as 10^6 S/m [38] compared to $10^{2\text{-}3}$ S/m for carbon black [39]. Moreover, due to the random stacking arrangement of carbon nanotubes, the electrolyte infiltrates easily contrary to graphene oxide [40]. Therefore, carbon nanotubes are a carbon source of choice.

In this chapter, the microstructure of vanadium pentoxide is first tailored through a one-step spray-drying process at the pilot scale without any energy-consuming post-treatment. This method is easy, inexpensive, and suitable for obtaining V_2O_5 microspheres. Furthermore, V_2O_5/xCNTs composite is prepared by adding carbon nanotubes before spray-drying in order to improve the electronic conductivity of the material. The influence of carbon addition on electrochemical properties is therefore investigated. The performance and the stability of vanadium pentoxide as cathode material for ZIBs are highly improved by combining these two methods: optimization of architecture design and carbon nanotubes addition.

2. Experimental section

2.1. Materials and chemicals

V_2O_5 powder (purity > 99.6%), zinc trifluoromethanesulfonate (purity, 98%), and polyvinylidene difluoride were purchased from Sigma Aldrich. The suspension of carbon nanotubes (Aquacyl AQ0302-nanocyl 3 wt%) was purchased from Aquacyl. Zinc foil (0.1 mm) (purity > 99.95%) was purchased from Goodfellow.

2.2. Synthesis of V_2O_5 and V_2O_5/xCNTs

V_2O_5 spheres were prepared by a spray-drying technique. The commercial V_2O_5 powder was first dispersed in water (9 wt%) and ball-milled for 1h (planetary miller Retsch PM400/2) using zirconia balls with a diameter of 0.5 mm. The suspension was then diluted to obtain a suspension of 5 wt% V_2O_5 and spray-dried. To prepare the V_2O_5/xCNTs composite, the 5 wt% V_2O_5 suspension was homogeneously mixed with the aqueous suspension of carbon nanotubes before spray-drying. Five suspensions with different ratios of carbon nanotubes were prepared based on V_2O_5 dried mass and then spray dried: 5 wt% CNT, 10 wt% CNT, 15 wt% CNT, 20 wt% CNT. These samples are called hereafter V_2O_5/xCNT with x equal to the CNT/V_2O_5 ratio in percentage.

The used spray-drying parameters (Niro Mobile Minor) are inlet temperature 180 °C, outlet temperature ~110 °C, air pressure 1 bar, bi-fluid injector, and feed rate of 25 mL min^{-1}. The yield is equal to 73%.

2.3. Material characterizations

Thermogravimetric analysis was conducted to determine the water content in the material. The morphological properties and particle size were characterized by scanning and transmission electron microscopy and laser diffraction granulometry. The structure of the material was investigated by X-ray diffraction technique. The specific surface area was determined by the BET technique. The electrochemical properties of the materials were investigated by cyclic voltammetry and galvanostatic charge/discharge analyses. The exact carbon content in V_2O_5/xCNT was determined with a carbon analyzer.

Thermogravimetric analysis

Thermogravimetric analysis was conducted using LABSYS evo STA, SETARAM instrumentation. The samples were heated under the air atmosphere from 50°C to 500°C with a heating ramp of 20°C min^{-1}.

Scanning and Transmission Electron Microscopy

The SEM analysis of the materials was performed using a FEG-ESEM XL30 (FEI) with an accelerating voltage of 15 kV under a high vacuum. The powders were deposited on carbon tapes. The sputtering deposition was done with a gold target under an argon atmosphere (Balzers, SCD004, Sputter coater).

The TEM morphological analysis of the materials was performed using a W-TEM-JEOL operating at 80 kV. Samples were put in suspension in water and deposited on a copper grid.

Laser diffraction granulometry

The particles were dispersed in water and then the analysis was performed on Malvern Mastersizer 2000 Hydro.

X-ray Diffraction

X-ray diffraction measurements were performed in Bragg-Brentano geometry using a Bruker D8 Twin-Twin diffractometer with Cu Kalpha radiation and Lynxeye XET 1D detector. Powders were analyzed over the 2θ range from 10° to 75°, with 0.2 s/channel step time and 15 rpm rotation speed. The TOPAS software was used for Rietveld refinement of the cell parameters, crystallite-size parameters, sample displacement and background in the Pmmn space group. The peak profile is a convolution of the instrumental contribution modeled by the fundamental parameters approach and a crystal size broadening modeled by a Lorentzian function [41]. The crystallite size is reported as LVol-IB, i.e., the weighted mean column length along the scattering direction.

X-ray photoelectron spectroscopy

XPS measurements were performed by means of Thermo Electron ESCALAB 250Xi spectrometer under high vacuum (10^{-9} mbar) with an Al K$_\alpha$ monochromatised X-ray source. Survey spectra and high-resolution core level spectra (V 2p) were recorded with a pass energies of 100 eV and 20 eV, respectively, at a 90° take-off angle of the photoelectrons in relation to the surface sample. The spectra were corrected for charging effect with reference to C 1s hydrocarbon at 285.0 eV. Peak fitting was carried out using Avantage software (version 5.9918). A Shirley-type background was used, and different constraints were

imposed for peak fitting, particularly on the full width at half maximum (FWHM) and intensity ratio of spin-orbit doublet.

Adsorption/desorption N_2

The BET surface area measurement was conducted using a Micromeritics Asap 2020 Plus instrument. Degassing was applied for 48 h at 60 °C with a heating ramp of 10 °C/min. The adsorption measurement was performed by the Rouquerol method under N_2 from 0 to 0.3 with a 0.03 step.

Carbon analyzer

The carbon content was measured with the carbon analyzer, Multi EA 4000, Analytik Jena. The sample is inserted into a furnace of 1200°C with an oxygen flow to determine the exact quantity of CNT in the V_2O_5/xCNT material. The quantity of carbon black added in the mixture to prepare the electrode before electrochemical measurements is adapted to reach the ratio of 70 wt% V_2O_5, 20 wt% C and 10 wt% binder.

Electrochemical measurements

Swagelok cells were assembled in ambient air to evaluate the electrochemical properties of V_2O_5 cathode materials. Zinc metal, glass fiber (Whatman), and 3 M $Zn(CF_3SO_3)_2$ solution were respectively used as the anode, separator, and electrolyte. The working electrode was prepared by mixing 70 wt% V_2O_5, 20 wt% conductive carbon (CNTs and/or carbon black), and 10 wt% binder (polyvinylidene fluoride) in a mortar with a pestle. The electrode was pressed by uniaxial pressing (6 tons) of about 1-2 mg of the mixture on a stainless-steel grid with a 10 mm diameter. Cyclic voltammetry was carried out on Bio-Logic Science Instruments within the range of 0.2-1.6 V at a scanning rate ranging from 0.1 to 3 mV s^{-1}. The galvanostatic charge and discharge cycling tests were performed at different constant current densities between 0.1 and 5 A g^{-1} using a LAND battery test system (Wuhan, China). The specific capacity was calculated based on the V_2O_5 cathode active material mass. All electrochemical tests were carried out at room temperature.

3. Results and discussion

3.1. Morphological and structural properties of V_2O_5 material

The size and the morphology of the material particles have a strong influence on the Zn^{2+} insertion/extraction reactions, and thus on the electrochemical performance of the cathode material of Zn-ion batteries. In this work, water-free V_2O_5 microspheres are shaped by the spray-drying method. The TGA curves of the commercial and spray-dried V_2O_5 materials do not show any significant mass loss between 50 and 500°C (Figure III-1).

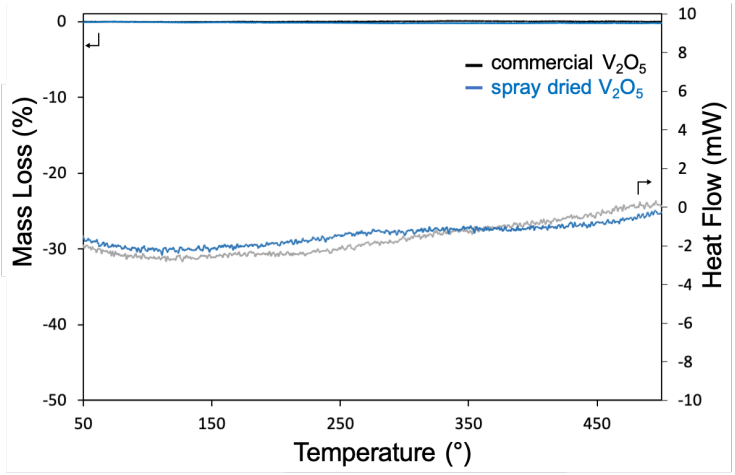

Figure III-1: TGA and DSC curves of commercial V_2O_5 and spray-dried V_2O_5 materials under the air atmosphere.

A comparative study of spray-dried V_2O_5 and commercial V_2O_5 powders has been realized in terms of morphology, particle size, and structure. SEM and TEM micrographs are shown in Figure III-2 and the particle size distribution curves are represented in Figure III-3. As observed in SEM and TEM images (Figure III-2 b, c), the initial commercial primary particles are irregularly shaped and agglomerated into bigger secondary particles (Figure III-2a) with a large particle size distribution with a d(0.5) of 55 µm (Figure III-3a). Therefore, before spray-drying, V_2O_5 material is ball-milled in water to deagglomerate the secondary particles and optimize the suspension. Figure III-3a illustrates the evolution of the particle size distribution of the commercial V_2O_5 before and after grinding. As shown in Figure III-3a, after 30 minutes of grinding, aggregates with a size bigger than 10 µm are still present. However, a good deagglomeration was achieved after 60 minutes of ball-milling and the d(0.5) is reduced to 200 nm. After grinding, the suspension is diluted in water and spray-dried under air. Solid microspheres (Figure III-2f) with particle size in the range of 1-10 µm (Figure III-3b) are collected after the spray-drying process. They result from the agglomeration of the initial primary particles as shown in Figure III-2e.

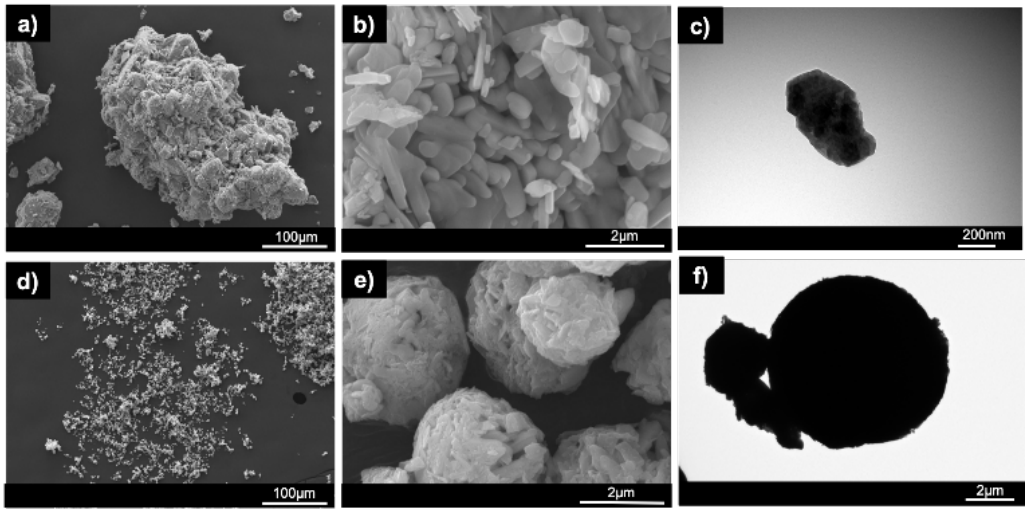

Figure III-2. SEM images of (a, b) commercial V_2O_5 and (d, e) spray-dried V_2O_5 materials and their corresponding TEM images (c) and (f) respectively.

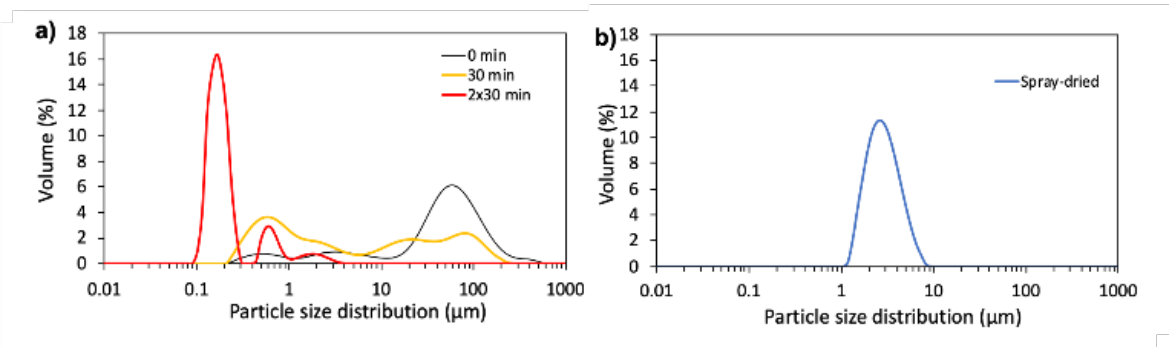

Figure III-3. (a) Evolution of the particle size distribution of the commercial V_2O_5 with ball milling time and (b) particle size distribution of spray-dried V_2O_5.

The EDX elemental mapping shows that V and O elements are homogeneously distributed in the powder for both materials (Figure III-4).

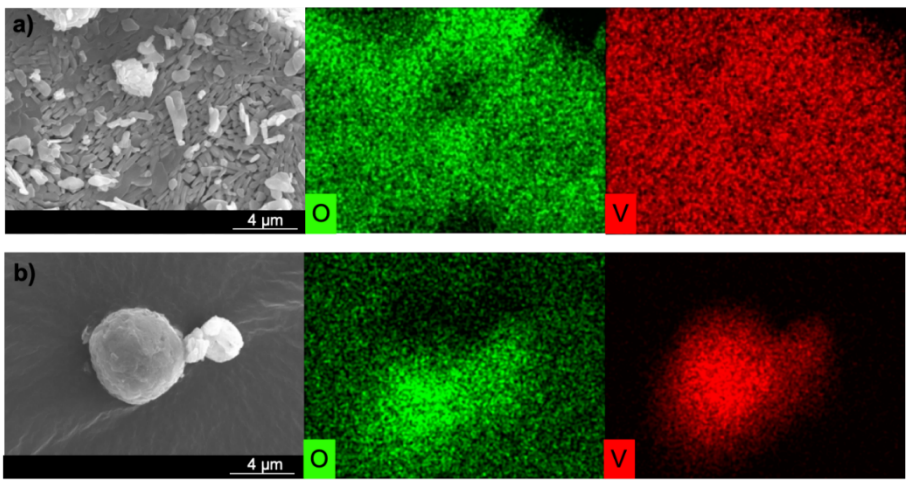

Figure III-4: V and O EDX mapping of the (a) commercial and (b) spray-dried V_2O_5 materials.

The crystal structure and the phase purity of the commercial and spray-dried V_2O_5 were analyzed by X-Ray diffraction technique. As illustrated in Figure III-5, all the characteristic peaks correspond to an orthorhombic phase of V_2O_5 with a space group of Pmmn(59) (JCPDS card 00-041-1426). This can be described as a layered structure composed of VO_5 square pyramids that share edges and corners. The lattice parameters of commercial and spray-dried V_2O_5 materials were determined by fitting the XRD patterns. The obtained lattice parameters were a =11.51 Å, b = 3.56 Å and c = 4.37 Å, which is consistent with values reported in the literature [32]. The c-parameter corresponds to the interlayer distance between the (001) planes. Its value of 4.37 Å proves that no water molecule is inserted into the structure [42]. This interlayer spacing is known to be receptive to the diffusion and transport of zinc ions.

Moreover, no impurity peak is detected, which confirms that the ball milling and spray-drying processes do not affect the purity of the V_2O_5 material. Sharp peaks confirm the high degree of crystallinity of the spray-dried V_2O_5 material. The diffraction peaks of spray-dried V_2O_5 are broader than those of the commercial V_2O_5 indicating a smaller crystallite size of spray-dried V_2O_5. Based on the fitting of the XRD patterns, the average crystallite size of commercial and spray-dried V_2O_5 are 150 and 100 nm, respectively.

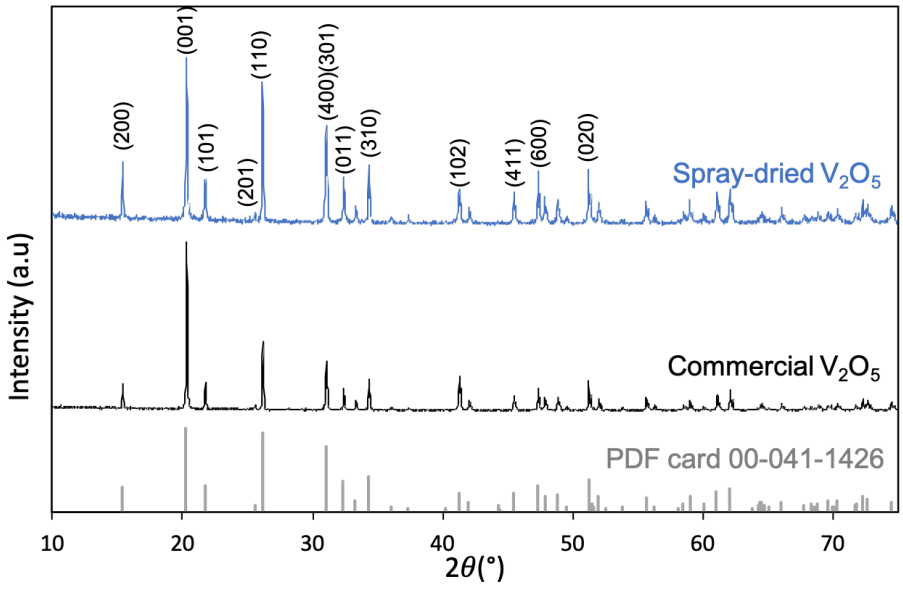

Figure III-5: X-Ray diffraction patterns of commercial and spray-dried V_2O_5 materials.

The specific surface area was determined by the BET technique. It increased from 3.7 m^2 g^{-1} for the commercial V_2O_5 material to 9.6 m^2 g^{-1} for the spray-dried V_2O_5 material. The higher BET surface area of spray-dried material is due to the smaller particle size and the lower aggregation of the V_2O_5 particles [43]. The morphological and structural analyses

demonstrate that the spray-drying method has a great influence on the particle and crystallite size, particle aggregation, morphology, and specific surface area. Besides, all these characteristics are very suitable to ease the zinc insertion/extraction during the discharge and charge process [23,42,44].

3.2. Electrochemical properties of V_2O_5 material

To investigate the influence of the morphological properties on the V_2O_5 electrochemical properties, spray-dried and commercial V_2O_5 materials were galvanostatically tested and compared as cathode material for Zn-ion batteries at 25 °C in the voltage range of 0.2-1.6 V. Swagelok cells were assembled in ambient air with zinc foil as anode and $Zn(CF_3SO_3)_2$ 3M aqueous solution as electrolyte. As mentioned in the literature and confirmed in Figure III-6, larger specific capacities are obtained with the concentrated $Zn(CF_3SO_3)_2$ 3M compared to $ZnSO_4$ 3M [23]. Therefore, all electrochemical measurements in this thesis have been conducted using $Zn(CF_3SO_3)_2$ 3M as electrolyte.

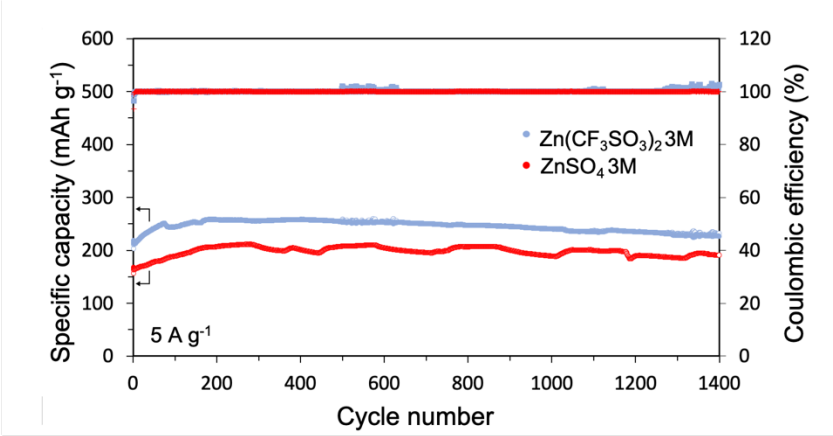

Figure III-6: Long cycling performance at 5 A g^{-1} of spray-dried V_2O_5 materials with $ZnSO_4$ 3M and $Zn(CF_3SO_3)_2$ 3M.

The galvanostatic charge/discharge curves of the commercial and spray-dried V_2O_5 materials recorded at 0.1 A g^{-1} are presented in Figure III-7a and Figure III-7b respectively. For both materials, the curves show the typical profile reported for the V_2O_5 cathode material for Zn-ion batteries [44], however, the spray-dried V_2O_5 delivers higher specific capacities which demonstrate the great influence of the morphological properties on the electrochemical performance of V_2O_5 [19,45]. For both electrodes, the specific capacities gradually increase during the initial cycles. This phenomenon has already been observed and is often called the "activation process" in the literature [16,31,42,45]. It corresponds to an evolution of the structure along with cycling which leads to the change in the

discharge/charge profiles (Figure III-7a,b) and to the shift of the cathodic peaks to higher potential and anodic peaks to lower potential as observed in the CV curves (see Figure III-7c,d). This is in good accordance with the plateaus detected on the charge/discharge curves represented in Figure III-7a,b. In the initial cycles, a charging plateau around 1.3 V is detected but disappears gradually in agreement with the CV curves (Figure III-7c,d). At the end of the activation process, two distinct discharging/charging peaks (Figure III-8a) are observed in both electrodes and correspond to the evolution from V^{5+} to V^{3+}, with an intermediate of V^{4+}. The electrode polarization is smaller, and the reaction mechanism is more reversible after the activation process. As shown in recent studies [26,46,47], both Zn^{2+} and H^{+} intercalation can occur in aqueous ZIBs.

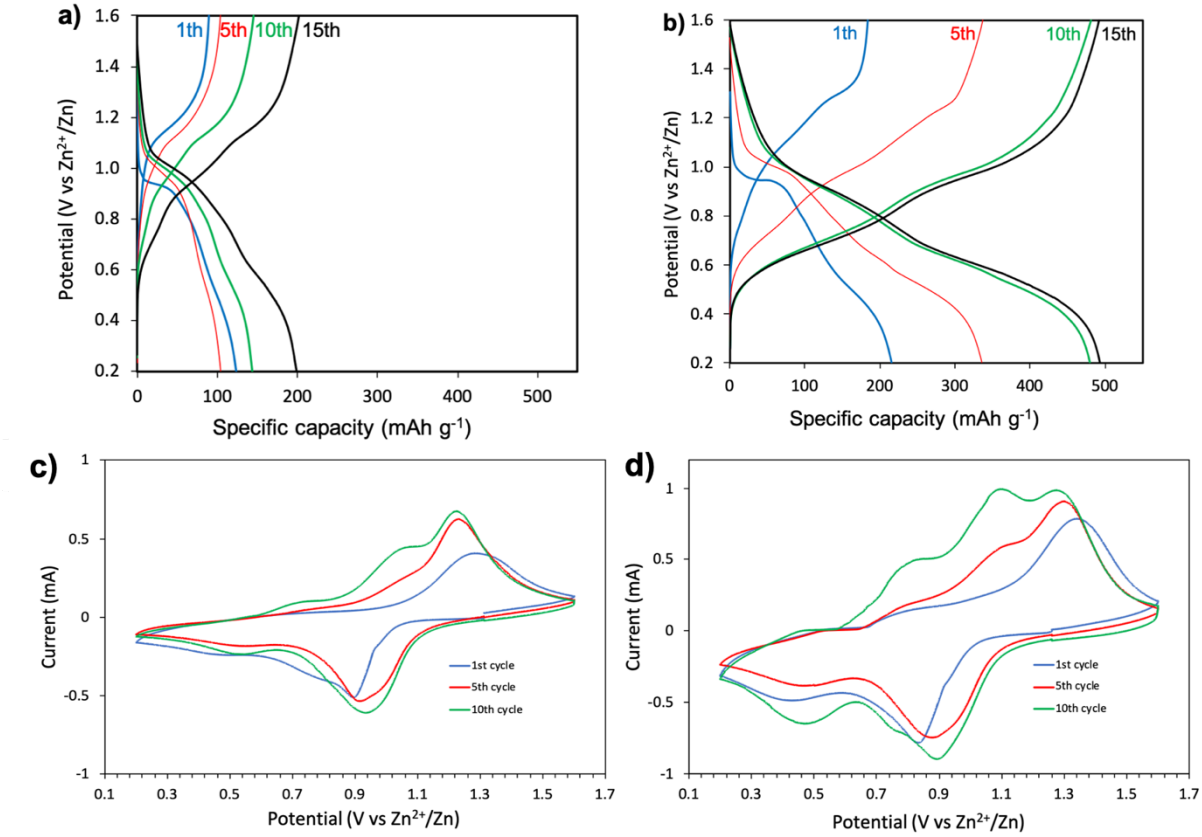

Figure III-7: Galvanostatic discharge/charge curves of commercial (a) and spray-dried (b) V_2O_5 at 0.1 A g^{-1} (1^{st}, 5^{th}, 10^{th}, and 15^{th} cycle) and CV curves of commercial (c) and spray-dried (d) V_2O_5 at 0.5 mV s^{-1}.

CV analyses were carried out at different scan rates from 0.1 to 3 mV s^{-1} to obtain deeper insights into the reaction kinetics of the spray-dried V_2O_5 electrode. Figure III-8a presents the CV curves obtained for the Zn/spray-dried V_2O_5 cell at indicated scan rates. An activation phase of 40 cycles at 0.5 mV s^{-1} has been realized previously on the cell. Two pairs of reduction/oxidation peaks are located at around 0.5/0.8 and 0.8/1.1 V and suggest a

multistep intercalation process. The capacitive and diffusive effect of the spray-dried V_2O_5 cathode material can be calculated by the following equation:

$$i = av^b$$

where i is the electric current, v is the scan rate and a and b are adjustable parameters. The previous relation can be rearranged as log (i) = b log (v) + log (a). Therefore, by fitting the plots of log (i) versus log (v), the b values can be determined by the slope of linear regression. A b value equal to 0.5 means that the current is controlled by a faradaic process (ionic diffusion) while a value equal to 1 suggests a capacitive behavior [1,23]. The corresponding plots of log(i) versus log(v) at cathodic and anodic peaks are represented in Figure III-8b. The obtained results show that the b values of the peaks 1-4 are 0.71, 0.85, 0.73, and 0.83 respectively suggesting that both diffusive and capacitive behavior affect the charge storage of spray-dried V_2O_5 cathode material for ZIBs.

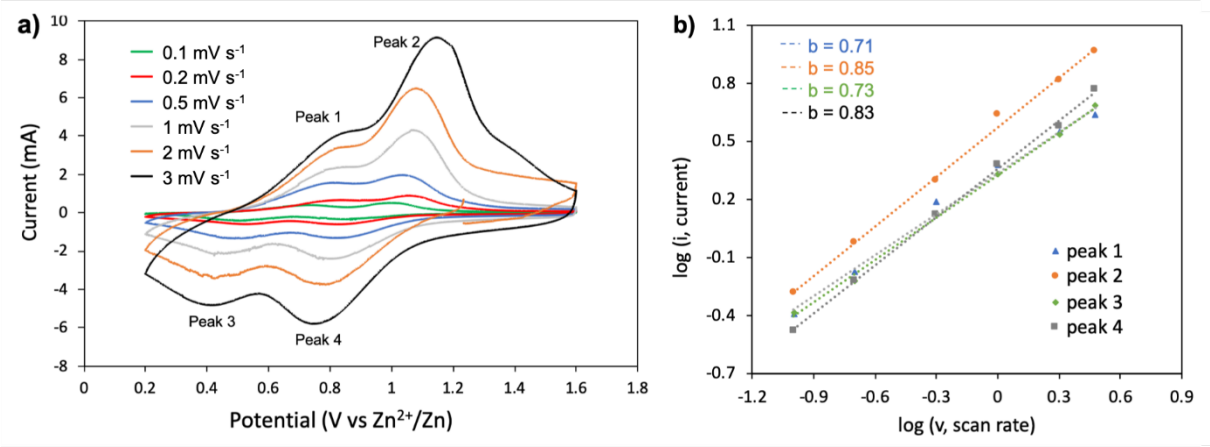

Figure III-8: (a) CV curves of the spray-dried V_2O_5 electrodes at different scan rates (0.1 to 3 mV s^{-1}), (b) Corresponding plots of log(i) versus log(v) at cathodic and anodic peaks.

To study the effect of the morphology of V_2O_5 cathode material on its electrochemical performance, the cycling performance at low and high current densities of the commercial and spray-dried V_2O_5 materials were investigated and compared. Figure III-9 gives the evolution of the discharge capacity and coulombic efficiency on cycling at current densities of 0.1 A g^{-1} (Figure III-9a) and 5 A g^{-1} (Figure III-9b). Low coulombic efficiencies (72 and 85 % for commercial and spray-dried V_2O_5 material respectively) are obtained for the first cycle and increased along cycling as represented in Figure III-9a. This is probably due to the trapping of Zn^{2+} in the cathode material. For both electrodes, the capacities increase along

cycling meaning that the number of active sites of V_2O_5 increases at the same time due to the gradual impregnation of electrolytes [1,48,49]. In the literature [33,42], this activation process has been attributed to the insertion of water molecules into the structure, leading to an increase in the interlayer distance and easier Zn^{2+} insertion in the new phase. In-situ XRD and *ex situ* XPS experiments will be needed to investigate the storage mechanism in the spray-dried V_2O_5 cathode material for ZIBs. For the spray-dried V_2O_5, the specific capacity is stabilized after only 15 cycles at 0.1 A g^{-1} while it takes 35 cycles for the commercial V_2O_5 (Figure III-9a). This positive effect is due to the morphological properties (particle and crystallite size, surface area, particle aggregation, and morphology) of the spray-dried V_2O_5 material which facilitates the infiltration of the electrolyte, increases the contact area at the electrode/electrolyte interface and decreases the diffusion path of zinc ions during discharge/charge processes [23,32,42,44]. Indeed, the spray-dried V_2O_5 material has different particle morphology with the smallest particle size, the lowest particle aggregation, and the highest surface area.

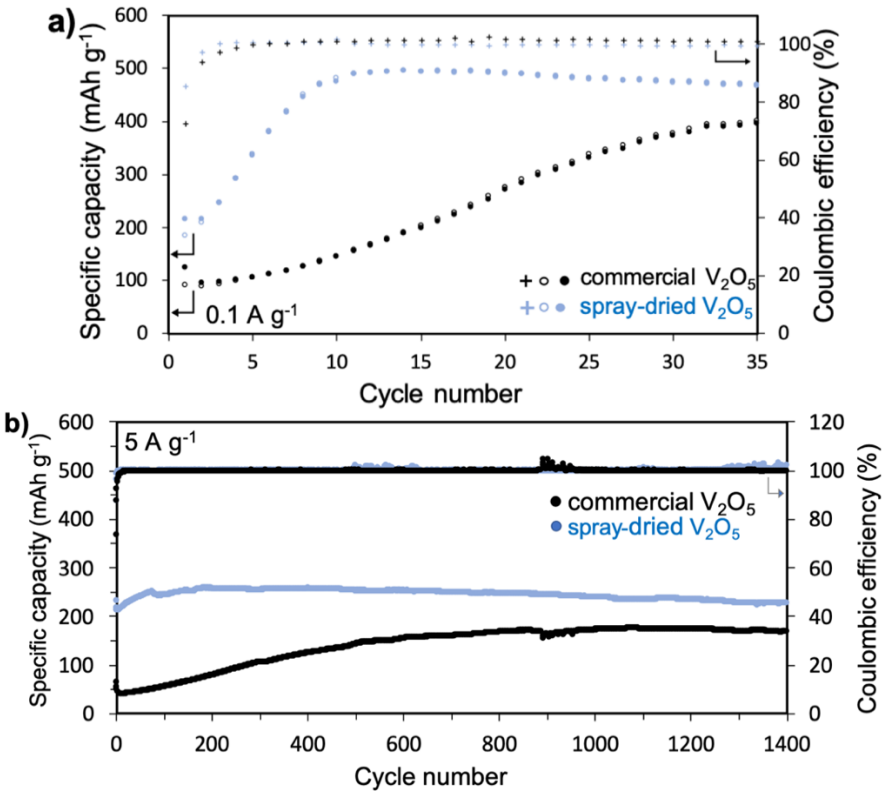

Figure III-9: (a) Cycle performance at 0.1 A g^{-1} and (b) long cycling performance at 5 A g^{-1} of commercial and spray-dried V_2O_5 materials.

The spray-dried V_2O_5 material delivers a remarkably high specific discharge capacity of 495 mAh g^{-1} after 15 cycles at a current density of 0.1 A g^{-1} compared to 198 mAh g^{-1} for commercial V_2O_5 (Figure III-9a). This is one of the best capacities reported in the literature (see Table III-1). In addition, even at high current density, a high discharge capacity with good capacity retention is delivered. The cycling performance of both electrodes has been evaluated at high current density (5 A g^{-1}). Compared with the commercial V_2O_5, spray-dried V_2O_5 demonstrates better performance with a high discharge capacity of 240 mAh g^{-1} and good capacity retention of 93 % after 1000 cycles and 89 % after 1400 cycles (Figure III-9b). This could be assigned to the morphological design that facilitates the insertion/extraction of Zn^{2+} in the structure of V_2O_5 cathode material as explained previously.

Table III-1: State of the art of electrochemical performances of V_2O_5 prepared via various procedures.

Ref	Material	Morphology	Treatment	Electrolyte	Capacity (mAh g^{-1})	Cycles	Retention (%)
[31]	V_2O_5	hollow spheres	solvothermal	$ZnSO_4$ saturated	280 (0.2 A g^{-1})	6200 (10 A g^{-1})	82.5
[16]	V_2O_5	microspheres	spray-drying	$Zn(CF_3SO_3)_2$ 2M	401 (0.1 A g^{-1})	1000 (5 A g^{-1})	73
[1]	V_2O_5	bulk	commercial	$Zn(CF_3SO_3)_2$ 3M	470 (0.2 A g^{-1})	4000 (5 A g^{-1})	91.1
[50]	V_2O_5 MOF	nanosheets	hydrothermal	$Zn(CF_3SO_3)_2$ 3M	450 (0.1 A g^{-1})	2000 (2 A g^{-1})	86.8
[9]	V_2O_5 (+CB)	nanosheets	hydrothermal	$Zn(CF_3SO_3)_2$ 3M	452 (0.1 A g^{-1})	5000 (10 A g^{-1})	92
[51]	$V_2O_5 \cdot 2.2H_2O$	nanosheets	in situ	$Zn(CF_3SO_3)_2$ 3M	450 (0.1 A g^{-1})	3000 (5 A g^{-1})	72
[52]	$V_2O_5 \cdot 1.6H_2O$	nanosheets	hydrothermal	$Zn(CF_3SO_3)_2$ 3M	426 (0.1 A g^{-1})	5000 (10 A g^{-1})	95
	Our work	**microspheres**	**spray-drying**	**$Zn(CF_3SO_3)_2$ 3M**	**495 (0.1 A g^{-1})**	**1000 (5 A g^{-1})**	**93**

The rate performance of the spray-dried particles is remarkably higher than the commercial V_2O_5 at the current densities ranging from 0.1 to 5 A g^{-1} as shown in Figure III-10a. The discharge capacities delivered by the spray-dried particles are 483, 478, 449, 419, 369, and 340 mAh g^{-1} at the current density of 0.1, 0.2, 0.5, 1, 3, and 5 A g^{-1}. At the end of the rate capability test, the current density returns to 0.2 A g^{-1}, and the discharge capacity is recovered, suggesting excellent structural stability of the V_2O_5 material. Moreover, the almost 100% coulombic efficiency means a highly reversible redox reaction even at high current density. The corresponding galvanostatic charge/discharge curves of spray-dried

V_2O_5 at different current rates are represented in Figure III-10b. The charge/discharge plateaus can be detected even at a high current density which could be attributed to the fast kinetics of Zn^{2+}.

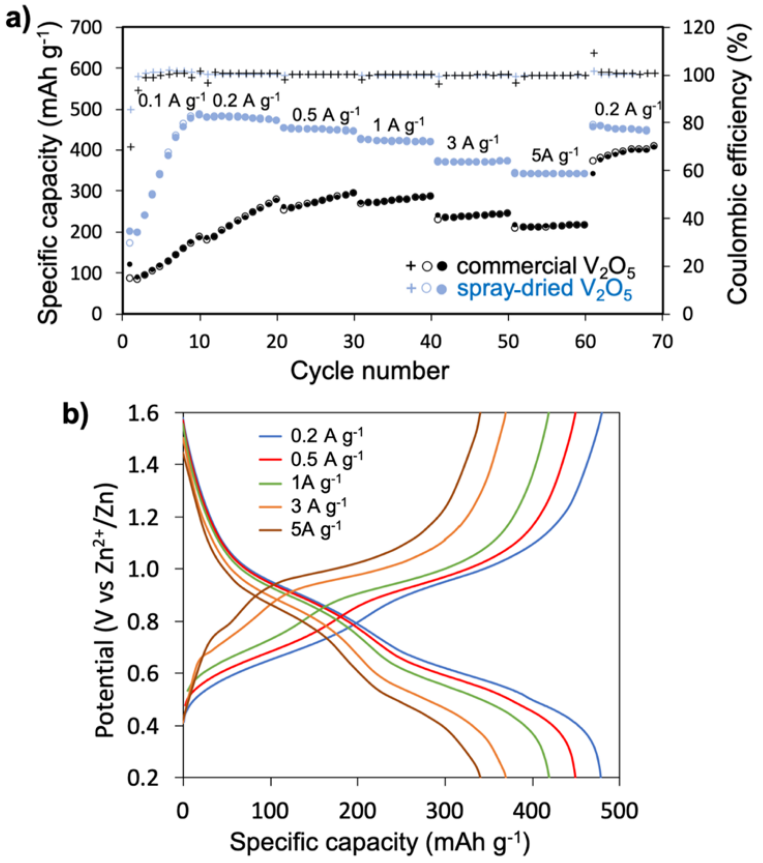

Figure III-10: (a) Rate capability of commercial and spray-dried V_2O_5 and (b) Galvanostatic charge/discharge profiles of spray-dried V_2O_5 at various current densities (0.2, 0.5, 1, 3, and 5 A g^{-1}).

3.3. Influence of the addition of carbon nanotubes on the structural, microstructural, and electrochemical properties of V_2O_5.

To enhance the electrochemical performance of spray-dried V_2O_5 material and address the issue of its low electronic conductivity, conductive carbon nanotubes were added to the suspension before spray-drying. Four spray-dried V_2O_5/xCNT materials were prepared by incorporating 5 wt% of CNT (V_2O_5/5CNT), 10 wt% of CNT (V_2O_5/10CNT), 15 wt% of CNT (V_2O_5/15CNT), and 20 wt% of CNT (V_2O_5/20CNT) in the V_2O_5 suspension. The ratios were calculated based on the V_2O_5 mass. The structural, morphological and electrochemical properties of these materials were investigated by combining different characterization

techniques such as XRD, SEM, laser granulometry, BET analysis and galvanostatic techniques.

The crystallographic structure and crystallinity of spray-dried V_2O_5/xCNT were investigated by XRD. The XRD patterns of spray dried V_2O_5 and V_2O_5/xCNT represented in Figure III-11 show sharp diffraction peaks which are attributed to the orthorhombic phase of V_2O_5 (JCPDS card 00-041-1426) with a high crystallinity. Moreover, no impurity peak is detected. The lattice parameters of spray-dried V_2O_5/xCNTs and the average crystallite size are determined by fitting the XRD patterns and presented in Figure III-14a. The introduction of CNT into the composite does not change the crystal lattice parameters. Given that no peak shift is detected in V_2O_5/xCNTs, no water molecule is inserted into the structure during the process [5]. However, the average crystallite size is affected and decreases from 100 nm for the spray-dried V_2O_5 material to 75 nm for the V_2O_5/10CNT (see Figure III-14a).

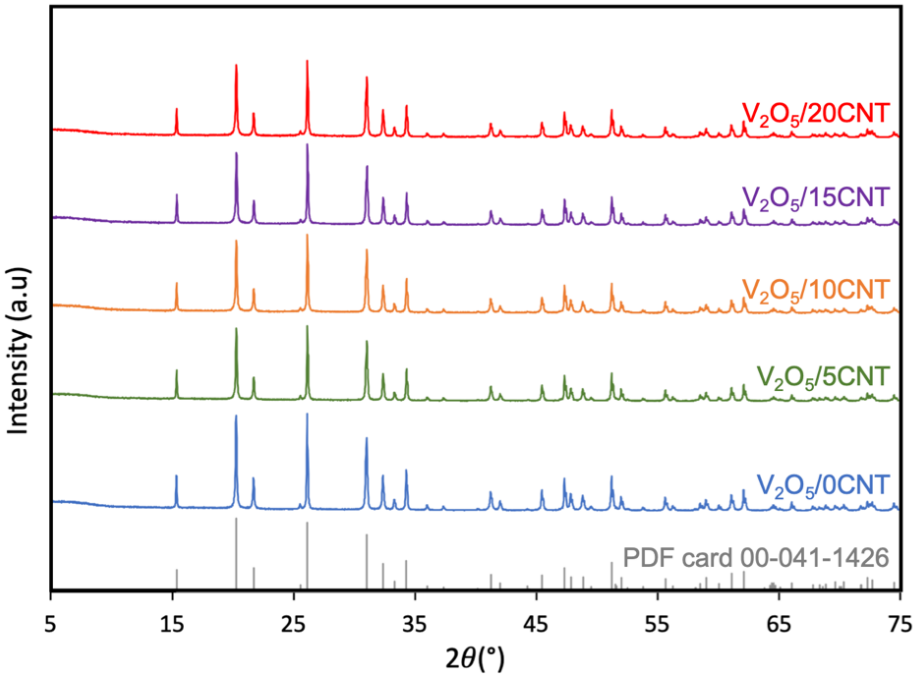

Figure III-11: X-Ray diffraction patterns of spray-dried V_2O_5 and V_2O_5 /xCNT materials.

Then, to evaluate the V^{4+}/V^{5+} ratio that can influence the electrochemical performance of the material, the XPS survey spectra for the commercial V_2O_5 and V_2O_5/xCNTs powder were acquired. As observed in Figure III-12, the addition of carbon nanotubes through the spray-drying process does not affect significantly the V^{4+} atomic percentage as demonstrated

in the V 2p core level. A slight increase in the signal at a lower binding energy of 516.5 (± 0.2) eV is observed which corresponds to the increase of V^{4+} at. % from 9 at.% for commercial V_2O_5 (Figure III-12a) to 10 at. % for V_2O_5/0NT and V_2O_5/5NT (Figure III-12b and c) and to 13 at. % V_2O_5/10NT (Figure III-12d).

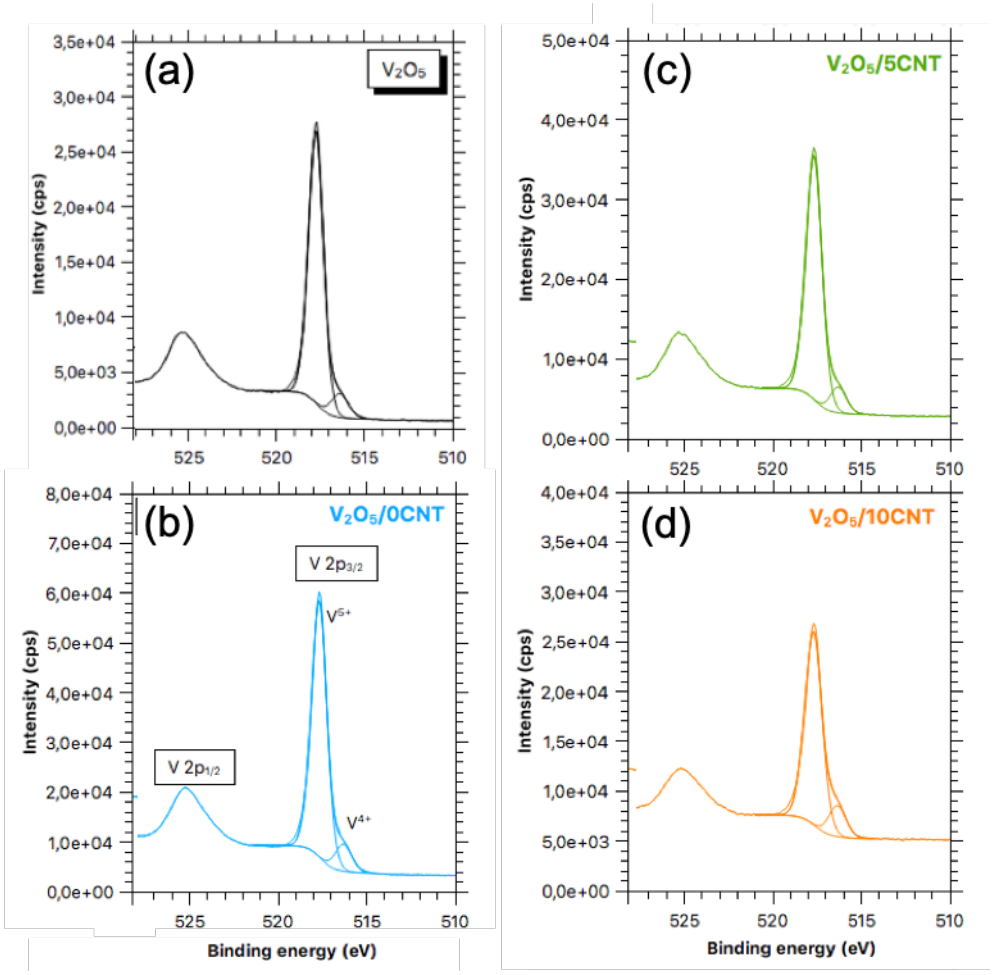

Figure III-12: XPS high resolution spectra of V 2p obtained for (a) commercial V_2O_5, (b) spray-dried V_2O_5, (c) V_2O_5/5CNT, (d) V_2O_5/10CNT.

The effect of carbon nanotubes addition on the morphology and microstructure of V_2O_5 was characterized by scanning electron microscopy and laser granulometry. Figure III-13 presents the SEM images of V_2O_5 and V_2O_5/xCNT materials. Solid microspheres resulting from the agglomeration of V_2O_5 primary particles are obtained after spray-drying (Figure III-13a). The SEM images of V_2O_5/xCNT show that microspheres are obtained whatever the ratio of carbon nanotubes (Figure III-13b, c, d and e). The image of a broken particle of V_2O_5/10CNT presented in Figure III-13f shows that the CNTs are well dispersed inside and on the surface of the V_2O_5 microspheres. Moreover, the particle size of V_2O_5/xCNTs is higher than V_2O_5 as determined by laser granulometry (Figure III-14b). The higher the

amount of CNTs, the larger the particle size. The specific surface area of the samples was measured with N_2 adsorption/desorption. Not surprisingly, the calculated BET surface area of the V_2O_5/xCNT presented in Figure III-14c increases with the increase of the ratio of CNTs in V_2O_5/xCNT materials. With only 5% of carbon nanotubes, the specific surface area is two times higher and increases even more with 10, 15, and 20% of carbon nanotubes. This result is attributed to the smaller crystallite size of V_2O_5 and to the large specific surface area of carbon nanotubes. This specific surface area increase can promote the Zn^{2+} transport which is beneficial for improving the electrochemical performance [44].

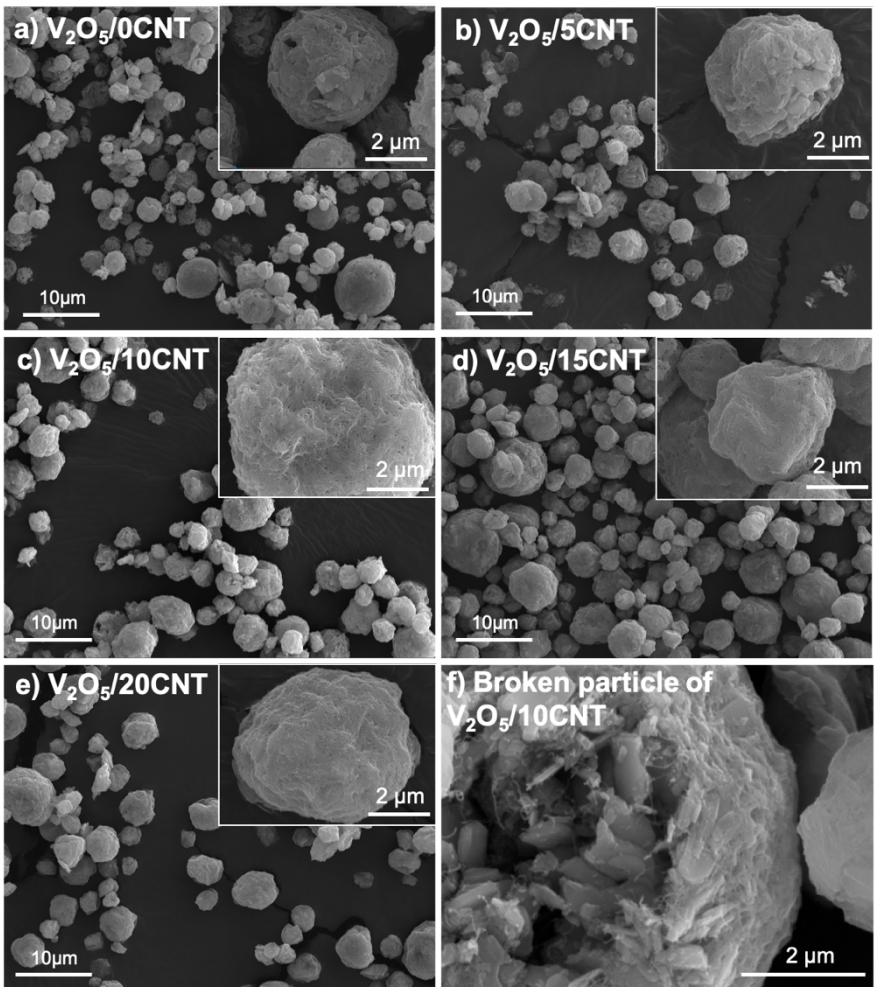

Figure III-13: (a-e) SEM images of (a) V_2O_5, (b) V_2O_5/5CNT, (c) V_2O_5/10CNT, (d) V_2O_5/15CNT, (e) V_2O_5/20CNT prepared by spray-drying and (f) a broken particle of V_2O_5/10CNT

(a)

	a (Å)	b (Å)	c (Å)	Crystal size (L-Vol-IB) (nm)
V_2O_5	11.5143(3)	3.5650(1)	4.3727(1)	98(2)
V_2O_5/5CNT	11.5148(2)	3.5652(1)	4.3732(1)	85(1)
V_2O_5/10CNT	11.5144(2)	3.5651(1)	4.3733(1)	76(1)
V_2O_5/15CNT	11.5150(2)	3.5654(1)	4.3735(1)	75(1)
V_2O_5/20CNT	11.5153(2)	3.5654(1)	4.3736(1)	75(1)

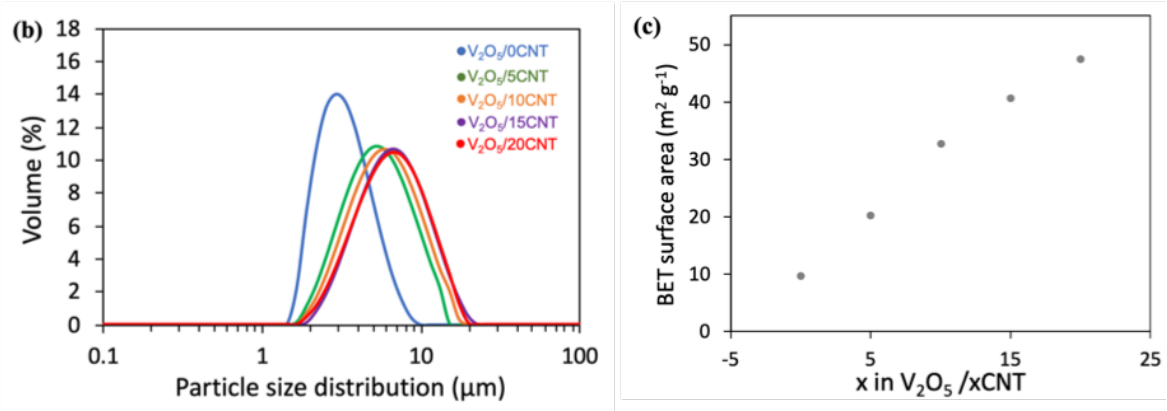

Figure III-14: (a) Lattice parameters and average crystallite size (with error bar) of spray-dried V_2O_5 and V_2O_5/xCNT materials obtained by the refinement of the XRD patterns, (b) the particle size distribution and (c) the specific surface area determined by BET technique of V_2O_5/xCNT (x=0, 5, 10, 15 and 20).

In order to investigate the electrochemical properties of spray-dried V_2O_5 /xCNT, working electrodes containing 70 wt% of V_2O_5, 20 wt% of conductive carbon (CNTs and/or carbon black), and 10 wt% of PVDF used as a binder were prepared. CV and galvanostatic discharge/charge tests were conducted and compared to spray-dried V_2O_5 experiments. The galvanostatic charge/discharge curves of the V_2O_5/xCNTs at 0.1 A g^{-1} represented in Figure III-15 show the characteristic profile of V_2O_5 material. The specific capacities gradually increase during the initial cycles corresponding to the activation phase of the V_2O_5 cathode active material. It means that the number of active sites of V_2O_5 increases along cycling due to the gradual impregnation of electrolyte into the internal space of V_2O_5 as discussed previously. It can be noted that the activation process is slightly shorter for spray-dried V_2O_5/xCNTs than for spray-dried V_2O_5 material because 10 cycles are enough. This result is in good agreement with the cyclic voltammetry curves presented in Figure III-16. The insertion of carbon nanotubes into the matrix leads to the increase of the specific surface area which is favorable for the insertion of Zn^{2+} ion into the structure [36,44]. Besides, the

specific capacity recuperated after the first cycle is higher for materials with carbon nanotubes. When the activation process is completed, the discharge capacity of V_2O_5/5CNT and V_2O_5/10CNT reaches ~ 500 mAh g^{-1} which is comparable to spray-dried V_2O_5 material. Nevertheless, for the V_2O_5/15CNT and V_2O_5/20CNT based electrodes, the specific capacity after activation is lower than without carbon nanotubes addition (Figure III-17a). In this case, the amount of carbon nanotubes around the surface is probably too high (Figure III-13d-e) and diminishes electrolyte penetration into the internal space of V_2O_5. In addition, the amount of carbon black added in these electrodes is lower which means that the contact between the spray-dried V_2O_5/15-20CNTs microparticles is probably not enough as shown on Figure III-18 [53,54]. A rate capability test has been conducted to study and compare the specific power that V_2O_5/xCNTs electrodes can drain.

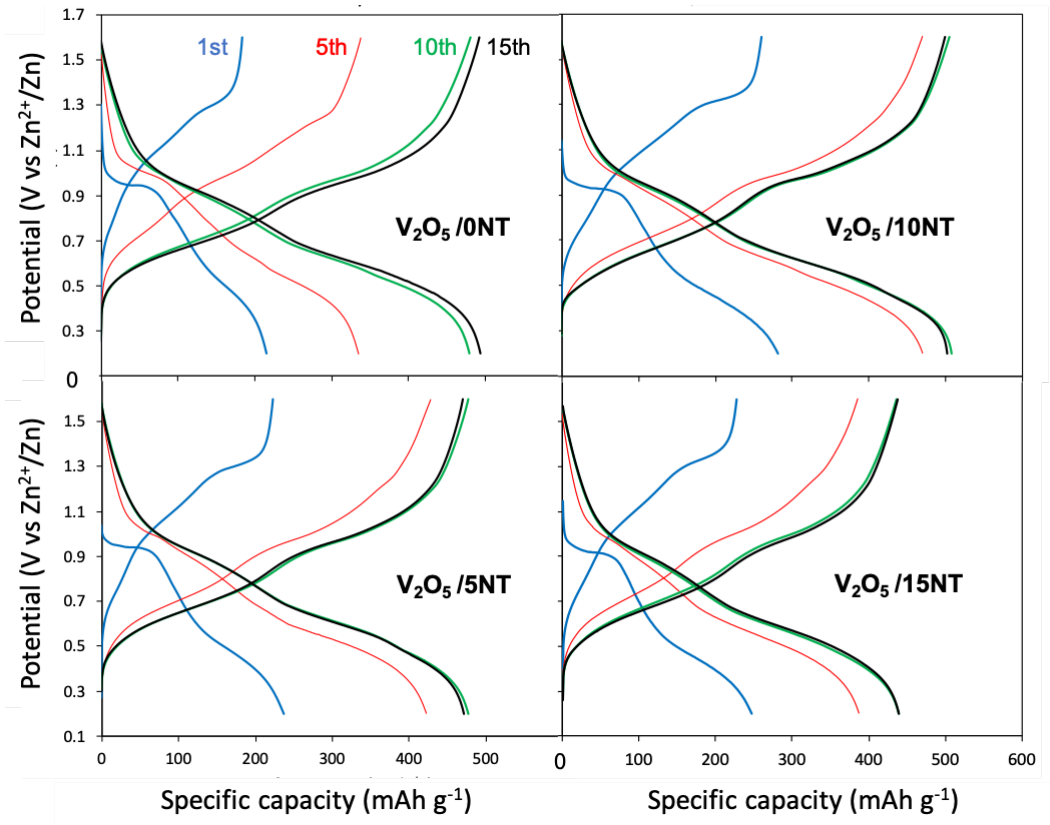

Figure III-15: Galvanostatic discharge/charge curves (1st, 5th, 10th , and 15th cycle) of spray-dried V_2O_5 and V_2O_5/xCNTs at 0.1 A g^{-1}.

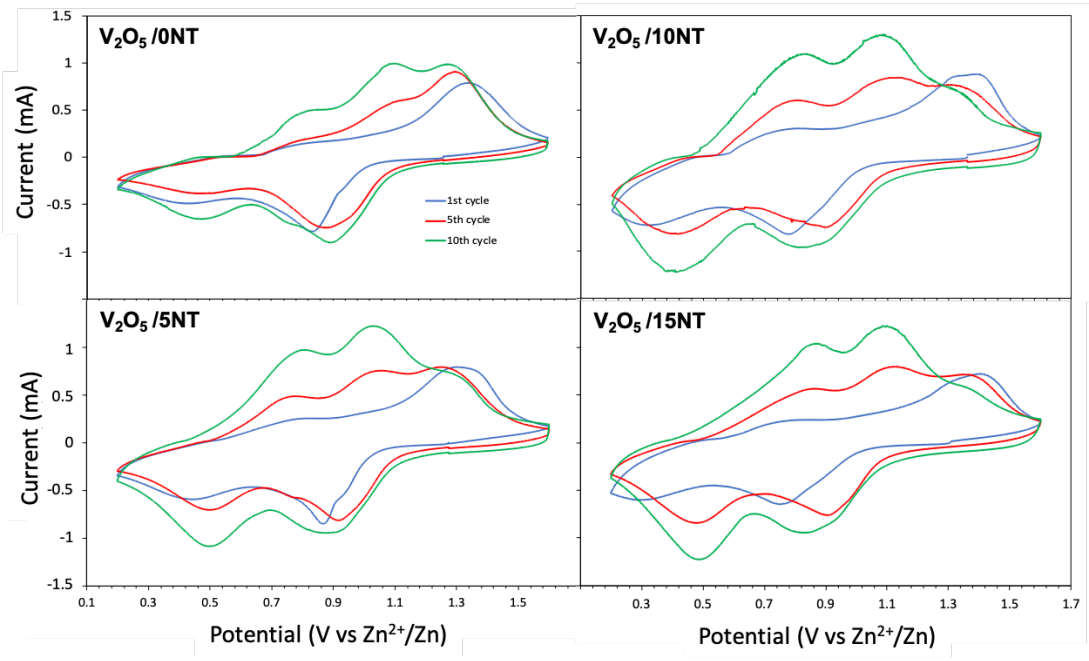

Figure III-16: CV curves of spray-dried V_2O_5 and V_2O_5/xCNTs at 0.5 mV s^{-1}.

The rate performance curves of spray-dried V_2O_5/xCNT are shown in Figure III-17b. The rate performance of spray driedV_2O_5/5CNT and V_2O_5/10CNT electrodes is better than spray-dried V_2O_5 material, particularly at high current densities. The optimal sample, spray-dried V_2O_5/5CNT material delivers specific capacities of 497, 495, 478, 463, 427 and 403 mAh g^{-1} compared to 483, 478, 449, 419, 369, and 340 mAh g^{-1} without CNT addition at the current densities of 0.1, 0.2, 0.5, 1, 3 and 5 A g^{-1} respectively. When the current density returns to 0.2 A g^{-1}, the capacity of 495 mAh g^{-1} is recovered. The carbon nanotubes network acts as a barrier to limit the degradation of V_2O_5 (Figure III-13b-f) [36], alleviates the volume variations of material during charge and discharge processes [37,55,56], and improve the utilization rate of the V_2O_5 materials by accelerating the electron transfer due to their excellent conductivity [27,57].

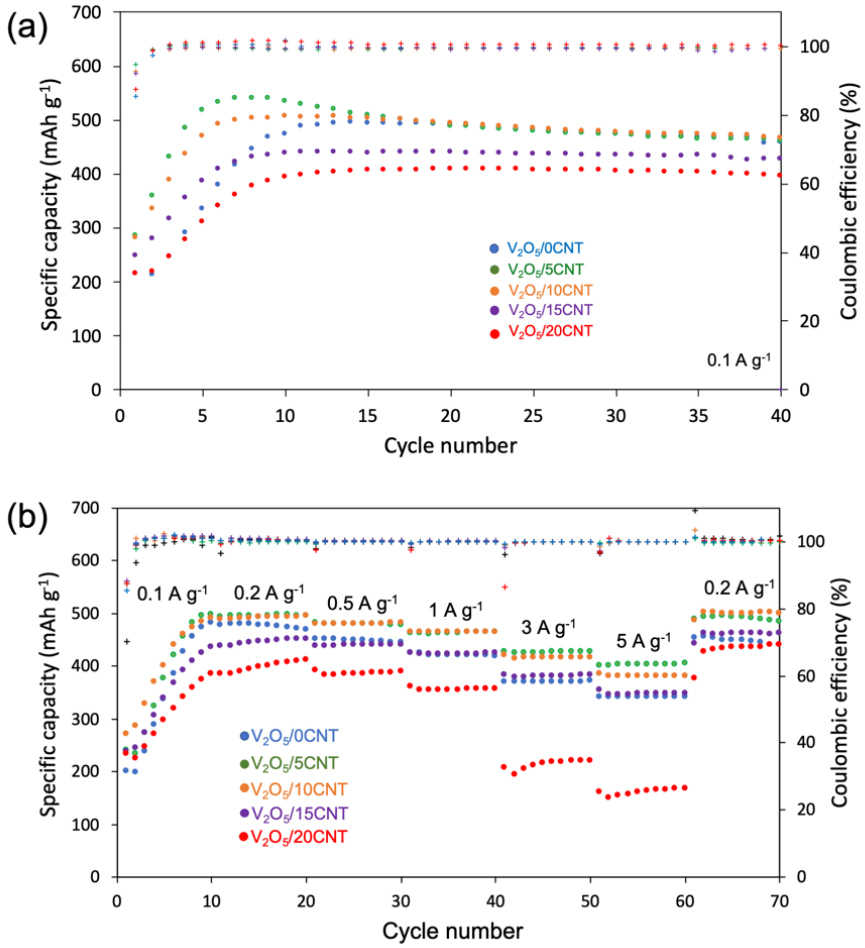

Figure III-17: (a) Cycle performance at 0.1 A g^{-1} and (b) Rate capability at 0.1, 0.2, 0.5, 1, 3 and 5 A g^{-1} of spray-dried V_2O_5/xCNTs.

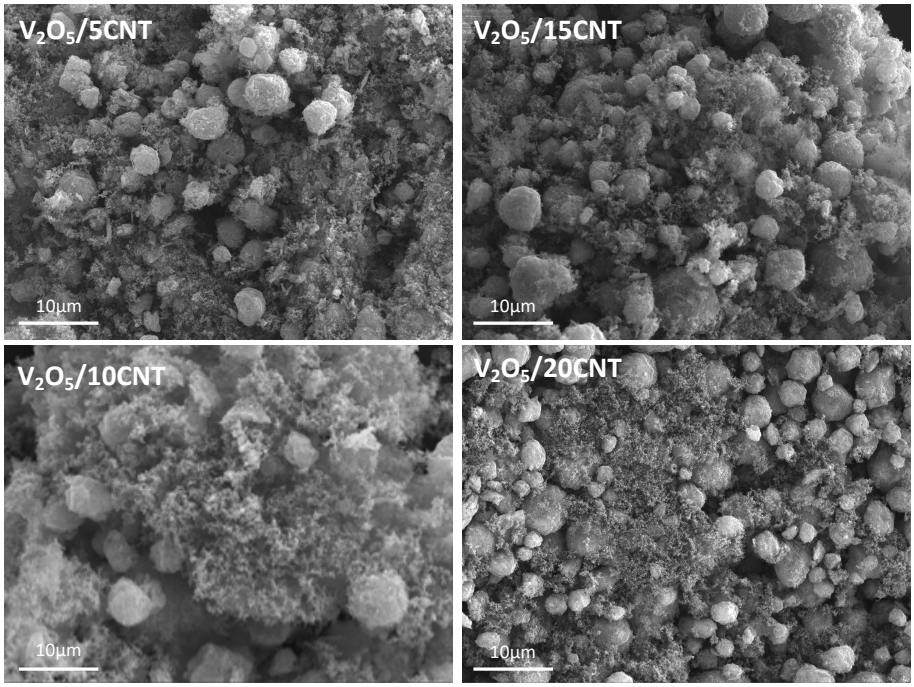

Figure III-18: SEM images of V_2O_5/xCNT with carbon black and PVDF.

Figure III-19 compares the cycling performance of spray-dried V_2O_5/0CNT and V_2O_5/5CNT at high current density of 5 A g^{-1} for 1000 cycles. Thanks to the addition of CNT, the electrode displays a higher reversible discharge specific capacity of 290 mAh g^{-1} compared to 240 mAh g^{-1} and a similar capacity retention higher than 90% after 1000 cycles. The conductive carbon nanotubes induce rapid electron transport during cycling which leads to enhanced electrochemical performance at high rates. Moreover, the higher specific surface area of this material (Figure III-14c) creates more active sites and leads to fast ion diffusion pathways.

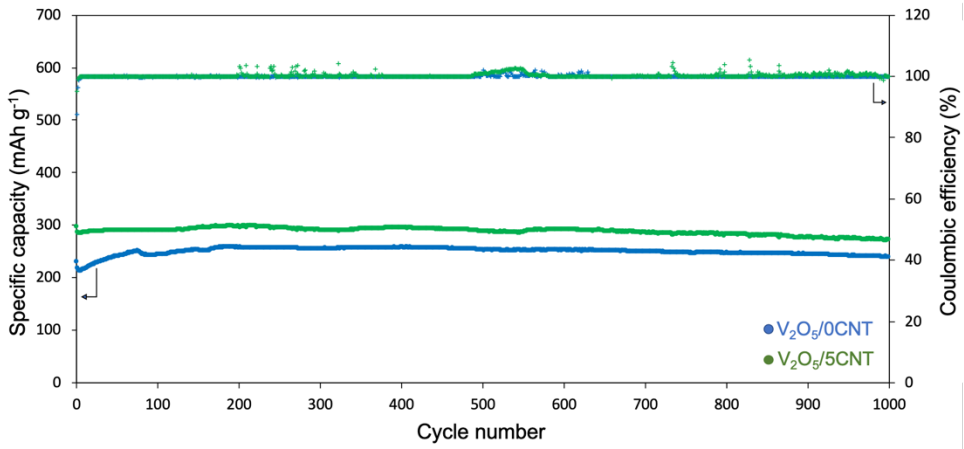

Figure III-19: Long cycling performance of V_2O_5/0CNT and V_2O_5/5CNT spray-dried materials at 5 A g^{-1}.

4. Conclusion

Firstly, V_2O_5 material was tailored through a one-step spray-drying process at a pilot scale. Solid microspheres with particle size in the range of 1-10 µm and with a specific surface area of 9.6 m^2 g^{-1} are obtained. A comparative study between spray-dried V_2O_5 and commercial V_2O_5 reveals the benefit of the morphological design of vanadium pentoxide cathode material on electrochemical performances for ZIBs. The end of the activation process is achieved in fewer cycles. Then, spray-dried V_2O_5 exhibits remarkably high capacities of 495 mAh g^{-1} and 240 mAh g^{-1} at low (0.1 A g^{-1}) and high current density (at 5 A g^{-1}) respectively, excellent rate capability, and good stability. Excellent capacity retention of 93 % is observed after 1000 cycles at high current density.

Secondly, V_2O_5/xCNTs were obtained by incorporating x wt% of carbon nanotubes into the V_2O_5 suspension before spray-drying in order to improve its electrochemical performance. The SEM images reveal that the CNTs are well dispersed and the obtained microspheres obtained are not agglomerated. By enhancing the electronic conductivity, protecting the V_2O_5 surface, and increasing the specific surface area, the carbon nanotubes addition is favorable to the electrochemical properties of vanadium pentoxide. It leads to an improvement of the rate capability particularly at high current density and an enhancement of the capacity retention upon cycling. A reversible capacity of 290 mAh g^{-1} is maintained for 1000 cycles for the prepared composite material.

5. References

1 N. Zhang, Y. Dong, M. Jia, X. Bian, Y. Wang, M. Qiu, J. Xu, Y. Liu, L. Jiao and F. Cheng, *ACS Energy Lett*, 2018, **3**, 1366–1372.

2 M. Song, H. Tan, D. Chao and H. J. Fan, *Adv Funct Mater*, 2018, **28**, 1–27.

3 A. R. Mainar, L. C. Colmenares, J. A. Blázquez and I. Urdampilleta, *Int J Energy Res*, 2018, **42**, 903–918.

4 S. Mallick and C. R. Raj, *ChemSusChem*, 2021, **14**, 1987–2022.

5 M. Yan, P. He, Y. Chen, S. Wang, Q. Wei, K. Zhao, X. Xu, Q. An, Y. Shuang, Y. Shao, K. T. Mueller, L. Mai, J. Liu and J. Yang, Advanced Materials, 2018, **30**, 1–6.

6 A. Konarov, N. Voronina, J. H. Jo, Z. Bakenov, Y. K. Sun and S. T. Myung, *ACS Energy Lett*, 2018, **3**, 2620–2640.

7 P. Hu, M. Yan, T. Zhu, X. Wang, X. Wei, J. Li, L. Zhou, Z. Li, L. Chen and L. Mai, *ACS Appl Mater Interfaces*, 2017, **9**, 42717–42722.

8 J. Ming, J. Guo, C. Xia, W. Wang and H. N. Alshareef, *Materials Science and Engineering R: Reports*, 2019, **135**, 58–84.

9 X. Wang, L. Ma and J. Sun, *ACS Appl Mater Interfaces*, 2019, **11**, 41297–41303.

10 B. Tang, L. Shan, S. Liang and J. Zhou, *Energy Environ Sci*, 2019, **12**, 3288–3304.

11 Y. Zhang, A. Chen and J. Sun, *Journal of Energy Chemistry*, 2021, **54**, 655–667.

12 D. Selvakumaran, A. Pan, S. Liang and G. Cao, *J Mater Chem A Mater*, 2019, **7**, 18209–18236.

13 V. Verma, S. Kumar, W. Manalastas, R. Satish and M. Srinivasan, *Adv Sustain Syst*, 2019, **3**, 1800111.

14 W. Xu and Y. Wang, *Nanomicro Lett*, 2019, **11**, 1–30.

15 Y. Wang, C. Wang, Z. Ni, Y. Gu, B. Wang, Z. Guo, Z. Wang, D. Bin, J. Ma and Y. Wang, *Advanced Materials*, 2020, **32**, 2000338

16 P. Hu, T. Zhu, J. Ma, C. Cai, G. Hu, X. Wang, Z. Liu, L. Zhou and L. Mai, *Chemical Communications*, 2019, **55**, 8486–8489.

17 F. Wan and Z. Niu, *Angewandte Chemie - International Edition*, 2019, **58**, 16358–16367.

18 W. Zhang, C. Zuo, C. Tang, W. Tang, B. Lan, X. Fu, S. Dong and P. Luo, *Energy Technology*, 2021, **9**, 1–20.

19 P. He, G. Zhang, X. Liao, M. Yan, X. Xu, Q. An, J. Liu and L. Mai, *Adv Energy Mater*, 2018, **8**, 1–6.

20 X. Guo, G. Fang, W. Zhang, J. Zhou, L. Shan, L. Wang, C. Wang, T. Lin, Y. Tang and S. Liang, *Adv Energy Mater*, 2018, **8**, 1–7.

21 Z. Peng, Q. Wei, S. Tan, P. He, W. Luo, Q. An and L. Mai, *Chemical Communications*, 2018, **54**, 4041–4044.

22 F. Ming, H. Liang, Y. Lei, S. Kandambeth, M. Eddaoudi and H. N. Alshareef, *ACS Energy Lett*, 2018, **3**, 2602–2609.

23 L. Wang, K. W. Huang, J. Chen and J. Zheng, *Sci Adv*, 2019, **5**, 1–11.

24 S. Huang, J. Zhu, J. Tian and Z. Niu, *Chemistry - A European Journal*, 2019, **25**, 14480–14494.

25 Q. Zhang, Y. Ma, Y. Lu, Y. Ni, L. Lin, Z. Hao, Z. Yan, Q. Zhao and J. Chen, *J Am Chem Soc*, 2022, **144**, 18435-18443

26 F. Wang, L. E. Blanc, Q. Li, A. Faraone, X. Ji, H. H. Chen-Mayer, R. L. Paul, J. A. Dura, E. Hu, K. Xu, L. F. Nazar and C. Wang, *Adv Energy Mater*, 2021, **11**, 2102016

27 H. Chen, H. Qin, L. Chen, J. Wu and Z. Yang*, J Alloys Compd*, 2020, **842**, 155912.

28 Q. Pang, C. Sun, Y. Yu, K. Zhao, Z. Zhang, P. M. Voyles, G. Chen, Y. Wei and X. Wang, *Adv Energy Mater*, 2018, **8**, 1–9.

29 D. Kundu, B. D. Adams, V. Duffort, S. H. Vajargah and L. F. Nazar, *Nat Energy*, 2016, **1**, 1–28.

30 D. Kundu, S. Hosseini Vajargah, L. Wan, B. Adams, D. Prendergast and L. F. Nazar, *Energy Environ Sci*, 2018, **11**, 881–892.

31 H. Qin, L. Chen, L. Wang, X. Chen and Z. Yang, *Electrochim Acta,* 2019, **306**, 307–316.

32 C. Q. Feng, S. Y. Wang, R. Zeng, Z. P. Guo, K. Konstantinov and H. K. Liu, *J Power Sources*, 2008, **184**, 485–488.

33 A. I. Volkov, A. S. Sharlaev, O. Ya. Berezina, E. G. Tolstopjatova, L. Fu and V. v. Kondratiev, *Mater Lett*, 2022, **308**, 0–4.

34 Y. Li, P. Xu, J. Jiang, J. Yao, B. Huang and J. Yang, *Mater Today Commun*, 2021, **26**, 101849.

35 B. Sambandam, V. Soundharrajan, S. Kim, M. H. Alfaruqi, J. Jo, S. Kim, V. Mathew, Y. K. Sun and J. Kim, *J Mater Chem A Mater*, 2018, **6**, 3850–3856.

36 Q. Li, Y. Chen, J. He, F. Fu, F. Qi, J. Lin and W. Zhang, *Energy Technology*, 2017, **5**, 665–669.

37 G. Li, L. Sun, S. Zhang, C. Zhang, H. Jin, K. Davey, G. Liang, S. Liu, J. Mao and Z. Guo, *Adv Funct Mater*, 2024, **34**, 2301291

38 Y. Wang, S. Lu, W. He, S. Gong, Y. Zhang, X. Zhao, Y. Fu and Z. Zhu, *Sci Rep,* 2022, **12**, 1–12.

39 D. Pantea, H. Darmstadt, S. Kaliaguine and C. Roy, *Appl Surf Sci,* 2003, **217**, 181–193.

40 B. Yin, S. Zhang, K. Ke, T. Xiong, Y. Wang, B. K. D. Lim, W. S. V. Lee, Z. Wang and J. Xue, *Nanoscale*, 2019, **11**, 19723–19728.

41 R. W. Cheary and A. Coelho, *J Appl Crystallogr*, 1992, **25**, 109–121.

42 R. Li, H. Zhang, Q. Zheng and X. Li, *J Mater Chem A Mater*, 2020, **8**, 5186–5193.

43 A. Mahmoud, J. M. Amarilla, K. Lasri and I. Saadoune, *Electrochim Acta*, 2013, **93**, 163–172.

44 L. Chen, Z. Yang, F. Cui, J. Meng, H. Chen and X. Zeng, *Appl Surf Sci*, 2020, **507**, 145137.

45 X. Chen, L. Wang, H. Li, F. Cheng and J. Chen, *Journal of Energy Chemistry*, 2019, **38**, 20–25.

46 W. Liu, L. Dong, B. Jiang, Y. Huang, X. Wang, C. Xu, Z. Kang, J. Mou and F. Kang, *Electrochim Acta*, 2019, **320**, 134565.

47 X. Liu, H. Euchner, M. Zarrabeitia, X. Gao, G. A. Elia, A. Groß and S. Passerini, *ACS Energy Lett*, 2020, **5**, 2979–2986.

48 Y. Liu, Q. Li, K. Ma, G. Yang and C. Wang, ACS Nano, 2019, **13**, 12081–12089.

49 X. Wang, L. Wang, B. Zhang, J. Feng, J. Zhang, X. Ou, F. Hou and J. Liang, *Journal of Energy Chemistry,* 2021, **59**, 126–133.

50 W. Zhou, J. Chen, M. Chen, X. Xu, Q. Tian, J. Xu and C. P. Wong, *RSC Adv*, 2019, **9**, 30556–30564.

51 J. Zhao, H. Ren, Q. Liang, D. Yuan, S. Xi, C. Wu, W. Manalastas, J. Ma, W. Fang, Y. Zheng, C. F. Du, M. Srinivasan and Q. Yan, *Nano Energy*, 2019, **62**, 94–102.

52 X. Wang, L. Ma, P. Zhang, H. Wang, S. Li, S. Ji, Z. Wen and J. Sun, *Appl Surf Sci*, 2020, **502**, 144207.

53 H. Li and H. Zhou, *Chemical Communications*, 2012, **48**, 1201–1217.

54 M. Gaberscek, R. Dominko and J. Jamnik, *Electrochem commun*, 2007, **9**, 2778–2783.

55 Z. Wu, W. Zhou, Z. Liu, Y. Zhou, G. Zeng and H. Chen, *Materials Express*, 2020, **10**, 1697–1703.

56 G. Xu, X. Liu, S. Huang, L. Li, X. Wei, J. Cao, L. Yang and P. K. Chu, *ACS Appl Mater Interfaces*, 2020, **12**, 706–716.

57 Y. Ma, *Int J Electrochem Sci*, 2020, **15**, 10315–10329.

Chapter IV: Self-standing V_2O_5/Polydopamine/CNT film as high-performance cathode material for advanced zinc-ion batteries

In this chapter, we report for the first time a self-standing V_2O_5/polydopamine/CNT (V_2O_5/PDA/CNT) electrode that shows outstanding electrochemical performance as cathode material for zinc-ion batteries. A polydopamine (PDA) coating was applied to the surface of V_2O_5 particles through a facile self-polymerization process of dopamine. The PDA coating was confirmed and studied by TEM, TGA, FTIR-ATR, and XPS (O 1s & V 2p, C 1s and N 1s). Polydopamine thin layer leads to the partial reduction of V^{5+} to V^{4+}. Combining V_2O_5/PDA with CNT allowed us to obtain a self-standing, binder-free cathode material with a high capacity of ~530 mAh g^{-1} at 0.1 A g^{-1}. The developed electrode demonstrates excellent rate capability. Indeed, even with a 25-fold increase in current density (from 0.2 A g^{-1} to 5 A g^{-1}), V_2O_5/PDA/CNT-b retains 94% of its capacity. In addition, the new electrode exhibits long-term cycle stability enduring up to 1000 cycles at high current density with excellent capacity retention. The combination of PDA coating with the incorporation of carbon nanotubes appears to be an excellent strategy for enhancing the electrochemical performance and stability of V_2O_5 for ZIBs.

Keywords: Zn-ion batteries, V_2O_5, polydopamine, composites, cathode materials.

E. Roex, A. Aqil, J. Światowska, C. Malherbe, F. Boschini, R. Cloots and A. Mahmoud, "Self-standing V_2O_5/Polydopamine/CNT film as high-performance cathode material for advanced zinc-ion batteries", *Journal of Power sources,* vol.616, October, 2024

1. Introduction

As previously explained, V_2O_5 materials face numerous challenges including a low operating voltage, low ion diffusion, poor electrical conductivity, vanadium dissolution in aqueous electrolyte, formation of byproducts with the electrolyte, and volume changes induced by Zn^{2+} insertion/extraction during cycling in ZIBs [1–4]. The particle size and morphology impact the electrochemical performance of V_2O_5 as demonstrated in Chapter III but do not prevent the cathode dissolution.

Another strategy to solve V_2O_5 issues is to incorporate a conductive polymer around V_2O_5 particles to obtain an organic-inorganic composite. Polymers can buffer the volume expansion and diminish the solubility of V_2O_5 in the aqueous electrolyte by acting as a barrier thanks to their stable and covalently connected structure. Polyaniline, polypyrrole, and poly(3,4-ethylenedioxythiophene have already been intercalated in V_2O_5 and also investigated as conductive and stable polymers for coating V_2O_5 material in zinc-ion batteries [5–9].

Polydopamine is a bioderived organic electrode material prepared through the polymerization of dopamine (DA). Dopamine has already been intercalated in V_2O_5 to enhance the diffusion kinetics of zinc ions inside the interlayer spacing [10] or used as carbon source after thermal treatment to enhance electronic conductivity of V_2O_3 in zinc-ion batteries [11]. Moreover, polydopamine grafted on carbon nanotubes has already been reported as a cathode material in lithium, potassium, and zinc-ion batteries [12,13]. Containing both catechol and amine groups, dopamine can be polymerized on a wide range of material surfaces through self-polymerization in the presence of an alkaline solution forming an adhesive polymer of polydopamine [14]. The polymerization process is simple and energy-saving and do not require the use of an organic solvent contrary to other coating polymers already reported in the literature [5,7,9]. Furthermore, in comparison to hydrophobic polymers (polyaniline, polypyrrole, and poly(3,4-ethylenedioxythiophene)), the hydrophilic properties of PDA lead to excellent wetting at the electrode/electrolyte interface [12,15]. In addition, the PDA film exhibits strong adhesive properties, good mechanical flexibility and favorable ionic permeability, enabling ions to pass through the coating [14,16]. These properties make it suitable for the modification of electrode materials. Therefore, with regard to

aqueous ZIBs, a polydopamine coating on V_2O_5 can help to improve the ionic conductivity, ensure good structural stability, and protect V_2O_5 from dissolution and unwanted side reactions during discharge/charge processes. The polydopamine coating has already been studied in lithium-ion and sodium-ion batteries (NIBs) and demonstrates its benefits [14,15,17–19]. It is also used as a source of nitrogen or carbon to improve the conductivity of electrode materials in NIBs or ZIBs [11,20]. Nevertheless, as far as our knowledge extends, a polydopamine protective coating on V_2O_5 has never been reported in rechargeable aqueous zinc-ion batteries.

In this work, we prepare V_2O_5/PDA/CNT composite cathode material for ZIBs. We show that polydopamine coating prevents V_2O_5 material from dissolution and enhances the stability of V_2O_5 material in rechargeable aqueous ZIBs. The addition of carbon nanotubes (CNT) permits the preparation of a self-standing, binder-free cathode material and improves the electronic conductivity of the electrode. By solving some issues of V_2O_5 material, the electrochemical performance of V_2O_5 is highly improved in this study. The V_2O_5/PDA/CNT-b electrode prepared delivers a high reversible capacity of more than 530 mAh g^{-1} at 0.1 A g^{-1} and demonstrates excellent rate capability, and good stability at high current densities.

2. Experimental part

2.1. Materials and chemicals

Vanadium oxide (purity ≥ 99.6%), zinc trifluoromethansulfonate (purity, 98%), and tris-(hydroxymethyl)-aminoethane (purity ≥ 99.8%) were purchased from Sigma-Aldrich. Dopamine was obtained from Tokyo chemical industry, carbon nanotubes (purity > 95%) from Nanocyl and zinc foil (0.1 mm) (purity > 99.95%) from Goodfellow. HCl (37%), N-Methyl-2-pyrrolidone (NMP) (purity ≥ 99%), and ethanol absolute (purity, 99.8%) were bought from VWR, Alfa Aesar, and Fisher Chemicals, respectively.

2.2. Self-polymerization of dopamine on vanadium pentoxide (V_2O_5/PDA)

Commercial V_2O_5 (40 mg) material was first dispersed in 20 ml tris buffer solution (pH=8.5) using a sonication bath for 10 min at 300 W intensity. 40 mg of dopamine was solubilized

in 20 ml of tris buffer solution, added directly to the V_2O_5 solution and then the suspension is stirred for 1, 2 and 4 hours at room temperature. The color of the prepared suspension changed from yellow to black which indicated the polymerization of dopamine. The self-polymerization is fast due to the redox reaction between dopamine and V_2O_5. The resulting modified nanoparticles were then washed from the solution by repeated centrifugation and redispersion into MilliQ water followed by vacuum drying in a vacuum oven at 80 °C for 12 h. The ratio of polydopamine in the V_2O_5/PDA powder is determined by thermogravimetric analysis. V_2O_5/PDA-a, -b and -c referred to V_2O_5/PDA prepared by stirring the suspension during 1, 2 and 4 hours respectively.

2.3. Electrode preparation (V_2O_5/PDA/CNT)

The modified V_2O_5/PDA/CNT composite electrode was prepared via a dispersing filtration process (Figure IV-1): 40 mg of MWCNT was first dispersed in 20 ml ethanol using an ultrasonic Vibra Cell VCX 750 homogenizer (Sonics & Materials Inc., USA) for 10 min (2 sec on, 1 sec off). Subsequently, 20 mg of V_2O_5-PDA (a, b or c) was then dispersed in 20 ml of ethanol and added directly to the MWCNT suspension. The mixture was sonicated for 10 min at 300 W and was then stirred for 2 hours. The resulting solution underwent filtration through a Whatman Anodisc membrane with a pore size of 0.45 µM, followed by a vacuum drying in a vacuum oven at 80 °C for 12 h to eliminate the solvent. The resulting composites V_2O_5/PDA/CNT-a, -b and -c films were directly employed as the self-standing cathode without the addition of any binders or additives. The V_2O_5/CNT electrode was prepared in the same way using commercial V_2O_5 without PDA coating. The area loading of V_2O_5 in self-standing electrodes is ~ 0.3 mg cm^{-2}.

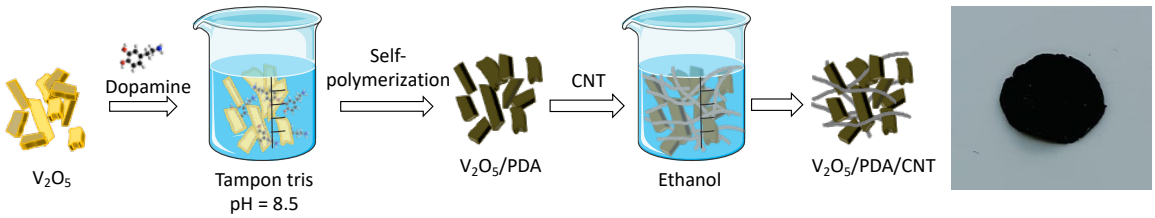

Figure IV-1: Schematic illustration of the preparation of the self-standing V_2O_5/PDA/CNT electrode.

The electrochemical performance of V_2O_5/PDA/CNT and V_2O_5/CNT is compared to the V_2O_5/PDA and commercial V_2O_5 powders without CNT. These no-self-standing electrodes, called V_2O_5/PDA/CB/PVDF and V_2O_5/CB/PVDF respectively, were prepared by mixing

33%wt V_2O_5/PDA (or commercial V_2O_5) 57%wt carbon black, and 10%wt PVDF. After grinding in a mortar, approximately 1.5 mg of the mixture was deposited and pressed onto a stainless-steel mesh.

2.4. Characterizations

Fourier transformed attenuated total reflectance infrared (FTIR-ATR) data were recorded on a few milligrams of powder using a Thermo Nicolet IS5 with ID7 ATR accessory equipped with a germanium crystal.

Thermogravimetric analysis was carried out under a stream of N_2 at a heating rate of 10°C/min using a TG/DTA6300 instrument.

X-ray photoelectron spectroscopy measurements were performed by means of Thermo Electron ESCALAB 250Xi spectrometer under high vacuum (10^{-9} mbar) with an Al K$_\alpha$ monochromatised X-ray source. Survey spectra and high-resolution core level spectra (V 2p, C 1s, O 1s, N 1s) were recorded with a pass energies of 100 eV and 20 eV, respectively, at a 90° take-off angle of the photoelectrons in relation to the surface sample. The spectra were corrected for charging effect with reference to C 1s hydrocarbon at 285.0 eV. Peak fitting was carried out using Avantage software (version 5.9918). A Shirley-type background was used, and different constraints were imposed for peak fitting, particularly on the full width at half maximum (FWHM) and intensity ratio of spin-orbit doublet (e.g. for V 2p).

X-ray diffraction patterns were recorded over the 2θ range from 10° to 70° using a D8 Twin-Twin powder diffractometer with Cu K_{alpha} radiation, with 0.2 s/channel step time and 15 rpm rotation speed. The whole powder pattern fitting procedure was conducted in the Pmmn(59) space group with the TOPAS software using the fundamental parameters approach to describe the instrumental contribution [21].

Scanning electron microscopy images were obtained with a FEG-ESEM XL30 (FEI) with an accelerating voltage of 15 kV under a high vacuum.

Transmission electron microscopy images were acquired with W-TEM-JEOL and 80 keV. The particle size distribution was studied by laser granulometry. The particles were dispersed in water and analyzed on Malvern Mastersizer 2000 Hydro.

2.5. Electrochemical measurements

Swagelok type cells were assembled in ambient air to assess the electrochemical properties of the resulting composite V_2O_5/PDA/CNT electrode. The cell configuration includes zinc metal as anode, glass fiber (Whatman) as the separator, and 3 M $Zn(CF_3SO_3)_2$ solution as electrolyte. Cyclic voltammetry (CV) was conducted on Bio-Logic Science Instruments within the range of 0.2-1.6 V at a scanning rate of 0.5 mV s^{-1}. Galvanostatic charge and discharge tests were carried out at different constant current densities between 0.1 and 5 A g^{-1} using Neware BTS4000 Electrochemical Test System (China) within the same range. 10 cycles at 0.1 A g^{-1} have been performed before rate capability and long cycling tests.

Electrochemical impedance spectroscopy (EIS) experiments were performed in 3 electrodes Swagelok-type cells. Zinc was used both as counter and reference electrode. EIS tests were carried out at open circuit voltage in the frequency range from 100 kHz to 100 mHz with 5 mV amplitude on Bio-Logic Science Instruments. Aftermath software was used to assess equivalent circuit modeling. The equivalent circuit used to fit the data was $R_e((R_{CT}.Q)/Q)$ with R_e the electrolyte resistance, R_{CT} the charge transfer resistance and Q the constant phase element replacing the double layer capacity. The quality of the fit was confirmed by a chi-square (χ^2) factor. All electrochemical tests were conducted at room temperature.

3. Results and discussion

Herein, V_2O_5 particles were coated with polydopamine with a simple and energy-saving technique consisting of self-polymerization of dopamine in a tris buffer solution. The V_2O_5/PDA powder was recovered after centrifugation and drying processes. The PDA content depends on the stirring time, and the sample exhibiting the most optimal electrochemical performance is prepared after 2 h of self-polymerization (V_2O_5/PDA-b). According to J.K. Jeong *et al*, a higher PDA content results in a thicker coating and higher electrical resistance [15]. However, it is important to use appropriate ratio of polydopamine to encapsulate all the V_2O_5 particles. Therefore, 2 h of polymerization is considered ideal. This particular sample is further examined in detail in this work.

The infrared and X-ray photoelectron spectroscopy analyses were conducted to provide the evidence of dopamine polymerization. The FTIR-ATR spectra presented in Figure IV-2

confirm the formation of polydopamine in the V_2O_5/PDA powder. The bands at 828 and 1009 cm^{-1} are characteristic of V_2O_5 and can be attributed to the stretching mode of V-O-V and V=O bonds, respectively [22]. All peaks above 1100 cm^{-1} in the PDA and V_2O_5/PDA spectra can be assigned to the functional groups of polydopamine [23,24]. The small broad band in the region of 3680 to 2800 cm^{-1} corresponds to the stretching of the -OH group. The absorption at 1650 and 1600 cm^{-1} are, respectively, due to N-H and C=C deformation mode of polydopamine and other bands at 1500 cm^{-1}, 1300 cm^{-1}, and 1285 cm^{-1} to the stretching of N-H, C-N, and C-O. All these bands confirm the coating of polydopamine on V_2O_5 [17,19].

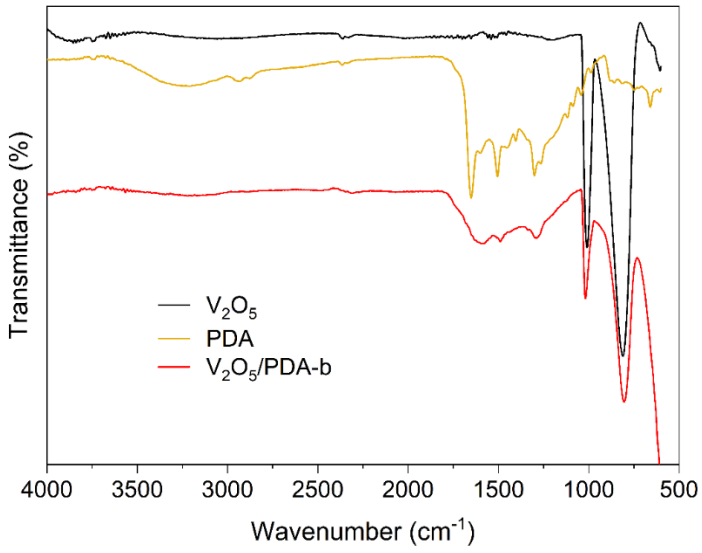

Figure IV-2: FTIR-ATR spectra of V_2O_5, polydopamine, and V_2O_5/PDA synthesized.

The PDA content in the V_2O_5/PDA powder is determined by thermogravimetric analysis in an inert atmosphere in comparison to the degradation of PDA alone (Figure IV-3). The major degradation corresponding to the decomposition of the PDA main chains was observed at ~350 °C [25]. The sample delivering the most optimal electrochemical performance is prepared after 2h of self-polymerization. The 7.7 % mass loss of V_2O_5/PDA-b proved that PDA was successfully polymerized and the PDA ratio is equal to 15.7 wt% in the modified V_2O_5.

The surface reactivity of V_2O_5 particles with PDA coating was also demonstrated by XPS analysis. To facilitate comparison, firstly, the XPS survey spectra for the V_2O_5 particles, the PDA, and the V_2O_5/PDA-b powders were acquired (Figure IV-4). The significant intensity increase of C 1s (at 285 eV) and N 1s (at 400 eV) peaks for the V_2O_5/PDA-b sample, evidences the formation of the polydopamine coating. However, the V 2p peak still can be detected, as on the V_2O_5 sample, which indicates that the coating forms a thin surface layer

on the vanadium oxide nanoparticles. In order to better understand the mechanism of reactivity of dopamine with V_2O_5 nanoparticles, high resolution spectra (O 1s & V 2p, C 1s and N 1s) were performed and they are shown in Figure IV-5.

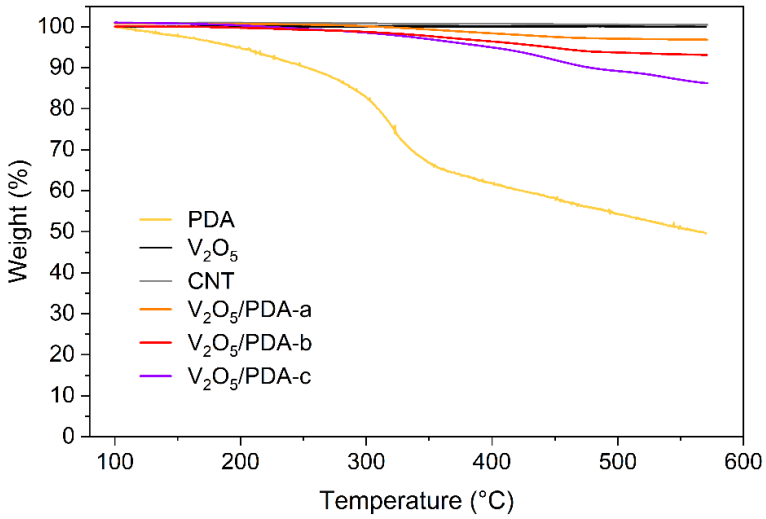

Figure IV-3: TGA curves of V_2O_5, PDA, V_2O_5/PDA-a, V_2O_5/PDA-b and V_2O_5/PDA-c powders recorded under inert atmosphere. No weight loss measured for V_2O_5 and CNT in these conditions. The weight loss of PDA, V_2O_5/PDA-a V_2O_5/PDA-b and V_2O_5/PDA-c is equal to 49%, 4%, 7.7% and 14.8% respectively.

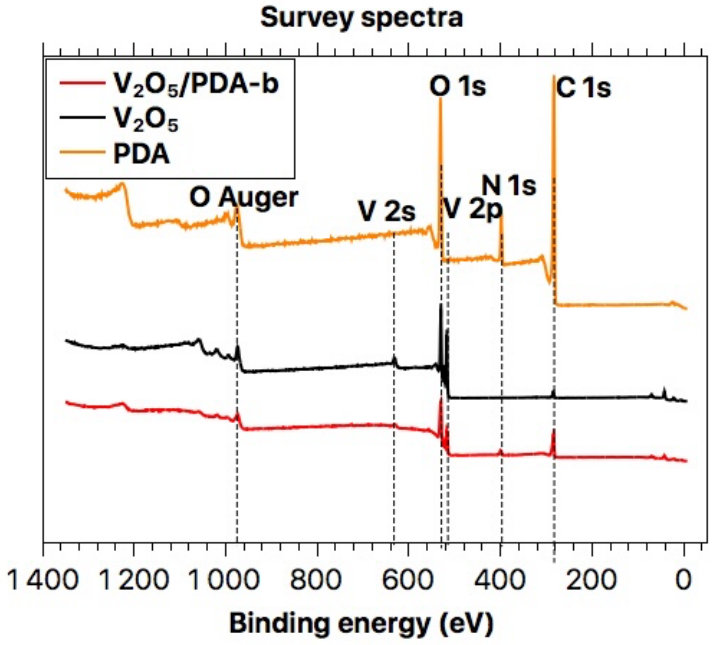

Figure IV-4: XPS survey spectra of V_2O_5/PDA-b, V_2O_5 and polydopamine (PDA).

The formation of a PDA coating on the surface of V_2O_5 particles leads to the reduction of V^{5+} to V^{4+} for the V_2O_5/PDA, as demonstrated in the V 2p core level in Figure IV-5a, indicating an interaction between the vanadium and polydopamine [26–28]. The reduction of vanadium oxide induced by PDA deposition is clearly observed on surface as a decrease of V $2p_{3/2}$ signal at 517.7 (± 0.2) eV corresponding to V^{5+} [29–32] from about 91 at. % (pristine V_2O_5 sample, Figure IV-5b) to 54 at. % (V_2O_5/PDA-b, Figure IV-5a). Additionally, there is an increase in the signal at a lower binding energy of 516.5 (± 0.2) eV, corresponding to V^{4+} [29–32] from 9 at. % (pristine V_2O_5 sample, Figure IV-5b) to 46 at. % (V_2O_5/PDA-b sample, Figure IV-5a). The pristine V_2O_5 sample, with the principal high intensity of V^{5+} at 517.7 (± 0.2) eV and O 1s at 530.4 (± 0.2) eV, corresponding to V_2O_5, is shown for comparison in Figure IV-5b. The stoichiometry of pristine V_2O_5 was also verified by calculating the O/V ratio, which is close to 2.5, confirming the presence of V_2O_5. The XPS results for the pristine V_2O_5 sample show also very low intensity signals for C-like contaminants and negligible traces of N, likely due to sample exposure to ambient air. The three components in the region of C 1 s peak can be assigned to C-C (hydrocarbons) at around 285 eV, C-O/C-N species at 286.6 (± 0.2) eV, and C=O at 288.8 (± 0.2) eV. The presence of C-O, C=O can be confirmed by the O 1s peak at a higher binding energy of 531.5 (± 0.2) eV, and C-N by the N 1s peak (Figure IV-5b) [30,32,33].

The C 1s core level region is significantly modified for V_2O_5/PDA-b (Figure IV-5a) in comparison to pristine V_2O_5 (Figure IV-5b). The V_2O_5 nanoparticles coated with PDA exhibit five components. The lowest binding energy peak at 284.4 (± 0.1) eV corresponds to the aromatic C, and the peak at 285 (± 0.1) eV to hydrocarbons that is always present at the extreme surface. The subsequent peaks at 286.0 (± 0.3) eV can be assigned to C –N, C – O, the peak at 287.6 (±0.3) to C=N / C-OH, and the one at 289 (±0.5) eV to C=O [34,35]. The presence of C-OH is further supported by the intense O 1s peak at 532.7 (± 0.3) eV in Figure IV-5c [35]. The peak at 531.3 (± 0.3) eV, attributed to C=O (Figure IV-5c), may result from minor contaminations or PDA decomposition. The pure polydopamine sample alone shows a very similar C signal profile with five components (Figure IV-5c). The presence of PDA coating on the surface of V_2O_5 particles is also confirmed from the analysis of N 1s core level (Figure IV-5a). Two contributions in the area of N 1 s peak can be assigned to aliphactic C-NH_2 at 401.6 (± 0.1) eV and to C-N=C at 400.0 (± 0.1) eV. Two nitrogen peaks are also observed in the case of PDA sample (Figure IV-5c); however, they exhibit much lower intensity in the higher binding energy peaks. These peaks, corresponding to the amino group

C-NH_2 (Figure IV-5a), are more pronounced for V_2O_5/PDA-b (Figure IV-5a) compared to pure PDA (Figure IV-5a), indicating increased reactivity between V_2O_5 and PDA.

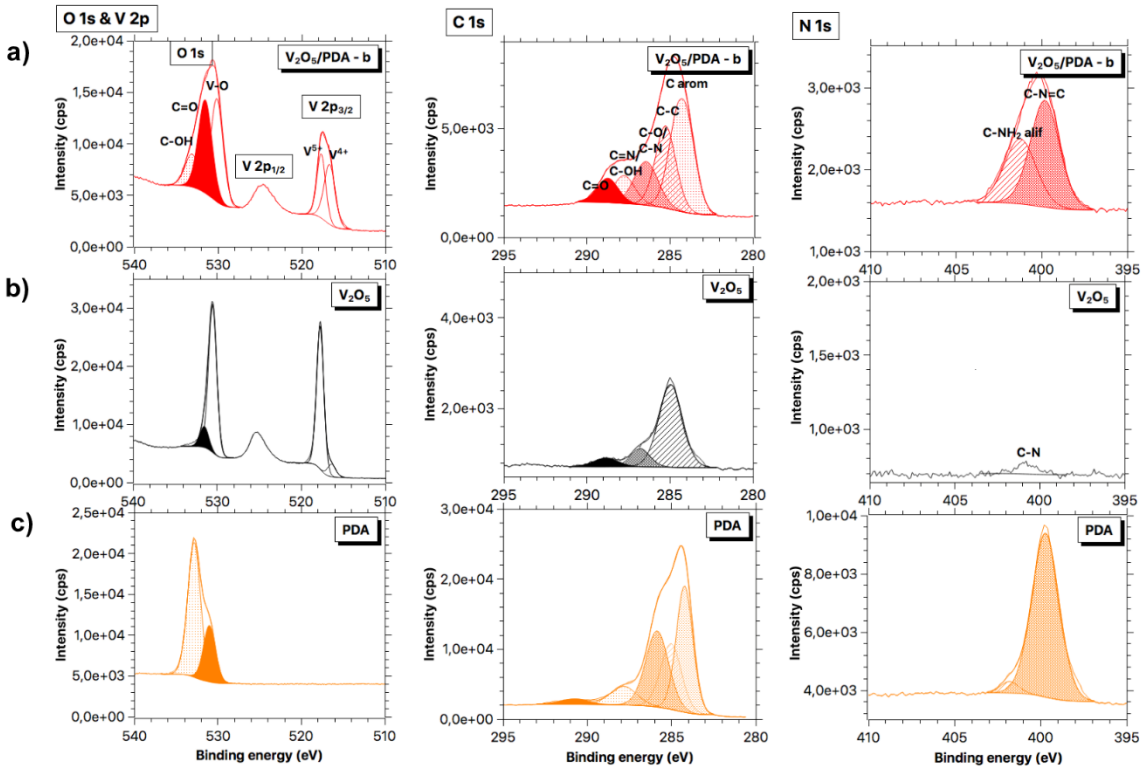

Figure IV-5: XPS high resolution spectra of O 1s & V 2p, C 1s and N 1s obtained for (a) V_2O_5/PDA-b, (b) V_2O_5 and (c) polydopamine (PDA).

The modified material, referred to as V_2O_5/PDA-b, is then homogenized with MWCNT to obtain a self-standing cathode with improved electronic conductivity that can be used as active cathode material in zinc-ion cells. The self-standing nature of the electrode is shown in Figure IV-1. As illustrated in Figure IV-6a, the self-polymerization of dopamine and the addition of MWCNT do not affect the orthorhombic phase of V_2O_5 with a space group of Pmmn(59) (JCPDS card 00-041-1426). The lattice parameters were determined by fitting the XRD patterns and presented in Table IV-1. The determined lattice parameters align with values reported in the literature [36]. The c value of 4.37 Å corresponds to the interlayer spacing between the (001) planes affirms the absence of water molecules between V_2O_5 layers [37]. It has been shown that this interlayer distance is recognized for enhancing the diffusion and transport of zinc ions during discharge and charge processes. The decreased

peak intensity can be attributed to the presence of MWCNT [6], and no impurity peak was detected.

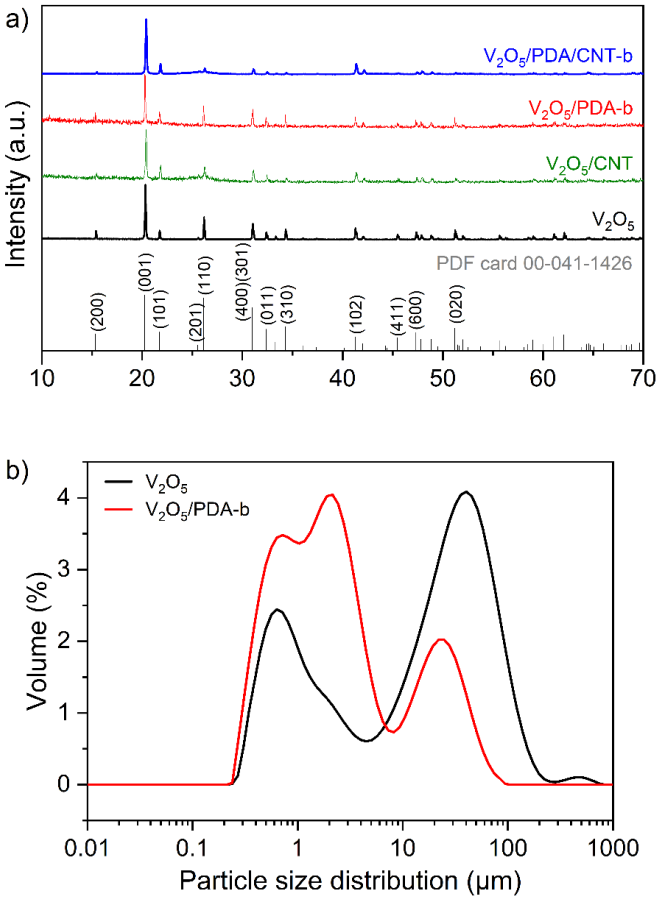

Figure IV-6: (a) X-ray diffraction patterns of V_2O_5 and V_2O_5/PDA-b materials, V_2O_5/CNT and V_2O_5/PDA/CNT-b electrodes. (b) Particle size distribution of the V_2O_5 and V_2O_5/PDA-b materials in water.

Table IV-1: Lattices parameters (with error bar) of V_2O_5, V_2O_5/PDA-b materials and V_2O_5/CNT, V_2O_5/PDA/CNT-b electrodes determined by fitting the XRD patterns.

	a (Å)	**b (Å)**	**c (Å)**
V_2O_5	11.5147(2)	3.5647(1)	4.3721(1)
V_2O_5/PDA-b	11.5132(7)	3.5650(2)	4.3713(3)
V_2O_5/CNT	11.5135(13)	3.5651(4)	4.3721(4)
V_2O_5/PDA/CNT-b	11.5112(17)	3.5650(6)	4.3735(3)

The SEM and TEM images are presented in Figure IV-7. It can be seen that the commercial primary particles are dense and exhibit irregular shapes, with particle size less than 1µm

(Figure IV-7b and e) but agglomerated into larger particles (Figure IV-7a). After coating with polydopamine, primary particles appear to be less sticky, and the aggregates are smaller than those in the commercial V_2O_5 (Figure IV-7c, d). Moreover, the TEM image in Figure IV-7f confirms that the V_2O_5 particles are well coated by PDA.

The particle size distribution has been evaluated by laser granulometry diffraction. As expected, the d(0.5) is much lower (2.1 µm) for V_2O_5/PDA-b compared to the commercial V_2O_5 (20.8 µm). It means that the primary particles are more isolated due to the PDA shell. Nevertheless, a broad particle size distribution is observed for both materials (Figure IV-6b).

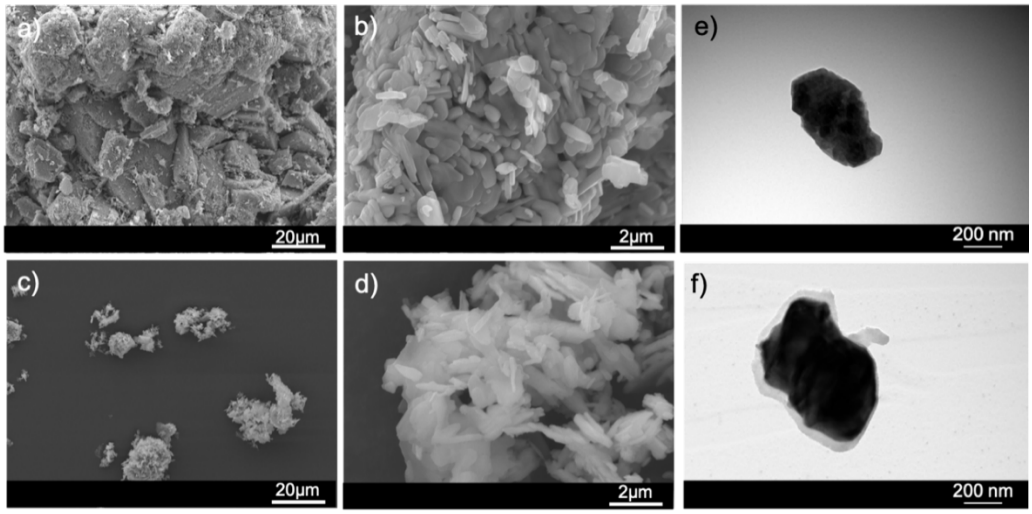

Figure IV-7: SEM images of (a, b) commercial V_2O_5 and (c, d) V_2O_5/PDA-b materials and their corresponding TEM images (e) and (f), respectively.

The SEM analysis of the V_2O_5/CB/PVDF composites reveals a homogeneous mixture, as observed in Figure IV-8a. Both V_2O_5 and V_2O_5/PDA were mixed with carbon nanotubes to create a flexible electrode and enhance electronic conductivity. SEM images (Figure IV-8b, c) of the self-standing electrodes, V_2O_5/CNT and V_2O_5/PDA/CNT-b, demonstrate the uniform dispersion of the active material within electrode.

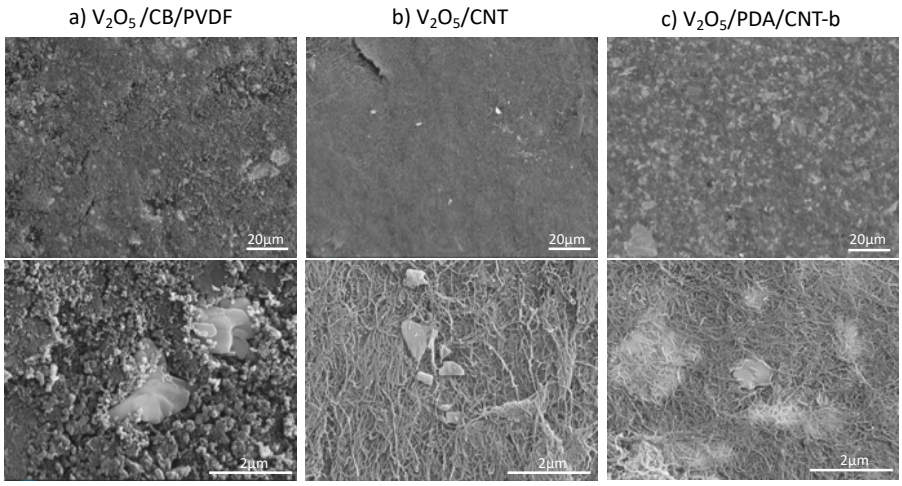

Figure IV-8: SEM images of electrodes: (a) V_2O_5 /CB/PVDF, (b) V_2O_5/CNT and (c) V_2O_5/PDA/CNT-b electrodes.

To evaluate the electrochemical performance of this novel composite material in rechargeable aqueous zinc-ion batteries, various tests have been conducted. First, cyclic voltammetry was carried out to evaluate the electrochemical behavior of V_2O_5/PDA/CNT-b as cathode material for zinc-ion batteries. As depicted in Figure IV-9, the CV profiles differ for the first, fifth, and tenth cycles. This result aligns with an activation process that has been previously reported in the literature [37–41]. The activation mechanism is associated with the introduction of water molecules into the V_2O_5 structure. This leads to an expansion of the interlayer distance, facilitating the insertion of Zn^{2+} ions into the V_2O_5 phase. The activation process of V_2O_5/PDA/CNT-b electrode is not as long as for V_2O_5 that requires more than 20 cycles. In a future, it would be interesting to investigate the reaction mechanism using in situ and *operando* characterization techniques such as: XRD, Raman and ex-situ XPS to provide additional insights and elucidate the actual storage mechanisms because no consensus has been reached so far [4]. After only ten cycles, two distinct cathodic (0.51/0.86 V) and anodic peaks (0.79/1.01 V) are detected for V_2O_5/PDA/CNT-b, suggesting a multistep (de)intercalation of Zn^{2+} into the V_2O_5 structure. These results are consistent with the two plateaus observed on the charge/discharge curves of V_2O_5/PDA/CNT-b, as shown in Figure IV-10c. Given that the shape of these last curves remains similar at different current densities and exhibits low polarization, it can be inferred that the Zn^{2+} diffusion kinetics are faster in V_2O_5/PDA/CNT-b electrode [7,41]. The enhanced ion diffusion can be attributed to the reduction of V^{5+} to V^{4+} in V_2O_5/PDA/CNT compared to V_2O_5 as shown by XPS (Figure IV-5) [42]. Indeed, as mentioned by M.S. Javed *et al.*, an active material with a mix of valence state of vanadium exhibits enhanced electrochemical activity, reduced polarization, and faster ion transport [43].

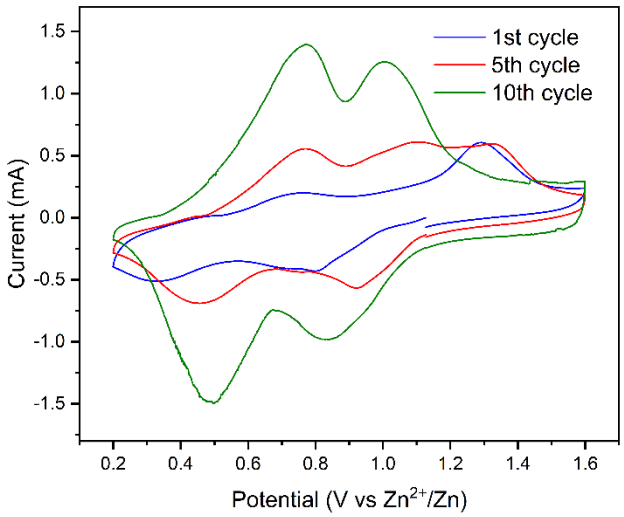

Figure IV-9: CV curves of V_2O_5/PDA/CNT-b electrode at 0.5 mV s^{-1}.

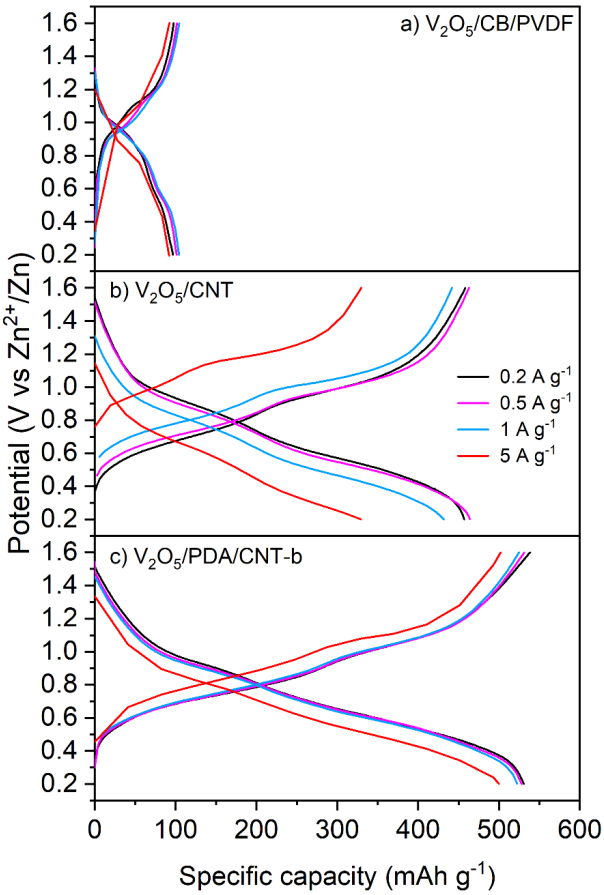

Figure IV-10: Galvanostatic Discharge/Charge profiles of (a) V_2O_5/CB/PVDF, (b) V_2O_5/CNT electrode and (c) V_2O_5/PDA/CNT-b electrode at 0.2, 0.5, 1 and 5 A g^{-1}.

Figure IV-11a displays the CV curves acquired for the Zn-V_2O_5/PDA/CNT cell at various scan rates aiming to obtain deeper insights into the reaction kinetics of the V_2O_5/PDA/CNT electrode. 20 cycles at 0.5mV s^{-1} as activation phase have been previously conducted on the cell. The capacitive and diffusive effect of the cathode material can be calculated by the following equation:

$$i = a\, v^b$$

Here, i represents the electric current, v denotes the scan rate and a and b are adjustable parameters. This relation can be rearranged as log (i) = b log (v) + log (a). Consequently, by fitting the plots of log (i) versus log (v), the b values can be determined by the slope of linear regression. A b value of 0.5 indicates that the reaction is dominated by a diffusion-controlled process while a value equal to 1 suggests a capacitive behavior. The prevalence of capacitive contribution to capacity has been well-documented for V_2O_5 materials in ZIBs [44]. The obtained results in the corresponding plots of log(i) versus log(v) (Figure IV-11b) show that the b values of the peaks 1-4 are 0.78, 0.73, 0.67, and 0.76 respectively suggesting that both diffusive and capacitive behaviors affect the charge storage of V_2O_5/PDA/CNT cathode material for ZIBs. However, the diffusive contribution is higher than in commercial V_2O_5 which indicates a favorable improvement in energy storage capacity [41].

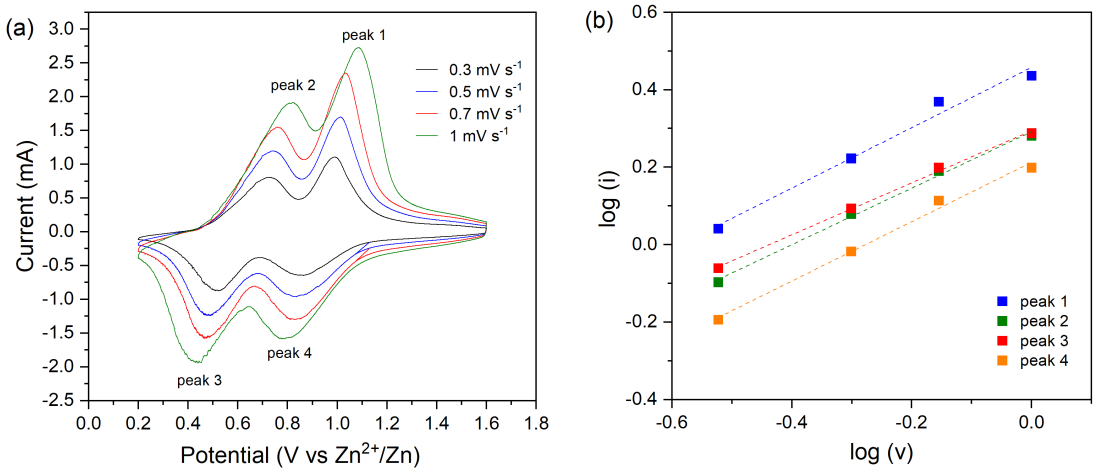

Figure IV-11: (a) CV curves of the V_2O_5/PDA/CNT electrode at different scan rates and (b) Corresponding plots of log(i) versus log(v) at cathodic and anodic peaks.

Secondly, we evaluated the specific capacity, cycling performance, and rate capability of V_2O_5/PDA/CNT-b electrode. As observed in Figure IV-12, the potential of anodic and

cathodic peaks of V_2O_5/PDA/CNT-b electrode do not correspond to those of polydopamine. The specific capacity is calculated based on the V_2O_5 active material mass.

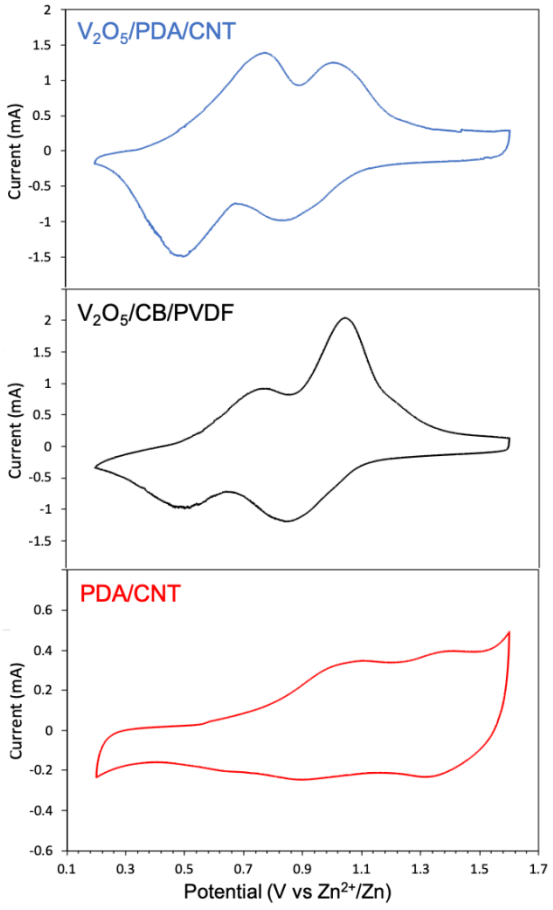

Figure IV-12: CV curves of V_2O_5/PDA/CNT-b, V_2O_5/CB/PVDF and PDA/CNT after activation at 0.5 mV s^{-1}.

Figure IV-13a shows a comparison of the cycling performance of V_2O_5/PDA/CNT-b to V_2O_5/CNT and V_2O_5/CB/PVDF at low current density (0.1 A g^{-1}). Low coulombic efficiencies are obtained for the first cycles, which can be attributed to the trapping of Zn^{2+} in the cathode material [37,45]. Consistent with the CV curves, the charge and discharge capacities increase over the first cycles which corresponds to an activation process, as discussed before, and/or to the formation of a stable solid electrolyte interface [7]. Nevertheless, the maximal discharge capacity of 530 mAh g^{-1} is achieved for V_2O_5/PDA/CNT-b after 15 cycles, which is considered the highest capacity compared with other self-standing electrodes or with V_2O_5 prepared with polymers reported in the literature as shown in Table IV-2. This improvement is firstly related to the improved electronic conductivity facilitated by CNT [39,46], and secondly, to the improved properties by PDA. The PDA disaggregates the V_2O_5 particles and leads to higher active surface area, enhances the

intimate binding between V_2O_5 and nanotubes [15] and improves the ionic conductivity of the electrode [14]. A self-standing CNT electrode was also prepared and cycled at 0.1 A g^{-1} to evaluate the contribution of CNT capacity. As shown in Figure IV-13a, the CNT electrode delivers a negligible capacity of 7 mAh g^{-1}.

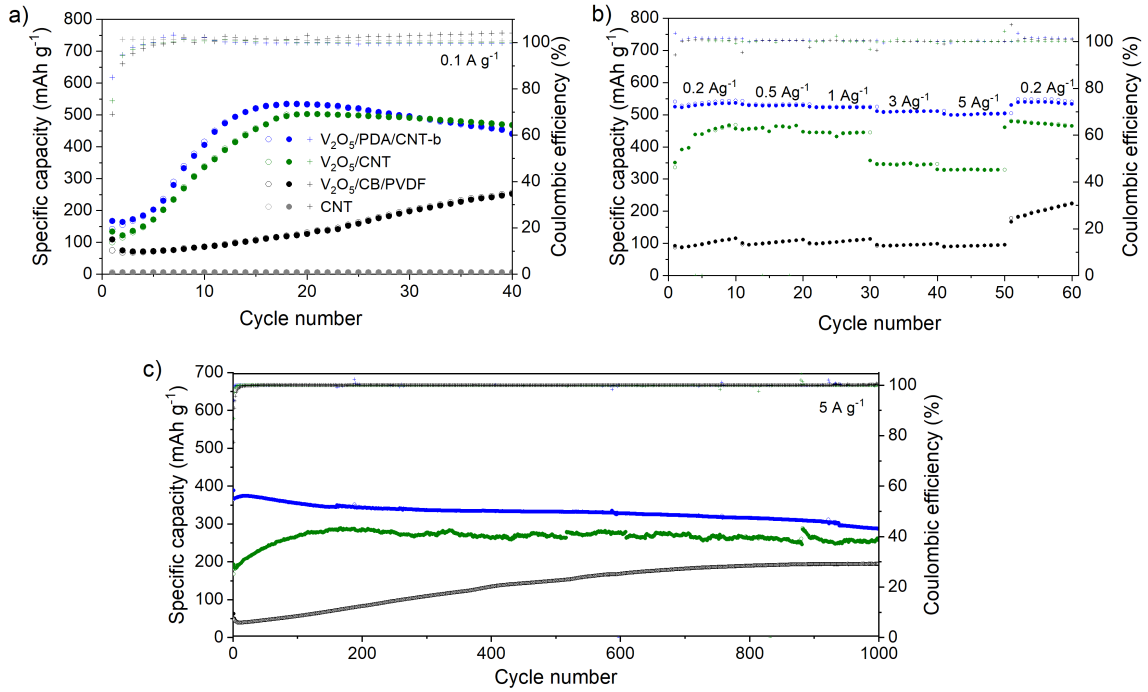

Figure IV-13: (a) Cycling performance at 0.1 A g^{-1}, (b) rate capability and (c) long cycling performance at 5 A g^{-1} of V_2O_5/CB/PVDF, V_2O_5/CNT and V_2O_5/PDA/CNT-b electrodes.

To complete a thorough study of this new composite material, a rate capability test was performed. The rate performance of coated V_2O_5 particles is remarkably high as illustrated in the Figure IV-13b. The charge/discharge curves obtained at different current densities for V_2O_5/CB/PVDF, V_2O_5/CNT and V_2O_5/PDA/CNT-b are represented in Figure IV-10a, b and c respectively. The discharge capacities of the V_2O_5/PDA/CNT-b are 530, 528, 523, 510, and 500 mAh g^{-1} at 0.2, 0.5, 1, 3, and 5 A g^{-1}, respectively, with an activation phase of ten cycles at 0.1 A g^{-1}. When the current density reverts to 0.2 A g^{-1}, the discharge capacity fully recovers, demonstrating excellent structural stability. Furthermore, even with a 25-fold increase in current density (from 0.2 A g^{-1} to 5 A g^{-1}), V_2O_5/PDA/CNT-b retains 94% of its capacity, in contrast to the 72% capacity retention observed for V_2O_5 without PDA coating (V_2O_5/CNT). This outcome validates the significant improvement in the rate performance of V_2O_5 achieved through the PDA coating because the same effect is observed for other PDA contents. V_2O_5/PDA/CNT-a and -c retain respectively 81 and 84% in the same conditions (Figure IV-14). This enhancement can be attributed to the presence of catechol

(C-OH) and amine (-NH_2) polar groups within the PDA, as observed by XPS, that facilitates excellent wetting and enhances the ionic conductivity of the electrode [12,14,15]. Like the carbon nanotubes network, the PDA coating layer can also act as a buffer for the volume changes experienced by the active material during electrochemical cycling [16,46,47]. Moreover, the improved electrochemical performance of V_2O_5/PDA/CNT-b compared to V_2O_5 may be due to the increased ratio of V^{4+}/V^{5+} as shown by XPS (Figure IV-5). The introduction of mixed valences of vanadium in electrode materials has a positive impact on the electrochemical performance [42].

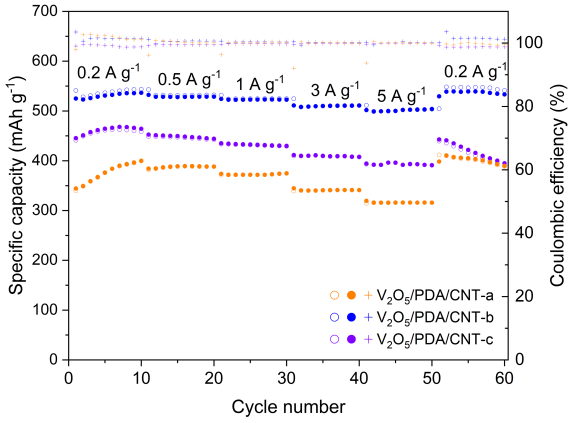

Figure IV-14: Rate capability of V_2O_5/PDA/CNT-a, V_2O_5/PDA/CNT-b, V_2O_5/PDA/CNT-c electrodes.

As depicted in Figure IV-15, the introduction of CNT is also beneficial for enhancing the rate capability, especially at high current density. Therefore, a combination of PDA coating and the introduction of CNT is a good strategy for enhancing the electrochemical performance of V_2O_5 in zinc-ion batteries.

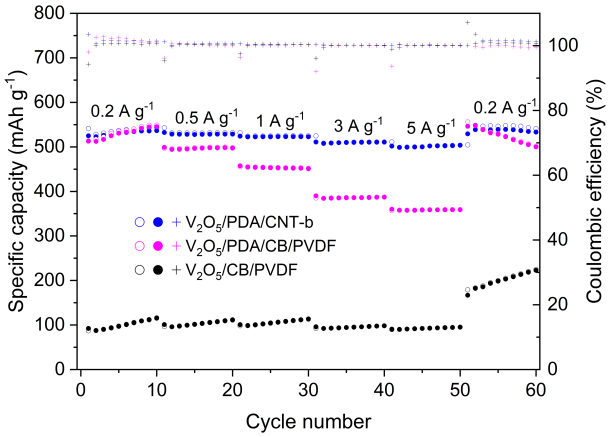

Figure IV-15: Rate capability of V_2O_5/PDA/CNT-b, V_2O_5/PDA/CB/PVDF, V_2O_5/CB/PVDF electrodes.

Table IV-2: State of the art of electrochemical performance of V_2O_5 with polymer coated or intercalated and self-standing electrodes.

Ref	Material	Morphology	Treatment	Electrolyte	Capacities ($mAh \cdot g^{-1}$) at - low current density - high current density	Cycles/ Retention (%)
[48]	V_2O_5@CNT	spheres	solvothermal	$ZnSO_4$ (3,65M)	268 (0.5 A g-1) 180 (5A g^{-1})	6000/ 72%
[49]	V_2O_5 nanofibers /CNT	nanopapers	dispersion - filtration	$ZnSO_4$ (2M)	375 (1 Ag-1) 219 (10 Ag^{-1})	500/ 80%
[50]	CNT@V2O5	nanopapers	Melting-filtration process	$Zn(CF_3SO_3)_2$ (3M)	356 (0.4 Ag^{-1}) 225 (2Ag^{-1})	500/ 80%
[51]	V_2O_5 nanobelts/CNT	films	hydrothermal	$Zn(CF_3SO_3)_2$ (3M)	380 (0.2 A g^{-1}) 290 (5A g^{-1})	1000/ 95%
[6]	V_2O_5@PANI	nano-composite 3D	Stirring	$Zn(CF_3SO_3)_2$ (3M)	361 (0.1 A g^{-1}) 200 (5 A g^{-1})	1000/ 94%
[5]	V_2O_5/PPy	nanowires	hydrothermal/ stirring	$Zn(CF_3SO_3)_2$ (3M)	466 (0.1 A g^{-1}) 174 (5 A g^{-1})	1000/ 95%
[7]	V_2O_5@PEDOT	nanosheets	Solvothermal/electrodeposition	$Zn(CF_3SO_3)_2$ (3M)	360 (0.1 A g^{-1}) 223 (5 A g^{-1})	1000/ 89%
[52]	V_2O_5/PANI	nanosheets	hydrothermal	$Zn(CF_3SO_3)_2$ (3M)	360 (0.1A g^{-1}) 270 (5 A g^{-1})	2000/ 90%
[53]	PPy/V2O5	foliated rocks	hydrothermal	$Zn(CF_3SO_3)_2$ (3M)	404 (0.2 A g^{-1}) 220 (10 A g^{-1})	2000/ 98%
[54]	PPy/$V_2O_5.nH_2O$	layered nanosheets	hydrothermal	$Zn(CF_3SO_3)_2$ (3M)	383 (0.1 A g^{-1})	2000/ 72%
[55]	V_2O_5@PEDOT	monolithic grains	stirring	$Zn(CF_3SO_3)_2$ (3M)	360 (1 A g^{-1}) 269(10 A g^{-1})	4500/ 77%
[56]	PEDOT- V_2O_5	nanobelts	liquid pathway	$Zn(CF_3SO_3)_2$ (3M)	449 (0.2 A g^{-1}) 325 (10 A g^{-1})	6000/ 94%
Our work	V_2O_5/PDA/CNT	sub-microparticles	stirring	$Zn(CF_3SO_3)_2$ (3M)	530 (0.1 A g^{-1}) 370 (5 A g^{-1})	1000/ 77%

To evaluate the material's stability during cycling, all three electrodes underwent testing at high current density (5 A g^{-1}) for a total of 1000 cycles. As shown in Figure IV-13c, V_2O_5/PDA/CNT-b once again exhibits superior performance, demonstrating a notable discharge capacity of 370 mAh g^{-1} and a good capacity retention of 77 % after 1000 cycles. The accelerated activation of the cathode observed in the initial cycles is associated with improved cycling stability at high current density [41]. The continuous increase of the capacity in commercial vanadium pentoxide is attributed to the gradual impregnation of electrolyte

into denser and more agglomerated V_2O_5 particles and can also be explained by a longer activation process [57]. The polydopamine coating acts as a protection layer by decreasing the formation of by-products and dissolution of V_2O_5 [7,14,15,19]. This result was confirmed by the colorless separator for V_2O_5/PDA/CNT after cycling contrary to V_2O_5/CNT (Figure IV-16). Moreover, the post mortem SEM analysis on V_2O_5/PDA/CNT electrode after cycling does not show any degradation of the electrode confirming the high stability of the V_2O_5/PDA/CNT material (Figure IV-17).

Figure IV-16: Separators after 40 cycles at 0.1 A g^{-1} of V_2O_5/CNT (left) and V_2O_5/PDA/CNT (right) electrodes.

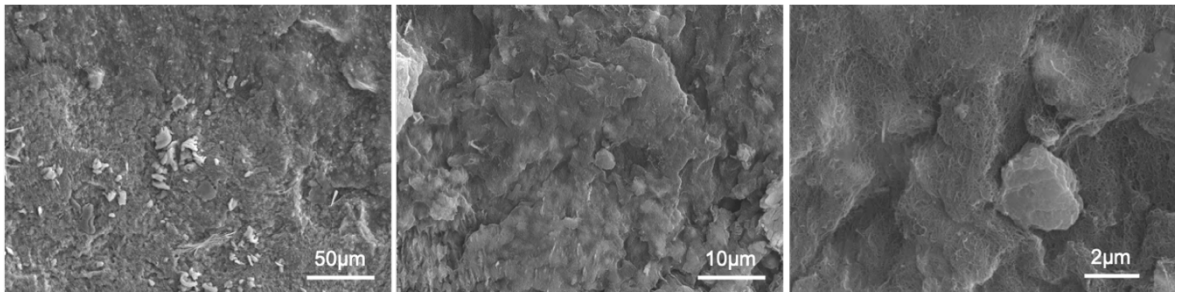

Figure IV-17: SEM images of V_2O_5/PDA/CNT electrode after long-term cycling at the end of charge at magnifications x1000, x5000, and x20000.

Figure IV-18 presents the Nyquist plots obtained for V_2O_5/CB/PVDF, V_2O_5/CNT and V_2O_5/PDA/CNT-b. The $R_e((R_{CT}.Q)/Q)$ equivalent circuit was used to fit the Nyquist plots in order to extract the resistance of the electrolyte and of the charge transfer presented in Figure IV-18b. The resistance of the electrolyte is low and similar for the three tested cells because the same aqueous electrolyte was used for the 3 electrodes. However, the charge transfer resistance is different for the three cells. Not surprisingly, V_2O_5/CB/PVDF exhibits the highest charge transfer resistance because the conductivity of carbon black is much lower than CNT [58,59]. Moreover, V_2O_5/PDA/CNT-b has the lowest charge transfer resistance which means that polydopamine has a slight positive effect on the enhancement of the electronic conductivity of the electrode. These results are in good agreement with the electrochemical performance obtained for the three electrodes.

a)

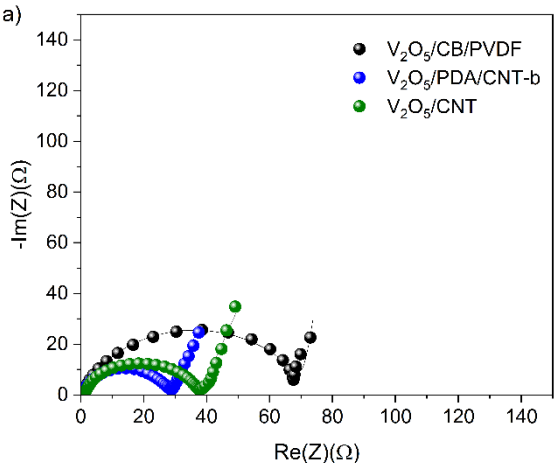

b)

Working electrode	R_e (Ω)	R_{CT}(Ω)
V_2O_5/CB/PVDF	0.42	71.1
V_2O_5/CNT	0.98	36.4
V_2O_5/PDA/CNT-b	0.43	27.8

Figure IV-18: (a) Impedance nyquist plot of V_2O_5/PDA/CB/PVDF, V_2O_5/CNT and V_2O_5/PDA/CNT-b at Open circuit voltage (Voc). (b) Calculated resistances using R_e ((R_{CT}.Q)/Q) equivalent circuit: the resistances of electrolyte (R_e) and charge transfer (R_{CT}) of V_2O_5/PDA/CB/PVDF, V_2O_5/CNT and V_2O_5/PDA/CNT-b.

4. Conclusion

V_2O_5/PDA/CNT composite cathode material was prepared to enhance the stability and the electrochemical performance of V_2O_5 active cathode material for rechargeable aqueous ZIBs. A polydopamine coating was applied to V_2O_5 particles through a self-polymerization process of dopamine. The V_2O_5/PDA material was characterized by SEM, TEM, TGA, FTIR-ATR and XPS. These analyses revealed that the V^{5+} was partially reduced to V^{4+} after the polymerization process, and that the polydopamine formed a thin layer around vanadium oxide microparticles. Combining V_2O_5/PDA with CNT allowed us to obtain a self-standing, binder-free cathode material with a high capacity of ~530 mAh g^{-1} at 0.1 A g^{-1}. The entangled CNT between the V_2O_5/PDA particles served as an excellent electron-conducting network. The PDA coating acted as a protective layer to diminish the formation of by-products and prevent structural deterioration. As a result, the electrochemical performances of V_2O_5/PDA/CNT-b surpassed that of V_2O_5/CNT and V_2O_5/CB/PVDF across a wide range of current densities. The V_2O_5/PDA/CNT-b electrode demonstrated impressive rate capability, delivering specific capacities of 530, 528, 523, 510, and 500 mAh g^{-1} at 0.2, 0.5, 1, 3, and 5 A g^{-1}, respectively, while also maintaining exceptional long-term cycle stability up to 1000 cycles at high current density. The combination of PDA coating with the incorporation of carbon nanotubes appears to be a good strategy for improving the electrochemical performance and stability of V_2O_5 for zinc-ion batteries.

5. References

1 A. Konarov, N. Voronina, J. H. Jo, Z. Bakenov, Y. K. Sun and S. T. Myung, *ACS Energy Lett*, 2018, **3**, 2620–2640.

2 Y. Zhang, A. Chen and J. Sun, *Journal of Energy Chemistry*, 2021, **54**, 655–667.

3 J. Ming, J. Guo, C. Xia, W. Wang and H. N. Alshareef, *Materials Science and Engineering R: Reports*, 2019, **135**, 58–84.

4 Y. Ding, L. Zhang, X. Wang, L. Han, W. Zhang and C. Guo, *Chinese Chemical Letters*, 2023, **34**, 107399.

5 X. Qin, X. Wang, J. Sun, Q. Lu, A. Omar and D. Mikhailova, *Front Energy Res,* 2020, **8**, 1–6.

6 Y. Du, X. Wang, J. Man and J. Sun, *Mater Lett*, 2020, **272**, 127813.

7 D. Xu, H. Wang, F. Li, Z. Guan, R. Wang, B. He, Y. Gong and X. Hu, *Adv Mater Interfaces*, 2019, **6**, 1–8.

8 E. G. Tolstopyatova, M. A. Kamenskii and V. V. Kondratiev, *Energies (Basel),* 2022, **15**, 8966.

9 L. Zhang, X. Qin, L. Wang, Z. Zhao, L. Mi and Q. Lu, *Front Chem Sci Eng*, 2023, **17**, 1244–1253.

10 Y. Liu and Y. Gong, *Nanoscale*, 2023, **15**, 6273–6284.

11 X. Chen, Q. Kong, X. Wu, X. An, J. Zhang, Q. Wang and W. Yao, *Chemical Engineering Journal*, 2023, **451**, 138765.

12 X. Yue, H. Liu and P. Liu, *Chemical Communications*, 2019, **55**, 1647–1650.

13 A. Abdelhafid, C. Jérôme, F. Boschini and A. Mahmoud, *Batter Supercaps*, 2020, 1–7.

14 H. Yue, T. Du, Q. Wang, Z. Shi, H. Dong, Z. Cao, Y. Qiao, Y. Yin, R. Xing and S. Yang, *ACS Omega*, 2018, **3**, 2699–2705.

15 Y. K. Jeong, S. H. Park and J. W. Choi, ACS *Appl Mater Interfaces*, 2018, **10**, 7562–7573.

16 Y. Deng, H. Xu, Z. Bai, B. Huang, J. Su and G. Chen, *J Power Sources*, 2015, **300**, 386–394.

17 Y. Bie, J. Yang, X. Liu, J. Wang, Y. Nuli and W. Lu, *ACS Appl Mater Interfaces*, 2016, **8**, 2899–2904.

18 B. Jiang, Y. He, B. Li, S. Zhao, S. Wang, Y. B. He and Z. Lin, *Angewandte Chemie - International Edition*, 2017, **56**, 1869–1872.

19 W. Liu, X. Yuan and X. Yu, *Nanoscale*, 2018, **10**, 16675–16682.

20 L. L. Zhang, D. Ma, T. Li, J. Liu, X. K. Ding, Y. H. Huang and X. L. Yang, ACS *Appl Mater Interfaces*, 2018, 10, 36851–36859.

21 R. W. Cheary and A. Coelho, *J Appl Crystallogr*, 1992, **25**, 109–121.

22 I. L. Botto, M. B. Vassallo, E. J. Baran and G. Minelli, *Mater Chem Phys*, 1997, **50**, 267–270.

23 J. Kong, W. A. Yee, L. Yang, Y. Wei, S. Lei Phua, H. Guan Ong, J. Ming Ang, X. Li and X. Lu, *Chemical Communications*, 2012, **48**, 10316–10318.

24 D. R. Dreyer, D. J. Miller, B. D. Freeman, D. R. Paul and C. W. Bielawski, *Langmuir*, 2012, **28**, 6428–6435.

25 Y. Liu, Y. Fang, J. Qian, Z. Liu, B. Yang and X. Wang*, RSC Adv*, 2015, **5,** 107652–107661.

26 R. Luo, L. Tang, J. Wang, Y. Zhao, Q. Tu, Y. Weng, R. Shen and N. Huang, *Colloids Surf B Biointerfaces*, 2013, **106**, 66–73.

27 W. He, B. Tao, Z. Yang, G. Yang, X. Guo, P. J. Liu and Q. L. Yan, *Chemical Engineering Journal*, 2019, **369,** 1093–1101.

28 X. Guo, H. Xu, X. Ma, S. Yang, T. Liu, Y. Nie, C. Wang, C. Wang and X. Jiang, *Vacuum*, 2022, **196**, 110776.

29 R. Lindström, V. Maurice, S. Zanna, L. Klein, H. Groult, L. Perrigaud, C. Cohen and P. Marcus, *Surface and Interface Analysis*, 2006, **38**, 6–18.

30 L. Santos, J. Światowska, V. Lair, S. Zanna, A. Seyeux, A. Melendez-Ceballos, P. Tran-Van, M. Cassir and P. Marcus, *J Power Sources,* 2017, **364**, 61–71.

31 J. Światowska-Mrowiecka, F. Martin, V. Maurice, S. Zanna, L. Klein, J. Castle and P. Marcus, *Electrochim Acta,* 2008, **53**, 4257–4266.

32 J. Światowska-Mrowiecka, V. Maurice, S. Zanna, L. Klein and P. Marcus, *Electrochim Acta*, 2007, **52**, 5644–5653.

33 Beamson G and Briggs D., *The Scienta ESCA 300 Database, John Wiley & Sons.*

34 J. Ederer, P. Janoš, P. Ecorchard, J. Tolasz, V. Štengl, H. Beneš, M. Perchacz and O. Pop-Georgievski, *RSC Adv*, 2017, **7**, 12464–12473.

35 S. Suárez-García, J. Sedó, J. Saiz-Poseu and D. Ruiz-Molina, *Biomimetics*, 2017, **2**, 22.

36 C. Q. Feng, S. Y. Wang, R. Zeng, Z. P. Guo, K. Konstantinov and H. K. Liu, *J Power Sources*, 2008, **184,** 485–488.

37 R. Li, H. Zhang, Q. Zheng and X. Li, *J Mater Chem A Mater*, 2020, **8**, 5186–5193.

38 H. Qin, L. Chen, L. Wang, X. Chen and Z. Yang, *Electrochim Acta*, 2019, **306**, 307–316.

39 P. Hu, T. Zhu, J. Ma, C. Cai, G. Hu, X. Wang, Z. Liu, L. Zhou and L. Mai, *Chemical Communications*, 2019, **55**, 8486–8489.

40 S. Mallick and C. R. Raj, *ChemSusChem*, 2021, **14,** 1987–2022.

41 N. Zhang, Y. Dong, M. Jia, X. Bian, Y. Wang, M. Qiu, J. Xu, Y. Liu, L. Jiao and F. Cheng, *ACS Energy Lett*, 2018, **3**, 1366–1372.

42 F. Liu, Z. Chen, G. Fang, Z. Wang, Y. Cai, B. Tang, J. Zhou and S. Liang, *Nanomicro Lett*, 2019, **11**, 1–11.

43 M. S. Javed, H. Lei, Z. Wang, B. tian Liu, X. Cai and W. Mai*, Nano Energy*, 2020, **70**, 104573.

44 L. Wang, K. W. Huang, J. Chen and J. Zheng, *Sci Adv*, 2019, **5**, 1–11.

45 X. Chen, L. Wang, H. Li, F. Cheng and J. Chen, *Journal of Energy Chemistry*, 2019, **38**, 20–25.

46 G. Xu, X. Liu, S. Huang, L. Li, X. Wei, J. Cao, L. Yang and P. K. Chu, *ACS Appl Mater Interfaces*, 2020, **12**, 706–716.

47 U. Ahuja, B. Wang, P. Hu, J. Rethore and K. E. Aifantis, *Electrochim Acta,* 2021, **392**, 138993.

48 H. Chen, H. Qin, L. Chen, J. Wu and Z. Yang, *J Alloys Compd,* 2020, **842**, 155912.

49 Y. Li, Z. Huang, P. K. Kalambate, Y. Zhong, Z. Huang, M. Xie, Y. Shen and Y. Huang, *Nano Energy*, 2019, **60**, 752–759.

50 X. Wang, L. Wang, B. Zhang, J. Feng, J. Zhang, X. Ou, F. Hou and J. Liang, *Journal of Energy Chemistry*, 2021, **59**, 126–133.

51 Y. Wang, X. Liu, G. Xu, Y. Liang, W. Ni, B. Wu and L. Yang, *Ionics (Kiel)*, 2022, **28**, 4709–4718.

52 S. Chen, K. Li, K. S. Hui and J. Zhang, *Adv Funct Mater*, 2020, **30**, 202003890.

53 W. Wang, D. He, Y. Fang, S. Wang, Z. Zhang, R. Zhao and W. Xue, *Electrochim Acta*, 2022, **416**, 140270.

54 Z. Feng, J. Sun, Y. Liu, H. Jiang, T. Hu, M. Cui, F. Tian, C. Meng and Y. Zhang, *J Power Sources*, 2022, **536**, 231489.

55 Z. Yao, Q. Wu, K. Chen, J. Liu and C. Li, *Energy Environ Sci*, 2020, **13**, 3149–3163.

56 Y. Du, X. Wang and J. Sun, *Nano Res*, 2021, **14**, 754–761.

57 E. Roex, F. Boschini, V. Delaval, A. Schrijnemakers, R. Cloots and A. Mahmoud, *Journal of Electroanalytical Chemistry*, 2023, **929**, 117133.

58 Y. Ma, Int *J Electrochem Sci*, 2020, **15**, 10315–10329.

59 D. Pantea, H. Darmstadt, S. Kaliaguine and C. Roy, *Appl Surf Sci*, 2003, **217**, 181–193.

Chapter V: Synthesis of three sodium vanadium oxides as cathode materials for zinc-ion batteries

The layered structure of the common V_2O_5 cathode material may collapse after numerous cycles due to the voluminous hydrated zinc ions and water molecules being inserted and extracted during the cycling process in rechargeable aqueous zinc-ion batteries. In this chapter, Na^+ ions are introduced into V_2O_5 to stabilize its structure. We report the synthesis of pure β-$Na_{0.33}V_2O_5$, featuring a tunnel structure, and pure $Na_{1.16}V_3O_8$ which has a layered structure, via an aqueous route involving stirring V_2O_5 powder in an aqueous NaCl solution, followed by heat treatment. The successful synthesis of the pure β-$Na_{0.33}V_2O_5$ phase through this process represents a novel achievement, not previously reported in the literature. The formation of β-$Na_{0.33}V_2O_5$ and $Na_{1.16}V_3O_8$ phases is elucidated by HTXRD.

Then, three samples of pure $Na_2V_6O_{16}\cdot 1.5H_2O$, β-$Na_{0.33}V_2O_5$ and $Na_{1.16}V_3O_8$ synthesized are compared in terms of morphology, specific surface area, and electrochemical performance as cathode materials in zinc-ion batteries. The tunnel structure of β-$Na_{0.33}V_2O_5$ demonstrates remarkable stability and maintains a consistent discharge capacity of about 265 mAh g^{-1} at 0.1 A g^{-1} but does not allow easy insertion of zinc ions at high current density. Conversely, the layered structure of $Na_2V_6O_{16}\cdot 1.5H_2O$ and $Na_{1.16}V_3O_8$ phases facilitates zinc ions insertion into the structure thereby playing a pivotal role in their electrochemical properties. Among them, the hydrated NVO material exhibits the highest specific capacity and displays superior stability during cycling attributed to sodium ions and water serving as stabilizing pillars for the structure.

Keywords: sodium vanadium oxides, barnesite, tunnel-like structure, layered-like structure, aqueous synthesis, nanobelts, aqueous zinc-ion batteries

M. Larry, **E. Roex**, A. Mahmoud, F. Boschini and B. Vertruyen, "Aqueous synthesis of three sodium vanadium oxides as cathode materials for aqueous zinc-ion batteries", 2024 (under preparation)

1. Introduction

The most promising cathode materials for ZIBs reported in the literature are vanadium and manganese oxides. Among these materials, vanadium pentoxide (V_2O_5) yields the most convincing capacities [1]. Unfortunately, as discussed in chapter III, V_2O_5 passes through an activation phase before reaching stable capacities. Furthermore, vanadium oxide material sometimes experiences stability problems during the electrochemical cycling, especially at high current density. This crash is often explained in literature by a collapse of the layered, crystallographic structure of V_2O_5 (Figure V-1) due to the voluminous zinc ions that are inserted into and extracted from the dense cathode material during cycling [2].

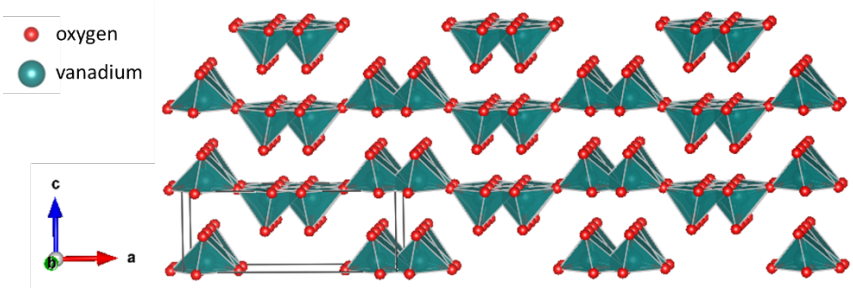

Figure V-1: Crystallographic structure of V_2O_5 drawn with Vesta [3] using lattice parameters and atomic positions from PDF 00-041-1426.

An approach to prevent this structural degradation consists in stabilizing the crystallographic structure of the material by inserting elements acting as pillars to expand the interlayer spacing and facilitate the insertion/extraction of Zn^{2+} [2]. In the case of V_2O_5, the spacing of the crystallographic framework could be achieved by inserting ions between the vanadium oxide layers, forming a metallic vanadate of the form $M_xV_{2+m}O_{5+n}$. The theoretical capacity will always be sacrificed at the cost of stability using this strategy compared to V_2O_5 [4]. However, since Nazar's group developed $Zn_{0.25}V_2O_5.nH_2O$ as a cathode material with a relatively high energy density and good cycling stability [5], a series of compounds have been tested by insertion of water molecules [6] and/or metal ions such as Na^+ [7,8], Ca^{2+} [9], K^+ [10], or Mg^{2+} [11], into the structure of V_2O_5. More spaced layered or tunnel structures can be obtained by this process. Examples are given in Figure V-2a and Figure V-2b with tunnel structure β-$Na_{0.33}V_2O_5$ and layered structure $Na_{1.16}V_3O_8$ respectively.

Because of the promising electrochemical results of vanadates and the convincing availability of sodium, more focus was put on the use of sodium vanadium oxides (NVO) as cathode material in ZIBs. The sodium vanadate family spans a broad range of compositions,

including anhydrous or hydrated crystalline phases as well as nanocrystalline or amorphous hydrated materials, reported in Table V-1.

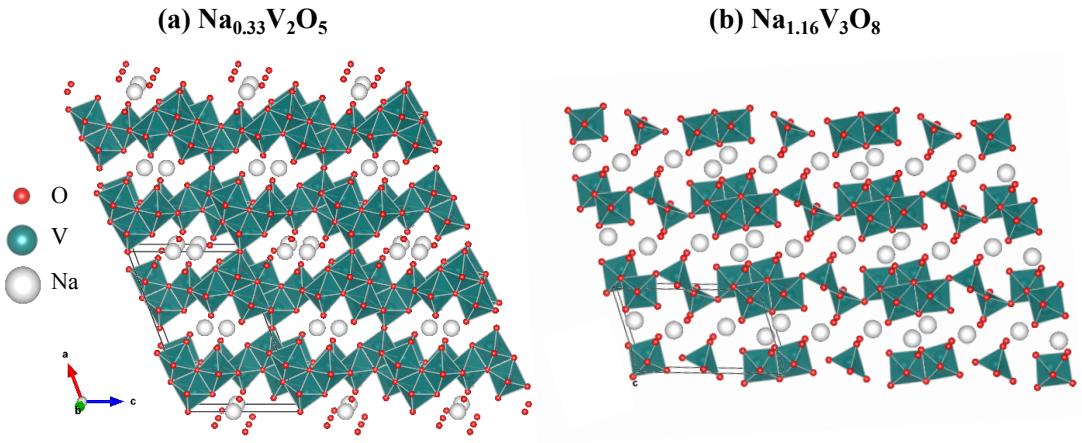

Figure V-2: (a) Tunnel structure of β-$Na_{0.33}V_2O_5$ and (b) layered structure of $Na_{1.16}V_3O_8$ drawn with Vesta [3] using lattice parameters and atomic positions from PDF 01-084-8341 and PDF 04-025-2006 respectively.

Table V-1: State of the art of sodium vanadium oxides materials used as cathode materials in zinc-ion batteries (adapted from [12]).

Material	Morphology	Treatment	Capacity (mAh g^{-1})	Current density (A g^{-1})	Cycles (high rates)	Retention	Ref
$Na_{0.33}V_2O_5$	Nanowires	Hydrothermal	367.1	0.1	1000	93%	[13]
$Na_{0.56}V_2O_5$	Nanobelts	Hydrothermal	417	0.05	1000	84%	[14]
$Na_{1.1}V_3O_{7.9}$	Nanoribbons	Hydrothermal	191	0.05	500	93%	[15]
$Na_{1.25}V_3O_8$	Nanowires	Sol-gel + annealing	156	0.1	100	85%	[16]
NaV_6O_{15}/V_2O_5	Skin-core nanowires	Hydrothermal	390	0.3	3000	92.3	[17]
$NaV_3O_8{\cdot}1.5\ H_2O$	Nanobelts	Liquid-solid stirring	380	0.05	1000	82%	[18]
$NaV_3O_8{\cdot}1.35H_2O$	Nanobelts	Liquid-solid stirring	366	0.1	200	97%	[10]
$NaV_8O_{20}{\cdot}2.89H_2O$	Nanowires	Hydrothermal	417.5	0.2	6000	96%	[19]
$Na_2V_6O_{16}{\cdot}2H_2O$	Thin slabs	Sol-gel	312	0.1	100	50%	[16]
$Na_2V_6O_{16}{\cdot}1.63H_2O$	Nanowires	Hydrothermal	352	0.05	6000	90%	[20]
$Na_2V_6O_{16}{\cdot}3\ H_2O$	Nanorods	Stirring + microwave	361	0.1	1000	85%	[21]

As observed in the previous table, aqueous solution routes are frequently used for the synthesis of these compounds, using a hydrothermal treatment or a heat treatment to promote crystallization. As we started from the premise that the synthesis method should not be complicated and as eco-friendly as possible, we focus on an aqueous route without hydrothermal treatment. Compared to other procedures, this process consumes less energy and does not require toxic or dangerous solvents. The reaction between the reagents can be performed in distilled water and no heating is required to obtain the hydrated phase. Generally, aqueous syntheses are readily put into practice and can effortlessly be adapted to a safe and ecological chemistry. Different authors used V_2O_5 and NaCl as precursors for their aqueous route and obtain different phases: V_2O_5 [22–24], $NaV_3O_8{\cdot}1.35H_2O$ [10], $NaV_3O_8{\cdot}1.5H_2O$ [18], $NaV_3O_8{\cdot}1.69H_2O$ [25]. Intriguingly, Rui *et al.* [24] and Wan *et al.*[18] respectively reported V_2O_5 nanobelts and $NaV_3O_8{\cdot}1.5H_2O$ nanobelts after stirring V_2O_5 in 2 mol/L NaCl solution for 3 or 4 days, using the same Na/V ratio.

Consequently, in this chapter, we first discuss the origin of the repeatability issues associated with this synthesis. Then, the crystallization of precursors of different compositions into mixtures or pure phases of V_2O_5, β-$Na_{0.33}V_2O_5$ and $Na_{1+x}V_3O_8$ phases is clarified by high temperature X-ray diffraction (HTXRD). It is shown that it is possible to selectively synthesize purely β-$Na_{0.33}V_2O_5$, a tunnel structure (Figure V-2a), or $Na_{1.16}V_3O_8$, a layered structure (Figure V-2b), phase through aqueous route. The synthesis of the pure β-$Na_{0.33}V_2O_5$ phase by aqueous route without hydrothermal treatment is an achievement that has, to our knowledge, never been reported in the literature before. The characterization of the $Na_{0.33}V_2O_5$ phase through XRD, SEM and BET gave an insight into the crystallographic structure, its nanobelt structure and its specific surface area. Finally, the electrochemical performance of the as-obtained $Na_{0.33}V_2O_5$ is evaluated as a positive electrode material in Zn-ion batteries and compared to the performance of the hydrated phase $Na_2V_6O_{16}{\cdot}1.5H_2O$, and to $Na_{1.16}V_3O_8$ that was synthesized as a pure phase in the same way.

2. Experimental part

2.1. Materials and chemicals

V_2O_5 (98 %), NaCl (99 %) and $Zn(CF_3SO_3)_2$ (98 %) were purchased from Sigma Aldrich. Carbon black (99.9 % purity) and polyvinylidene fluoride (PVDF) were purchased from Alfa Aesar. A 0.1 mm thick zinc foil was purchased from Goodfellow.

2.2. Aqueous synthesis of $Na_2V_6O_{16}·1.5H_2O$, β-$Na_{0.33}V_2O_5$ and $Na_{1.16}V_3O_8$

NVO powders were prepared by stirring V_2O_5 powder in an aqueous NaCl solution, followed by heat treatment of the lyophilized precursors. In each experiment, the appropriate amount of NaCl to reach the target NaCl concentration (see Table V-2) was dissolved in 30 mL of deionized water before adding 2 g V_2O_5 and stirring the suspension with a magnetic bar for 2 days at room temperature. The red precipitates were separated by centrifugation, washed with deionized water (3 dispersion/centrifugation cycles) and freeze-dried for 24 hours with an Alpha 2-4 LSC basic freeze-dryer from Martin Christ gmbh.

Samples from the as-obtained powders were heated in air at 500°C either in a muffle furnace with a 150°C/h heating ramp or in the HTK1200N Anton Paar chamber of the X-ray diffractometer with a 120°C/h heating ramp.

Table V-2: Labels of the NVO powders, synthesis conditions, and crystalline phases observed in X-ray diffractograms (● V_2O_5; ■ β-$Na_{0.33}V_2O_5$; ◆ $Na_{1.16}V_3O_8$; "◆" $Na_{1+x}V_3O_8$).

Label	V_2O_5 mass loading	NaCl molar concentration	Stirring	Phases in uncalcined powder	Phases in calcined powder
A	67 g/L	0.21 M	2 days	V_2O_5, (NVO)	■ ●
B	67 g/L	0.37 M	2 days	V_2O_5, NVO	■ "◆"
C	67 g/L	0.73 M	2 days	V_2O_5, NVO	■
D	67 g/L	2 M	2 days	NVO, (V_2O_5), NaCl	"◆" ■
E	67 g/L	2 M	2 days	NVO, V_2O_5, NaCl	◆
F	67 g/L	2 M	2 days	NVO	"◆" (■)

2.3. Structural and morphological characterization

Room temperature X-ray diffractograms were collected in a Bruker D8 Twin-twin diffractometer (Bragg-Brentano geometry, Cu Kα radiation, Lynxeye XET 1D detector, 2θ = 5-80°, 0.02° step size and 0.1 s/channel step time). In situ high-temperature diffractograms were collected on powder samples packed in 0.4 mm deep alumina holders placed in the

HTK1200N Anton Paar chamber (Figure V-3). 5 min scans (2θ = 8-17° or 2θ = 25-34°, 0.02° step size) were collected continuously during the heating and the beginning of the dwell times. 20 min scans (2θ = 6-70°, 0.02° step size) were collected before the experiment, at the end of the dwell time, and after the experiment. The Bruker Topas software was used to extract peak positions and intensities by peak fitting or to refine the cell parameters and phase percentages by Rietveld refinement, using atomic positions taken from the PDF4+ database of the International Center for Diffraction Data (PDF 01-084-8341 for β-$Na_{0.33}V_2O_5$; PDF 04-025-2006 for $Na_{1.16}V_3O_8$ and PDF 00-041-1426 for V_2O_5). The room temperature cell parameters were refined on the ex-situ datasets to minimize the sample displacement error, while the phase percentages were estimated on in situ datasets because they were less affected by preferential orientation effects. In all cases, the fundamental parameters approach was used to model the instrumental contribution [26].

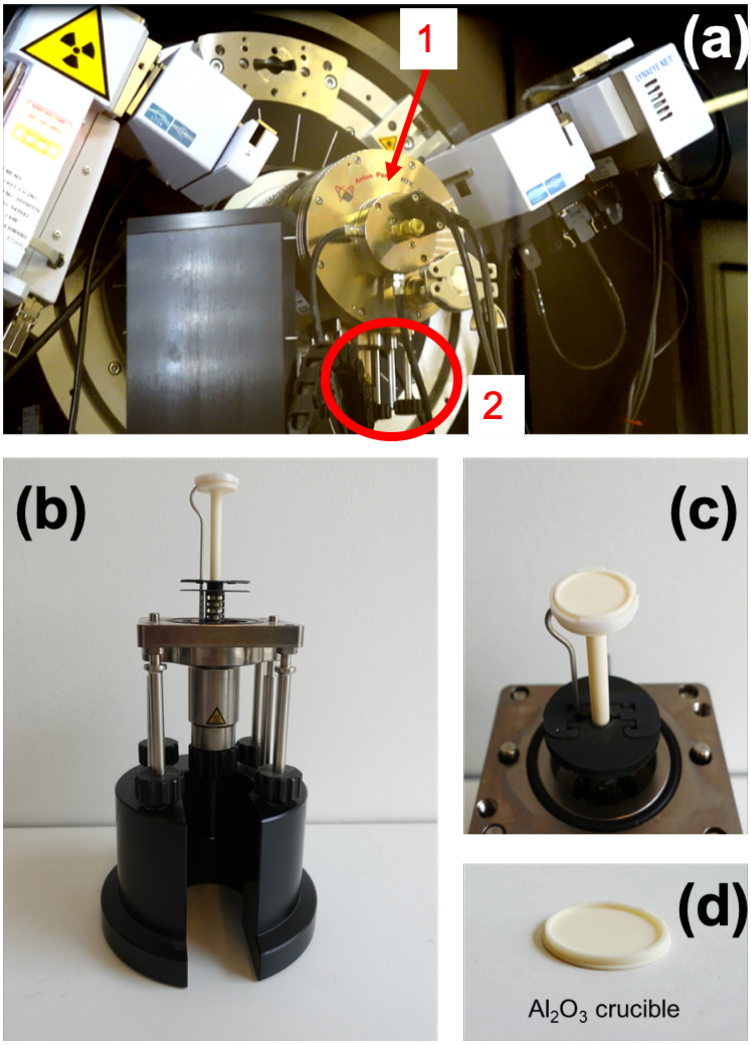

Figure V-3: Photos of (a) high temperature HTK1200 chamber (arrow 1); the sample holder is introduced at the bottom (circle 2); (b) sample holder on its external stand; (c) top of the sample holder and (d) flat alumina crucible.

Thermogravimetric analysis was performed in air at 2 °C min^{-1} with a LABSYS evo TGA 1150 instrument. A triplicate was performed on sample F, previously dried at 110 °C for 72 h under air, to determine the number of moles of water inserted into the NVO structure. Scanning electron micrographs were obtained on gold-coated powders under high vacuum and 15 kV using a Clara FEG-SEM from TESCAN coupled to energy dispersive X-ray (EDX). The specific surface area was determined by the BET technique. using a Micromeritics Asap 2020 Plus instrument. Degassing was applied for 48 h at 60 °C with a heating ramp of 10 °C min^{-1}. The adsorption measurement was performed by the Rouquerol method under N_2 from 0 to 0.3 with a 0.03 step.

2.4. Electrochemical characterization

Electrochemical measurements were performed using Swagelok cells assembled in an ambient atmosphere. Zinc foil, Whatman©-type glass fiber filter, and 3 M zinc triflate solution were used as the anode, separator, and electrolyte, respectively. The working electrode was prepared by manual grinding of the NVO active material with carbon black and polyvinylidene fluoride in 70:20:10 ratio, followed by pressing 1.5 mg of this mixture onto a stainless-steel grid under a load of 6 tons. Galvanostatic charge and discharge cycling tests were performed at different constant current densities in a range of 0.1 A g^{-1} to 5 A g^{-1} at room temperature using a LAND battery test system (Wuhan, China). The specific capacity is calculated based on the cathode active material mass. Cyclic voltammetry was carried out at room temperature with a Bio-Logic VMP3 galvanostat within the range of 0.2 V-1.6 V *vs* Zn/Zn^{2+} with a scanning rate of 0.5 mV s^{-1}.

3. Results and discussion

3.1. Repeatability

This study was based on experiments where V_2O_5 powder was dispersed with a mass loading of 67 g/l in NaCl solutions of various concentrations (between 0.21 and 2 M) and stirred for 2 days at room temperature. The red powder collected after centrifugation, washing and drying was then heated in air at 500°C.

The selection of samples in Table V-2 includes several “repeat experiments" (D-E-F). As can be seen from the columns summarizing the crystalline phases observed in each sample before and after calcination, the repeatability of the syntheses was unreliable. Figure V-4 shows the XRD patterns of samples D, E and F prepared in nominally identical conditions (stirring in 2 mol/L NaCl for 2 days). The samples actually differ by the amounts of residual V_2O_5 and NaCl, and the position of some (but not all) of the peaks of the nanocrystalline NVO phase. Amongst our own set of samples, we observed slight shifts in the position of some reflections (especially the (001) reflection near 11° 2θ), as already shown in Figure V-4 for the samples D-E and F. All these indications point to a degree of variability in the composition of the barnesite-like NVO phase.

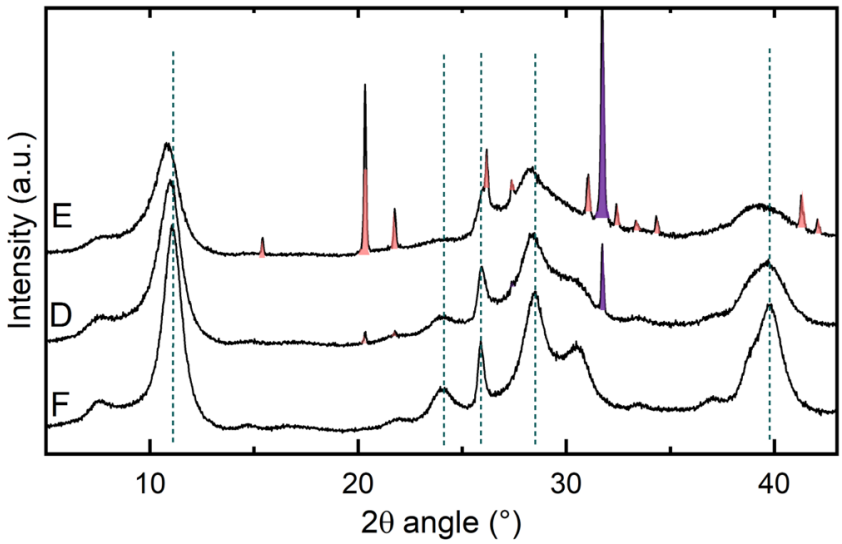

Figure V-4: XRD patterns of the uncalcined samples D, E and F, prepared in nominally identical conditions (stirring in 2M NaCl for 2 days). The peaks highlighted in red and purple correspond to V_2O_5 and NaCl. Other peaks correspond to the nanocrystalline NVO phase (dotted lines are guides for the eyes).

The XRD pattern (Figure V-4) of sample F can be indexed to a pure barnesite-like NVO phase. As shown in Figure V-5, there is a reasonably good match between the broad reflections of sample F and the database pattern PDF 00-016-0601, referenced to a 1963 publication by Weeks et *al.* [27] reporting on "barnesite $Na_2V_6O_{16}.3H_2O$”. However, there are two other database entries with similar peak positions and chemical compositions which are sometimes used in the literature and represented in Figure V-5. Therefore, in Table V-2, this barnesite-like phase is simply written as "NVO", because it may have a slightly different composition from $Na_2V_6O_{16}.3H_2O$. In literature, authors who prepared powders by stirring V_2O_5 in a solution of a sodium salt report water contents between 1.63 and 3 [10,16,18,20].

The amount of water contained in sample F can be calculated from the weight loss observed on the thermogravimetric analysis (TGA) curve (Figure V-6). The sample was dried at 110°C for 72 h and the NVO phase was controlled by XRD analysis before conducting the TGA measurement. Based on the weight loss of 4.3 wt% (Figure V-6), it could be estimated that there are 1.5 mol of water in our barnesite-like NVO phase of sample F.

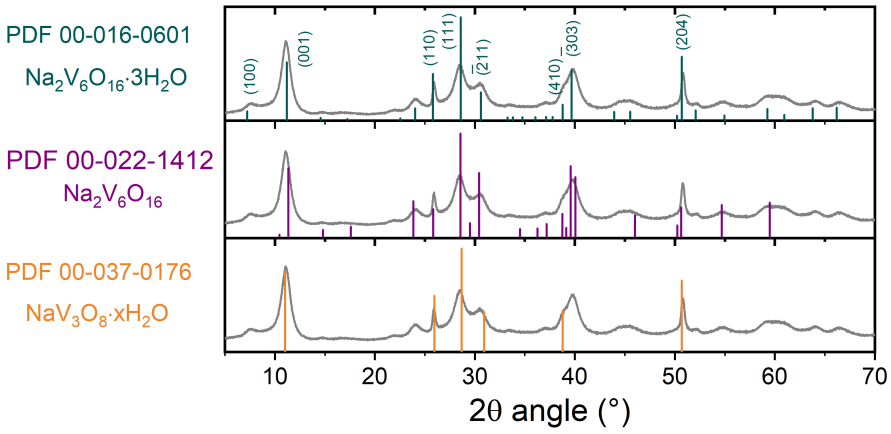

Figure V-5: Comparison of reference patterns PDF 00-016-0601, PDF 00-022-1412 and PDF 00-037-0176 with the diffractogram of sample F.

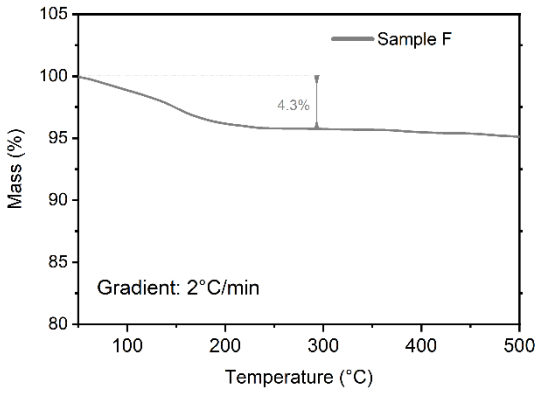

Figure V-6: Thermogravimetric curve of sample F conducted under air at 2 °C min^{-1}.

In agreement with other authors [18,24,28–30], we found that the progressive formation of barnesite-like NVO was accompanied by a consistent set of experimental observations: (i) a change in the suspension color from orange-yellow to dark-orange to red (see Figure V-7), (ii) a decrease in pH from 3.5 to 2 and (iii) an increase in viscosity. However, the rate of progress could be significantly different from batch to batch.

Some of the variability certainly comes from the fact that the nominally identical conditions are not really identical: over 2 days, even small differences in stirring efficiency probably

build up into a significant effect; the washing step is undeniably a weak point in process control, since the reddish color of the washing water indicates that vanadium is lost at the same time as NaCl is washed away. The residual NaCl in several samples of Table V-2 is a consequence of the compromises made at that stage. However, such experimental issues are relatively common and, in our experience, do not necessarily lead to the variability observed here. Considering the intricate mechanisms described by Durupthy et al. [31] for the formation of $Na_2V_6O_{16}.3H_2O$ using a different aqueous route, we suspect that some of the variability observed in our case might be intrinsic to the process and linked to phenomena such as a dissolution onset or a V^{4+} concentration threshold. These reasons could explain why Rui *et al.* [24] and Wan *et al.*[18], using the same Na/V ratio obtain different phases: V_2O_5 and $NaV_3O_8 \cdot 1.5H_2O$ respectively.

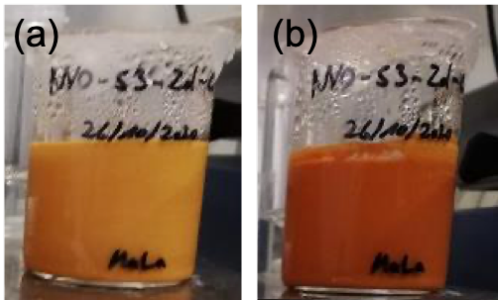

Figure V-7: Suspension color of sample C (a) at the beginning and (b) at the end of the synthesis.

Finally, heat treatment at 500°C led to the crystallization of mixtures or pure phases depending on the lyophilized precursors (see Table V-3). For the next discussions, the sequence presented in Table V-3 will be used because the phases in calcined powders are directly linked with the phases in uncalcined powders and not always linked with the NaCl molar concentration used.

Table V-3: Labels of the crystalline phases observed in X-ray diffractograms for uncalcined and calcined powders (● V_2O_5; ■ β-$Na_{0.33}V_2O_5$; ◆ $Na_{1.16}V_3O_8$; "◆" $Na_{1+x}V_3O_8$).

Label	Phases in uncalcined powder	Phases in calcined powder
A	V_2O_5, (NVO)	■ ●
C	V_2O_5, NVO	■
B	V_2O_5, NVO	■ "◆"
D	NVO, (V_2O_5), NaCl	"◆" ■
F	NVO	"◆" (■)
E	NVO, V_2O_5, NaCl	◆

3.2. Phase transformation during calcination

As shown in Table V-3, the uncalcined powders frequently contain NVO and V_2O_5 (Figure V-8).

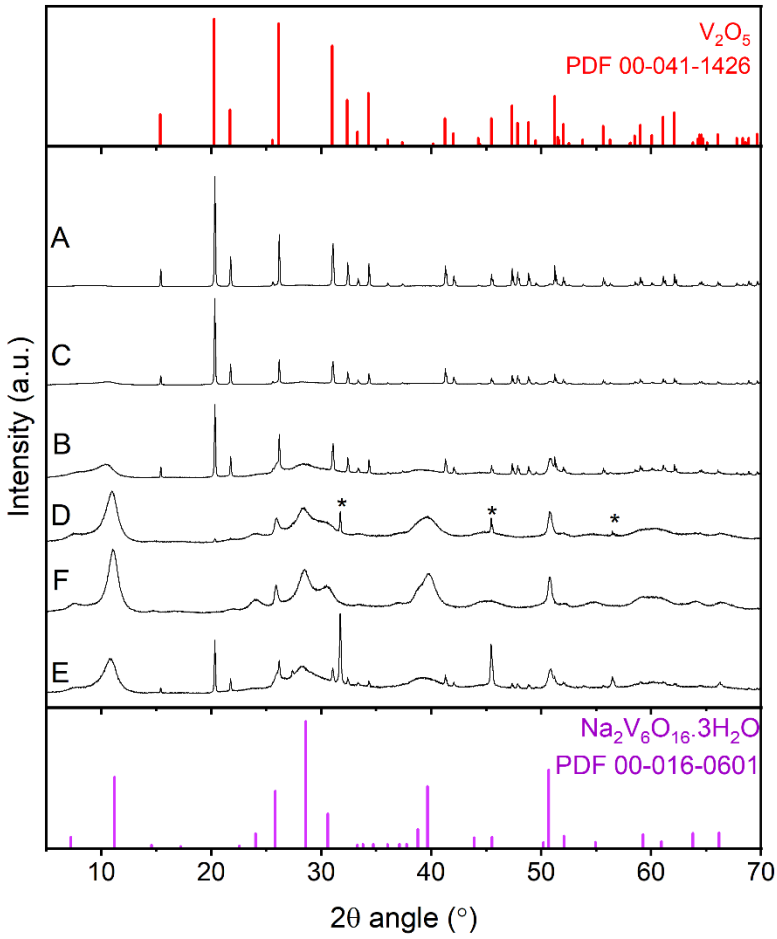

Figure V-8: XRD patterns of samples A-B-C-D-E-F before heat treatment for comparison with database reference patterns for V_2O_5 (PDF 00-041-1426) and $Na_2V_6O_{16}.3H_2O$ (PDF 00-016-0601). The asterisks correspond to NaCl reflections.

After calcination in air at 500°C, samples E-500 and C-500 transformed into single phases with peak positions matching reference patterns for $Na_{1.16}V_3O_8$ (◆ - PDF 04-025-2006) and β-$Na_{0.33}V_2O_5$ (■ - PDF 01-084-8341) respectively (Figure V-9). However, other calcined samples contain a mixture of two crystalline phases: A-500 is composed of V_2O_5 and β-$Na_{0.33}V_2O_5$ while B-500, D-500 and F-500 contain β-$Na_{0.33}V_2O_5$ and a phase that we will call $Na_{1+x}V_3O_8$ (Figure V-9).

Indeed, as shown on the XRD pattern of sample F-500 for example (Figure V-9), the calcined material is a mixture of a small amount of β-$Na_{0.33}V_2O_5$ with a phase where the peaks of $Na_{1.16}V_3O_8$ are shifted to larger 2θ angles (smaller interplanar distances). This phase will be called $Na_{1+x}V_3O_8$ in the following and appears with the symbol "◆" in Table V-3. The lattice parameters obtained by refinement for sample F-500 and those collected by Onoda *et al* [32] for a $Na_{1.16}V_3O_8$ single crystal in the $P2_1/m$ space group are reported in Table V-4. These results suggest that the *a* cell parameter is the most affected parameter in our sample but that the difference is lower than 1%. Based on a comparison of the cell parameters in our sample with the composition dependence of the lattice constants reported in Onoda *et al.* [32], the x value in our $Na_{1+x}V_3O_8$ is likely to be ≤0.1 for the phase "◆".

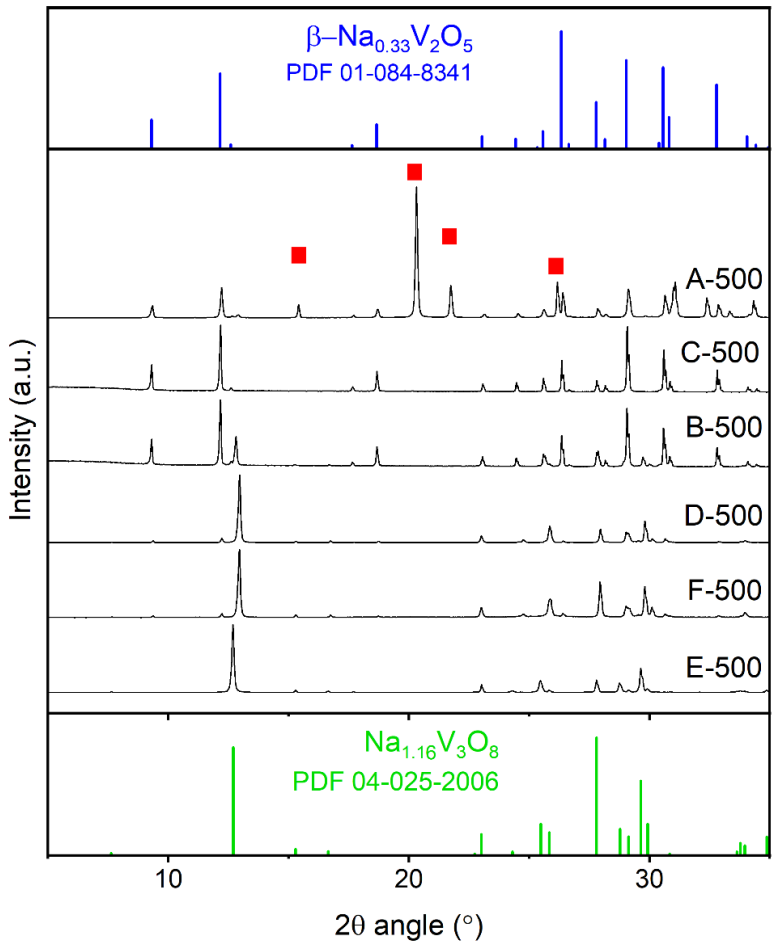

Figure V-9: XRD patterns of samples A-B-C-D-E-F after heat treatment at 500°C, for comparison with database reference patterns for $Na_{1.16}V_3O_8$ (PDF 04-025-2006) and β-$Na_{0.33}V_2O_5$ (PDF 01-084-8341). The ■ corresponds to V_2O_5 reflections.

Table V-4: Lattice parameters of the $Na_{1.16}V_3O_8$ determined by Onoda et al [32], and $Na_{1+x}V_3O_8$ (sample F-500) obtained by Rietveld refinement via Bruker TOPAS software (with error bar).

	a (Å)	**b (Å)**	**c (Å)**	***β(°)***
PDF 04-025-2006 $Na_{1.16}V_3O_8$	7.318(2)	3.610(1)	12.165(2)	107.75(2)
Sample F-500 $Na_{1+x}V_3O_8$	7.2561(3)	3.6068(2)	12.1855(7)	107.789(3)

The sequence of crystalline phase transformation was studied more deeply by in situ high-temperature X-ray diffraction for samples A-E. After heating to 500°C in the high-temperature chamber of the diffractometer, they form respectively (i) β-$Na_{0.33}V_2O_5$ with approx. 40 wt% V_2O_5 (sample A), (ii) pure β-$Na_{0.33}V_2O_5$ (sample C), (iii) β-$Na_{0.33}V_2O_5$ with approx. 12 wt% $Na_{1+x}V_3O_8$ (sample B), (iv) $Na_{1+x}V_3O_8$ with approx. 35 wt% β-$Na_{0.33}V_2O_5$ (sample D) and (v) pure $Na_{1.16}V_3O_8$ (sample E).

Diffractograms were collected in a narrow 2θ window while the temperature was increased continuously at a rate of 2 ° min^{-1}, i.e., the temperature increased by 10 °C during the recording of each 5-min scan. Figure V-10 shows a selection of the collected scans.

Up to ~250 °C, the broad peak of the nanocrystalline barnesite-like NVO phase progressively shifted from 10.5° 2θ towards higher 2θ angles, i.e., smaller interplanar distances. This is particularly clear in the graph for samples D and E.

Starting at ~275 °C, this broad peak progressively narrowed down into two characteristic peaks of the β-$Na_{0.33}V_2O_5$ and $Na_{1+x}V_3O_8$ phases. The two peaks then grew side by side up to a temperature of about 350 °C. Beyond this temperature, samples A, B and C entered a second stage of transformation, where the intensity of the peaks of V_2O_5 and $Na_{1+x}V_3O_8$ decreased while the intensity of the β-$Na_{0.33}V_2O_5$ peaks increased concomitantly. This evolution proceeded until the complete disappearance of the peak of either $Na_{1+x}V_3O_8$ (sample A) or V_2O_5 (sample B and C). The second stage did not exist in sample D since it did not contain any V_2O_5. In sample E, the small amount of β-$Na_{0.33}V_2O_5$ phase formed beyond 275 °C was rapidly transformed into the sodium rich phase, $Na_{1.16}V_3O_8$ given that sample E still contains NaCl.

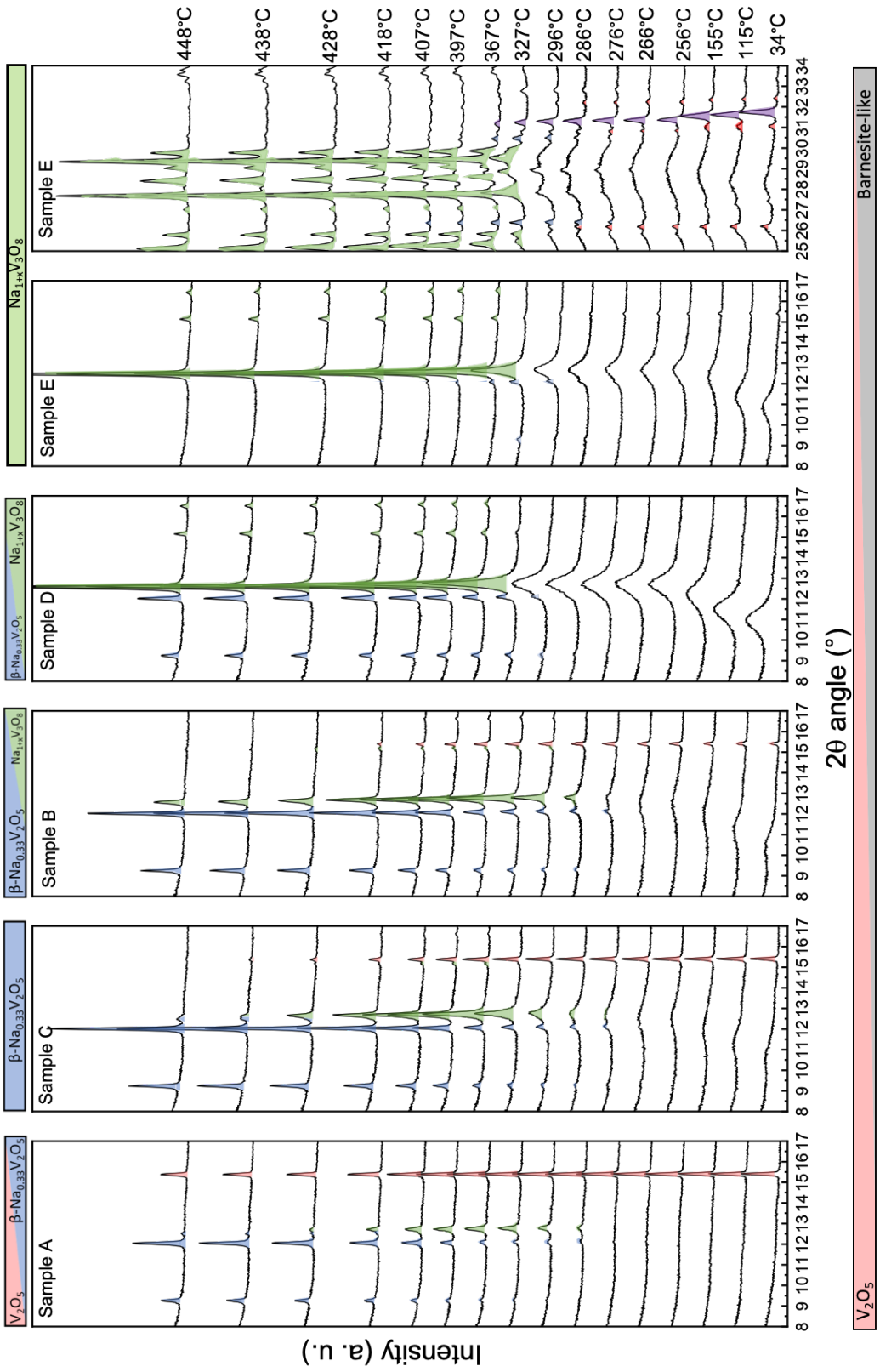

Figure V-10: High-temperature X-ray diffraction study of samples A, B, C, D and E: selection of 5-min diffractograms collected during the heating at 2°C min^{-1}. 2 x 5-min diffractograms are shown for sample E to detect NaCl peak in the second range of 2θ. The end temperature of each scan is shown at the right of the figure. The peaks highlighted in red, purple, blue and green correspond to V_2O_5, NaCl, β-$Na_{0.33}V_2O_5$ and $Na_{1+x}V_3O_8$, respectively. The broad peak moving to higher 2θ angle in the low temperature range corresponds to the barnesite-like NVO nanocrystalline phase.

As a complement to this qualitative description, Figure V-11 shows the temperature dependence of (a) the interplanar d values corresponding to the maxima of the deconvoluted peaks, (b) the peak intensities (= areas of the deconvoluted peaks) and (c) the mass loss measured by thermogravimetric analysis, in the case of sample C which transforms into the pure β-$Na_{0.33}V_2O_5$ phase.

The 5% mass loss below 200°C supports the assumption that the shift of the broad peak to smaller interplanar distances corresponds to a dehydration of the barnesite-like phase [33]:

$$Na_2V_6O_{16}\cdot xH_2O \rightarrow Na_2V_6O_{16} + x\ H_2O$$

It is interesting to note that the formation of distinct $Na_{0.33}V_2O_5$ and $Na_{1+x}V_3O_8$ phases occurred only once the dehydration was complete. This is in general agreement with ex-situ diffractograms reported by Fan *et al.* [30] for a sodium vanadate material prepared by stirring V_2O_5 in a Na_2SO_4 solution.

The second, smaller mass loss above ~380°C happened in the same temperature range as the transformation of V_2O_5 and $Na_{1+x}V_3O_8$ into $Na_{0.33}V_2O_5$ (Figure V-11c). The equation

$$2\ Na_{1+x}V_3O_8 + (3+6x)\ V_2O_5 \rightarrow (6+6x)\ Na_{0.33}V_2O_5 + 0.5\ O_2$$

suggests that this mass lost could be explained by a release of oxygen due to the partial reduction of V^{5+} into V^{4+}.

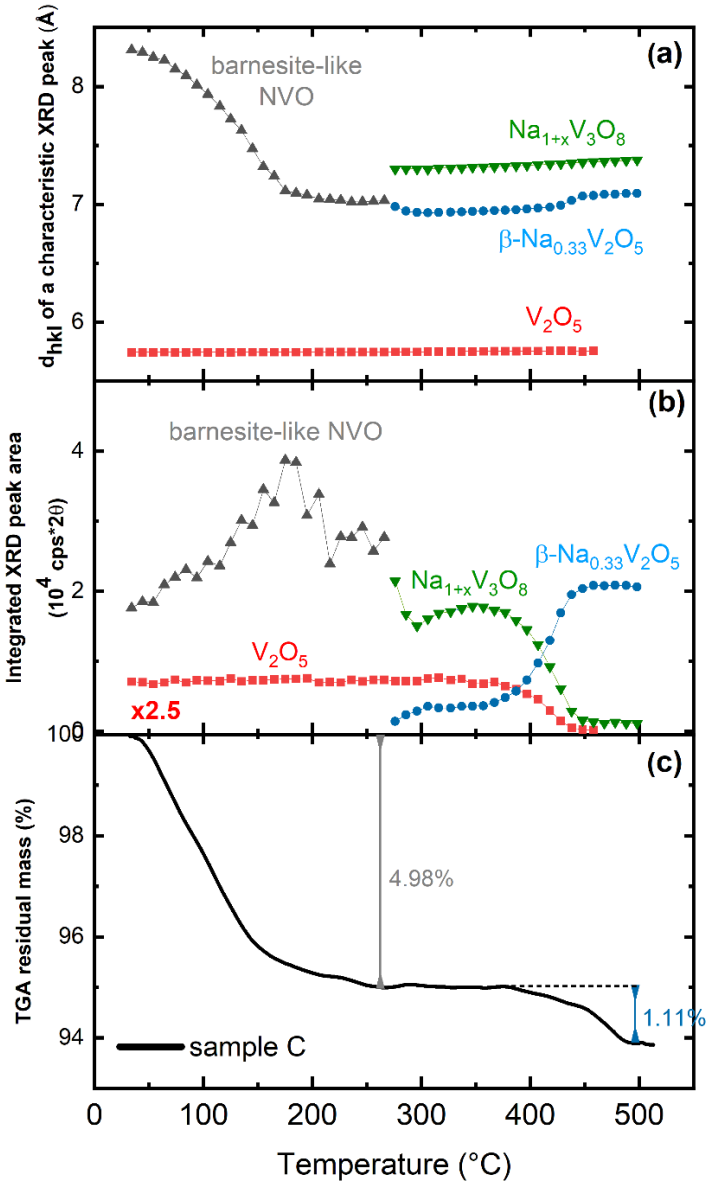

Figure V-11: (a,b) Temperature dependence of the interplanar spacing and the integrated intensity of one characteristic peak for each crystalline phase detected during the high temperature X-ray diffraction experiment on sample C; (c) thermogravimetric curve of sample C performed at the same heating rate as the HTXRD experiment.

This phase transformation scenario is consistent with the crystallographic results for all the samples in Table V-3. Most of the samples transformed into mixtures of $Na_{1+x}V_3O_8$ and β-$Na_{0.33}V_2O_5$, with a larger contribution of β-$Na_{0.33}V_2O_5$ when the peaks of residual V_2O_5 were more prominent in the uncalcined powder. This is logical when considering the nominal Na/V ratios of the different phases: 0.333 in $Na_2V_6O_{16}\cdot xH_2O$, 0.367 in $Na_{1.1}V_3O_8$ and 0.165 in $Na_{0.33}V_2O_5$.

In case of very high residual V_2O_5 (such as sample A in Figure V-10), there was not enough sodium provided by the barnesite-like NVO; therefore, unreacted V_2O_5 was still present in the calcined material, in combination with β-$Na_{0.33}V_2O_5$. At the other side of the range, true $Na_{1.16}V_3O_8$ (i.e., with peak positions at the expected 2θ angles) was only obtained in samples where NaCl having survived the washing step provided an extra source of sodium (Figure V-10, sample E). This assumption is supported by TGA measurement (Figure V-12) and EDX analysis conducted on sample E before and after calcination at 500°C (Figure V-13). As explained before, the ~5% mass loss below 200°C observed in Figure V-12 corresponds to a dehydration of the barnesite-like phase that is in agreement with the shift of the broad peak to smaller interplanar distances and higher 2θ angles (Figure V-10, sample E). The second mass loss above 300°C is higher than for sample C and is probably due to the release of O_2 and also Cl_2 [34]. It happened in the same temperature range as the transformation of V_2O_5, NaCl and $Na_{0.33}V_2O_5$ into the rich sodium phase $Na_{1.16}V_3O_8$ (Figure V-10, sample E). After calcination at 500°C, no chlorine is detected by EDX in sample E-500 suggesting that the extra source of sodium comes from NaCl (Figure V-13).

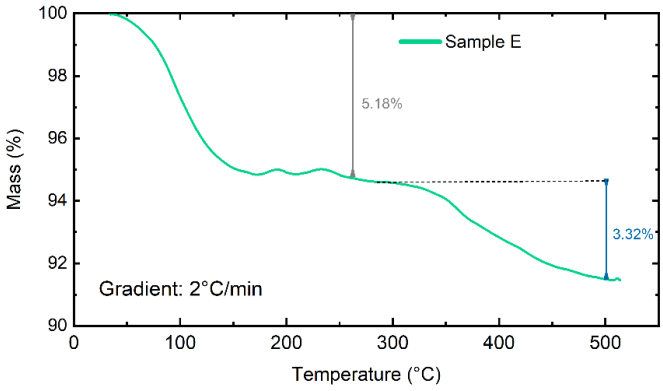

Figure V-12: Thermogravimetric curve of sample E performed at the same heating rate as the HTXRD experiment.

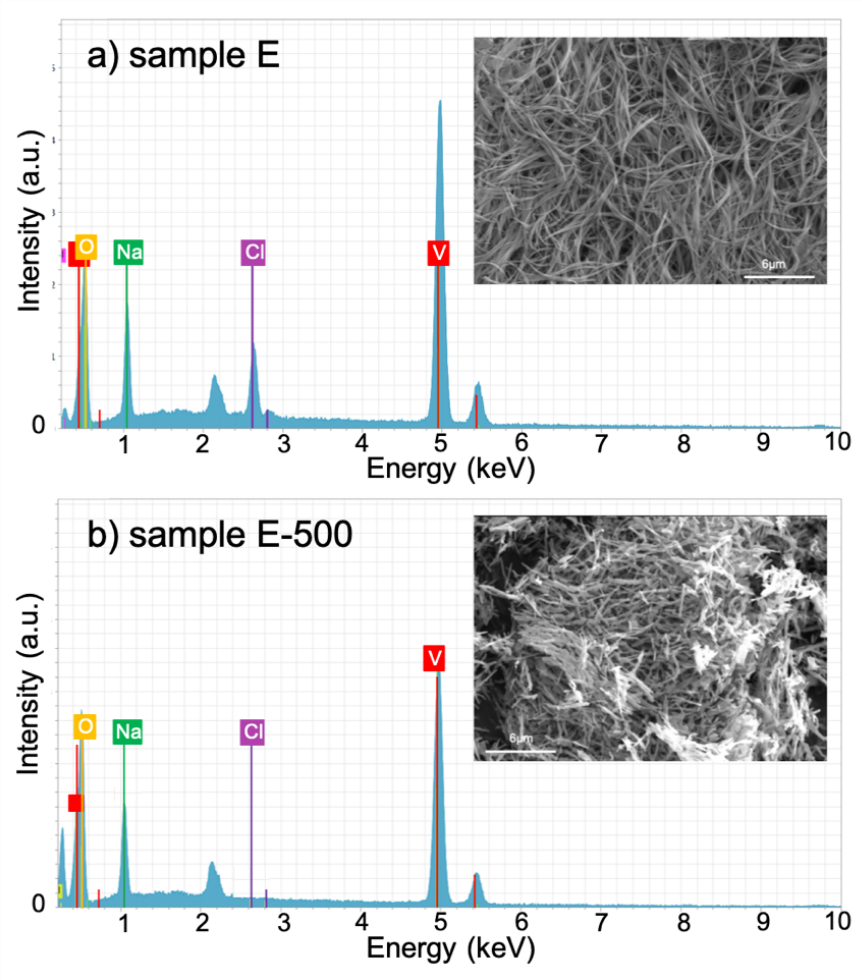

Figure V-13: EDX pattern of sample E (a) before and (b) after calcination at 500°C.

3.3. Morphological and electrochemical characterizations of $Na_2V_6O_{16}\cdot 1.5H_2O$ (sample F), β-$Na_{0.33}V_2O_5$ (sample C-500), $Na_{1.16}V_3O_8$ (sample E-500)

The pure phase β-$Na_{0.33}V_2O_5$ formed by aqueous route followed by heat treatment was then characterized by SEM to get an insight into the microstructural properties of $Na_{0.33}V_2O_5$. The SEM images of sample C before its calcination shows the presence of nanobelts and some platelet-like particles (Figure V-14a). The observed platelet-like particle size varies from one micrometer to several micrometers with a strong similarity to the commercial V_2O_5 particles that have initially been put into the reactional mixture. This confirms the hypothesis that the progressive insertion of sodium ions into the crystallographic structure of V_2O_5 is creating a new phase with a different morphology, nanobelts. After the calcination, the nanobelts seem to have been shortened and form nanoribbons as observed in Figure V-14b. Furthermore, the particles of V_2O_5 are no longer visible which is consistent with the results

obtained by HTXRD for sample C (Figure V-10). Moreover, it can be noted that the specific surface area decreases from 14.80 $m^2 g^{-1}$ to 6.84 $m^2 g^{-1}$ after calcination.

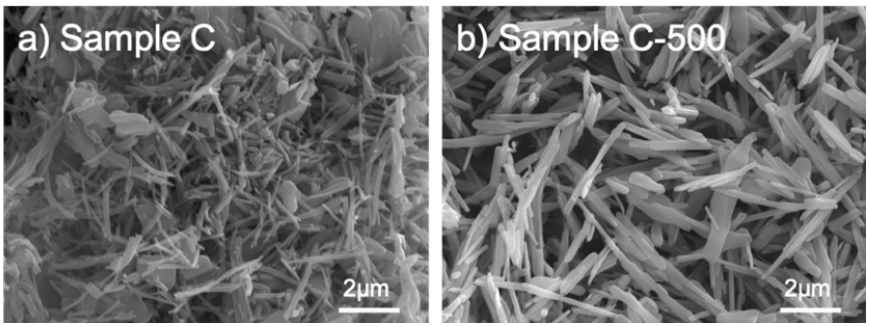

Figure V-14: SEM images of sample C (a) before and (b) after calcination at 500 °C.

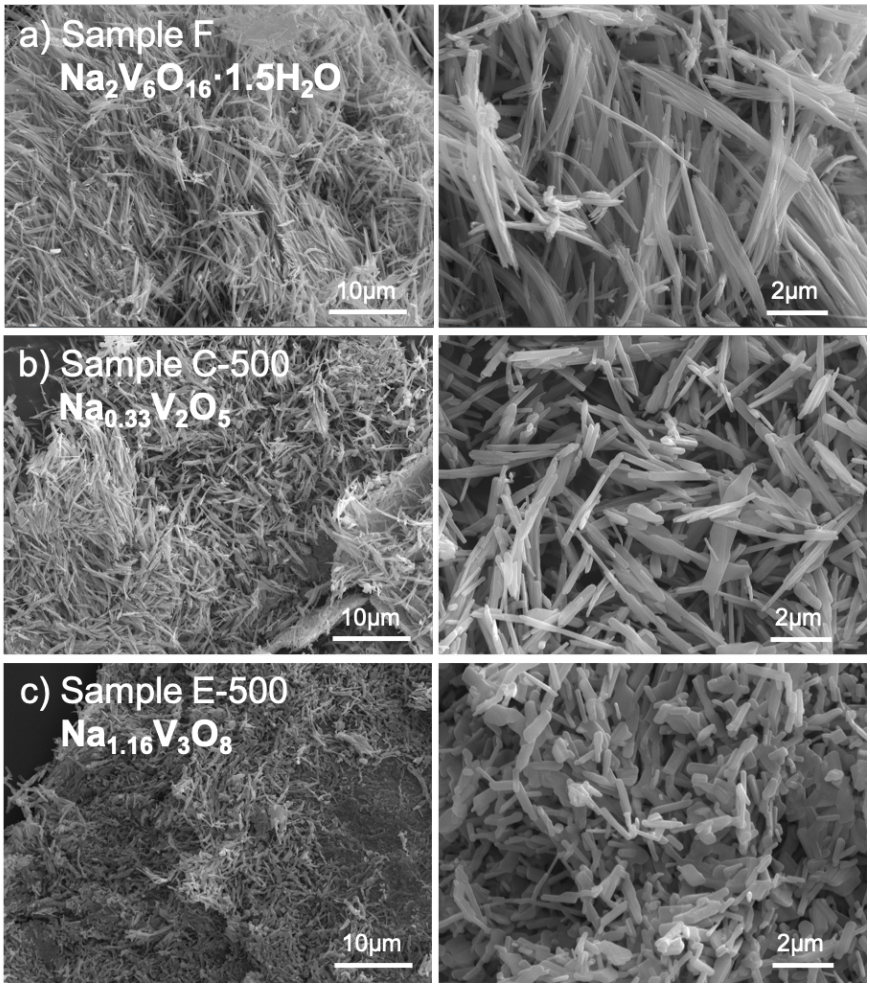

Figure V-15: SEM images of (a) sample F, (b) sample C calcined at 500 °C, (c) sample E calcined at 500°C at magnifications x5000 and x20000.

The results for $Na_{0.33}V_2O_5$ are compared with two other samples composed of pure phases: $Na_2V_6O_{16}·1.5H_2O$ (sample F) and $Na_{1.16}V_3O_8$ (sample E-500). As shown in Figure V-15,

nanobelts with different size and shape are formed. The $Na_2V_6O_{16}\cdot 1.5H_2O$ powder present long and thin nanobelts that appear like fibers (Figure V-15a). After calcination, the nanobelts are thicker and shorter. The $Na_{0.33}V_2O_5$ powder is composed of nanoribbons while the $Na_{1.16}V_3O_8$ powder offers such small nanoribbons that they look like microparticles. Furthermore, the specific surface area determined by the BET technique for the three samples, the highest specific surface area for the uncalcined sample 18.75 $m^2\ g^{-1}$ against 6.84 and 4.24 $m^2\ g^{-1}$ for β-$Na_{0.33}V_2O_5$ and $Na_{1.16}V_3O_8$ respectively.

Finally, we report the data of the electrochemical characterization of the three samples, $Na_2V_6O_{16}\cdot 1.5H_2O$, $Na_{0.33}V_2O_5$ and $Na_{1.16}V_3O_8$, performed in Swagelok cell against Zn anode, using $Zn(CF_3SO_3)_2$ 3M as electrolyte solution. Figure V-16 (a, b and c) shows the cyclic voltammograms of $Na_2V_6O_{16}\cdot 1.5H_2O$, $Na_{0.33}V_2O_5$ and $Na_{1.16}V_3O_8$ materials at 0.5 mV s^{-1} in the voltage range of 0.2-1.6 V. $Na_2V_6O_{16}\cdot 1.5H_2O$ presents two pairs of discharging (0.48/0.77 V) and charging peaks (0.73/1.06 V) suggesting a multistep intercalation/deintercalation of Zn^{2+} into the structure (Figure V-16a). The cathodic peaks of $Na_2V_6O_{16}\cdot 1.5H_2O$ are slightly shifted for the first cycle but the CV curves present similar shape for following cycles suggesting a good reversibility as detected also on the discharge curves at 0.1 A g^{-1} (Figure V-16d). The CV curves of $Na_2V_6O_{16}\cdot 1.5H_2O$ (Figure V-16a) are quite similar to $Na_{1.16}V_3O_8$ (Figure V-16c) in terms of shape and potentials. Thus, it can be hypothesized that the cathode material is not considerably altered during the insertion and extraction of the zinc ions, which confirms once more the stability and steadiness of sodium vanadate materials [12].

In $Na_{0.33}V_2O_5$ (Figure V-16b), there are initially two pairs of cathodic (0.45/1.1 V) and anodic peaks (0.86/1.4 V) but they are located in a different domain suggesting a different mechanism than $Na_2V_6O_{16}\cdot 1.5H_2O$ or $Na_{1.16}V_3O_8$. The discrepancy between the working potentials obtained for $Na_{1.16}V_3O_8$ /$Na_2V_6O_{16}\cdot 1.5H_2O$ and $Na_{0.33}V_2O_5$ can be explained by crystallographic structures that induce different electrochemical behaviors [4]. During cycling, a third peak is detected at 0.8V and 1V in discharge and charge respectively as visible also on the discharge/charge curves (Figure V-16e). After that, the CV curves of $Na_{0.33}V_2O_5$ show similar shape, which indicates a high reversibility of charge/discharge process.

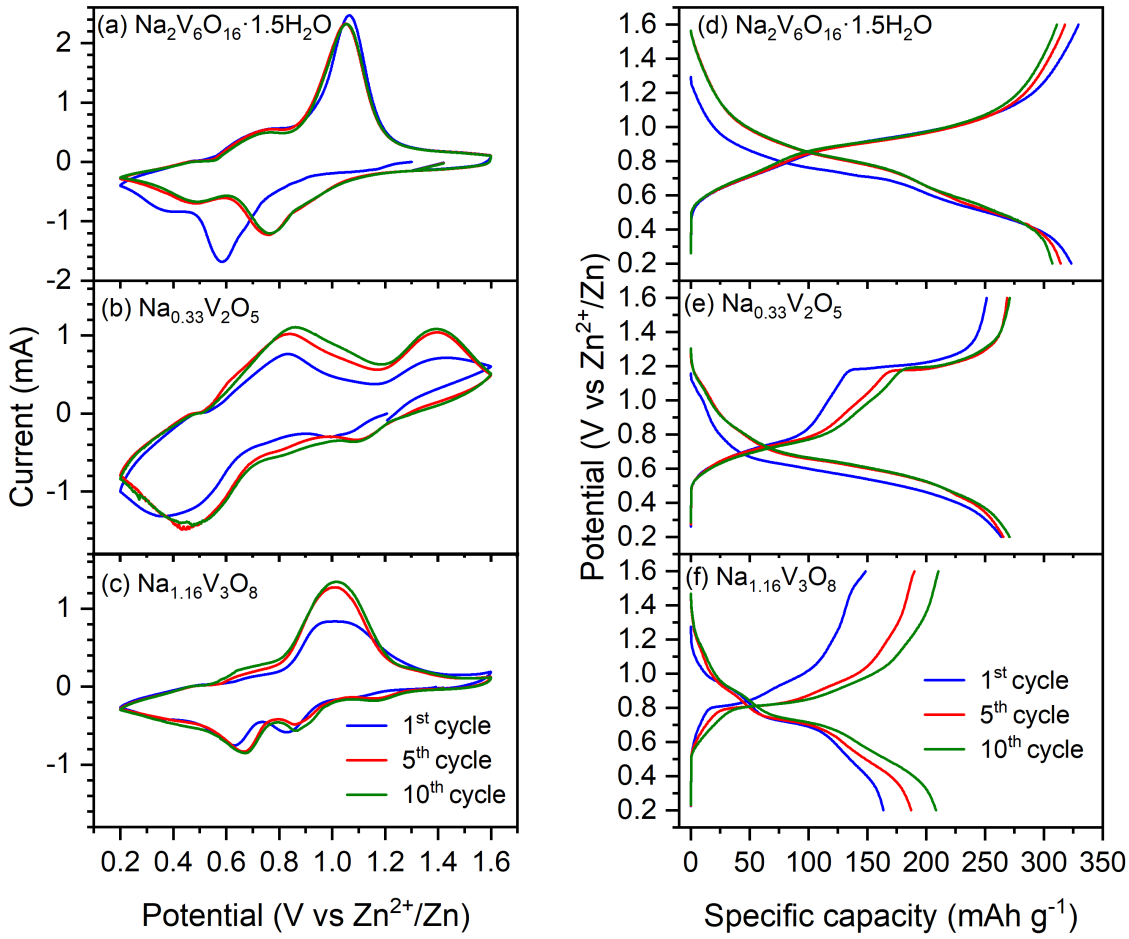

Figure V-16: CV curves at 0.5 mV s^{-1} (a, b and c) and charge/discharge curves at 0.1 A g^{-1} (d, e and f) of $Na_2V_6O_{16}.1.5H_2O$ - sample F, $Na_{0.33}V_2O_5$ – sample C-500 and $Na_{1.16}V_3O_8$ – sample E-500 for the 1st, 5th and 10th cycle in the voltage range of 0.2-1.6 V.

Figure V-17a displays the cycling performance of the three electrodes at a current density of 0.1 A g^{-1}. The $Na_{0.33}V_2O_5$ material exhibits a very stable discharge capacity of about 265 mAh g^{-1} for 40 cycles thanks to its tunnel structure [4]. The highest discharge capacity, 320 mAh g^{-1} is detected for $Na_2V_6O_{16}\cdot 1.5H_2O$ and decreases slowly along cycling. The capacity retention is equal to 84 % after 40 cycles. In contrast, the $Na_{1.16}V_3O_8$ material delivers initially the lowest capacity of 165 mAh g^{-1} but the capacity increases along cycling meaning that the number of active sites increases at the same time due to the gradual impregnation of electrolytes. As explained in previous chapter for V_2O_5, this activation process can also be attributed to the insertion of water molecules into the structure, leading to an increase in the interlayer distance and easier Zn^{2+} insertion [35,36]. Indeed, $Na_{1.16}V_3O_8$ and V_2O_5 exhibit both a layered crystallographic structure. The coulombic efficiencies of the three different samples are around 100 % suggesting good reversibility of these materials. However, it has

to be noted that theses capacities are low compared to the theoretical capacities of these materials, respectively equals to 518 mAh g^{-1} for $Na_{0.33}V_2O_5$ and 422 mAh g^{-1} for $Na_2V_6O_{16}\cdot 1.5H_2O$ and $Na_{1.16}V_3O_8$.

Rate performance of the three electrode materials are determined and presented in Figure V-17b. The discharge capacities of $Na_2V_6O_{16}\cdot 1.5H_2O$ are 270, 230, 205, 159 and 135 at current densities of 0.2, 0.5, 1, 3 and 5 A g^{-1}. The $Na_{1.16}V_3O_8$ and $Na_{0.33}V_2O_5$ electrodes deliver 191, 168, 148, 106, 83 and 245, 166, 100, 28, 11 respectively at current densities of 0.2, 0.5, 1, 3 and 5 A g^{-1}. The $Na_{1.16}V_3O_8$ and $Na_2V_6O_{16}\cdot 1.5H_2O$ electrodes exhibit a good cycling performance at various current densities while the $Na_{0.33}V_2O_5$ electrode suffers from a rapid capacity fading at increased current density. However, the materials did not seem to be significantly degraded during the high current density cycles since the recovery at 0.2 A g^{-1} is correct.

The cycling performance of the three electrodes at a current density of 5 A g^{-1} is further investigated and shown in Figure V-17c. The three electrodes exhibit outstanding cycling stability with excellent capacity retention. Not surprisingly, the $Na_2V_6O_{16}\cdot 1.5H_2O$ material delivers the highest specific capacity and is the most stable during cycling. The structure of $Na_2V_6O_{16}\cdot 1.5H_2O$ is stabilized by sodium ions and water molecules that function as “pillars” [4,16,37]. Moreover, the higher specific surface area of this material creates more active sites and leads to fast ion diffusion pathways. $Na_{0.33}V_2O_5$ electrode maintains a discharge capacity lower than 30 mAh g^{-1} which is consistent with the rate capability test. The low electrochemical performance of $Na_{0.33}V_2O_5$ at high current density can be explained by its tunnel-like structure that is less appropriate for the insertion of zinc ion at high current rate [16,38].

Overall, these results can be rated as a fairly good performance for an unoptimized electrode based on a powder that was prepared by a very simple procedure using widely available starting materials. Moreover, these results clearly suggest that the layered structure $Na_2V_6O_{16}\cdot 1.5H_2O$ is more superior in both capacity and rate performance by comparison with the non-hydrated $Na_{1.16}V_3O_8$ and tunnel-like structure β-$Na_{0.33}V_2O_5$.

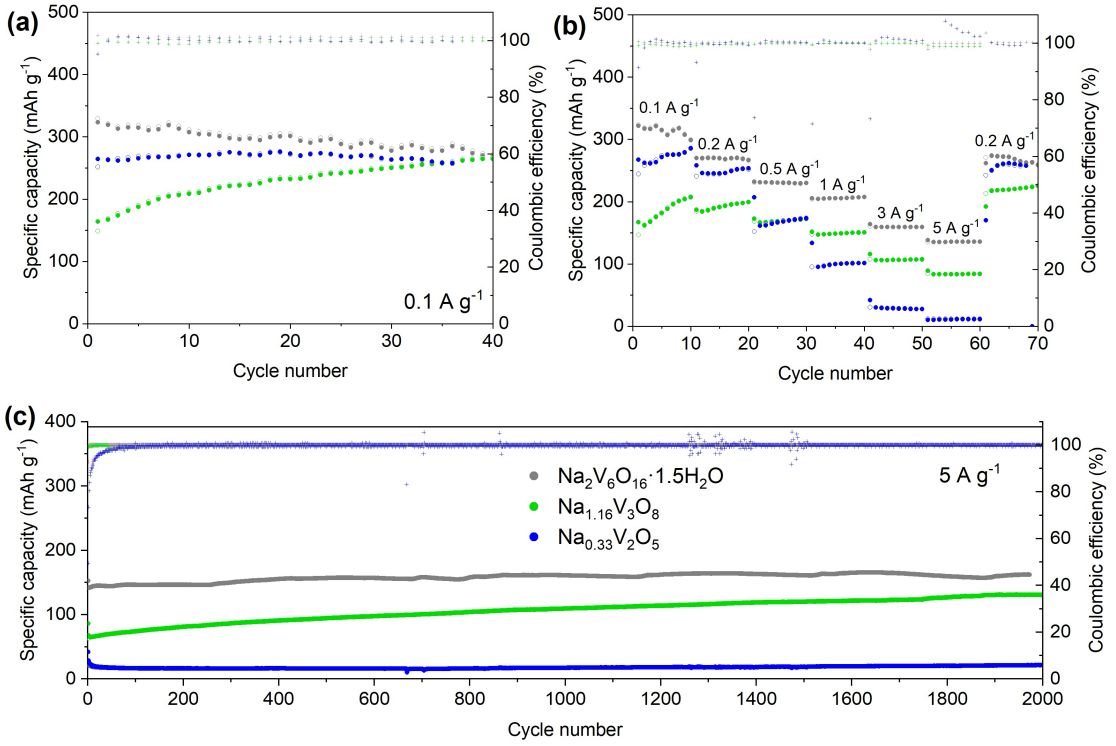

Figure V-17: (a) Cycling performance at 0.1 A g^{-1},(b) rate capability and (c) long cycling performance at 5 A g^{-1} of $Na_2V_6O_{16}·1.5H_2O$ (sample F), $Na_{0.33}V_2O_5$ (sample C-500) and $Na_{1.16}V_3O_8$ (sample E-500).

4. Conclusion

In this chapter, pure β-$Na_{0.33}V_2O_5$ phase was obtained by an aqueous route based on stirring V_2O_5 and NaCl. We studied by HTXRD the crystallization of lyophilized precursors of different compositions into mixtures or pure phases of V_2O_5, β-$Na_{0.33}V_2O_5$ and $Na_{1+x}V_3O_8$. We found that pure β-$Na_{0.33}V_2O_5$ could be obtained through heat treatment of a precursor powder containing the proper ratio of NVO and residual V_2O_5. However, the β-$Na_{0.33}V_2O_5$ phase does not form directly but through the reaction of V_2O_5 with a $Na_{1+x}V_3O_8$ intermediate. Then, we showed that barnesite-like NVO phase transforms into a $Na_{1+x}V_3O_8$-rich material, $Na_{1.16}V_3O_8$, if extra source of sodium, NaCl, is available.

Three samples composed of pure $Na_2V_6O_{16}\cdot 1.5H_2O$, β-$Na_{0.33}V_2O_5$ and $Na_{1.16}V_3O_8$ phases were compared in terms of morphology and electrochemical performance. $Na_2V_6O_{16}\cdot 1.5H_2O$ presents long and thin nanobelts that appear like fibers. After calcination, nanobelts are thicker and shorter evolving towards nanoribbons for the $Na_{0.33}V_2O_5$ sample and to small nanoribbons that seem like microparticles for the $Na_{1.16}V_3O_8$ sample. Then, their electrochemical performance was evaluated as cathode materials in zinc-ion batteries. The tunnel-like structure of $Na_{0.33}V_2O_5$ is very stable but not suitable for the insertion of zinc ions at high current density. The $Na_{0.33}V_2O_5$ material exhibits a very stable discharge capacity of about 265 mAh g^{-1} at 0.1 A g^{-1} but the capacity fades to 30 mAh g^{-1} when the current density increases to 5 A g^{-1}. As for V_2O_5, the layered structure of $Na_2V_6O_{16}\cdot 1.5H_2O$ and $Na_{1.16}V_3O_8$ phases facilitates the insertion of zinc ions into the structure during electrochemical cycling. These different structures and configurations play a key role in the determination of the electrochemical properties. Sodium ions and water act as pillars to stabilize the structure. Hence, the hydrated material, $Na_2V_6O_{16}\cdot 1.5H_2O$ seems to be the most appropriate material for zinc-ion batteries in terms of synthesis, capacity, and stability.

5. References

1 N. Zhang, Y. Dong, M. Jia, X. Bian, Y. Wang, M. Qiu, J. Xu, Y. Liu, L. Jiao and F. Cheng, *ACS Energy Lett*, 2018, **3**, 1366–1372.

2 F. Wan and Z. Niu, *Angewandte Chemie - International Edition*, 2019, **58**, 16358–16367.

3 K. Momma and F. Izumi, *J Appl Crystallogr*, 2011, **44**, 1272–1276.

4 X. Guo, G. Fang, W. Zhang, J. Zhou, L. Shan, L. Wang, C. Wang, T. Lin, Y. Tang and S. Liang, *Adv Energy Mater*, 2018, **8**, 1–7.

5 D. Kundu, B. D. Adams, V. Duffort, S. H. Vajargah and L. F. Nazar, *Nat Energy*, 2016, **1**, 1–28.

6 M. Yan, P. He, Y. Chen, S. Wang, Q. Wei, K. Zhao, X. Xu, Q. An, Y. Shuang, Y. Shao, K. T. Mueller, L. Mai, J. Liu and J. Yang, *Advanced Materials*, 2018, **30**, 1–6.

7 P. He, G. Zhang, X. Liao, M. Yan, X. Xu, Q. An, J. Liu and L. Mai, *Adv Energy Mater*, 2018, **8**, 1–6.

8 B. She, L. Shan, H. Chen, J. Zhou, X. Guo, G. Fang, X. Cao and S. Liang, *Journal of Energy Chemistry*, 2019, **37**, 172–175.

9 C. Xia, J. Guo, P. Li, X. Zhang and H. N. Alshareef, *Angewandte Chemie - International Edition*, 2018, **57**, 3943–3948.

10 Z. Xie, J. Lai, X. Zhu and Y. Wang, *ACS Appl Energy Mater*, 2018, **1**, 6401–6408.

11 F. Ming, H. Liang, Y. Lei, S. Kandambeth, M. Eddaoudi and H. N. Alshareef, *ACS Energy Lett*, 2018, **3**, 2602–2609.

12 M. Larry, Master thesis, University of Liege, 2021.

13 P. He, G. Zhang, X. Liao, M. Yan, X. Xu, Q. An, J. Liu and L. Mai, *Adv Energy Mater*, 2018, **8**, 1-6

14 P. Gao, Q. Ru, H. Yan, S. Cheng, Y. Liu, X. Hou, L. Wei and F. Chi-Chung Ling, *ChemElectroChem*, 2020, **7**, 283–288.

15 Y. Cai, F. Liu, Z. Luo, G. Fang, J. Zhou, A. Pan and S. Liang, *Energy Storage Mater*, 2018, **13**, 168–174.

16 S. J. Kim, C. R. Tang, G. Singh, L. M. Housel, S. Yang, K. J. Takeuchi, A. C. Marschilok, E. S. Takeuchi and Y. Zhu, *Chemistry of Materials*, 2020, **32**, 2053–2060.

17 L. Fan, Z. Li, W. Kang and B. Cheng, *Journal of Energy Chemistry*, 2021, **55**, 25–33.

18 F. Wan, L. Zhang, X. Dai, X. Wang, Z. Niu and J. Chen*, Nat Commun*, 2018, **9**, 1–11.

19 N. Qiu, Z. Yang, Y. Wang, Y. Zhu and W. Liu, *Chemical Communications*, 2020, **56**, 9174–9177.

20 P. Hu, T. Zhu, X. Wang, X. Wei, M. Yan, J. Li, W. Luo, W. Yang, W. Zhang, L. Zhou, Z. Zhou and L. Mai, *Nano Lett,* 2018, **18**, 1758–1763.

21 V. Soundharrajan, B. Sambandam, S. Kim, M. H. Alfaruqi, D. Y. Putro, J. Jo, S. Kim, V. Mathew, Y. K. Sun and J. Kim, *Nano Lett*, 2018, **18**, 2402–2410.

22 S. Wang, T. Yu, Y. Li, H. Fu and C. Sun, *Mater Res Bull*, 2019, **111**, 284–288.

23 C. Peng, M. Jin, D. Han, X. Liu and L. Lai, *Mater Lett*, 2022, **320**, 132391.

24 X. Rui, Y. Tang, O. I. Malyi, A. Gusak, Y. Zhang, Z. Niu, H. T. Tan, C. Persson, X. Chen, Z. Chen and Q. Yan, *Nano Energy*, 2016, **22**, 583–593.

25 M. Rashad, H. Zhang, M. Asif, K. Feng, X. Li and H. Zhang, *ACS Appl Mater Interfaces*, 2018, **10**, 4757–4766.

26 R. W. Cheary and A. Coelho*, J Appl Crystallogr*, 1992, **25**, 109–121.

27 A. D. Weers, *Journal of the minerological society of America*, 1963, **48**, 1187–1195.

28 H. Liu, Y. Wang, L. Li, K. Wang, E. Hosono and H. Zhou, *J Mater Chem*, 2009, **19**, 7885.

29 A. Vedpathak, T. Shinde, M. A. Desai, B. R. Thombare, R. Humane, S. A. Raut, R. Kalubarme, S. D. Sartale and S. Bhagwat, *ACS Appl Energy Mater*, 2023, **6**, 4693–4703.

30 L. Fan, Z. Li and W. Kang, *ACS Sustain Chem Eng*, 2021, **9**, 5095–5104.

31 O. Durupthy, N. Steunou, T. Coradin, J. Maquet, C. Bonhomme and J. Livage, *J. Mater. Chem*., 2005, **15**, 1090–1098.

32 M. Onoda, *Journal of Physics: Condensed Matter*, 2004, **16**, 8957–8969.

33 C. R. Tang, G. Singh, L. M. Housel, S. J. Kim, C. D. Quilty, Y. Zhu, L. Wang, K. J. Takeuchi, E. S. Takeuchi and A. C. Marschilok, *Physical Chemistry Chemical Physics,* 2021, **23**, 8607–8617.

34 M. Trypuć, M. Chałtat and K. Mazurek, *J Chem Eng Data*, 2006, **51**, 322–325.

35 A. I. Volkov, A. S. Sharlaev, O. Ya. Berezina, E. G. Tolstopjatova, L. Fu and V. v. Kondratiev, *Mater Lett*, 2022, **308**, 0–4.

36 R. Li, H. Zhang, Q. Zheng and X. Li, *J Mater Chem A Mater*, 2020, 8, 5186–5193.

37 W. Xu and Y. Wang, *Nanomicro Lett*, 2019, **11**, 1–30.

38 Y. Liu and X. Wu, *Journal of Energy Chemistry*, 2021, **56**, 223–237.

Chapter VI: Scaling-up using pouch cell configuration

In this chapter, the transition from lab-scale Swagelok cells to larger-scale pouch-type cells for zinc-ion batteries (ZIBs) is investigated. Cathode materials tested include spray-dried V_2O_5 and three different sodium vanadium oxides (NVO) materials, optimized in chapters III and V. Detailed preparation of these materials into films and their integration into pouch cells is provided. Galvanostatic tests reveal that spray-dried V_2O_5 achieves high initial capacities in pouch cells, however, it suffers from rapid capacity decay due to material dissolution, gas production, and zinc dendrite growth during electrochemical cycling. $Na_{1.16}V_3O_8$ exhibits excellent capacity retention over cycles, although lower than in lab-scale tests. $Na_2V_6O_{16}\cdot 1.5H_2O$ and $Na_{0.33}V_2O_5$ materials tested in pouch cells deliver high initial capacities similar to Swagelok cells but decrease slightly over cycling. The findings highlight the need for optimization in pouch cell design and materials preparation to enhance capacity retention and cycle life for large-scale ZIB applications.

Keywords: Vanadium pentoxide, NVO materials, aqueous zinc-ion batteries, pouch cell, large scale application, scaling-up

1. Introduction

In the previous chapters, the cathode material was pressed onto a stainless-steel mesh and all electrochemical measurements were conducted in Swagelok configuration (Figure VI-1a). In literature, the majority of ZIB studies were conducted on a small scale in laboratory settings using coin cells or Swagelok cells, while only a limited number of studies have shown their application on a larger scale using pouch-type cells [1]. MnO_2 [2,3], $Na_3V_2(PO_4)_2F_3$@C [4], $Ti_{0.2}V_{1.8}O_{4.9}$ [5], $NH_4V_4O_{10}$ [6], $Zn_{0.125}V_2O_5 \cdot 0.95H_2O$ [7], VO_2 [8,9] and V_2O_5 [10] have been tested as cathode material in pouch cells with aqueous electrolytes like $ZnSO_4$ or $Zn(CF_3SO_3)_2$. In this last chapter of results, we conducted galvanostatic tests using pouch-type cell configuration (Figure VI-1b) as a measurement cell. Pouch cells simulate more closely the operational conditions of commercial batteries used in real-world applications. They provide a larger electrode area and more representative cell geometry with high energy density, which better mimics the environment where the battery will be deployed. Testing in pouch cells is necessary to bridge the gap between research findings and practical applications, ensuring that promising cathode materials can meet the performance and durability requirements of commercial batteries. The improved materials studied in chapters III and V, spray-dried V_2O_5 and the three NVOs phases synthesized, have been investigated as cathode materials in ZIBs pouch cell configuration.

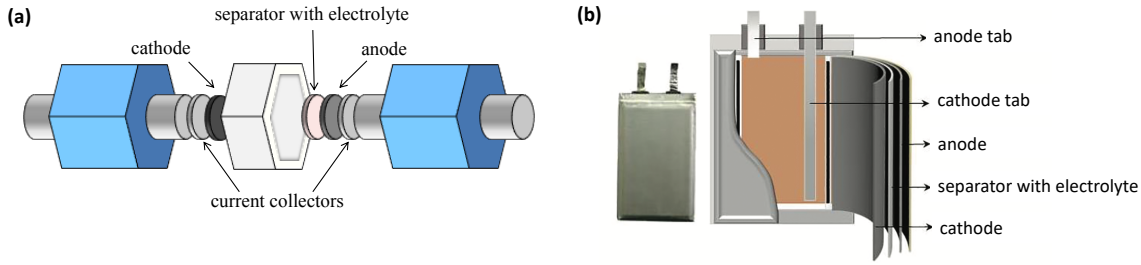

Figure VI-1: Schematic drawing of (a) Swagelok cell and (b) pouch cell configurations (adapted from [11]).

2. Experimental part

2.1. Materials

Spray-dried V_2O_5, $Na_2V_6O_{16} \cdot 1.5H_2O$, $Na_{0.33}V_2O_5$ and $Na_{1.16}V_3O_8$ were synthesized previously. $Zn(CF_3SO_3)_2$ (98%) were purchased from Sigma Aldrich. Carbon black (99.9% purity) and polyvinylidene fluoride (PVDF) were purchased from Alfa Aesar. A 1 mm thick zinc foil and 0.025 mm stainless-steel foil were purchased from Goodfellow.

2.2. Electrode preparation and electrochemical measurements

The electrochemical performance of four samples optimized in this thesis has been investigated in pouch cell configurations: spray-dried V_2O_5, $Na_2V_6O_{16}\cdot 1.5H_2O$, $Na_{0.33}V_2O_5$, and $Na_{1.16}V_3O_8$.

The working electrode was prepared by mixing the active material with carbon black and PVDF in a 70:20:10 weight ratio in N-methyl-2-pyrrolidone. The suspensions were mixed in a speedmixer (Hauschild) from 1200 to 2000 rpm for 3 minutes. The suspension was then spread onto a stainless-steel foil (thickness: 0.025 mm) previously cut in 5 x 8 cm (Figure VI-2a). The active mass is approximately equal to 30 mg against 1-2 mg in the Swagelok cell. The electrodes were dried for 12 h at 80 °C under vacuum to remove the solvent. Electrochemical measurements were conducted in pouch cell configuration using zinc metal foil, Whatman©-type glass fiber filter, and 3 M zinc triflate solution as the anode, separator, and electrolyte, respectively (Figure VI-2b). All cells were tested within a fixed voltage window, between 0.2 and 1.6 V *vs.* Zn/Zn^{2+} in galvanostatic mode at 0.1 A g^{-1} at room temperature using a LAND battery test system (Wuhan, China) (Figure VI-2c).

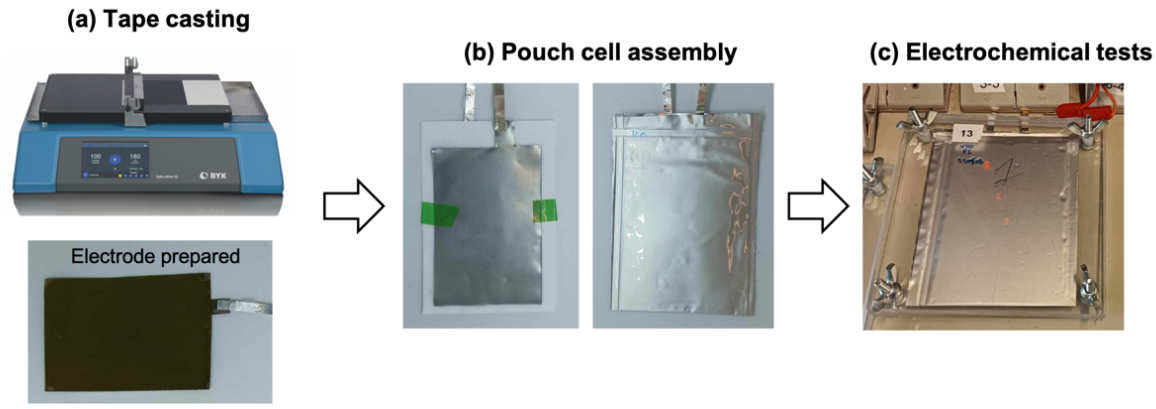

Figure VI-2: (a) Tape casting [12] of cathode material on a stainless-steel foil, (b) assembly of the cathode, separator, and zinc foil with current collectors tabs in pouch cell configuration; and (c) electrochemical measurements configuration.

3. Results and discussion

3.1. Spray-dried V_2O_5 material

As observed on Figure VI-3, the film prepared by mixing spray-dried V_2O_5, CB, and PVDF is uniform, and the integrity of the microspheres is preserved.

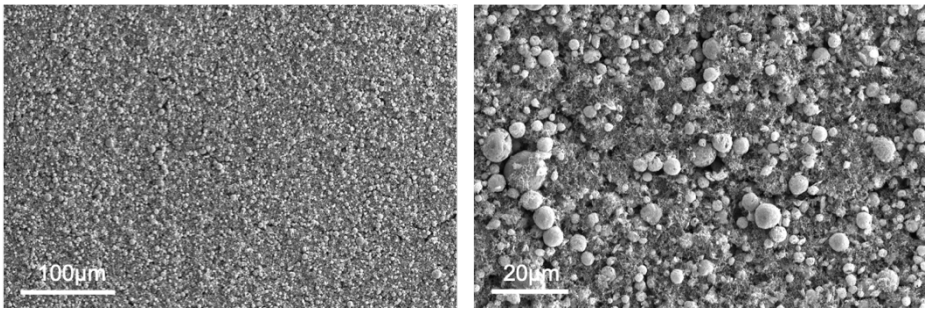

Figure VI-3: SEM images of spray-dried V_2O_5 film before cycling.

Figure VI-4 compares the cycling performance of the spray-dried V_2O_5 materials assembled in Swagelok and pouch-type cells at 0.1 A g^{-1}. Similar to the Swagelok configuration, the charge and discharge capacity of spray-dried V_2O_5 in pouch cell configuration increases over the first 20 cycles due to the activation process as it can be observed in Figure VI-5b. The capacities reach 400 mAh g^{-1} but decrease more rapidly. Moreover, the charge capacity is always higher than the discharge capacity, meaning that coulombic efficiencies are often higher than 100%, indicating that the electrode degrades during cycling. These observations are in good accordance with the galvanostatic discharge/charge curves of the 1st, 10th, 20^{th,} and 30th cycle of spray-dried V_2O_5 material cycled at 0.1 A g^{-1} in Swagelok and pouch cell configurations as represented in Figure VI-5b. The 30th discharge curve in pouch cell configuration is irregular and the two plateaus are not distinguishable anymore, suggesting that undesirable reactions are occurring. The post-mortem pictures of the electrode and the separator are reported in Figure VI-6b. A peeling of the film from the stainless-steel foil and a dissolution of the active material are observed. These observations are in agreement with the electrochemical results. Moreover, in sealed large-format cells, we cannot neglect the Zn anode problems (see section I.4.3.) including Zn dendrite growth and a parasitic hydrogen evolution reaction (HER) at the anode-electrolyte interface that leads to H_2 accumulation and battery swelling as observed on Figure VI-6a [13].

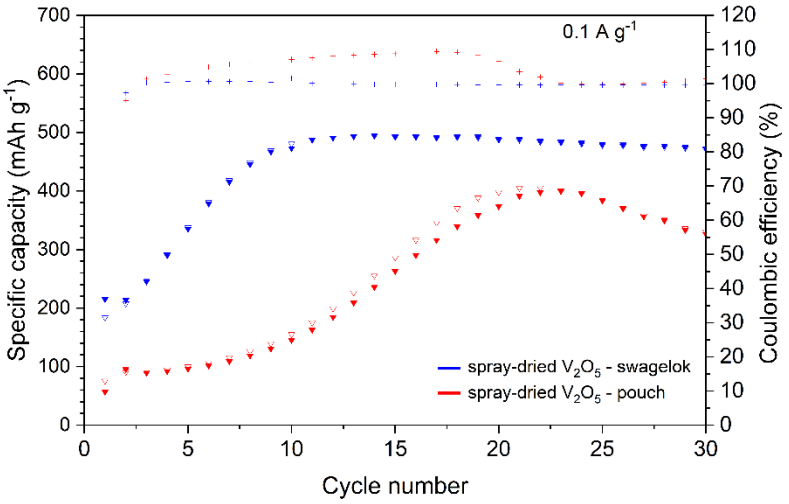

Figure VI-4: Cycling performance at 0.1 A g^{-1} of spray-dried V_2O_5 electrodes assembled in a Swagelok and pouch cell configuration.

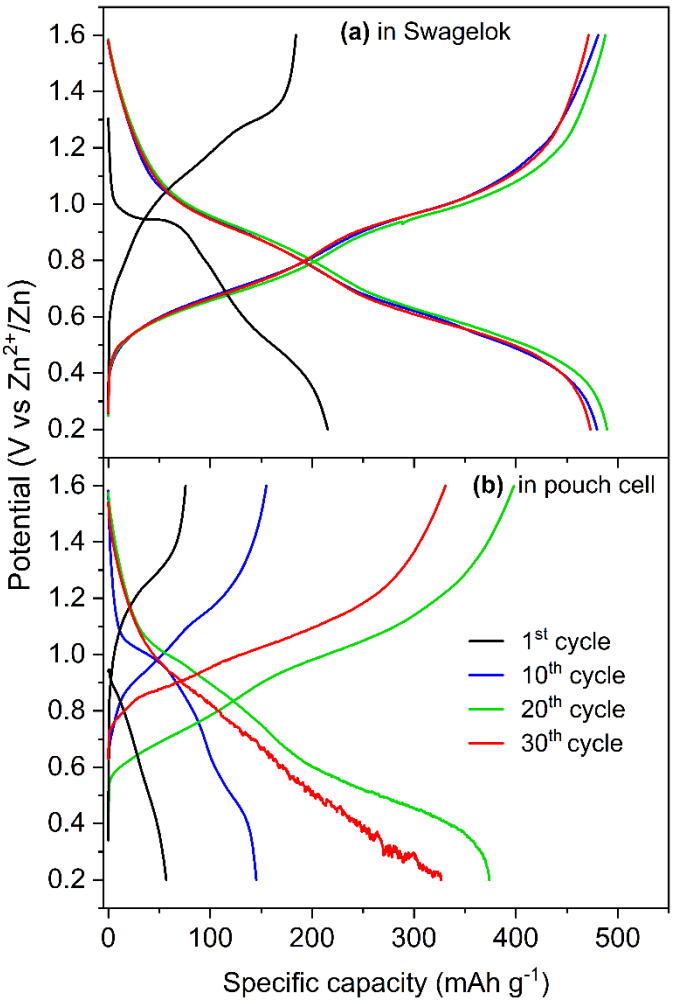

Figure VI-5: Galvanostatic discharge/charge curves (1st, 10th, 20th, and 30th cycle) of spray-dried V_2O_5 material cycled at 0.1 A g^{-1} in (a) a Swagelok cell and (b) a pouch cell configuration.

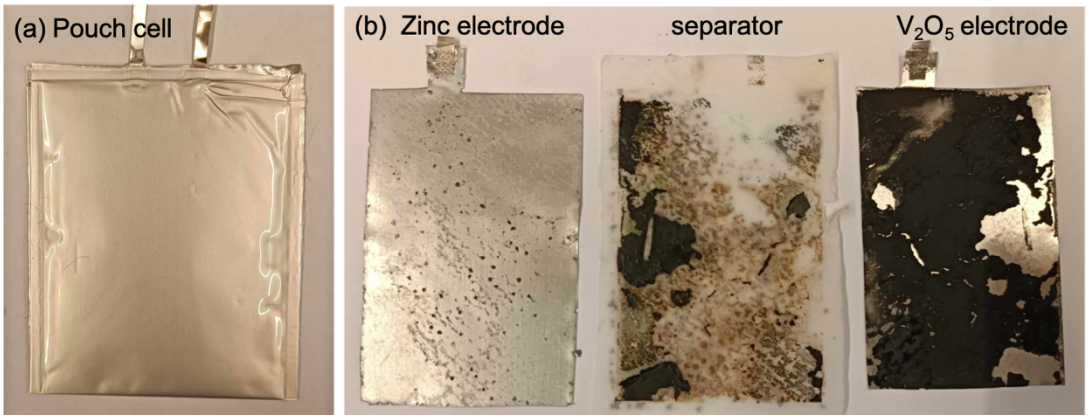

Figure VI-6: Post-mortem pictures of (a) a closed pouch cell and (b) zinc electrode, separator and spray-dried V_2O_5 electrode after 30 cycles at 0.1 A g^{-1} in pouch cell configuration.

Based on these results, we confirm that spray-dried V_2O_5 delivers high capacity in pouch cell configuration, but further optimization of the parameters affecting pouch cell performance (including electrode preparation, electrolyte quantity and type, and sealing) is needed to improve the battery's cycle life.

3.2. NVOs materials

Figure VI-7 reports the cycling performance of $Na_2V_6O_{16}\cdot 1.5H_2O$, $Na_{0.33}V_2O_5$ and $Na_{1.16}V_3O_8$ as electrode materials in zinc-ion pouch cell configuration at 0.1 A g^{-1}. The corresponding charge and discharge curves of the 1st, 15th and 30th cycles are represented in Figure VI-8.

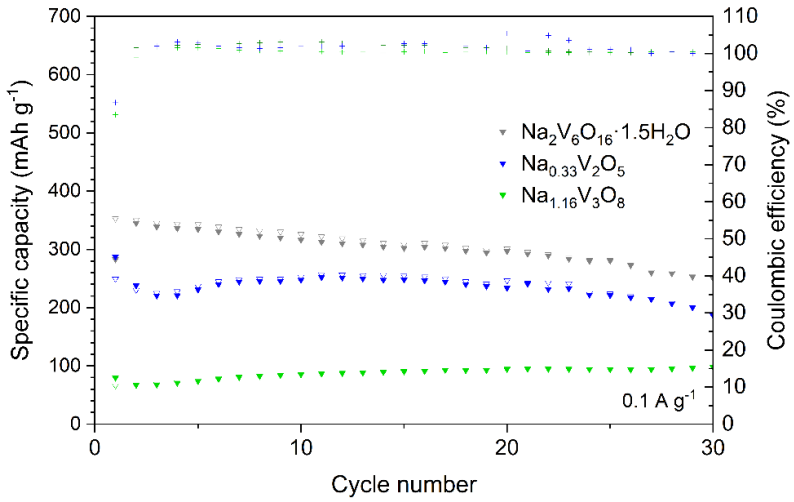

Figure VI-7: Cycling performance at 0.1 A g^{-1} of $Na_2V_6O_{16}\cdot 1.5H_2O$, $Na_{0.33}V_2O_5$ and $Na_{1.16}V_3O_8$ in pouch cell configuration.

The $Na_{1.16}V_3O_8$ material initially exhibits a low capacity of 70 mAh g^{-1} that increases to 100 mAh g^{-1} along cycling, indicating that the number of active sites also rises over time due to the gradual impregnation of electrolyte. However, the specific capacities obtained for $Na_{1.16}V_3O_8$ are much lower than in lab-scale tests.

It can be seen in Figure VI-7 that the capacities decreased for the first two cycles for $Na_{0.33}V_2O_5$. The corresponding coulombic efficiencies are lower than 100% which can be attributed to the trapping of Zn^{2+} or the formation of irreversible by-products. As in Swagelok configuration (Figure V-16), the discharge/charge curves evolve during cycling; no plateau is detected at 0.8 and 1V during discharge and charge respectively for the first cycle (Figure VI-8b). Then, the capacities increase for the following cycles to reach a high capacity of 250 mAh g^{-1} against 265 mAh g^{-1} in the Swagelok cell (Figure V-17a). Not surprisingly, the highest capacities are detected for $Na_2V_6O_{16}\cdot 1.5H_2O$. While the initial capacities of $Na_2V_6O_{16}\cdot 1.5H_2O$ and $Na_{0.33}V_2O_5$ are similar in both configurations (comparison with Figure V-17a), the capacities decrease more rapidly during cycling in the pouch cell than in Swagelok configuration. Moreover, irregularities are observed in the 30th discharge curve as for spray-dried V_2O_5 meaning that this phenomenon is not directly linked with the cathode material but with the pouch cell configuration itself. It can be seen in pictures presented in Figure VI-9 that the NVOs materials do not dissolve during cycling but that a zinc metal deposition is observed through the separator.

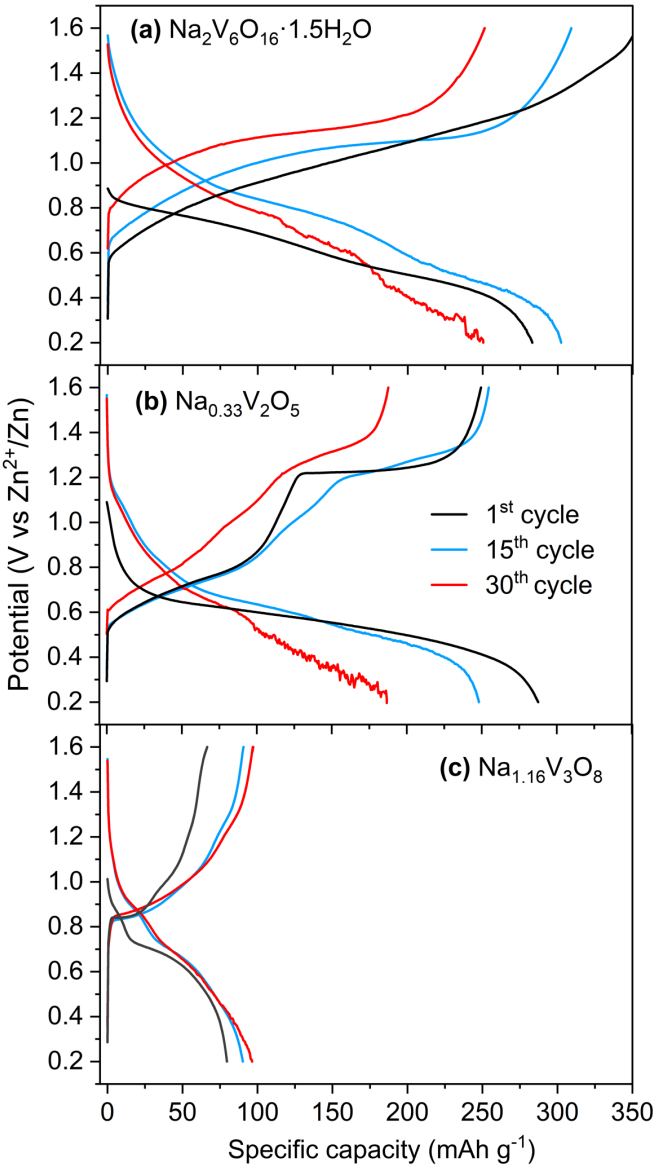

Figure VI-8: Galvanostatic discharge/charge curves (1st, 15th and 30th cycle) of $Na_2V_6O_{16}\cdot1.5H_2O$, $Na_{0.33}V_2O_5$ and $Na_{1.16}V_3O_8$ cycled at 0.1 A g^{-1} in pouch cell configuration.

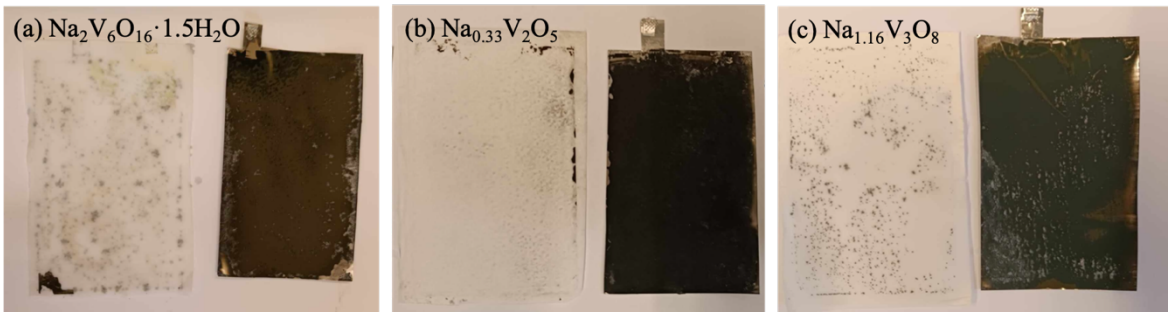

Figure VI-9: Post-mortem picture of (a) $Na_2V_6O_{16}\cdot1.5H_2O$, (b) $Na_{0.33}V_2O_5$ and (c) $Na_{1.16}V_3O_8$ electrodes and their separators after cycling in pouch cell configurations at 0.1 A g^{-1}.

4. Conclusion

In this chapter, the cycling performance of $Na_2V_6O_{16}\cdot 1.5H_2O$, $Na_{0.33}V_2O_5$ and $Na_{1.16}V_3O_8$ and spray-dried V_2O_5 were evaluated at 0.1 A g^{-1} in pouch cell type, a larger scale application with an aqueous electrolyte. The active material quantity tested is 15 to 30 times higher than in the Swagelok configuration.

Even if the number of activation cycles is slightly higher, with 20 cycles, the spray-dried V_2O_5 material reaches good capacities with 400 mAh g^{-1} in the pouch cell. However, the capacities decrease more rapidly meaning that the electrode is damaged. Then, although capacities obtained for $Na_2V_6O_{16}\cdot 1.5H_2O$ and $Na_{0.33}V_2O_5$ decrease slightly during cycling in pouch cell, the initial capacities are similar to in Swagelok. However, the specific capacities exhibited by $Na_{1.16}V_3O_8$ materials are two times lower than in the Swagelok configuration. For all cathode materials tested, swelling of the pouch cell probably due to H_2 accumulation and zinc metal deposition is observed meaning that further anode optimizations are needed before using large-scale format. Moreover, while further studies focusing on the electrode preparation and degradation are needed for extended cycling, these pouch cells preliminary tests show a promising electrochemical performance for V_2O_5 or $Na_2V_6O_{16}\cdot 1.5H_2O$, $Na_{0.33}V_2O_5$ cathode material for ZIBs.

5. References

1 S. Mallick and C. R. Raj, *ChemSusChem*, 2021, **14**, 1987–2022.

2 Y. Huang, J. Liu, Q. Huang, Z. Zheng, P. Hiralal, F. Zheng, D. Ozgit, S. Su, S. Chen, P. H. Tan, S. Zhang and H. Zhou, *Flexible Electronics*, 2018, **2**

3 P. Chen, W. Zhou, Z. Xiao, S. Li, Z. Wang, Y. Wang and S. Xie, *Nano Energy*, 2020, **74**, 104905.

4 W. Li, K. Wang, S. Cheng and K. Jiang, *Energy Storage Mater*, 2018, **15**, 14–21.

5 Z. Wei, X. Wang, T. Zhu, P. Hu, L. Mai and L. Zhou, *Chinese Chemical Letters*, 2024, **35**, 108421.

6 H. Li, L. Yang, S. Zhou, J. Li, Y. Chen, X. Meng, D. Xu, C. Han, H. Duan and A. Pan, *Adv Funct Mater*, 2024, **34**, 1–9.

7 J. J. Ye, P. H. Li, H. R. Zhang, Z. Y. Song, T. Fan, W. Zhang, J. Tian, T. Huang, Y. Qian, Z. Hou, N. Shpigel, L. F. Chen and S. X. Dou, *Adv Funct Mater*, 2023, **33**, 1–10.

8 W. Deng, Z. Xu, G. Li and X. Wang, *Smal*l, 2023, **19**, 2207754

9 X. Dai, F. Wan, L. Zhang, H. Cao and Z. Niu, *Energy Storage Mater*, 2019, **17**, 143–150.

10 L. Wang, W. Huang, W. Guo, Z. H. Guo, C. Chang, L. Gao and X. Pu, *Adv Funct Mater*, 2022, **32**, 1–9.

11 Y. Liang, C. Z. Zhao, H. Yuan, Y. Chen, W. Zhang, J. Q. Huang, D. Yu, Y. Liu, M. M. Titirici, Y. L. Chueh, H. Yu and Q. Zhang*, InfoMat*, 2019, **1**, 6–32.

12 BYK tape casting, https://www.byk-instruments.com/en/Physical-Properties/Paint-Application/Automatic-Film-Applicators/Large-Automatic-Film-Applicator/c/p-6135?variant=2131, (accessed 4 June 2024).

13 F. Wang, J. Zhang, H. Lu, H. Zhu, Z. Chen, L. Wang, J. Yu, C. You, W. Li, J. Song, Z. Weng, C. Yang and Q. H. Yang, *Nat Commun*, 2023, **14**, 1–10

Chapter VII: Conclusions and outlooks

1. Conclusions

Rechargeable batteries hold a predominant position among energy storage systems, owing to their wide array of applications such as portable devices, electric vehicles and grid storage. The development of efficient energy storage systems must address current energy and technological needs while also considering environmental and safety concerns.

This thesis delves into the exploration of two distinct battery types: lithium-ion batteries (LIBs) and zinc-ion batteries (ZIBs). Each battery type possesses unique attributes that render it noteworthy in specific domains: LIBs are expected to maintain their dominance in the market for electronic devices and mobility applications, owing to their well-established performance and compatibility. Conversely, ZIBs emerge as a compelling option for grid energy storage applications, offering distinct advantages such as safety, cost-effectiveness, and potentially superior scalability and recyclability. By investigating both LIBs and ZIBs, this work aims to contribute to the development of diverse battery technologies capable of addressing various energy challenges posed by the evolving needs of society.

This thesis focuses on two research axes: the development of anode active material for Li-ion batteries and the study and the optimization of cathode active material in aqueous zinc-ion batteries.

1.1. Organopalladium complexes ($XPd(4\text{-}AcOC_6H_4)(PPh_3)_2$, with X = I, Br and Cl) as anode materials for Li-ion batteries

The first part of this thesis focused on synthesizing and examining three novel pure palladium complexes: trans-$XPd(4\text{-}AcOC_6H_4)(PPh_3)_2$, where X represents I, Br, and Cl, for their potential use as anode active materials in lithium-ion batteries. Our research revealed that the type of halogen ligand (X = I, Br, and Cl) significantly influences the reaction mechanism during the initial discharge and cycling performance. Further analysis was conducted on the iodine ligand [$IPd(4\text{-}AcOC_6H_4)(PPh_3)_2$], which demonstrated the most promising electrochemical performance, with an average discharge capacity of approximately 170 mAh g^{-1} at 50 mA g^{-1}. However, this capacity remains relatively low compared to other organometallic compounds and graphite (the commercial anode for LIBs). To address this, we employed the double emulsion-evaporation technique to modify the

particle architecture, resulting in spherical hollow or dense micro- and nanoparticles. The as-prepared iodocomplex spheres, after a week of homogenization, showed a significantly enhanced capacity of around 800 mAh g^{-1} at a current density of 50 mA g^{-1} for the first discharge and 1100 mAh g^{-1} after 110 cycles. This capacity is three times higher than that of graphite. These findings highlight the crucial role of electrode architecture design and homogenization duration in improving the electrochemical performance of organopalladium complexes as anode materials for lithium-ion batteries.

1.2. Improving electrode performance of V_2O_5 as cathode materials for Zn-ion batteries

The second part of this thesis focused on V_2O_5 as cathode materials for rechargeable aqueous zinc-ion batteries. V_2O_5 emerges as a promising candidate for rechargeable aqueous zinc ion batteries because it has the highest theoretical capacity of vanadium-based cathode material and a structure well-suited for zinc ion insertion/extraction. Nonetheless, its application in large-scale settings encounters some limitations, including vanadium dissolution, structural instability, low electronic conductivity, and restricted practical capacity. Addressing these challenges necessitates innovative solutions to enhance the overall performance and viability of V_2O_5 in practical applications. The electrochemical performance of all materials studied and optimized in this work is summarized in Table VII-1.

In this part, we first tailored the morphological design of vanadium pentoxide cathode material through a one-step spray-drying process. The solid microspheres obtained exhibited remarkable performance, showcasing high capacities of 495 mAh g^{-1} at 0.1 A g^{-1} after only 15 cycles of activation and 240 mAh g^{-1} at 5 A g^{-1}. Conversely, the specific capacity of commercial V_2O_5 stabilized at 400 mAh g^{-1} after 35 cycles at 0.1 A g^{-1} and reached barely 155 mAh g^{-1} at high rate. Furthemore, excellent capacity retention of 93% was observed after 1000 cycles at high current density for spray-dried V_2O_5. Subsequently, V_2O_5/xCNTs composites were synthesized by integrating x (from 5 to 20) wt% of carbon nanotubes into the V_2O_5 suspension before spray-drying. The incorporation of carbon nanotubes effectively boosted electronic conductivity and expanded the specific surface area, thereby positively influencing the electrochemical properties of vanadium pentoxide. This CNT integration resulted in significant enhancement in rate capability, especially at elevated current

densities. Remarkably, the composite material sustained a capacity of 290 mAh g^{-1} over 1000 cycles, highlighting its potential for prolonged cycling stability and its suitability for practical utilization in rechargeable battery systems.

Following this, V_2O_5 particles were coated with polydopamine through a self-polymerization process of dopamine. Analyses including SEM, TEM, TGA, FTIR-ATR and XPS revealed a partial reduction of V^{5+} to V^{4+} and the formation of a thin polydopamine layer around V_2O_5 microparticles, with 15% PDA being the optimal amount of polymer. Combining V_2O_5/PDA with CNT allowed us to obtain a self-standing, binder-free cathode material with a high capacity of ~530 mAh g^{-1} at 0.1 A g^{-1}. The entangled CNT network between V_2O_5/PDA particles facilitated excellent electron conduction, while the PDA coating served as a protective barrier, mitigating vanadium dissolution, reducing by-product formation, and preventing structural deterioration. The electrochemical performance of the optimized V_2O_5/PDA/CNT surpassed that of V_2O_5/CNT and V_2O_5/CB/PVDF across various current densities. The V_2O_5/PDA/CNT electrode demonstrated impressive rate capability, delivering specific capacities of 530, 528, 523, 510, and 500 mAh g^{-1} at 0.2, 0.5, 1, 3, and 5 A g^{-1}, respectively, while also maintaining exceptional long-term cycling stability up to 1000 cycles at high current density. This synergistic combination of PDA coating with carbon nanotubes incorporation emerges as a promising strategy for enhancing the electrochemical performance and stability of V_2O_5 in zinc-ion batteries.

The last strategy explored in this thesis concerned the incorporation of Na^+ ions into the structure of V_2O_5, acting as stabilizing pillars during cycling. Three sodium vanadium oxide phases were synthesized purely by initially mixing V_2O_5 powder in NaCl solution: $Na_2V_6O_{16}\cdot 1.5H_2O$, β-$Na_{0.33}V_2O_5$ and $Na_{1.16}V_3O_8$. The crystallization of lyophilized precursors was monitored by high-temperature X-ray diffraction. We discovered that pure β-$Na_{0.33}V_2O_5$ can be produced by the heat treatment of a precursor powder with the correct proportion of NVO and residual V_2O_5, transitioning through an intermediate $Na_{1+x}V_3O_8$ phase. Additionally, it was shown that the barnesite-like NVO phase converts to $Na_{1.16}V_3O_8$ when an extra sodium source, such as NaCl, is present.

$Na_2V_6O_{16}\cdot 1.5H_2O$ particles initially appeared as long and thin nanobelts similar to fibers but became thicker and shorter nanobelts after calcination into β-$Na_{0.33}V_2O_5$ and $Na_{1.16}V_3O_8$. The β-$Na_{0.33}V_2O_5$ material exhibited a very stable discharge capacity of about 265 mAh g^{-1}

at 0.1 A g^{-1} though this capacity dropped to 30 mAh g^{-1} when the current density increased to 5 A g^{-1}. This decrease is attributed to the tunnel-like structure of β-$Na_{0.33}V_2O_5$ which, while stable, limits zinc ion insertion/extraction at high current densities. Conversely, the layered structure of $Na_2V_6O_{16}\cdot 1.5H_2O$ and $Na_{1.16}V_3O_8$ phases facilitated the zinc ions insertion during electrochemical cycling. These structural variances and configurations significantly influence the electrochemical properties. The hydrated material, NVO, emerges as the most suitable sodium vanadium oxide candidate for zinc-ion batteries considering its synthesis process and electrochemical performance.

Table VII-1: Electrochemical performance of all materials developed in this thesis – capacities at low and high current densities, number of activation cycles at 0.1 A g^{-1}, number of cycles at 5 A g^{-1} and corresponding capacity retention, capacity retention obtained for the rate capability passing from 0.2 to 5 A g^{-1}.

Material	**Capacities at low current density (0.1 A g^{-1})**	**Number activation cycles (0.1 A g^{-1})**	**Capacities at high current density (5 A g^{-1})**	**Cycles - Retention (%)**	**Retention (%) from 0.2 to 5 A g^{-1}**
Commercial V_2O_5	400 mAh g^{-1}	35	155 mAh g^{-1}	Constant increase	/
Spray-dried V_2O_5	495 mAh g^{-1}	15	240 mAh g^{-1}	1000 - 93%	71
V_2O_5/5CNT	500 mAh g^{-1}	10	290 mAh g^{-1}	1000 - 90%	81
V_2O_5/PDA/CNT	530 mAh g^{-1}	20	370 mAh g^{-1}	1000 - 77%	94
$Na_2V_6O_{16}\cdot 1.5H_2O$	315 mAh g^{-1}	/	160 mAh g^{-1}	2000 - ~100%	50
$Na_{0.33}V_2O_5$	265 mAh g^{-1}	/	30 mAh g^{-1}	2000 - ~100%	5
$Na_{1.16}V_3O_8$	250 mAh g^{-1}	30	130 mAh g^{-1}	Constant increase	43

As the final step of this research, the cycling performance of spray-dried V_2O_5 and three sodium vanadium oxide materials ($Na_2V_6O_{16}\cdot 1.5H_2O$, $Na_{0.33}V_2O_5$, and $Na_{1.16}V_3O_8$) was evaluated in larger-scale pouch-type zinc-ion batteries (ZIBs) to evaluate the feasibility of these cathode materials in commercial batteries. Spray-dried V_2O_5 reaches a capacity of 400 mAh g^{-1} after 20 activation cycles, but its capacity declines rapidly, indicating electrode damage. The capacities exhibited by $Na_2V_6O_{16}\cdot 1.5H_2O$ and $Na_{0.33}V_2O_5$ slightly decrease during cycling but the initial capacities are similar to those in Swagelok cells. All cathode materials tested show a pouch cell swelling, likely due to hydrogen accumulation, and zinc metal deposition, suggesting the need for anode optimizations. Despite these challenges, the preliminary pouch cell tests demonstrated promising electrochemical performance for V_2O_5, $Na_2V_6O_{16}\cdot 1.5H_2O$, and $Na_{0.33}V_2O_5$ as cathode materials for large-scale ZIB applications, but emphasized the necessity for further optimization in pouch cell design and electrode preparation to improve cycle life.

2. Outlooks

The perspectives of this thesis are numerous as the topics addressed are recent and relevant, especially for V_2O_5 as cathode materials for zinc-ion batteries.

First, it would be interesting to deeply investigate the reaction mechanism to explain the activation process of V_2O_5 as cathode materials in ZIBs because it is still under debate. *Operando, in-situ or ex-situ* XRD, XPS and Raman experiments will be needed to investigate the storage mechanism in the spray-dried V_2O_5 cathode material for ZIBs. We developed an *operando* XRD setup in aqueous medium (Figure I-1a), but the preliminary results do not yet allow us to draw conclusions on the reaction mechanisms during discharge and charge processes.

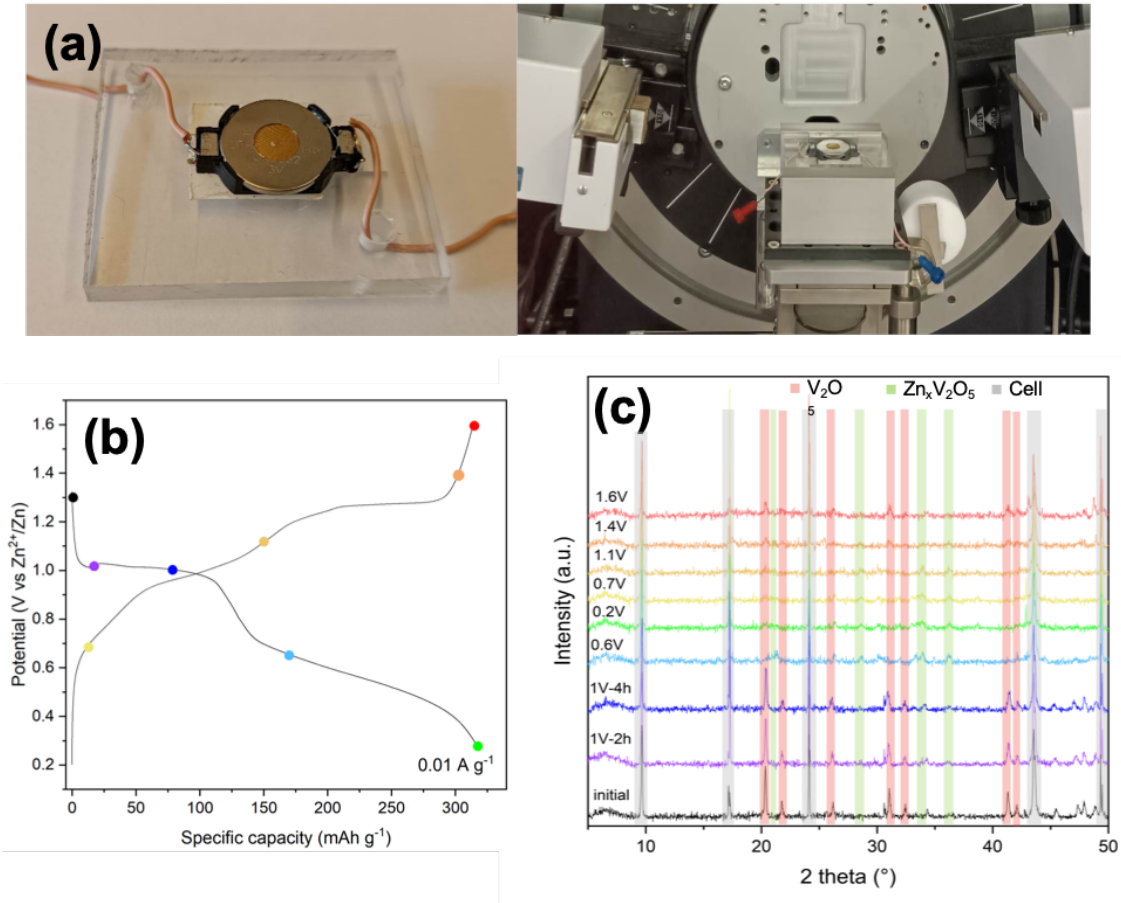

Figure I-1: (a) Pictures of handmade setup for operando XRD experiments; (b) discharge/charge cycling curves and (c) operando XRD measurements conducted at 0.01 A g^{-1} on spray-dried V_2O_5 material.

Figure I-1c displays some relevant diffractograms of the *operando* measurements conducted on spray-dried V_2O_5 for the first cycle. During the discharge to 0.2 V, the V_2O_5 peaks intensities decrease, and some small peaks appear at 0.6 V that could be partially attributed

to a new Zn intercalation phase, $Zn_xV_2O_5$ [1]. After the charge at 1.6 V, the V_2O_5 peaks are detected revealing the reversible insertion/extraction of Zn^{2+} but with a lower degree of crystallinity. *Operando* Raman measurements have also been tested on spray-dried V_2O_5 cathode material (Figure I-2). During the discharge to 0.2 V, the characteristic peaks of V_2O_5 gradually decrease. However, no new peak can be detected with *operando* Raman setup. After the first charge at 1.6 V, the V_2O_5 peaks are detected with lower intensity as for XRD measurements. Understanding the reaction mechanism will require additional work and experiments with complementary *ex-situ* techniques at the initial state and after activation.

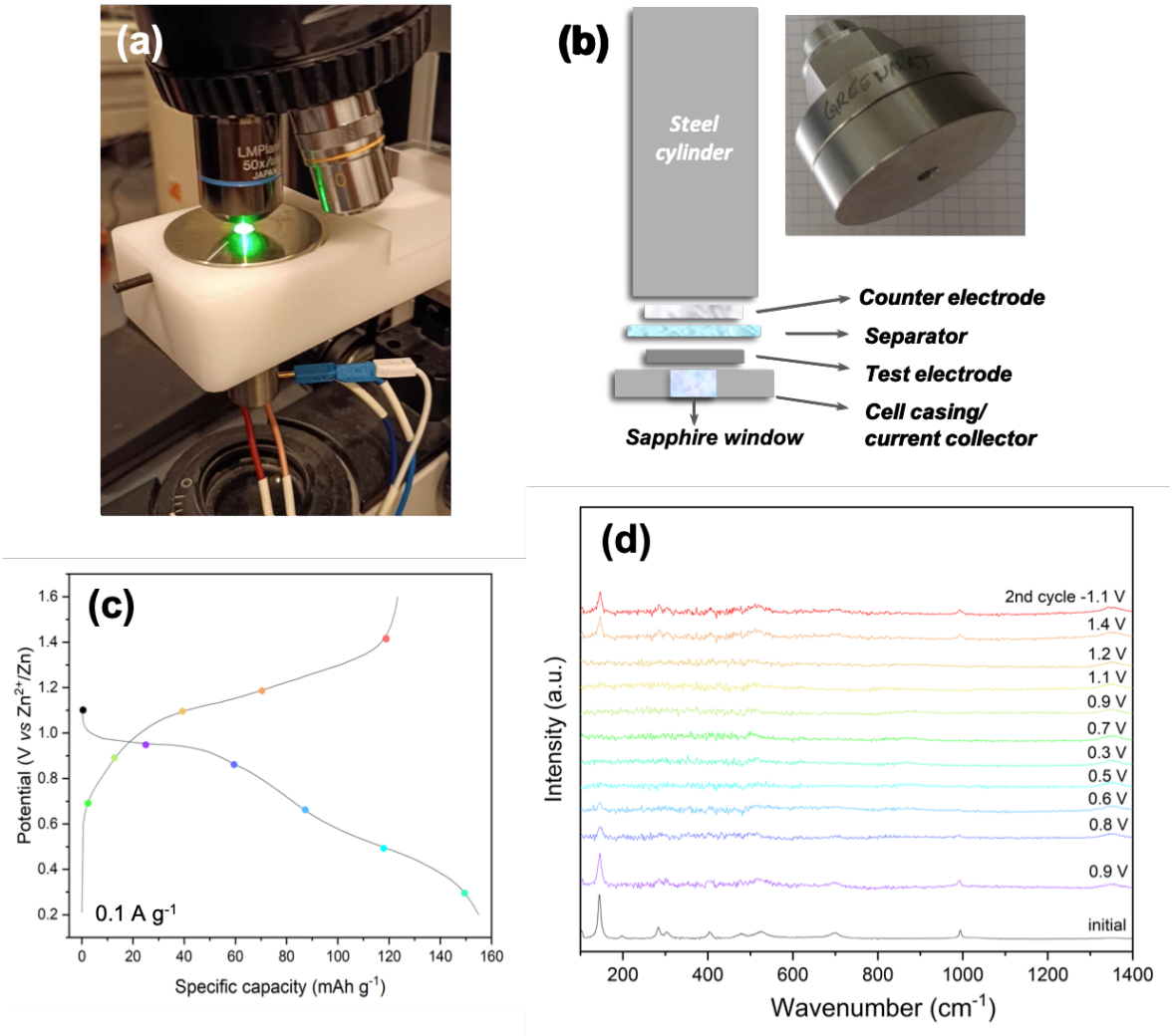

Figure I-2: (a) Picture of operando Raman setup; (b) Illustration and picture of operando Raman cell; (c) discharge/charge cycling curves and (d) operando Raman measurements conducted at 0.1 A g^{-1} on spray-dried V_2O_5 material.

Then, it would be intriguing to combine various strategies explored in this study. For example, using a spray-drying process, which is readily scalable, to create a core-shell structure with a polymer could be beneficial for customizing the morphological design and mitigating vanadium dissolution. Through this approach, carbon additives could be easily incorporated to enhance electronic conductivity as investigated in this thesis.

NVO materials synthesized in this work have not been yet optimized. Tailoring the morphology and adding carbon additives could help to improve their electrochemical performance, especially at high current density.

Regarding electrode preparation, in Swagelok tests, active materials are pressed onto a stainless-steel mesh, which is suboptimal for achieving homogeneity and thickness control. Optimizing the parameters of electrode preparation by using a slurry that can be spread onto a foil is crucial for large-scale applications. Additionally, as mentioned earlier, for large-scale applications, a post-mortem analysis of electrode during long-term cycling should be conducted for the investigation of the degradation phenomena.

3. References

1 P. Byeon, Y. Hong, H. Bin Bae, J. Shin, J. W. Choi and S. Y. Chung, *Nat Commun*, 2021, **12**, 1–11.